

WAVELENGTH CONVERSION IN DOMAIN-DISORDERED QUASI-PHASE
MATCHING SUPERLATTICE WAVEGUIDES

by

Sean Jorge Wagner

A thesis submitted in conformity with the requirements
for the degree of Doctor of Philosophy
Graduate Department of The Edward S. Rogers Sr. Department of
Electrical and Computer Engineering
University of Toronto

Copyright © 2011 by Sean Jorge Wagner

Abstract

Wavelength Conversion in Domain-Disordered Quasi-Phase Matching Superlattice
Waveguides

Sean Jorge Wagner
Doctor of Philosophy

Graduate Department of The Edward S. Rogers Sr. Department of Electrical and
Computer Engineering
University of Toronto

2011

This thesis examines second-order optical nonlinear wave mixing processes in domain-disordered quasi-phase matching waveguides and evaluates their potential use in compact, monolithically integrated wavelength conversion devices. The devices are based on a GaAs/AlGaAs superlattice-core waveguide structure with an improved design over previous generations. Quantum-well intermixing by ion-implantation is used to create the quasi-phase matching gratings in which the nonlinear susceptibility is periodically suppressed.

Photoluminescence experiments showed a large band gap energy blue shift around 70 nm after intermixing. Measured two-photon absorption coefficients showed a significant polarization dependence and suppression of up to 80% after intermixing. Similar polarization dependencies and suppression were observed in three-photon absorption and nonlinear refraction. Advanced modeling of second-harmonic generation showed reductions of over 50% in efficiency due to linear losses alone. Self-phase modulation was found to be the dominant parasitic nonlinear effect on the conversion efficiency, with reductions of over 60%. Simulations of group velocity mismatch showed modest reductions in efficiency of less than 10%.

Experiments on second-harmonic generation showed improvements in efficiency over previous generations due to low linear loss and improved intermixing. The improvements

permitted demonstration of continuous wave second-harmonic generation for the first time in such structures with output power exceeding 1 μ W. Also, Type-II phase matching was demonstrated for the first time. Saturation was observed as the power was increased, which, as predicted, was the result of self-phase modulation when using 2 ps pulses. By using 20 ps pulses instead, saturation effects were avoided. Thermo-optically induced bistability was observed in continuous wave experiments.

Difference frequency generation was demonstrated with wavelengths from the optical C-band being converted to the L- and U-bands with continuous waves. Conversion for Type-I phase matching was demonstrated over 20 nm with signal and idler wavelengths being separated by over 100 nm. Type-II phase matched conversion was also observed. Using the experimental data for analysis, self-pumped conversion devices were found to require external amplification to reach practical output powers. Threshold pump powers for optical parametric oscillators were calculated to be impractically large. Proposed improvements to the device design are predicted to allow more practical operation of integrated conversion devices based on quasi-phase matching superlattice waveguides.

Acknowledgements

First and foremost, I would like to thank my supervisors, Prof. J. Stewart Aitchison and Prof. Amr Helmy. Their support, resources, advice, experience, and guidance were instrumental in the completion of this work.

Many thanks and much appreciation are owed to Prof. David C. Hutchings and his group at the University of Glasgow. Prof. Hutchings initiated this project, and gladly included myself as a collaborator. Discussions with Prof. Hutchings either in person, by conference calls, or via E-mail helped a great deal. Dr. Barry M. Holmes and Dr. Usman Younis produced the superlattice waveguide samples that were characterized in this thesis. Without their hard work, this project would not have been possible and they deserve much appreciation for their efforts.

Thank you to Prof. Majid Ebrahim-Zadeh and his group at the Institut de Ciències Fotòniques in Barcelona for participating in this project. Prof. Ebrahim-Zadeh provided much guidance and graciously allowed me to conduct work using his facilities and equipment. Mr. Omid Kokabee built the 20 ps laser system used in this study according to our needs and his efforts are appreciated. I would also like to thank Mr. S. Chaitanya Kumar Suddapalli for his help in conducting the experiments at ICFO and for useful discussions.

As with my previous work, Dr. Daniele Modotto of the Università di Brescia deserves much appreciation for contributing his BPM simulation code for simulations of nonlinear and dispersion effects in waveguides. Mr. Ahmed Al-Muhairi, an undergraduate student at the University of Toronto, extended the code to add new capabilities necessary for the work in this thesis. It was a pleasure to work with Mr. Al-Muhairi and I wish him all the best in his career.

I would also like to extend my gratitude to several of my fellow students and colleagues who aided with the work in this thesis. Dr. Aaron Zilkie helped out with the laboratory work and my discussions with him were always helpful. Mr. Iliya Sigal helped with laboratory measurements and mathematical derivations. His involvement in this project was instrumental and I wish him all the best in his career. Dr. Henry Lee and Mr. Yimin Zhou deserve my gratitude for helping me with the equipment in the cleanroom.

Thank you as well to Mr. Bhavin Bijlani, Mr. Payam Abolghasem, Mr. Chris Sapiano, Dr. Junbo Han, Dr. Rajiv Iyer, Dr. Scott Kuntze, Dr. Ksenia Dolgaleva, and Mr. Muhammed Alam for their many insightful discussions, helpful advice, and work in the laboratory and in the cleanroom.

I would like to thank my committee members, Prof. Joyce Poon, Prof. Edward Sargent, Prof. Wai Tung Ng, and Dr. Siegfried Janz for volunteering their time and efforts.

Thank you to NSERC for providing financial support in the form of a Postgraduate Scholarship. The Ontario Centres of Excellence provided an International Scholarship, allowing me to conduct research at the University of Glasgow and the Institut de Ciències Fotòniques, for which I am grateful. Thank you as well to SPIE for awarding me a Scholarship in Optical Science and Engineering. I also extend my gratitude to the Edward S. Rogers Department of Electrical and Computer Engineering for their financial support through fellowships and teaching assistantships.

To my friends and family, your support in this endeavor was very much appreciated and I am grateful. Lastly, thank you to Kathleen for your support, kindness, understanding, and companionship.

Contents

List of Tables	x
List of Figures	xv
Abbreviations	xvi
1 Introduction	1
1.1 Motivation for Compact Wavelength Converters	1
1.2 Nonlinear Optics	3
1.3 Photonic Integrated Circuits in Compound Semiconductors	6
1.4 Single-Chip Wavelength Conversion Devices	7
1.5 Quantum Well Intermixing	9
1.6 Semiconductor Superlattices	11
1.7 Domain-Disordered Quasi-Phase Matching	12
1.8 Scope and Outline of Thesis	13
2 Phase Matching in Semiconductors	15
2.1 Introduction	15
2.2 Basic Theory	16
2.2.1 Coupled Mode Equations	16
2.2.2 Type-I and Type-II Interactions	19
2.2.3 Conversion Efficiency	22
2.3 Phase-Matching Techniques	24
2.3.1 Form-Birefringent Phase Matching	25

2.3.2	Modal Phase Matching	27
2.3.3	Quasi-Phase Matching	29
2.3.4	Domain Disordered QPM	33
2.3.5	Comparison of Phase Matching Methods	37
2.4	Conclusions	38
3	Superlattice Waveguides: Design and Characterization	40
3.1	Introduction	40
3.2	Waveguide Structure	41
3.3	Linear Optical Properties	43
3.3.1	Photoluminescence of As-grown and Intermixed Superlattice . . .	43
3.3.2	Etch Depth and Mode Profiles	45
3.3.3	Transmission and Linear Loss at Second-Harmonic/Pump Wavelengths	49
3.3.4	Effective Index and Predicted QPM Periods	52
3.4	High-Order Nonlinear Properties	54
3.4.1	Experimental Setup	55
3.4.2	Two- and Three-Photon Absorption Coefficients	56
3.4.3	Nonlinear Refractive Index	60
3.5	Conclusions	63
4	Advanced Modeling of QPM Waveguides	65
4.1	Introduction	65
4.2	Nonlinear Propagation Equations	66
4.3	Effect of Linear Loss	69
4.4	Conversion Bandwidth	71
4.5	Modulation Depth of $\chi^{(2)}$	74
4.6	High-Order Nonlinear Effects	76
4.7	Group Velocity Mismatch and Dispersion	79
4.8	Conclusions	82

5 Characterization of SHG	85
5.1 Introduction	85
5.2 DD-QPM Waveguide Fabrication	86
5.2.1 Grating Formation	87
5.2.2 Waveguide Formation	90
5.3 2-ps Pulse Experiments	92
5.3.1 Experimental Setup	92
5.3.2 Results	94
5.4 Continuous Wave Experiments	108
5.4.1 Experimental Setup	108
5.4.2 Results	110
5.5 20-ps Pulse Experiments	121
5.5.1 Experimental Setup	122
5.5.2 Results	123
5.6 Analysis	127
5.6.1 Effective Index Mismatch	127
5.6.2 Effective $\chi^{(2)}$	129
5.7 Conclusions	132
6 Wavelength Conversion by DFG	135
6.1 Introduction	135
6.2 Modeling	136
6.2.1 Conversion Bands	137
6.2.2 Conversion Efficiency and Coupling Coefficient	141
6.3 Conversion Experiments	143
6.3.1 Experimental Setup	143
6.3.2 Results	146
6.4 Application to Integrated Wavelength Conversion Devices	150
6.4.1 Parametric Converter	151
6.4.2 Optical Parametric Oscillator	154

6.5	Design Improvements	160
6.5.1	Fabrication Optimization	161
6.5.2	High Confinement Waveguides	162
6.5.3	Vertical Integration	164
6.5.4	Potential Device Performance	166
6.6	Conclusions	169
7	Conclusions	171
7.1	Summary of Results	171
7.2	Future Work	174
A	Nonlinear Propagation Equations	177
A.1	Three-Wave Mixing	177
A.2	Effective Areas and Nonlinear Coefficients	184
A.3	Second-Harmonic Generation	187
B	Detailed Waveguide Properties	190
B.1	Effective Mode Index	190
B.2	Group Velocity and Dispersion	191
B.3	Second-Order Nonlinear Coefficients	192
Bibliography		193

List of Tables

2.1	SHG performance for wavelengths between 1500 nm to 2000 nm of various phase matching types from literature	38
4.1	Parameter values used in simulations of high-order nonlinear effects with DD-QPM waveguides for the Type-I SHG interaction	77
4.2	Parameter values used in simulations of high-order nonlinear effects with DD-QPM waveguides for the Type-II SHG interaction	80
4.3	Parameter values used in simulations of dispersion effects with 1.0 μm -deep DD-QPM waveguides for SHG.	81
5.1	Designed and actual duty cycles in the ion implantation mask	89
5.2	Summary of SHG performance for Sample A and Sample B with 2 ps pulses	95
5.3	Continuous wave SHG performance of Sample A QPM waveguides for Type-I phase matching	113
5.4	Summary of the best second harmonic generation conversion efficiency results	133
B.1	Coefficients for the quadratic regression of the waveguide mode effective index for 1.0 and 1.3 μm deep ridges.	191

List of Figures

1.1	Schematic of self-pumped optical parametric wavelength converter	8
1.2	Schematic of self-pumped optical parametric oscillator	9
1.3	Quantum-well intermixing process by ion implantation	10
2.1	Polarization modes in semiconductor waveguides.	20
2.2	Waveguide structures for different phase matching methods	25
2.3	Bragg reflection waveguide for modal phase matching	28
2.4	Comparison of exact phase matching, domain-reversal quasi-phase matching, and domain-disordered quasi-phase matching over intervals of the coherence length for the SHG process	30
2.5	Fabrication of DD-QPM gratings by sputtered silica cap IFVD and ion-implantation	36
3.1	Superlattice waveguide layer structure	42
3.2	Superlattice wafer photoluminescence at 300K	44
3.3	Photoluminescence from as-grown and intermixed superlattice samples .	45
3.4	Mode profiles at 775 nm in a 3.0 μm -wide, 1.0 μm -deep ridge waveguide .	47
3.5	Mode profile of a 3.0 μm -wide, 1.3 μm -deep ridge waveguide for the TE polarization at 775 nm.	48
3.6	Transmission data with sigmoidal fits for 1.3 μm -deep waveguides at pump/second-harmonic wavelengths	50
3.7	Absorption loss coefficient at pump/second-harmonic wavelengths.	51
3.8	Calculated effective mode indexes for 3.0 μm -wide, 1.3 μm -deep superlattice waveguides	52

3.9	Predicted phase matching wavelength versus QPM period.	54
3.10	Experimental setup for measuring self-phase modulation and nonlinear absorption in superlattice waveguides.	56
3.11	Measured values of the two-photon absorption coefficient for the superlattice core layer	58
3.12	Measured values of the three-photon absorption coefficient for the superlattice core layer	59
3.13	Measured output spectral broadening in as-grown waveguides at 1545 nm for the TM polarization	61
3.14	Measured values of the nonlinear refraction coefficient for the superlattice core layer	62
4.1	Contour plot of the conversion efficiency loss factor dependence on the second-harmonic and fundamental loss coefficients for a 1 mm-long waveguide.	70
4.2	Conversion efficiency loss factor dependence on the waveguide length . .	71
4.3	Computed tuning curve for Type-I SHG in a QPM waveguide with a 3.8 μm period, 50:50 duty cycle, and 1 mm length	72
4.4	Computed tuning curves and FWHM of phase matching peak versus length for Type-I SHG in a QPM waveguide with a 3.8 μm period	72
4.5	Comparison of tuning curves for Type-I SHG in a QPM waveguide when using a continuous wave source and short pulses	74
4.6	Effect of modulation in $\chi^{(2)}$ on SHG conversion efficiency	75
4.7	Simulated output second-harmonic power for Type-I phase matching in 1.0 μm -deep waveguides with SPM and TPA	78
4.8	Simulated output second-harmonic power for Type-I phase matching in 1.0 and 1.3 μm -deep waveguides with SPM, TPA, and linear loss	79
4.9	Simulated output second-harmonic power for Type-I and Type-II phase matching in 1.0 μm -deep waveguides	80

4.10 Effect of GVM and linear loss on Type-I SHG, and output second-harmonic pulses with and without GVM	82
4.11 Effect of group velocity mismatch with large linear loss on Type-I SHG over propagation distance	83
5.1 Fabrication process for forming QPM gratings in a superlattice via IID.	87
5.2 Scanning electron microscope image of the ion implantation mask for Sample A after electroplating	88
5.3 Scanning electron microscope image of QPM ridge waveguide samples . .	91
5.4 Schematic of the experimental setup for SHG experiments with a 2-ps pulsed source	93
5.5 SHG tuning curves for Sample A waveguides with 2 ps pulses	98
5.6 Spectrum of second harmonic pulses on and off phase match	98
5.7 Phase matching wavelengths for Type-I and Type-II SHG in Sample A .	99
5.8 Phase matching wavelengths for Type-I and Type-II SHG in Sample B .	100
5.9 Power dependence of phase matched SHG for several QPM periods in Sample A	102
5.10 Power dependence SHG at the phase matching wavelengths for Type-I and Type-II interactions in Sample A	103
5.11 Power dependence of Type-I SHG at the phase matching wavelengths for Sample A and Sample B	104
5.12 Average power conversion efficiency variation with power for a waveguide in Sample A with a QPM period of 3.5 μm	105
5.13 Power dependence of Type-I SHG normalized average power conversion efficiency for Sample A and Sample B	106
5.14 Low power Type-I SHG normalized conversion efficiency with 2 ps pulses	108
5.15 Schematic of the experimental setup for SHG experiments with a continuous wave source	109
5.16 Transmission of fundamental through a QPM waveguide with a 3.5 μm period	111

5.17 Tuning curve for continuous wave SHG	115
5.18 Filtered envelopes of tuning curves for continuous wave SHG at different input powers	116
5.19 Hysteresis loop in second-harmonic power when tuning the wavelength in upward direction, followed by downward direction.	118
5.20 Dependence of output fundamental and second-harmonic power on input continuous wave fundamental power	119
5.21 Second-harmonic power generated over time after applying an input step of three different continuous wave fundamental powers	120
5.22 Schematic of the experimental setup for SHG experiments with a 20-ps pulsed source.	123
5.23 Power dependence of second-harmonic power for 20-ps pulses and 2-ps pulses	125
5.24 Power dependence of the SHG conversion efficiency for 20-ps pulses and 2-ps pulses	126
5.25 Effective refractive index mismatch values extracted from the measured phase matching wavelengths for Samples A and B	129
5.26 Effective $\chi^{(2)}$ values for Type-I and Type-II SHG in Sample B using data from 2-ps experiments	131
5.27 Modulation in $\chi_{xyz}^{(2)}$ and $\chi_{zxy}^{(2)}$ between as-grown and intermixed superlattice for SHG in Sample B using data from 2-ps experiments	132
 6.1 Simulated Type-I DFG conversion band for Sample B waveguide	138
6.2 Simulated Type-I DFG conversion bands for Sample B waveguide with several different pump wavelengths	139
6.3 Simulated Type-II DFG conversion bands for a Sample B waveguide	140
6.4 Predicted power levels for generated idler in Sample B waveguide	143
6.5 Schematic of the experimental setup for DFG experiments	145
6.6 Output spectrum from a Sample B waveguide with QPM period of 3.8 μm for several signal wavelengths in Type-I DFG experiment	147

6.7	Output spectrum from a Sample B waveguide with QPM period of 3.7 μm for Type-I DFG experiment	149
6.8	Output spectrum from a Sample B waveguide with QPM period of 3.4 μm for Type-II DFG	150
6.9	Simulated idler power generated in integrated parametric devices with different QPM waveguide lengths	153
6.10	Schematic of all-optical wavelength converter based on an integrated parametric conversion device with a DD-QPM waveguide	153
6.11	Predicted signal gain versus input pump power for Type-I phase matching in Sample B under the undepleted pump approximation	156
6.12	Predicted signal gain versus input pump power for Type-I phase matching in Sample B under the undepleted pump approximation for several different QPM waveguide lengths	157
6.13	Predicted SRO OPO threshold pump powers for different QPM waveguide lengths	158
6.14	Predicted SRO OPO round trip signal gain with pump loss included for a QPM waveguide length of 5 mm in the Type-I DFG configuration	159
6.15	Optical mode profile of high confinement waveguide at 1550 nm in the TE polarization	163
6.16	Simplified schematic of a vertical integration structure	166
6.17	Output power from a potential integrated parametric converter with improvements under different cases	168
6.18	Round trip signal gain in a potential integrated singly-resonant OPO with improvements under different cases	168
B.1	Theoretical values for $\chi_{xyz}^{(2)}$ and $\chi_{zxy}^{(2)}$ in a 14:14 monolayer GaAs/AlAs superlattice	192

Abbreviations

3PA	Three-photon absorption
ACQW	Asymmetric coupled quantum well
AQW	Asymmetric quantum well
ASE	Amplified spontaneous emission
BPM	Birefringence phase matching
BRW	Bragg reflection waveguide
CME	Coupled mode equation
DWDM	Dense wavelength division multiplexing
DFG	Difference frequency generation
DD-QPM	Domain-disordered quasi-phase matching
DR-QPM	Domain-reversal quasi-phase matching
DRO	Doubly-resonant oscillator
DS-QPM	Domain-suppression quasi-phase matching
EBL	Electron beam lithography
EDFA	Erbium-doped fiber amplifier
EPM	Exact phase matching
FBPM	Form birefringence phase matching
FFT	Fast Fourier transform
FH	Fundamental harmonic
FSR	Free spectral range
FWHM	Full width at half maximum
GVD	Group velocity dispersion
GVM	Group velocity mismatch

HSQ	Hydrogen silsesquioxane
ICFO	Institut de Ciències Fotòniques
IFVD	Impurity-free vacancy disordering
IID	Ion-implantation disordering
IPA	Isopropyl alcohol
MIBK	Methyl isobutyl ketone
MOCVD	Metal-organic chemical vapour deposition
MPM	Modal phase matching
MQW	Multiple-quantum well
NLSE	Nonlinear Schrödinger equation
NPM	Non-phase matched
OEO	Optical-electrical-optical
OP-GaAs	Orientation patterned gallium arsenide
OPA	Optical parametric amplifier
OPO	Optical parametric oscillator
OSA	Optical spectrum analyzer
PAID	Photoabsorption-induced disordering
PBC	Polarizing beam cube
PECVD	Plasma-enhanced chemical vapour deposition
PIC	Photonic integrated circuit
PMMA	polymethyl methacrylate
PPLN	Periodically-poled lithium niobate
QPM	Quasi-phase matching
QWI	Quantum-well intermixing
RIE	Reactive ion etching
RTA	Rapid thermal annealing
SFG	Sum frequency generation
SHG	Second-harmonic generation
SOA	Semiconductor optical amplifier
SPDC	Spontaneous parametric downconversion

SPM	Self-phase modulation
SRO	Singly-resonant oscillator
TE	Transverse electric
TIR	Total internal reflection
TM	Transverse magnetic
TMAH	Tetramethylammonium hydroxide
TPA	Two-photon absorption
TWM	Three-wave mixing

Chapter 1

Introduction

1.1 Motivation for Compact Wavelength Converters

Modern optical technology has been used with great success in two key areas: communications and spectroscopy. Telecommunications systems have increasingly provided better performance with faster bit rates and more flexibility, which is largely due to the development of fiber optic technology. Optical spectroscopy systems have enabled fast and accurate detection of chemicals and gases relevant to medicine, security, and industrial processes due to advancements in laser and spectrometer technology. Continued research and development efforts aim not only to improve the speed, accuracy, and functionality of these systems, but also to reduce their cost, power consumption, and size.

Current telecommunications systems consist of a blend of microelectronics and optics. Microelectronic devices are responsible for most signal processing functions including switching and routing. Optics mostly handles the transmission of data on high capacity, long distance lines. However, as integrated circuit technology nears performance limitations imposed by the underlying physics of microelectronic devices, new optical technologies will be required to handle high speed signal processing functions. One such function is channel conversion in dense wavelength division multiplexing (DWDM) systems, in which data on one wavelength channel is converted to another channel operating with a different wavelength. At present, channel conversions are handled by converting the incoming optical signal into an electrical signal, routing the electrical signal through

a microelectronic switching fabric, and then retransmitting the signal via a laser emitting at the wavelength of the desired channel. Such a process is known as an optical-electrical-optical (OEO) conversion. This method has high power consumption, requires several discrete components that take up ample space, and is limited in speed by the intervening microelectronics. In order to maintain the agility enabled by this function in future systems at higher bit rates, a compact, highly-integrated all-optical technology will be required. At present, some all-optical technologies have been proposed for carrying out this function and are based on semiconductor optical amplifiers (SOA) [1, 2, 3], and nonlinear frequency conversion in silicon [4], and in dielectric crystals such as chalcogenides [5] and lithium niobate [6]. However, SOAs are limited in speed by carrier recovery times [7], and the integration potential of silicon and dielectric crystals is low due to their inability to emit light.

Today's spectroscopy systems for gas and chemical detection tend to consist of several large, discrete optical components. One such component is the laser source. Tunable systems are preferred over fixed wavelength systems since the range of chemicals that can be detected is large. Also, detecting chemicals by their mid-infrared vibrational resonances is desired for greater specificity. Semiconductors do not generally emit in this range such that simple laser diodes could be fashioned. Quantum cascade lasers have been engineered to emit in the mid-infrared [8], but their tunable ranges are limited and, in many cases, they require cryogenic temperatures to operate. Better tunability with wider ranges and continuous scanning can be achieved by using optical parametric oscillators (OPO) based on nonlinear optical crystals [9]. Recent advances with periodically-poled lithium niobate (PPLN) have led to the development of mid-infrared OPOs operating with femtosecond pulses [10] and continuous wave pumps [11]. However, such systems are limited by the transparency range of ferroelectric crystals, the large power requirements, and their large physical size.

To solve the problems described above, what is needed is a compact all-optical wavelength conversion device. Using nonlinear optical effects to perform the conversion is well suited for both applications as these processes are fast enough to keep up with high bit rates and cover a wide range of spectrum. Ideally, such a device should include all of

the necessary components to carry out the conversion on the same chip. This includes the nonlinear wave mixer, couplers, waveguides, oscillator cavities, and pump laser. In a similar manner to microelectronics, a monolithically integrated optical device would benefit from lower costs, potentially lower power consumption, and higher robustness.

This thesis examines the potential for creating compact, wavelength conversion devices based on photonic integrated circuit (PIC) technology and engineered semiconductor microstructures. The envisioned device is built on a platform of GaAs/AlGaAs superlattice for its strong nonlinear optical properties and ability to efficiently emit light. Quantum well intermixing (QWI) is used to periodically modify the superlattice in order to facilitate integration and to form a quasi-phase matching (QPM) grating to mediate the nonlinear conversion process. Most of the research presented here focuses on the QPM component. The performance of this component is studied in detail through analytical modeling, computer simulations, and laboratory experiments with fabricated QPM devices. Based on the findings of these studies, the power requirements and operating ranges of fully integrated wavelength conversion and generation devices are determined.

1.2 Nonlinear Optics

Under most ordinary conditions, materials have a linear response to the intensity of light. The polarization density created in response to a driving electric field is related to the electric susceptibility, χ , such that $\vec{P} = \epsilon_0\chi\vec{E}$. However, at extreme field strengths, an additional nonlinear response to the driving field occurs. This nonlinear polarization density component is described in the frequency domain as

$$\vec{P}_{NL} = \epsilon_0[\overleftrightarrow{\chi}^{(2)} : \vec{E}\vec{E} + \overleftrightarrow{\chi}^{(3)} : \vec{E}\vec{E}\vec{E} + \dots] \quad (1.1)$$

where $\overleftrightarrow{\chi}^{(i)}$ is the i -th order nonlinear susceptibility tensor. These high-order susceptibilities are usually weak and only become significant at high optical intensities. However, with the use of high power lasers and waveguide devices that confine light into tight spaces, such intensities can be reached and nonlinear phenomena become significantly

strong. Ordinarily, nonlinearities of fourth order and greater are extremely weak, and thus the second- and third-order nonlinearities dominate. These nonlinearities result in several phenomena that can be useful for several purposes, or detrimental to the performance of those effects that are useful.

The second-order nonlinearity gives rise to a number of useful phenomena. One of the most widely studied and used is three-wave mixing (TWM). In this effect, three different optical waves interact in a medium and transfer power between each other. For this to take place, the waves involved must satisfy the *frequency matching condition*

$$\omega_3 = \omega_1 + \omega_2 \quad (1.2)$$

where ω_i is the angular frequency of wave i . Ordinarily in TWM, only two waves are initially present upon entering the nonlinear material. In this case, the third wave is generated with a frequency dictated by the frequency matching condition by power transfer from one or both of the initial waves. This gives rise to two specific processes: 1) sum-frequency generation (SFG) in which the two low frequency ω_1 and ω_2 waves produce the high frequency ω_3 wave, and 2) difference-frequency generation (DFG) in which the initial waves ω_3 (*pump*) and ω_1 (*signal*) mix to generate ω_2 (*idler*). In the degenerate case where there is only one low frequency initial wave, $\omega_1 = \omega_2$ and a wave at frequency $\omega_3 = 2\omega_1$ is generated in a process known as second-harmonic generation (SHG). The reverse process of SFG and SHG is spontaneous parametric downconversion (SPDC), a process in which pump photons at ω_3 spontaneously split into two lower frequency photons at ω_1 and ω_2 . Overall, TWM has found wide spread use for generating coherent light sources at optical frequencies that would otherwise not be possible using conventional laser materials and structures.

Efficient power transfer in TWM processes requires that the waves involved obey the *phase matching condition*. This states that the propagation constants of each wave, β_i , add up such that

$$\beta_3 = \beta_1 + \beta_2. \quad (1.3)$$

If this condition is not met, power will flow to the generated wave, and then back to the

pumping wave(s) after a certain distance with no net power transfer. Since all materials are naturally dispersive, meeting this condition is challenging. One widely used method for achieving the required phase matching is to use the natural birefringence in nonlinear crystals such as KDP, BBO, and lithium niobate. However, if linearly isotropic materials such as compound semiconductors are to be used for TWM, an artificial means of meeting the phase matching condition must be implemented.

A number of phenomena result from the third-order nonlinear susceptibility. The most widely known is the optical Kerr effect (or nonlinear refraction), in which the index of refraction of a material becomes dependent on the optical intensity such that

$$n = n_0 + n_2 I \quad (1.4)$$

where n_0 is the linear index of refraction, I is the optical intensity, and n_2 is the nonlinear refractive index (or Kerr coefficient). This leads to an effect known as *self phase modulation* (SPM) in which an optical wave imposes a nonlinear phase shift on itself. Nonlinear refraction has been employed for a number of useful purposes, most notably in all-optical switching devices [12]. However, SPM can be detrimental to other processes such as TWM by impacting the phase matching condition.

Multiphoton absorption processes are another set of phenomena related to the nonlinear susceptibilities. Two-photon absorption (TPA) is a third-order nonlinear effect in which two photons are absorbed simultaneously. This happens most readily when the two photons have energies at or above half of the energy band gap of the material. TPA increases with optical intensity, and thus the total loss coefficient is intensity dependent such that

$$\alpha = \alpha_0 + \alpha_2 I \quad (1.5)$$

where α_0 is the linear loss coefficient and α_2 is the TPA coefficient. At photon energies below half the energy gap, TPA is negligible and three-photon absorption (3PA) becomes the dominant nonlinear absorption mechanism. As a fifth-order nonlinearity, the amount of 3PA is proportional to the square of the optical intensity such that the additional loss is $\Delta\alpha = \alpha_3 I^2$ where α_3 is the 3PA coefficient. While nonlinear absorption is useful for

certain types of devices such as all-optical switches [13], it is more often a parasitic effect that adds more attenuation of the optical waves. As a result, useful intensity-dependent nonlinear effects such as TWM and nonlinear refraction will be compromised.

1.3 Photonic Integrated Circuits in Compound Semiconductors

Photonic integrated circuit technology has been developed over a number of decades with the goal of miniaturizing optical components for better space efficiency and lower cost. Such circuits have been implemented using dielectric materials such as silica glass and lithium niobate. Silicon has also been exploited in the last decade for creating several integrated devices [14, 15]. However, the primary limitation of using such materials is that they do not emit light. Integration of electrically-injected light-emitting devices, such as amplifiers and lasers, requires hybrid integration with light emitting semiconductors such as has been done with silicon and InP [16]. The nonlinear optical properties of most nonlinear crystals are also weak, requiring large optical powers and long crystals to induce TWM. Additionally, silicon lacks the strong second-order nonlinearity from electric dipole interactions due to its centrosymmetric lattice structure. While second-order effects can occur due to multipole interactions, these are usually weak and not useful for practical applications [17].

Compound semiconductors such as those based on InP and GaAs do emit light efficiently due to their direct band gaps, and they are the key materials used in laser diodes. Thus, it is possible to integrate lasers, detectors, passive waveguides, and (de)multiplexers all on the same chip. In recent years, these semiconductors have been used for high-speed multiple-wavelength optical transmitters [18, 19] and detectors [20, 21] for DWDM telecommunications systems. Compound semiconductors also exhibit strong optical nonlinearities. In particular, AlGaAs-based materials have Kerr coefficients that are nearly 500 times larger than silica [22]. Also, compound semiconductors lack centrosymmetry and thus have a second-order nonlinearity. Measurements of the magnitude of $\chi^{(2)}$ in

GaAs place it as being over six times stronger than in lithium niobate [23]. Thus, nonlinear optical devices made with GaAs-based materials can be several times shorter than in other nonlinear materials. This could make nonlinear devices compact enough to fit onto a microchip with other devices. Also, the power requirements would be less.

Another key advantage to using compound semiconductors for PICs is the availability of mature microfabrication processes. These include metal-organic chemical vapour deposition (MOCVD) epitaxy for building lattice-matched multi-layered waveguide structures and quantum-well structures, and plasma-enhanced reactive ion etching (RIE) for creating optical waveguides and grating structures. Wide availability of these processes allows mass production of complex, highly-integrated semiconductor PICs at low cost.

1.4 Single-Chip Wavelength Conversion Devices

To address the need for compact optical wavelength conversion devices, unique designs for PICs have been devised by Hutchings [24] based on AlGaAs semiconductors and monolithic integration technology. The first such device depicted in Figure 1.1 is an optical parametric converter. All of the components necessary to perform wavelength conversion are present on a single chip. A pump laser with a ring cavity is integrated directly onto the chip. The amplified spontaneous emission (ASE) seed source is used to force the pump laser into unidirectional operation as has been demonstrated in other ring lasers [25]. Dichroic couplers combine and separate the pump and signal wavelengths. The idler wavelength is generated through a phase-matched DFG process in the wave mixer. The DFG process also produces photons at the signal wavelength, and thus the device also acts as an optical parametric amplifier (OPA). The wave mixer is placed within the pump laser cavity in order to take advantage of the high circulating pump powers to enhance the DFG process. Amplitude modulations present on the signal wavelength will be transferred to the idler wavelength as the amount of idler power generated depends on the amount of signal power. Hence, if the signal contains data, that data will be converted over to the idler. This functionality can be used for performing channel conversions in a DWDM system. Additionally, if the signal wavelength is set to be close to the pump

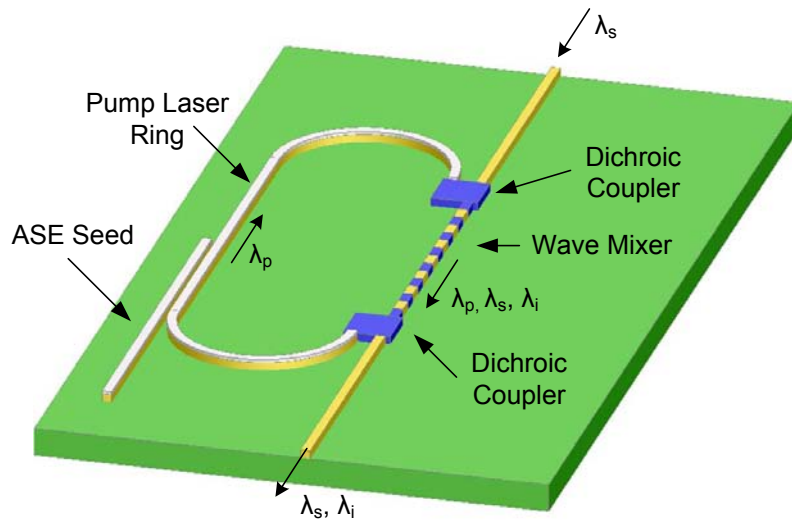


Figure 1.1: Schematic of self-pumped optical parametric wavelength converter. The circulating pump power at wavelength λ_p interacts with the signal wavelength at λ_s to produce the idler wavelength at λ_i in the wave mixer.

wavelength such that their frequency difference is small, idler wavelengths in the mid-infrared can be generated.

The second device envisioned is a monolithically integrated optical parametric oscillator. This device is used only to generate light, not to convert external input light to another wavelength. The underlying structure is the same as the parametric converter, except that a second ring cavity is added to form the parametric oscillator. The signal and idler wavelengths, initially generated by SPDC, are circulated through this ring to build up their intensities and further enhance the DFG process in the wave mixer. A tap waveguide is located on the outside of the OPO ring to siphon a small amount of the signal power and guide it out from the device. The wavelengths of the generated signal and idler pair will be those that best satisfy the phase matching condition. Tuning of these wavelength is achieved by changing the pump wavelength from the ring laser. Because of the high rate of change in the index of refraction with wavelength near the semiconductor band gap, minute changes to the pump wavelength causes large changes to the phase matching condition. In turn, this allows the signal and idler wavelengths to be tuned over a large range. For spectroscopic chemical sensor systems, this means that a large portion of mid-infrared spectrum can be generated. Such a device could also

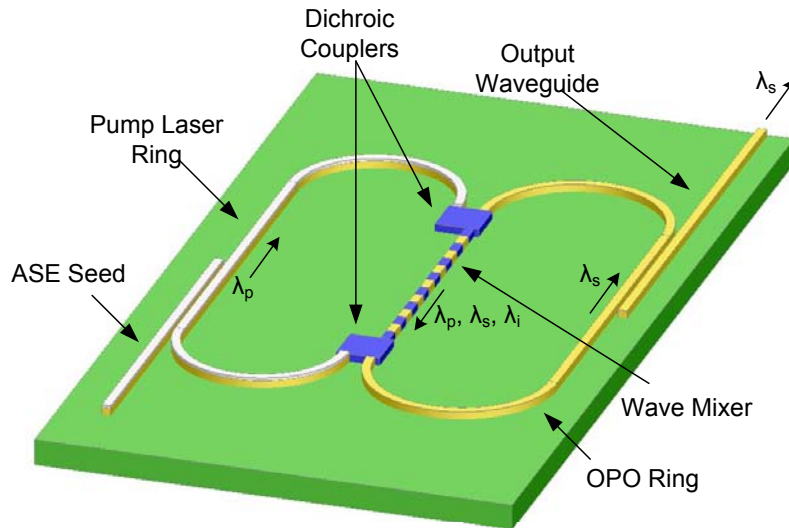


Figure 1.2: Schematic of self-pumped optical parametric oscillator. Pump light photons (λ_p) are converted to signal (λ_s) and idler (λ_i) photons which are circulated in the OPO ring to enhance the interaction in the wave mixer.

be used as a tunable laser source at telecommunications wavelength for use in diagnostic equipment and agile DWDM systems.

There are two central challenges to creating these devices. First, ideally, the pump laser should be made from the same waveguiding layers used in the rest of the device for simplicity and to reduce cost. However, components such as the dichroic couplers will absorb the pump light which will raise the threshold currents for lasing. Instead, it would be beneficial if the couplers were formed out of a passive material with a larger band gap than the laser gain material. Second, the wave mixer requires a mechanism for phase matching the DFG process for efficient operation. Since AlGaAs is isotropic, an artificial means of phase matching must be employed, most likely requiring manipulation of the waveguide materials. Fortunately, techniques have been developed that yield solutions for both of these challenges.

1.5 Quantum Well Intermixing

Quantum well intermixing is a set of post wafer growth methods that alters the properties of a semiconductor quantum well structure [26]. The core layer of the optical waveguide

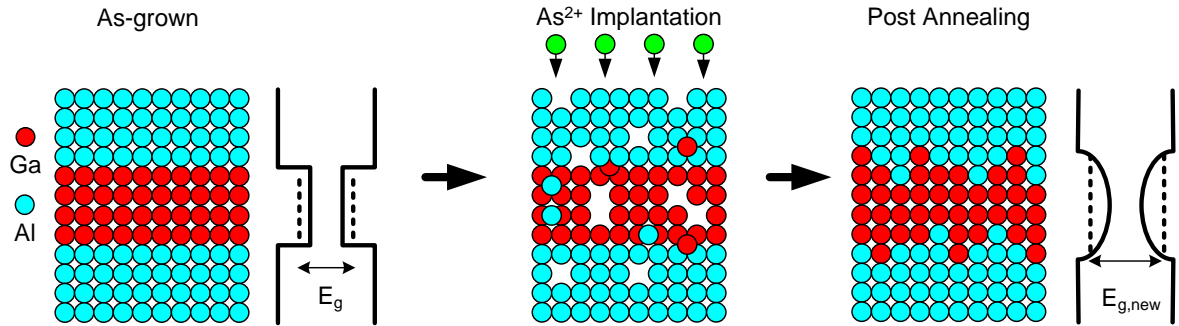


Figure 1.3: Quantum-well intermixing process by ion implantation. The Group-III sublattice is represented. The as-grown quantum well structure (left) is subjected to As²⁺ implantation which creates defects in the crystal lattice (middle) that promote interdiffusion during annealing leading to compositional and structural changes that alter the potential well profile (right).

usually contains a multiple-quantum well (MQW) structure to be manipulated. Figure 1.3 depicts the QWI process for a single GaAs well with AlAs barriers. The quantum well is subjected to one of several processes that disorder the semiconductor crystal lattice. The most common disordering processes include impurity-free vacancy disordering (IFVD), ion implantation disordering (IID)[27], and photoabsorption-induced disordering (PAID) [28]. The sample is then heated to high temperature by rapid thermal annealing (RTA) which allows the lattice atoms to diffuse, a mechanism which is enhanced by the presence of the defects formed by the disordering process. This diffusion process has the effect of repairing the crystal lattice, which reduces scattering centers and lowers optical losses. It also alters the composition and structure of the quantum wells. The potential profile of the quantum wells changes, which usually causes the energy gap between the lowest conduction and valence states to widen. Thus, the optical absorption peak of the quantum wells is shifted to shorter wavelengths. In tandem, optical properties, such as the linear index of refractive, have their resonance features shifted along with the absorption peak. If the degree of intermixing is so much such that all of the atoms from the well and barrier layers are mixed together, *complete intermixing* is achieved. In this case, multiple quantum well structure is destroyed and the average alloy is formed. At this point, the largest possible compositional change and band gap energy shift is achieved.

QWI has been used successfully as a means to shift the absorption band outward

in lithographically defined regions which allows lasers to be mixed with passive optical components. Furthermore, different areas of the chip can be manipulated with varying degrees of intermixing to have different absorption/emission bands and optical properties [29]. The intermixing process has also been shown to alter the nonlinear optical properties of the quantum-well structure [30]. This has been useful for creating new types of nonlinear optical devices such as monolithic nonlinear optical switching devices integrated with linear components [31, 32]. Overall, selective area intermixing opens new possibilities for creating complex monolithically integrated photonic integrated circuits and systems.

1.6 Semiconductor Superlattices

Semiconductor superlattices are an extension of MQW structures. Ordinarily, MQWs employ thick barrier layers to isolate each quantum well. In a superlattice, the barriers are made thin such that the electronic wave functions overlap adjacent wells. As a result, the energy states broaden into minibands of quasi-continuous energy states. By adjusting the layer thicknesses and composition, the energy gap between the lowest conduction miniband and the highest valence miniband can be set to suit the specific requirements of the target device. In particular, the band gap can be placed such that certain resonances in the linear and nonlinear optical properties are near the operating wavelengths. This can result in strong optical nonlinearities and better performance in a wavelength conversion device.

A consequence of using a heterostructure such as a superlattice is that translational symmetry is broken due to the non-equivalence of the in-plane and vertical directions relative to the layers. This leads to the emergence of new independent, nonzero elements in the susceptibility tensors that would otherwise not be found in bulk zinc-blende structures. Furthermore, the electronic band structure has a lifted degeneracy between the light- and heavy-hole valence bands. Due to the selection rules [33], the absorption peaks for the transverse electric (TE) and transverse magnetic (TM) polarizations will occur at different photon energies. Overall, the structural asymmetry and the lifted

band degeneracy leads to polarization dependencies in the linear and nonlinear optical properties.

The key advantage of using superlattices over MQWs is the potential for creating large shifts in the band gap energy by QWI. With thin barrier layers, the Ga and Al atoms need only diffuse over a short distance of a few monolayers in order to cause large compositional changes and potentially complete intermixing. Studies of short-period, symmetric GaAs/AlAs superlattices showed that the band gap energy can be increased by up to 25% after QWI [34]. As a result, large shifts in the nonlinear susceptibilities have been predicted [35]. With such large potential modulation depths in the nonlinear properties, selected regions of the superlattice can be rendered relatively linear, providing a means to mix linear and nonlinear components onto a single chip. This allows better performance from each device and greater integration potential.

1.7 Domain-Disordered Quasi-Phase Matching

Quasi-phase matching is an artificial means of meeting the phase matching condition in a medium with insufficient birefringence to achieve phase matching naturally. In all forms of QPM, the starting material is modified such as to create a grating in which the second-order nonlinear optical coefficients are modulated. Domain-disordering quasi-phase matching (DD-QPM) is one specific form of QPM which utilizes a MQW or superlattice, and QWI to impress a grating structure [36]. Phase matching is achieved by periodically suppressing the second-order susceptibility and power flow between the participating waves when they become out of phase with each other. In this manner, back conversion to the pumping waves is limited and power flow is ultimately directed to the intended wavelengths. By appropriately choosing the grating period and duty cycle, the wavelengths at which phase matching occurs can be set to suit the application.

The efficiency of DD-QPM is directly related to the magnitude of the modulation of second-order nonlinearity. With more suppression of $\chi^{(2)}$, there is less back conversion that must be overcome. By using a GaAs/AlGaAs superlattice as the core layer of a waveguide structure, a large modulation in the magnitude of $\chi^{(2)}$ can be achieved with

QWI, especially for wavelengths near the band gap energy where there is a resonance [37]. Furthermore, creating devices in which the QPM waveguide is monolithically integrated with other components becomes simpler. For instance, for the wavelength conversion devices discussed in Section 1.4, only a single intermixing step is required to create the QPM grating and the passive regions for the dichroic couplers. As such, the overall fabrication process is simpler, faster, and less costly.

1.8 Scope and Outline of Thesis

The objective of this thesis is to evaluate the performance of wavelength conversion processes in GaAs/AlGaAs superlattice domain-disordered quasi-phase matching waveguides. The purpose of studying this is to determine operating parameters such as the phase matching wavelengths in order to select appropriate design parameters for the wave mixer component of an integrated wavelength conversion device. Most of the analysis and all of the experiments are limited to wavelength conversion around the 1550 nm telecommunications band as the available equipment was limited to this range. Thus, most of the results and predictions are most relevant to applications of this technology to telecommunications systems. However, since some of the underlying material properties and behavioural trends are evaluated, the research presented here provides some insights which could be extended to other wavelength ranges such as the mid-infrared.

Chapter 2 examines the basic theory for second-order nonlinear wave mixing processes and discusses several means of phase matching in semiconductors. The simplified theory will allow simple analysis of results on wavelength conversion reported in the literature such that the various phase matching techniques can be compared to each other. Chapter 3 discusses the design of the waveguide structure, and examines the linear and nonlinear optical properties of the waveguides. In Chapter 4, an advanced model for three-wave mixing and second-harmonic generation is developed. Using this model, the performance of DD-QPM waveguides is predicted, and the impact of linear loss, dispersion, and high-order nonlinear effects on that performance is evaluated. Chapter 5 examines the results obtained from SHG experiments with DD-QPM waveguides. The

performance with several different laser systems is compared and the data is used to calculate the modulation depth in $\chi^{(2)}$. In Chapter 6, difference frequency generation is examined beginning with theoretical predictions of performance based on data obtained in SHG experiments, and following with an examination of actual experiments in which wavelength conversion is achieved. Using the data, predictions on the performance of self-pumped, monolithically integrated wavelength conversion devices based on superlattice DD-QPM waveguides are presented.

The research project presented in this thesis was done in collaboration with Prof. D. C. Hutchings's group at the University of Glasgow. A portion of the work was also done with the assistance and facilities of Prof. M. Ebrahim-Zadeh's group at the Institut de Ciències Fotòniques (ICFO) in Barcelona, Spain.

Chapter 2

Phase Matching in Semiconductors

2.1 Introduction

The key requirement for achieving efficient frequency conversion in a three-wave mixing process is to meet the phase matching condition. As AlGaAs has a zinc-blende cubic structure, which is optically isotropic, the phase matching condition cannot be ordinarily met as is done in birefringent nonlinear crystals. In order to gain substantial power transfer between the participating waves, an artificial form of phase matching must be employed. This can done either by altering the waveguide layer structure to induce an artificial birefringence, by propagating one or more waves in higher order modes, or by periodically correcting the phase mismatch along the length of the waveguide. Each method has tradeoffs between parametric gain, fabrication complexity, optical attenuation, and integration potential, all of which influence the overall conversion efficiency of the device.

In this chapter, the basics of second-order nonlinear processes and phase matching techniques will be reviewed. Starting with the simplified coupled mode equations, the basic behaviour of three-wave mixing and second-harmonic generation in a waveguide will be discussed. From this, metrics for evaluating the device efficiency will be derived and examined. Several phase matching techniques for achieving phase matching in AlGaAs waveguides will be explained and devices for each of these techniques reported in the available literature will be reviewed.

2.2 Basic Theory

In this section, basic theory on second-order nonlinear optical processes will be discussed. The model presented is simplified to consider only the behaviour of second-order nonlinear processes in waveguide structures. This will allow basic comparisons between the various phase matching techniques discussed in Section 2.3. The model will be expanded to cover a broader range of phenomena in Chapter 4.

2.2.1 Coupled Mode Equations

The waveguide structures examined here employ semiconductor materials such as AlGaAs which are non-magnetic and isotropic. Thus, the model shall be limited to such materials. This allows use of the simple scalar wave equation. Under these assumptions, the electric field can be defined as

$$E_i = \frac{1}{2} \left[\tilde{E}_i(x, y, z, t) \exp[j(\omega_i t - \beta_{0,i} z)] + c.c. \right] \quad (2.1)$$

for each wave i where \tilde{E} is the field amplitude, ω is the angular frequency, β is the propagation constant, and $c.c$ denotes the complex conjugate. Substituting this into Equation 1.1 for the nonlinear polarization, the nonlinear coupled mode equations (CME) can be derived. A full derivation can be found in Appendix A for the general case in which several effects such as high-order nonlinearities, dispersion, and linear loss are included. In the present discussion, these effects are not considered for simplicity. Under this assumption, if the field amplitude is defined as

$$\tilde{E}_i(x, y, z, t) = \gamma_i F_i(x, y) A_i(z, t) \quad (2.2)$$

where $\gamma_i = (2/c\epsilon_0 n_i)^{-1/2}$, and F_i represents the transverse field distribution such that $A(z, t)$ is the time-dependent amplitude envelope in units of \sqrt{W} , the coupled mode equations for three-wave mixing become

$$\frac{\partial A_1}{\partial z} = -j \frac{\kappa_1}{\lambda_1} A_2^* A_3 \exp[-j\Delta\beta z] \quad (2.3a)$$

$$\frac{\partial A_2}{\partial z} = -j \frac{\kappa_2}{\lambda_2} A_1^* A_3 \exp[-j\Delta\beta z] \quad (2.3b)$$

$$\frac{\partial A_3}{\partial z} = -j \frac{\kappa_3}{\lambda_3} A_1 A_2 \exp[j\Delta\beta z] \quad (2.3c)$$

where $\Delta\beta = \beta_3 - \beta_2 - \beta_1$ is the mismatch in the propagation constants. The coupling coefficients κ are defined as

$$\kappa_i = \pi \chi^{(2)} \sqrt{\frac{2}{c \epsilon_0 n_{0,1} n_{0,2} n_{0,3} A_{\text{eff},i}^{(2)}}} \quad (2.4)$$

where $n_{0,i}$ is the index of refraction for wave $i = 1, 2, 3$, and $\chi^{(2)}$ is the complex-valued second-order nonlinear susceptibility. Under the assumption of a uniform medium for simplicity, the second-order effective overlap areas, $A_{\text{eff},i}^{(2)}$, are defined as

$$A_{\text{eff}}^{(2)} = \frac{\left[\iint_{-\infty}^{\infty} |\tilde{F}_1|^2 dx dy \right] \left[\iint_{-\infty}^{\infty} |\tilde{F}_2|^2 dx dy \right] \left[\iint_{-\infty}^{\infty} |\tilde{F}_3|^2 dx dy \right]}{\left[\iint_{-\infty}^{\infty} \tilde{F}_1^* \tilde{F}_2^* \tilde{F}_3 dx dy \right]^2}. \quad (2.5)$$

for waves 1 and 2. They are complex-valued in general and are defined such that $A_{\text{eff},1}^{(2)} = A_{\text{eff},2}^{(2)} = A_{\text{eff},3}^{(2)*}$. For the majority of cases, the imaginary component of the overlap areas will be small compared to the real part, especially when using simple dielectric waveguide structures and fundamental transverse modes. In this case, $A_{\text{eff},1}^{(2)} = A_{\text{eff},2}^{(2)} = A_{\text{eff},3}^{(2)}$ and $\kappa_1 = \kappa_2 = \kappa_3 = \kappa$. In the more general case of a nonuniform medium, $\chi^{(2)}$, $n_{0,i}$, and $A_{\text{eff}}^{(2)}$ also take into account the finite overlap of the waveguide modes across several material layers each with a different value of $\chi^{(2)}$ for the given wavelengths and polarizations (see Appendix A).

In the specific case of sum frequency generation, power from A_1 and A_2 is transferred to A_3 . Under the assumption that the amount of power depleted from waves 1 and 2 is small such that $|\Delta A_1|^2 \ll |A_1|^2$ and $|\Delta A_2|^2 \ll |A_2|^2$ and that wave 3 initially has no power, A_1 and A_2 can be taken as constant over the propagation distance z . Integrating Equation 2.3c gives

$$P_3 = \frac{|\kappa|^2}{\lambda_3^2} P_1 P_2 L^2 \frac{\sin^2[\frac{1}{2}\Delta\beta L]}{\left[\frac{1}{2}\Delta\beta L\right]^2} \quad (2.6)$$

where $P_i = |A_i|^2$ are the optical powers, and L is the propagation distance. For the opposite process, difference frequency generation, power is transferred from the pump wave (A_3) to the signal wave (A_1) and the idler wave (A_2). Again, assuming that the pump is not depleted appreciably and that the gain in the signal is insignificant, the power generated in wave 2 can be found by integrating 2.3b which gives

$$P_2 = \frac{|\kappa|^2}{\lambda_\omega^2} P_1 P_3 L^2 \frac{\sin^2 [\frac{1}{2}\Delta\beta L]}{[\frac{1}{2}\Delta\beta L]^2}. \quad (2.7)$$

In both cases, the power in the generated wave grows quadratically with length and linearly with each of the powers in the other two waves. Also, the amount of conversion increases quadratically with the value of $\chi^{(2)}$.

For the case of degenerate second-harmonic generation, the coupled mode equations are

$$\frac{\partial A_\omega}{\partial z} = -j \frac{\kappa_\omega}{\lambda_\omega} A_\omega^* A_{2\omega} \exp[-j\Delta\beta z] \quad (2.8a)$$

$$\frac{\partial A_{2\omega}}{\partial z} = -j \frac{\kappa_{2\omega}}{\lambda_\omega} A_\omega A_{2\omega} \exp[j\Delta\beta z] \quad (2.8b)$$

where A_ω is the envelope amplitude of the fundamental, $A_{2\omega}$ is the envelope amplitude of the second-harmonic, and κ is the coupling coefficient defined as

$$\kappa_i = \pi \chi^{(2)} \sqrt{\frac{2}{c \epsilon_0 n_\omega^2 n_{2\omega} A_{\text{eff},i}^{(2)}}} \quad (2.9)$$

where $A_{\text{eff},2\omega}^{(2)} = A_{\text{eff},\omega}^{(2)*}$. Again, assuming that the imaginary component of the overlap areas is small, $A_{\text{eff},2\omega}^{(2)} = A_{\text{eff},\omega}^{(2)}$ and $\kappa_\omega = \kappa_{2\omega} = \kappa$. Assuming the undepleted pump approximation, the fundamental is constant and the power generated in the second harmonic wave is

$$P_{2\omega} = \frac{|\kappa|^2}{\lambda_\omega^2} P_\omega^2 L^2 \frac{\sin^2 [\frac{1}{2}\Delta\beta L]}{[\frac{1}{2}\Delta\beta L]^2}. \quad (2.10)$$

Here, the power of the second-harmonic wave increases quadratically with the fundamental power in addition to the length.

The conversion bandwidth for both TWM and SHG depends on the dispersion of the

phase mismatch/length product $\Delta\beta L$. Longer waveguide lengths will result in a narrower conversion bandwidth. Also, the more rapidly $\Delta\beta$ changes with wavelength, the narrower the bandwidth. In most cases, the propagation constant of the shortest wavelength changes rapidly due to proximity to the electronic resonances of the semiconductor. Thus, SFG and SHG processes tend to have narrow conversion bandwidths with a sinc^2 function profile. In DFG processes, the shorter wavelength is usually kept stationary around the SHG phase matching wavelength to function as the pump beam while the two longer wavelengths are varied. Conversion bandwidths in this case tend to be on the order of 100 nm.

2.2.2 Type-I and Type-II Interactions

The second-order nonlinearity is in general described by a third-rank tensor. In bulk zinc-blende semiconductor crystals, where the Cartesian directions are defined by the Miller indices such that

$$x = [100], y = [010], z = [001], \quad (2.11)$$

the symmetry of the $\bar{4}3m$ cubic lattice structure reduces the number of nonzero tensor elements to six:

$$\chi_{xyz}^{(2)} = \chi_{xzy}^{(2)} = \chi_{yxz}^{(2)} = \chi_{yzx}^{(2)} = \chi_{zxy}^{(2)} = \chi_{zyx}^{(2)}. \quad (2.12)$$

As they are all equal to each other, there is only one independent element, $\chi_{xyz}^{(2)}$. In the case of a heterostructure such as a superlattice in which the layers are grown in the $[001]$ direction, symmetry is broken between the in-plane and normal directions relative to the layer interfaces. As a result, $\chi_{zxy}^{(2)}$ and $\chi_{zyx}^{(2)}$, which are equal to each other, become independent of the other tensor elements and a polarization dependence in second-order nonlinear processes results.

For a (100) grown semiconductor wafer, the core/cladding interface is along the (100) plane and rib waveguides are drawn along the [011] direction according to natural breaking of the wafer along the (011) planes. The principle guided polarization modes are defined in reference to the core/cladding interface. The TE polarization has the electric field directed in the plane of the core/cladding interface and thus has components in

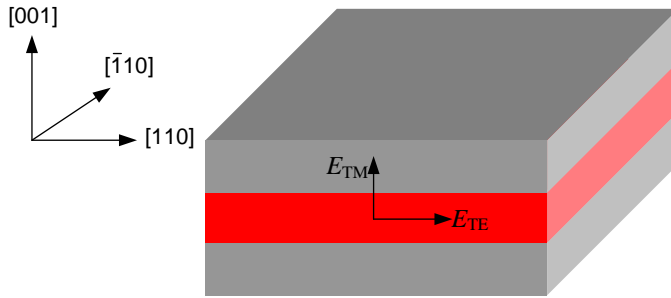


Figure 2.1: Polarization modes in semiconductor waveguides.

transverse xy -direction as shown in Figure 2.1. For the TM polarization, the electric field is primarily directed in the z -direction. In general, two-dimensional confinement in a dielectric waveguide requires that there be components in propagation direction as well. However, for the fundamental transverse modes, that component is much smaller than the dominating components in the transverse plane. Thus, while the polarization modes are neither truly TE or TM, they are considered to be so for simplicity.

The second-order nonlinear polarization from 1.1 can be expressed as

$$\vec{P}_{NL}^{(2)} = \epsilon_0 \overleftrightarrow{\chi}^{(2)} : \vec{E} \vec{E}. \quad (2.13)$$

Given the allowable polarization modes in a waveguide structure and the available tensor elements, there are two possible configurations for SHG. In the Type-I configuration, the input fundamental wave is TE polarized and the second-harmonic produced is TM polarized such that

$$E_f(TE) \xrightarrow{\chi_{zxy}^{(2)}} E_s(TM). \quad (2.14)$$

In the Type-II configuration, both the TE and TM polarizations of the fundamental are used and the second-harmonic is produced in the TE polarization according to

$$E_f(TE) + E_f(TM) \xrightarrow{\chi_{xyz}^{(2)}} E_s(TE). \quad (2.15)$$

Type-II SHG behaves like sum-frequency generation as the degeneracy at the fundamental frequency is lifted, and the TE and TM polarized waves are independent. Thus, for the

purposes of modeling, Type-II SHG must be treated as a three-wave mixing process.

Due to birefringence, the phase matching condition will likely occur for different wavelengths for each process. Thus, second harmonic generation will peak at different wavelengths for Type-I and Type-II phase matching. While the waveguide induced birefringence may be small, structures such as multiple quantum well layers and superlattices may provide a significant material birefringence so as to separate the Type-I and Type-II phase matching wavelengths by a large amount. This is important as both Type-I and Type-II interactions will occur simultaneously in a dielectric waveguide structure if fundamental is split between the TE and TM polarizations. However, only one interaction will be phase matched at a time, which allows the two processes to be isolated from each other.

Similar interactions occur for DFG. For this process, the *pump* is defined as the shortest of the three wavelengths, while the *signal* and *idler* are the two longer wavelengths. The Type-I interaction refers to the case where the signal and idler waves are both in the TE polarization while the pump is in the TM polarization such that

$$E_{\text{pump}}(\text{TM}) + E_{\text{sig}}(\text{TE}) \xrightarrow{\chi_{zxy}^{(2)}} E_{\text{idl}}(\text{TE}). \quad (2.16)$$

In this case, the phase matching degeneracy pump wavelength coincides with the phase matching second-harmonic wavelength of Type-I SHG. For the Type-II interaction, the signal and idler are in orthogonal polarizations while the pump is in the TE polarization such that

$$E_{\text{pump}}(\text{TE}) + E_{\text{sig}}(\text{TE}) \xrightarrow{\chi_{xyz}^{(2)}} E_{\text{idl}}(\text{TM}) \quad (2.17\text{a})$$

or

$$E_{\text{pump}}(\text{TE}) + E_{\text{sig}}(\text{TM}) \xrightarrow{\chi_{xyz}^{(2)}} E_{\text{idl}}(\text{TE}). \quad (2.17\text{b})$$

For the purposes of monolithic integration, Type-II phase matching is of greater interest. Quantum-well-based semiconductor lasers ordinarily emit in the TE polarization due to quantum mechanical selection rules. Thus, Type-II becomes the more natural choice for frequency conversion on a single microchip with an integrated pump source.

2.2.3 Conversion Efficiency

An important metric for frequency conversion by second-order nonlinear processes is the conversion efficiency. Several definitions for the conversion efficiency are used in the available literature. For the SHG process, the simplest definition of conversion efficiency is the percentage of power transferred from the fundamental to the second-harmonic such that

$$\eta_s = \frac{P_{2\omega}}{P_\omega} \times 100\%. \quad (2.18)$$

However, this definition does not take into account the quadratic scaling of the second-harmonic power with the fundamental power. Thus, another definition is

$$\eta_q = \frac{P_{2\omega}}{P_\omega^2} \times 100\% \quad (2.19)$$

which has units of % W⁻¹. While this definition is better, it ignores the dependence of the second-harmonic power on the propagation length. As seen in Section 2.2.1, all processes scale quadratically with length. Under the undepleted pump approximation and assuming a perfectly phase matched process such that $\Delta\beta = 0$, Equation 2.10 can be rearranged such that

$$\eta_{\text{SHG,I}} = \frac{P_{2\omega}}{P_\omega^2 L^2} \times 100\% \quad (2.20)$$

which is known as the *normalized conversion efficiency* [38, 39] and has units of %W⁻¹cm⁻². When comparing Equation 2.20 with the Equation 2.10, note that $\eta_{\text{SHG,I}} = |\kappa|^2/\lambda_\omega^2$ at perfect phase matching, and thus the conversion efficiency reflects the magnitude of the coupling coefficient and the strength of the nonlinear susceptibility $\chi^{(2)}$. This definition is most appropriate for the case of Type-I SHG. For Type-II SHG, the TE and TM polarized waves are independent and each can have a different power level. Thus, it must be treated as SFG. Rearranging Equation 2.6 gives

$$\eta_{\text{SHG,II}} = \frac{P_{2\omega}(\text{TE})}{4P_\omega(\text{TE})P_\omega(\text{TM})L^2} \times 100\%. \quad (2.21)$$

such that $\eta_{\text{SHG,II}} = |\kappa|^2/\lambda_\omega^2$. In the case where the fundamental power is evenly split between the TE and TM modes such that $P_\omega(\text{TE}) = P_\omega(\text{TM}) = 1/2P_\omega$, the normalized conversion efficiency for the Type-II SHG process is the same as the Type-I SHG process as defined in Equation 2.20.

Similar definitions for the normalized conversion efficiency can be derived for DFG. Assuming that the phase mismatch is zero, rearranging Equation 2.7 gives

$$\eta_{\text{DFG}} = \frac{P_{\text{idl}}}{P_{\text{pump}}P_{\text{sig}}L^2} \times 100\%. \quad (2.22)$$

as the normalized conversion efficiency. In this case, η_{DFG} reflects the power transfer factor $|\kappa|^2/\lambda_{\text{idl}}^2$.

The conversion efficiencies defined above are for the case of continuous wave beams. If a train of pulses is used, the average power and instantaneous power are not the same, and calculations tend to inflate the conversion efficiency value if average powers are used in the above definitions. Thus, Equations 2.20, 2.21 and 2.22 do not directly reflect the coupling coefficient κ . To rectify this, the pulses must be taken into account. The fundamental can be defined as a Gaussian pulse $P_\omega = P_{\omega,0} \exp[-t^2/T_0^2]$ with T_0 as the temporal $1/e$ half-width and $P_{\omega,0}$ as the peak pulse power. Substituting this into Equation 2.10 for Type-I SHG gives the second harmonic pulse as

$$P_{2\omega} = \frac{|\kappa|^2}{\lambda_\omega^2} L^2 P_{\omega,0}^2 \exp[-2t^2/T_0^2]. \quad (2.23)$$

Integrating the above equation over all time under the assumption that the pulses do not overlap, and multiplying by the pulse repetition rate f gives the average second harmonic power

$$\bar{P}_{2\omega} = \frac{|\kappa|^2}{\lambda_\omega^2} L^2 \bar{P}_\omega^2 \frac{1}{T_0 f \sqrt{2\pi}} \quad (2.24)$$

where the overbars signify average power. After rearranging this equation, it is found that the *average power conversion efficiency* $\bar{\eta}$ and the *instantaneous power conversion efficiency* η are related by

$$\bar{\eta} = \frac{1}{T_0 f \sqrt{2\pi}} \eta. \quad (2.25)$$

As $T_0 f$ is usually $\ll 1$ for most ultrafast laser systems, the average power conversion efficiency value when using short pulses will appear to be larger than the conversion efficiency for continuous wave conversion by several orders of magnitude. In contrast, the instantaneous efficiency directly reflects κ and $\chi^{(2)}$. Furthermore, if the conversion bandwidth is assumed to be much larger such that $\Delta\beta \approx 0$ across the pulse spectrum, the instantaneous efficiency is essentially the same as the efficiency obtained for the continuous wave case. Thus, η in Equation 2.25 can be considered to be the *equivalent instantaneous conversion efficiency*. This is a good measure of the performance of a phase matching waveguide as it relates to the nonlinear strength of the waveguide material and structure. It also provides a common basis of comparison when examining the performance of different phase matching schemes when different pulse lengths are used in each experiment. However, Equations 2.20, 2.21, and 2.22 are still appropriate for evaluating the performance within a specific pulse length regime as they are directly related to the average photon flux and are representative of the *quantum conversion efficiency*, which is the number of photons produced per unit of pump photons. Thus, using short pulses should produce photons in the target wavelength at a higher average rate than longer pulses or continuous wave due to the stronger interaction at the higher peak pulse power.

All of the above definitions assume that the pumping waves are undepleted and thus do not account for saturation effects that occur when the interactions are strong. They also do not account for losses (whether linear or nonlinear) in the participating waves. However, for the sake of evaluating device performance, the above definitions serve as all-encompassing metrics by which comparisons can be made between different devices. In the following section, various phase matching techniques and devices shall be compared in this manner using the normalized conversion efficiencies defined here.

2.3 Phase-Matching Techniques

Numerous techniques and associated waveguide structures have been investigated over the last two decades to phase match second-order nonlinear processes. In general, the

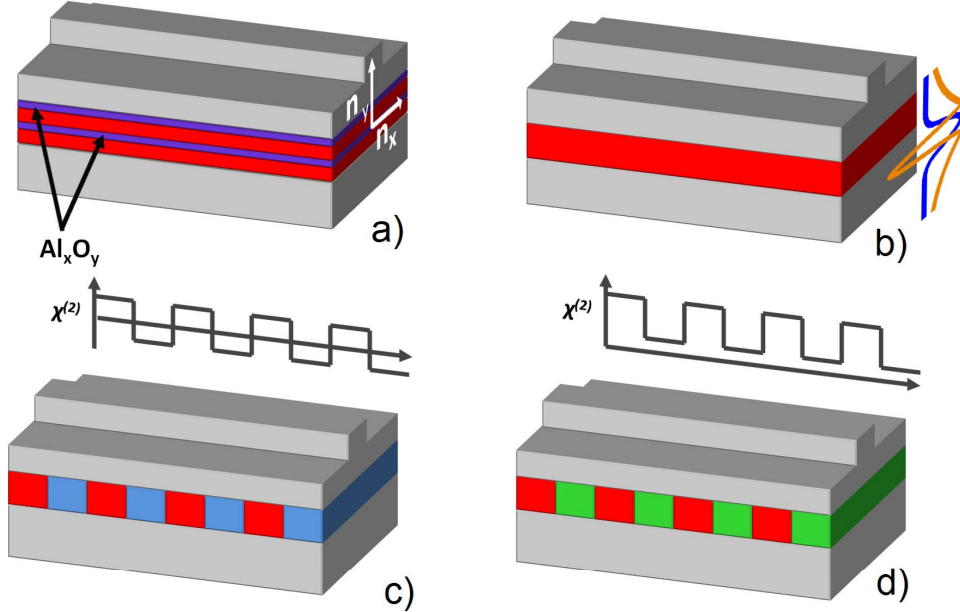


Figure 2.2: Waveguide structures for a) form-birefringence phase matching, b) modal phase matching, c) domain-reversal quasi-phase matching, and d) domain-disordered quasi-phase matching. Source: [40]. ©Wiley-VCH Verlag GmbH & Co. KGaA. Reproduced with permission.

phase matching methods can be grouped as either exact phase matching (EPM) methods, or quasi-phase matching (QPM) methods. For exact phase matching, form-birefringence phase matching (FBPM) and modal phase matching (MPM) are reviewed. Several QPM methods are also reviewed, including work with domain-disordered quasi-phase matching. Since the devices in this thesis are based on AlGaAs, the discussion in this section is limited in scope to other AlGaAs-based devices that have been reported in the literature.

2.3.1 Form-Birefringent Phase Matching

The primary obstacle to achieving phase matching in AlGaAs is the lack of birefringence as a natural material property. To overcome this, researchers have investigated multi-layered structures engineered to provide an artificial form-birefringence. As shown in Figure 2.2a), such form-birefringent waveguides can be fabricated in AlGaAs by adding thin aluminum oxide (Al_xO_y) layers in the waveguiding core. The large refractive index difference between the AlGaAs ($n = 3.3$) and Al_xO_y ($n = 1.6$) layers is sufficient to induce

similar effective indexes for the TE and TM modes of different wavelengths and hence EPM can be achieved. The Alox layers are formed by selective oxidation of AlGaAs layers with high aluminum content (>80%) originally grown into the structure by epitaxy. Other AlGaAs layers with less aluminum content remain as intact semiconductor crystals with their nonlinear properties preserved. As the Alox layers are thin, significant overlap of the optical mode is maintained with the highly nonlinear AlGaAs layers. This technique is attractive because it does not require wafer bonding, oxide deposition, or regrowth epitaxy of AlGaAs to fabricate the structure. Tuning of the phase matching wavelength can be achieved by changing the waveguide ridge width.

AlGaAs/Alox waveguides have been fabricated by several groups. Moutzouris et al. [41] demonstrated SHG utilizing a waveguide structure with a GaAs/Alox core. Output second harmonic powers of up to 650 μW and conversion efficiencies of 1000 %W $^{-1}$ cm $^{-2}$ by 200 fs pulses at a wavelength of 2.01 μm . Ravaro et al. [42] achieved record-high conversion efficiencies of 1500 %W $^{-1}$ cm $^{-2}$ in continuous wave. Difference frequency generation was achieved by Fiore et al. [43] in deeply-etched GaAs/Alox waveguides. A mid-infrared wavelength at 5.3 μm with 80 nW of power was produced from 1.058 μm and 1.32 μm inputs. Parametric fluorescence was demonstrated [44], resonantly enhanced SHG [45], and parametric amplification [46].

While several devices have been demonstrated, FBPM waveguides have several issues to be resolved. First, linear losses are significantly high (> 20 dB/cm) for both the fundamental and second-harmonic wavelengths. This is primarily due to the amorphous Alox layers and roughness at the interfaces between the Alox and AlGaAs layers. Second, FBPM devices have been reported to have low damage thresholds, which is likely due to the presence of defect states at the Alox interfaces which leads to excessive absorption and heating. Third, integrating active devices would be a considerable challenge given that Alox is electrically insulating and thus a barrier to current injection for lasers. Furthermore, even the presence of unoxidized high aluminum content layers presents a challenge for doping to form p-type and n-type material for a laser diode. Lastly, the oxidation of these devices is complex requiring tight control over the process parameters, and deviations from these parameters can result in low yield.

2.3.2 Modal Phase Matching

Exact phase matching can also be achieved in semiconductor waveguides by using a technique known as modal phase matching (MPM). In this method, a multimode waveguide structure is designed such that the fundamental modes of one or two of the wavelengths in the three-wave mixing processes are phase matched with a higher-order mode of the other wavelength, as shown in Figure 2.2b). The longer wavelengths are further away from the band gap resonance in the material index and thus tend to have lower effective indexes than shorter wavelengths. Since the effective index of a waveguide tends to decrease as the mode order increases, it is the shortest wavelength of the process (the second-harmonic in SHG, the pump in DFG) that propagates in a higher order mode.

SHG by MPM has been demonstrated in AlGaAs waveguides at wavelengths around 1550 nm using a 250 fs pulsed source [47] yielding an average power conversion efficiency of 347 %W⁻¹cm⁻². Later, Ducci et al. [48] designed an improved AlGaAs MPM waveguide and used a continuous wave source to produce output second-harmonic powers in excess of 1 μ W and conversion efficiencies of 30 %W⁻¹cm⁻².

Modal phase matching does have some limitations. Losses generally increase with higher-order modes. The shorter wavelength, which already has a higher Rayleigh scattering loss with the sidewall roughness and absorption loss due to proximity to the band gap energy, would experience more loss due to reduced confinement and increased overlap with rough surfaces. Furthermore, losses in waveguide bends would be larger for higher-order modes which limits the potential for integration with curved devices such as ring resonators. The overlap area between the low- and high-order modes involved in the mixing process is also of concern. The variation of the phase across the higher order modes' profile as well as their dissimilar mode distribution with respect to the fundamental limits the interaction between the modes and reduces the potential conversion efficiency.

A variation of MPM is to propagate the interacting waves using different guiding mechanisms in a single guiding structure. Bragg reflection waveguides (BRW) are one such structure [49]. As shown in Figure 2.3, one mode is guided by cumulative reflections

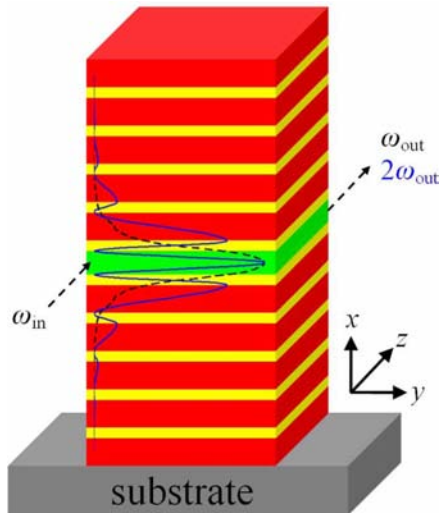


Figure 2.3: Bragg reflection waveguide for modal phase matching. The Bragg mode distribution is shown in solid blue. The TIR mode distribution is shown in dashed blue. Reprinted with permission from [51]. ©2007, American Institute of Physics.

in the Bragg stacks on either side of the core layer. Other modes are propagated by total internal reflection (TIR) as in ordinary dielectric waveguides. By appropriately designing the refractive indexes and thickness of the Bragg stack layers, the propagation constants can be set to provide phase matching between the Bragg modes and the TIR modes. This method has great flexibility allowing the dispersion properties to be engineered over a wide range [50].

Much progress has been made in using BRWs for phase matching second-order nonlinear processes. Bijlani et al. [52] made the original demonstrations of SHG in ridge BRW waveguides and produced average power conversion efficiencies of $205 \text{ \%W}^{-1}\text{cm}^{-2}$ using a pulsed 2-ps source. Recently, Abolghasem et al. [53] showed enhanced second harmonic powers of up to 650 μW using in a modified BRW structure containing matching layers to provide better spatial overlap between the BRW and TIR modes. Average power conversion efficiencies reached as high as $11400 \text{ \%W}^{-1}\text{cm}^{-2}$, representing nearly two orders of magnitude improvement. Difference frequency generation within the telecommunications band using BRWs has also been recently demonstrated [54].

While the performance of BRWs shows promise, there are some challenges to this method of phase matching. First, the Bragg modes tend to be lossy which limits the

conversion efficiency possible. This may be remedied by adding additional layers to the Bragg stacks, however this would make epitaxy of the structure challenging. Monolithic integration with other optical components may also be difficult because of the large number of layers in the structure. For instance, QWI by conventional means would be a challenge given the large depth of the core layer below the wafer surface.

2.3.3 Quasi-Phase Matching

The alternative to exact phase matching is quasi-phase matching (QPM). In this technique, originally proposed by Armstrong et al. [55], the participating waves are allowed to propagate in a nonphase-matched fashion. The phase mismatch accumulated is, however, periodically corrected along the length of the waveguide by modulating $\chi^{(2)}$ and thus forming a $\chi^{(2)}$ grating. In the same way that a linear grating corrects the phase mismatch between two coupled modes, the QPM grating introduces an additional term in the phase mismatch equation

$$\Delta\beta = \beta_3 - \beta_1 - \beta_2 - \frac{2\pi m}{\Lambda} \quad (2.26)$$

where Λ is the period of the $\chi^{(2)}$ modulation and m is the order of the grating. When the grating term balances the equation such that $\Delta\beta = 0$, the process is termed as being quasi-phase matched. When this happens, the flow of power between the waves is mediated by the structure such that back conversion to the source waves is limited and the target wave obtains a net gain in power.

Several methods for quasi-phase matching are possible. In the domain-reversal QPM (DR-QPM) technique, $\chi^{(2)}$ is alternated in sign from positive to negative. Such a structure is depicted in Figure 2.2c). In the SHG process, this results in a quasi-continuous power transfer to the generated wave as shown in Figure 2.4. In another QPM method referred to here as domain-suppressed QPM (DS-QPM), the magnitude of $\chi^{(2)}$ is periodically suppressed such that it alternates between regions of high nonlinearity and low nonlinearity, as depicted in Figure 2.2d). Power is transferred to the second-harmonic wave in regions where the high nonlinearity remains intact. The regions in which $\chi^{(2)}$ is

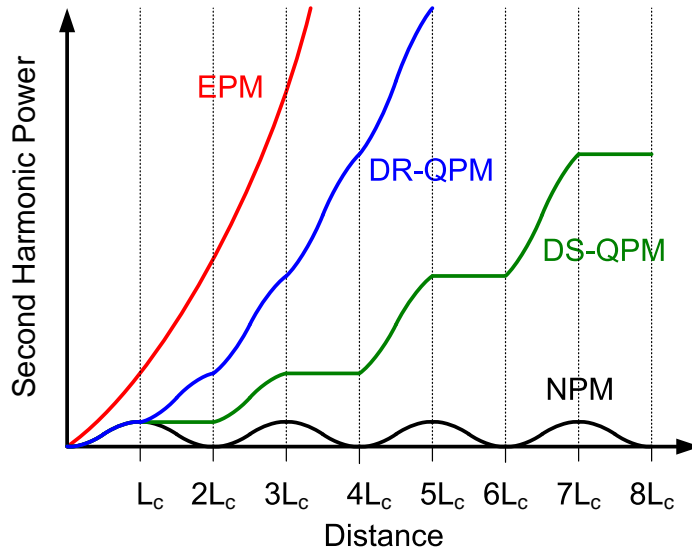


Figure 2.4: Comparison of exact phase matching (EPM), domain-reversal quasi-phase matching (DR-QPM), and domain-disordered quasi-phase matching (DD-QPM) over intervals of the coherence length for the SHG process. Non-phase matched (NPM) SHG is also shown.

suppressed produce little or no back conversion to the fundamental wave, and thus serve only to correct the phase mismatch. As a result, power is transferred in a stair-step pattern with each step being two coherence lengths. In both methods, the phase matching wavelength is determined by the period and duty cycle of the grating.

All things being equal, QPM by either technique does not result in as much power transfer per unit length as EPM techniques. Furthermore, feature sizes for first-order QPM gratings in AlGaAs-based semiconductors can be less than 2 μm , which presents a challenge to the fabrication processes. Often, high-order gratings are necessary to meet the resolution limitations. This leads to more optical losses and reduced normalized conversion efficiency. However, the magnitude of $\chi^{(2)}$ in semiconductors is large, and as a result, even the effective $\chi^{(2)}$ value for QPM can be larger than that of bulk nonlinear crystals. Thus, conversion efficiencies in semiconductor QPM devices can potentially exceed that of EPM. Also, losses are potentially significantly lower than in form-birefringence waveguides and multimode waveguides used in MPM. Thus, QPM waveguides can be made longer yielding higher conversion ratios.

Domain Reversal QPM

DR-QPM is achieved in AlGaAs waveguides by periodically rotating the orientation of the crystal by 90° about the $\langle 001 \rangle$ crystal axes. The rotated anti-phase domains have a $\chi^{(2)}$ value opposite in sign to the normal domains, which is equivalent to shifting the relative phase of the waves by 180° . Creating rotated domains can be achieved by one of two methods: 1) wafer bonding, and 2) orientation-patterned regrowth. In the former, a grating pattern is etched into two different wafers, with one wafer oriented 90° relative to the other. That wafer is then flipped over and aligned to the other wafer such that the gratings fit into each other. The substrate of the flipped wafer is then etched off and ridge waveguides are formed by lithography. Yoo et al. used this fabrication technique with AlGaAs waveguides to demonstrate SHG [56] and DFG [57]. While this technique has shown some success, the etching and wafer bonding leads to rough and uneven interfaces between grating domains leading to high scattering losses.

To address issues of wafer bonding, orientation-patterned regrowth methods for III-V compound semiconductors such as GaAs have been developed [58, 59]. In this technique, the QPM grating pattern is created by periodically replacing the starting material with regrown material in the anti-phase crystal orientation by a technique known as sublattice reversal epitaxy [60]. First, the QPM pattern is etched into the waveguide structure via photolithography and dry etching. Then, a thin layer of an elemental semiconductor such as germanium is first grown into the etched areas. Lastly, the original compound semiconductors are regrown in the etched areas, but with the anti-phase orientation.

The first demonstration of orientation-patterned GaAs (OP-GaAs) waveguides was by Skauli et al. who showed SHG from a pulsed mid-IR source [61]. Later, both Yu et al. [62] and Kondo and Shoji [60] produced quasi-phase matched SHG with a near infrared source. Yu's group managed to improve the fabrication procedures to demonstrate continuous wave SHG conversion efficiencies of $92\%W^{-1}cm^{-2}$ [63]. The work by Yu was extended by Kuo et al. who improved the fabrication processes further for OP-GaAs and demonstrated mid-IR continuum generation [64]. Later work by the same group lead to the development of a terahertz source using OP-GaAs as the wave mixer [65]. Recently,

Bloom et. al [66] used OP-GaAs-based system as a parametric amplifier for a quantum cascade laser operating at 4.5 μm , yielding gains of up to 53 dB. While this method of fabrication has the advantage of reducing scattering losses at the domain interfaces and improved performance, complete bonding of the crystalline structure cannot be achieved due to the anti-phase orientation of the lattice, which ultimately leads to scattering. Furthermore, roughness at the interfaces introduced during the reactive-ion etching process results in high losses. Also, any misalignment of the core layer in the regrown material during epitaxy can lead to mode profile oscillations and the formation of an effective index grating. Progress has been made recently to reduce the scattering loss of the fundamental to below 10 dB/cm by improved fabrication processes, but substantial losses at the second-harmonic in excess of 30 dB/cm must still be overcome to raise conversion efficiencies to practical levels [67].

Another method for achieving DR-QPM is to use an asymmetric quantum well (AQW) structure. Asymmetry induces additional $\chi^{(2)}$ tensor elements such as $\chi_{zzz}^{(2)}$ not ordinarily found in zinc-blende semiconductors. Inverting the order of the layers in the structure has the effect of reversing the sign of $\chi^{(2)}$ [68]. Thus, QPM can be achieved by periodically reversing the AQW. Quasi-phase matched SHG was demonstrated in such structures [69, 70]. However, since this structure is inherently surface emitting, it is not appropriate for larger scale monolithic integration. Additionally, the tensor elements induced by the structure tend to be small, thus limiting conversion efficiency.

Domain Suppression QPM

Domain-suppression can also be achieved by altering the material composition along the waveguide. In the case of AlGaAs, higher aluminum content results in a lower $\chi^{(2)}$ value since the band gap energy is shifted to lower wavelengths. In one method of DS-QPM, a grating is etched and the removed material is replaced with one which has a different value for $\chi^{(2)}$ [71]. While DS-QPM is less efficient over length compared with DR-QPM, as depicted in Figure 2.4, it can be achieved without encountering the anti-phase interface problem, which reduces scattering losses. The advantage of using AlGaAs over other materials is the lattice match across all Al mole ratios, which ensures

minimal regrowth defects. Furthermore, unlike DR-QPM, each domain has the same crystal orientation and smoother domain interfaces are achievable. Lastly, the fabrication method is technologically simpler than OP-GaAs since it involves less processing steps. Rafailov et al. [72] formed such a QPM grating by periodically replacing the originally grown GaAs waveguide core layer with regrown $\text{Al}_{0.4}\text{Ga}_{0.6}\text{As}$. However, while perfectly crystalline interfaces are possible, scattering between domains is still unavoidable due to the deep-etching process creating rough interfaces. Furthermore, the regrowth process invariably leads to misalignment of the core layers, as with the DR-QPM techniques.

Another method for suppressing $\chi^{(2)}$ is to amorphize the material via ion implantation [73]. Amorphization destroys the crystalline structure and results in a centrosymmetric material that has no second-order nonlinearity. However, amorphization also raises the scattering loss by over an order of magnitude the crystalline material, in the range of 30 dB/cm. This would be highly detrimental to conversion efficiency.

2.3.4 Domain Disordered QPM

The challenges of the QPM methods mentioned are numerous, hence the reason to pursue another solution. Achieving lower loss is necessary for efficient conversion, thus there is a need to simplify the fabrication process. There is also a need to integrate QPM structures with other optical devices, thus requiring that the fabrication processes allow this with a degree of ease and flexibility. One approach to DS-QPM is to use a waveguiding core composed of a multiple quantum well structure and to selectively modify it spatially using QWI without the need for additional epitaxy. This approach has several advantages over EPM and other QPM methods, including simplicity and greater integration possibilities.

Two possibilities exist for suppressing $\chi^{(2)}$ in a MQW structure to form a QPM grating. In the first, referred to as the *symmetry modulation technique*, an AQW structure is used as the starting material. The $\chi^{(2)}$ elements induced by the asymmetry vanish after QWI as the material reverts a bulk alloy of AlGaAs and establishes a more symmetric structure. Thus, this provides modulation between the high value of the induced $\chi^{(2)}$ element in non-intermixed ACQ material, and zero in intermixed bulk-like material. In the second method for suppressing $\chi^{(2)}$, referred to here as the *band gap modulation*

technique, QWI increases the energy band gap and thus shifts the dispersion curves of the optical properties (such as the index of refraction and the nonlinear susceptibilities). By operating at wavelengths near the half-band gap energy of the starting or “as-grown” material, $\chi^{(2)}$ can be significantly suppressed as the $\chi^{(2)}$ resonance peak at this energy is shifted to shorter wavelengths after QWI. Using either method, QPM gratings can be formed by periodically intermixing the quantum-well structure to suppress $\chi^{(2)}$ [74]. As such, this technique is known as domain-disordered quasi-phase matching. The key advantage of this method is that it does not require etch-and-regrowth processes, hence it has the potential for creating smooth and defect-free domain interfaces to keep scattering losses low. Furthermore, the QPM periods are patterned by standard lithographic means, which allows great flexibility and cost advantages in setting the desired phase matching wavelength without altering the waveguide structure.

Early work on modulating $\chi^{(2)}$ for AlGaAs-based DD-QPM structures utilized AQWs in the core layer of the waveguide and the symmetry modulation technique. SHG was demonstrated in AQW waveguide structure in which QWI modulated the $\chi_{zzz}^{(2)}$ tensor element utilized in the $\text{TM}_{\text{FHin}} \rightarrow \text{TM}_{\text{SHout}}$ polarization configuration [75]. However, $\chi_{zzz}^{(2)}$ was found to be weak and the modulation depth small (about 0.02 pm/V), ultimately leading to poor conversion efficiency. Instead, work on DD-QPM has turned toward the band gap modulation technique by modulating the large-valued bulk-like $\chi_{zxy}^{(2)}$ tensor element. While modulation of $\chi_{zxy}^{(2)}$ in asymmetric coupled quantum well (ACQW) waveguides was observed [74], it was still too small to be practical. The problem was that the maximum amount of band gap shift was limited by both the aluminum mole ratios and the thicknesses of the MQW layers.

In all work that followed, GaAs/AlGaAs superlattices were used instead of ACQWs. The layers of the superlattice were alternated between GaAs and AlAs, the extremity points in aluminum mole ratios for AlGaAs. The periods were also kept short to reduce the diffusion length required of the lattice constituents during the QWI process. This opened the possibility of fully intermixing the superlattice. This potentially provides the maximal amount of shift in the band gap energy and $\chi^{(2)}$. Calculation of the electronic band structure showed that a short-period symmetric superlattice of 14:14 monolayer

GaAs/AlAs provided both a half-band gap energy near the 1550 nm telecommunications band and a large band gap energy shift of nearly 25% of the total band gap energy [76]. Theoretical calculations of $\chi_{zxy}^{(2)}$ for this superlattice showed a potential 35% reduction after intermixing [35], nearly double that measured in ACQWs. Furthermore, the nonequivolency of the perpendicular and in-plane directions of the superlattice breaks the degeneracy between $\chi_{zxy}^{(2)}$ which is involved in Type-I phase matching and $\chi_{xyz}^{(2)}$ which is involved with the Type-II interaction. Predictions place the modulation of $\chi_{xyz}^{(2)}$ at more than twice as large as $\chi_{xyz}^{(2)}$ [35], which leads to potentially greater efficiency.

Initial superlattice DD-QPM waveguides were fabricated using IFVD methods for QWI [77]. For this particular method, silica is deposited on the surface by two methods. Sputtered silica promotes intermixing underneath it by forming defects at the surface due to outdiffusion of gallium atoms into the silica during rapid thermal annealing. As shown in Figure 2.5a, those defects then diffuse downward to the superlattice core layer and cause interdiffusion of lattice constituents. Silica deposited by plasma-enhanced chemical vapour deposition (PECVD) tends to suppress the intermixing process thus leaving the superlattice below it intact. Using a superlattice of 14:14 monolayer GaAs/AlAs, QPM gratings were realized by the silica cap method [36]. A photoluminescence peak shift of 45 nm was observed in intermixed regions. Type-I SHG was demonstrated using an ultrafast 100-fs laser system operating near 1550 nm. However, second-harmonic powers generated were low, yielding only a conversion efficiency of $13\text{ \%W}^{-1}\text{cm}^{-2}$, which may be attributed to several reasons. Coupling losses and linear losses of the fundamental wavelength were high, which limited the amount of power available for conversion. Secondly, sputtered silica IFVD methods are limited to feature sizes of around 3 μm [78] due to lateral diffusion of defects from the surface during intermixing. This is too large considering that the coherence length for three-wave mixing in AlGaAs is on the order of 1.5 - 2.5 μm depending on the wavelengths. Also, the resolution is highly dependent on how deep the quantum-well layers are from the surface. The limited resolution of the silica cap method necessitated the use of third-order QPM gratings which reduced the conversion efficiency. Lastly, lateral spreading of the defects causes a small amount of intermixing in the superlattice regions that are supposed to be left as-grown. This caused

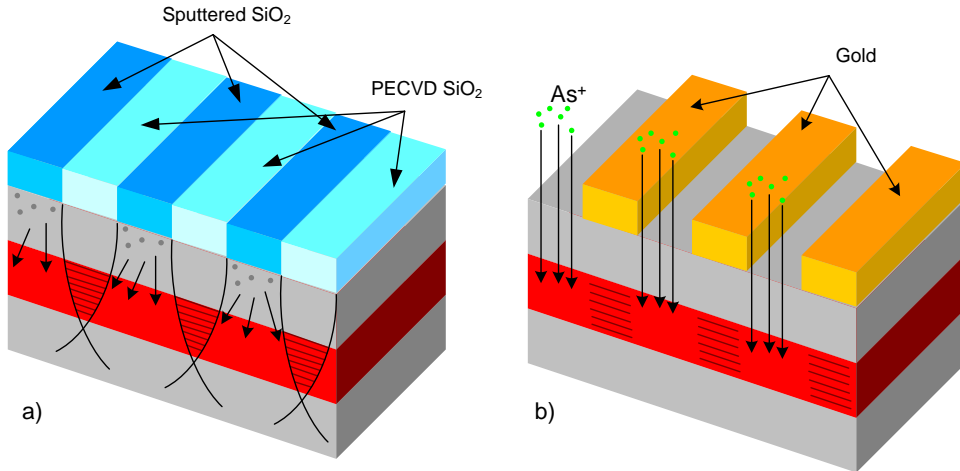


Figure 2.5: Fabrication of DD-QPM gratings by a) sputtered silica cap IFVD, and b) ion-implantation

some suppression in $\chi^{(2)}$ and limited the effective amount of modulation in $\chi^{(2)}$ between the as-grown and intermixed regions.

In subsequent work, ion-implantation induced disordering was used to create the QPM gratings. As shown in Figure 2.5b, As^+ ions are implanted directly into the superlattice layer by appropriately setting the ion beam energy. Ions pass through windows in a patterned metal implantation mask, leaving some areas disordered and others intact. This form of QWI is superior for several reasons. First, the resolution is significantly greater since defects are formed at the buried superlattice layer itself instead of at the surface. This limits lateral diffusion of the defects. Using microRaman spectroscopy, it was shown that IID was able to produce the necessary feature sizes for first-order QPM gratings [34]. Another reason for using IID is that the degree of intermixing can be easily controlled by altering the ion dosage. For instance, using the same 14:14 monolayer GaAs/AlAs superlattice as before, the band gap shift could be varied from 10 - 54 nm [79]. Lastly, optical losses can be reduced through careful control of the parameters for ion-implantation and RTA. However, caution must be taken to ensure that the implantation process does not cause amorphization of the superlattice, which would greatly increase the losses.

Using a similar superlattice-core waveguide structure as that used in the IFVD DD-QPM waveguides, IID was employed to form first-order QPM gratings. Shifts in the

band gap energy of 54 nm after IID were recorded. In nonlinear experiments, output second-harmonic powers exceeded 1 μW for the first time in DD-QPM waveguides and the conversion ratio was tripled over previous waveguides made by the silica cap method [79]. However, the conversion efficiency was still limited by the large optical losses (21 dB/cm) at the fundamental wavelength which was caused by surface damage from etching off the gold implantation mask. Furthermore, the large spectral bandwidth of the 100-femtosecond pulses far exceeded the conversion bandwidth of the QPM grating, thus limiting the amount of SHG possible. In the subsequent generation of devices, an attempt to reduce linear losses was made by adding a protective layer of silicon nitride between the gold implantation mask and the epitaxial layers. Using a 2-ps source, the conversion efficiency was doubled over the previous generation [80]. However, difficulties in removing the silicon nitride layers led to significant losses that still limited the SHG process. Also, Type-II phase matching was not observed, which was likely due to poor confinement of the second-harmonic TE mode in that waveguide design.

2.3.5 Comparison of Phase Matching Methods

Table 2.1 summarizes the performance of the various phase matching schemes in AlGaAs waveguides for second harmonic generation. The normalized conversion efficiencies have been calculated with the data available in each publication. For demonstrations of SHG with pulsed sources, the average power normalized efficiencies are converted into their equivalent instantaneous efficiencies by Equation 2.25. For the cases where CW excitation was used, the efficiency stands as-is. Doing this allows a more direct comparison to be made.

Thus far, the best overall conversion efficiency was demonstrated in BRWs using picosecond pulses. That same experiment also boasts the best equivalent instantaneous conversion efficiency by nearly two orders of magnitude over the FBPM waveguide in Ref. [41]. However, this still does not overcome the measured conversion efficiency any of the continuous wave demonstrations with FBPM, MPM, or DR-QPM. DD-QPM waveguides have up to this point performed much more poorly than the other types of phase matching structures. However, equivalent conversion efficiencies have been steadily

Table 2.1: SHG performance for wavelengths between 1500 nm to 2000 nm of various phase matching types from literature. Quoted efficiencies for pulsed excitation are normalized according to Equation 2.25 to provide the equivalent instantaneous efficiency.

PM Method	Excitation	Quoted η [%W ⁻¹ cm ⁻²]	Equivalent η	Ref.
FBPM	200 fs	1000	0.054	[41]
FBPM	cw	1389	-	[45]
FBPM	cw	1500	-	[42]
MPM	250 fs	347	0.024	[47]
MPM	cw	30	-	[48]
MPM BRW	2.0 ps	205	0.093	[52]
MPM BRW	1.8 ps	11400	4.68	[53]
DR-QPM (wafer bond)	cw	167	-	[57]
DR-QPM (OP-GaAs)	cw	92	-	[63]
DD-QPM (IFVD)	100 fs	13	0.0003	[36]
DD-QPM (IID)	100 fs	145	0.01	[79]
DD-QPM (IID)	1.7 ps	66	0.027	[80]

improving achieving nearly two orders magnitude in improvement in less than five years. Advances in fabrication processes for DD-QPM which led to lower linear losses and improved $\chi^{(2)}$ modulation were responsible for this gain. Since the last demonstration in 2004, fabrication and waveguide design have continued to improve. The results of these improvements form the discussion in the remainder of this thesis.

2.4 Conclusions

In this chapter, the basic theory of second-order nonlinear processes was discussed and various phase matching techniques for AlGaAs waveguides have been reviewed. From the coupled mode equations, simplified analytical equations were derived showing the power and length scale dependencies of the various frequency conversion processes. Several definitions of the conversion efficiency were presented and it was shown that the normalized conversion efficiency best reflects the overall performance of a device. Furthermore, the equivalent instantaneous conversion efficiency was defined such that a better comparison could be made between the various phase matching devices reviewed. Each of these devices utilized either exact phase matching or quasi-phase matching to yield high SHG

output powers and to demonstrate other processes such as difference frequency generation. While most of the device outperformed the DD-QPM devices in terms of conversion efficiency, all had high losses and several obstacles to monolithic integration with a pump laser diode. Furthermore, DD-QPM waveguides have shown a great deal of improvement owing to better fabrication processes and waveguide design.

Chapter 3

Superlattice Waveguides: Design and Characterization

3.1 Introduction

Achieving efficient frequency conversion by three-wave mixing requires careful design of the waveguiding structure and measurement of its various optical properties. Several parameters must be considered and various tradeoffs made. For instance, high confinement of the optical mode to the waveguide core layer is desired to increase the overlap of the interacting wavelengths. However, raising the intensity through high confinement also raises the strength of higher-order nonlinear effects such as self-phase modulation that can hinder, or even stall the conversion process. Also, while the superlattice is designed to provide optimum performance within a certain spectral region, it is necessary to measure and simulate both the linear and nonlinear properties of the superlattice waveguides to determine the specific operating wavelengths for efficient operation.

In this chapter, several aspects of the waveguide design and optical properties will be examined. Beginning with the waveguide layer structure, several improvements made to the superlattice core layer and their impact on device performance will be discussed. From here, the linear optical properties of the superlattice waveguides will be presented, including the measurements of the photoluminescence, mode distribution, and waveguide effective index. Lastly, results from experiments of the third- and fifth-order nonlinear

properties of the waveguide will be examined, and their impact on the conversion efficiency of a QPM device will be discussed.

3.2 Waveguide Structure

The original waveguide structure for DD-QPM was designed by Hutchings and Kleckner [76]. The core layer consisted of a superlattice with alternating well layers of GaAs and barrier layers of AlAs each 14 monolayers (4 nm) in thickness. This was found to provide the optimum band gap energy such that the half-band gap was located near 1500 nm, thus placing the resonance feature of $\chi^{(2)}$ near the telecommunications bands. However, this superlattice design had several issues. First, AlAs oxidizes quickly if left in air. The original superlattice-based QPM waveguides were found to stop working a few months after being fabricated and oxidation was suspected as the cause. Second, the top and bottom of the superlattice were terminated with well layers of GaAs. This unintentionally created asymmetric quantum wells at either end of the superlattice. As the energy states of these wells were different from the band gap energies of the superlattice, several parasitic resonance features were discovered in the linear and nonlinear optical properties of the superlattice [81].

To remedy the problems of the original superlattice, two changes were made and a new core structure was created. AlAs layers in the superlattice were replaced by $\text{Al}_{0.85}\text{Ga}_{0.15}\text{As}$ since reducing the Al mole ratio is known to reduce the oxidation rate [82]. However, as $\text{Al}_{0.85}\text{Ga}_{0.15}\text{As}$ has a lower band gap energy than AlAs, the energy barrier height in the superlattice band structure is reduced, which in turn reduces the band gap energy of the superlattice overall. A commensurate shift in the absorption edge and resonance features of the optical susceptibilities to longer wavelengths was expected. Furthermore, the maximum achievable energy gap shift after quantum well intermixing will be reduced due to this substitution. In the original superlattice, full intermixing would have resulted in an average alloy of $\text{Al}_{0.50}\text{Ga}_{0.50}\text{As}$, whereas the new superlattice would revert to $\text{Al}_{0.425}\text{Ga}_{0.575}\text{As}$ due to the lower overall mole ratio of aluminum in the structure. The difference in the energy of the direct Γ transition between these two

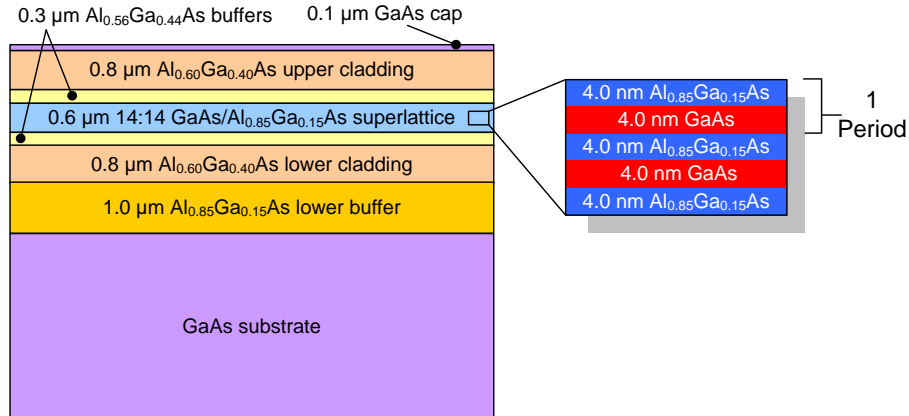


Figure 3.1: Superlattice waveguide layer structure

compositions as per Adachi's empirical model [83] is 0.11 eV, nearly 7% of the predicted band gap energy of the superlattice.

The second major change to the superlattice was to terminate either end with barrier layers instead of well layers. This avoids the formation of asymmetric quantum wells at the edges and the presence of unwanted peaks in the absorption spectrum and susceptibility coefficients. However, growing high-quality terminating $\text{Al}_{0.85}\text{Ga}_{0.15}\text{As}$ layers presented a challenge for the epitaxy process, hence the reason why this was not done in the original superlattice.

Figure 3.1 shows the overall structure of the new superlattice wafer. The substrate was a semi-insulating GaAs wafer, and waveguiding layers were grown by Prof. C. Stanley's group at the University of Glasgow using molecular beam epitaxy. The waveguide core was a 75 period 14:14 monolayer $\text{GaAs}/\text{Al}_{0.85}\text{Ga}_{0.15}\text{As}$ superlattice with terminating barrier layers amounting to a total thickness of 604 nm. Buffer layers of 300 nm-thick $\text{Al}_{0.56}\text{Ga}_{0.44}\text{As}$ were placed on either side of the core to expand the optical mode profile and improve end-fire coupling efficiency. The cladding layers were 800 nm-thick and were composed of $\text{Al}_{0.60}\text{Ga}_{0.40}\text{As}$. A 1000 nm-thick isolation layer of $\text{Al}_{0.85}\text{Ga}_{0.15}\text{As}$ was added below the lower cladding layer to prevent optical leakage to the substrate. A 100 nm cap layer of GaAs was added to the top of the wafer.

3.3 Linear Optical Properties

Various linear optical properties of the waveguides will impact the performance of a quasi-phase matching process. The band gap energy of the superlattice will dictate the workable wavelength range in which absorption of the second-harmonic/pump wavelength and two-photon absorption of the fundamental/signal wavelength are low. The shift in the band gap energy after intermixing will affect the suppression of $\chi^{(2)}$ and the overall efficiency of wavelength conversion. The amount of light that remains contained within the superlattice core is important, and thus, it is instructive to examine the theoretical mode profiles. Lastly, the effective modal index of the wavelengths involved in a three-wave mixing process are necessary to predict the QPM grating periods and duty cycles.

3.3.1 Photoluminescence of As-grown and Intermixed Superlattice

Photoluminescence of the wafer was measured at room temperature by Prof. Stanley's group at the growth facility. The system utilized a 532 nm excitation source at a power of 15 mW. Figure 3.2 shows the resulting photoluminescence spectrum from the wafer. The photoluminescence peaks at a wavelength of 768.47 nm, a red shift of 15 nm relative to the previous GaAs/AlAs superlattice [81]. This is the result of altering the superlattice barrier layers to an AlGaAs composition with a lower aluminum mole ratio. As a consequence of this shift, the second- and third-order nonlinear susceptibilities were expected to peak at a wavelength 30 nm longer than before, extending into the middle of the 1550 nm telecommunications window. Furthermore, the tail of the photoluminescence on the long-wavelength side of the peak indicates that linear absorption will be significant until above 800 nm. This will impact SHG efficiency for waveguides with fundamental phase matching wavelengths below 1600 nm, and will limit DFG pump wavelengths to 800 nm and higher. Lastly, the maximal composition change in the superlattice after QWI would lead to bulk $\text{Al}_{0.425}\text{Ga}_{0.575}\text{As}$, which has a band gap at 625 nm. Thus, the maximum shift is 143 nm in the new superlattice, whereas the previous superlattice demonstrated a shift of nearly 160 nm.

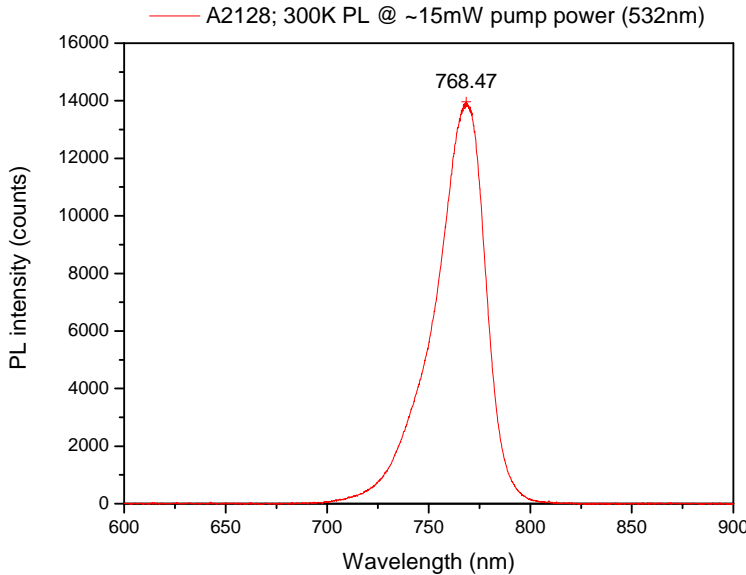


Figure 3.2: Superlattice wafer photoluminescence at 300K (image courtesy of Prof. C. Stanley)

Several intermixed samples were prepared with varying parameters by Dr. B. M. Holmes of the University of Glasgow. First, ion implantation with 4 MeV As²⁺ was applied to each sample at different dosage levels between $0.5\text{--}5 \times 10^{13}$ ions/cm². This was followed by rapid thermal annealing at temperatures ranging from 625–825°C for 60 s. During this process, a piece of GaAs was placed on top of the sample to provide an over pressure such that Ga would not outgas from the samples. Band gap shifts generally increased with temperature for all dosage levels, which is indicative of higher thermal diffusion rates of the lattice constituents. However, temperatures above 775°C caused damage to the wafer surface, and thus these samples were not considered. Further studies proceeded with samples annealed at 775°C, which provided an appropriate balance between band gap shift and surface damage.

Measurements of the photoluminescence at a temperature of 77K were carried out by Dr. Holmes for as-grown and intermixed samples, and the results are shown in Figure 3.3. The peak in the as-grown sample is found at 738 nm. Shifts in the intermixed samples ranged from 68 nm for the lowest dosage to 85 nm for the highest dosage. This represents a shift of 9.5–11.5% in the band gap energy. The expected energy shift for complete intermixing is 18.6%, meaning that the shifts achieved here are at most 62% of the

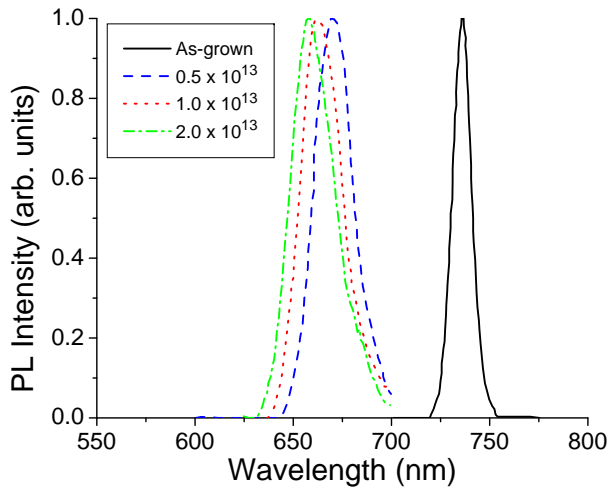


Figure 3.3: Photoluminescence from as-grown and intermixed superlattice samples at various ion dosages (units of ions/cm²) measured at 77K. Each curve is normalized to its own peak value.

maximum. As a result, suppression of $\chi^{(2)}$ is expected to be less than the complete intermixing case. However, the shift in the lowest dosage of 0.5×10^{13} ions/cm² was 24-55% larger than in a previous attempt in which a larger dosage of 1×10^{13} ions/cm² was used [79]. It was also at least 25% larger than a more recent attempt in which a similar dosage of 2×10^{13} ions/cm² was used [80]. Thus, modulation in $\chi^{(2)}$ was expected to be larger in the new superlattice samples than in previous studies.

3.3.2 Etch Depth and Mode Profiles

Selecting the proper etch depth for the ridge waveguides is dependent on several competing requirements. Low scattering losses are desired to keep optical power levels high enough to sustain three-wave mixing over long propagation lengths, which leads to higher overall parametric gain and conversion efficiency. This is best achieved with a shallow etch, which keeps the optical mode buried below the surface and away from damage formed during the etching process. Also, less of the optical mode distribution is exposed to roughness in the sidewalls of the ridge. However, high optical confinement is also desired in order to raise the optical intensity and the overlap of the mode distributions of the waves participating in three-wave mixing. Such high confinement is achieved

by etching deep to reduce lateral extension of the mode distribution across the waveguide slab. Two wavelengths are investigated: 775 nm, which is close to the expected second-harmonic/pump wavelength for the DD-QPM waveguides, and 1550 nm, which is representative of the fundamental and signal/idler wavelength region.

The wafer layer structure of Figure 3.1 was input into the Lumerical MODE Solutions mode solver software. The semi-empirical model of Gehrsitz et al. [84] was used to calculate refractive index values for the AlGaAs buffer, cladding, and isolation layers. Refractive index values for the superlattice core layer were obtained from previous work [81] in which the index of the previous GaAs/AlAs superlattice was back-calculated using a 1-dimensional mode solver and measured effective slab index data [85]. To approximate the index of the new GaAs/Al_{0.85}Ga_{0.15}As superlattice as-grown, the dispersion curve of the refractive index was shifted to longer wavelengths by an amount equivalent to the observed 15 nm difference in the photoluminescence peak between the previous and new superlattice. This adds an error equivalent to the difference in index values between the previous and shifted dispersion curves. For intermixed superlattice, data from the previous superlattice was used as-is.

Initially, a 3.0 μm -wide ridge waveguide with an etch depth of 1.0 μm was simulated. The resulting mode profile for an as-grown waveguide is shown in Figure 3.4a for a wavelength of 775 nm in the TE polarization. In order to obtain convergence in the mode solver for this case, a wide simulation area over 60 μm wide was necessary. As can be seen, confinement was very poor as the mode distribution extends horizontally well beyond the waveguide ridge. While 95% of the mode power is contained within the superlattice layer, the confinement directly beneath the ridge is about 42.1%. This poor confinement is attributed to the relatively tight vertical confinement of 775 nm light to the superlattice layer. The fractional index contrast between the superlattice core layer and the Al_{0.56}Ga_{0.40}As buffer layer is 0.049, which is relatively high. This is expected since 775 nm is close to the band gap energy of the superlattice where the refractive index peaks, while it is sufficiently far from the band gap energy of Al_{0.56}Ga_{0.40}As such that the index remains low. Because of tight vertical confinement, the mode does not extend well enough beyond the core layer to be exposed to the ridge. From the effective index theory

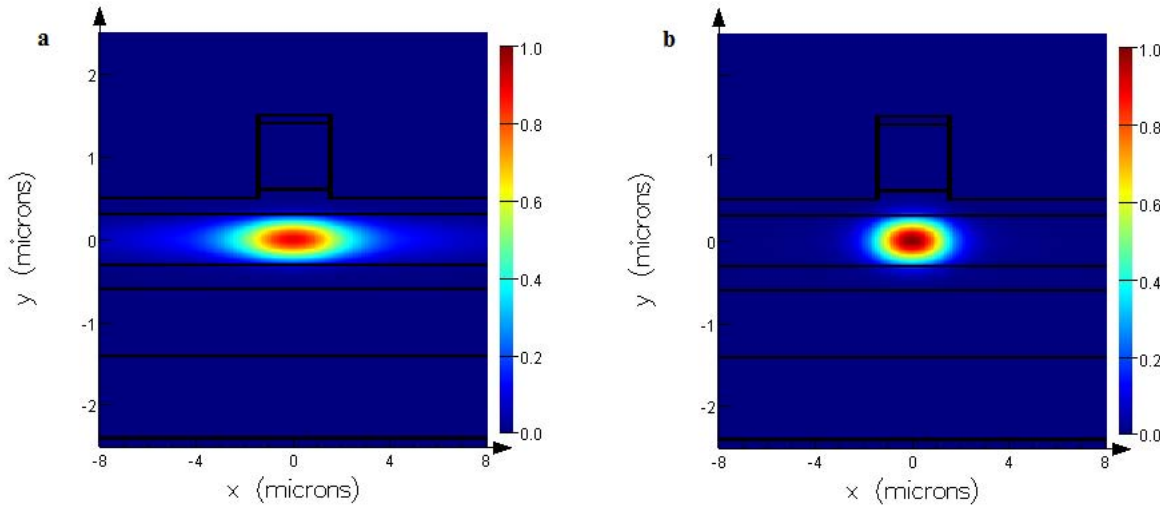


Figure 3.4: Mode profiles at 775 nm in a 3.0 μm -wide, 1.0 μm -deep ridge waveguide for the a) TE, and b) TM polarizations.

[86] point-of-view, the slab mode index below the ridge is not much larger than the slab mode index on either side of the ridge, hence approaching the cutoff condition. Thus, it is expected that the TE mode at 775 nm will have large radiation losses. In contrast, the TM mode at 775 nm, shown in Figure 3.4b is reasonably well confined with 74.7% of the light being contained beneath the ridge. Intermixing the superlattice reduces its refractive index considerably, leading to less vertical confinement and expansion of the mode beyond the core layer. Hence, the horizontal confinement improves such that 66% of the 775 nm TE mode power lies below the ridge.

Improved confinement is desired to reduce losses in the 775 nm TE mode. To this end, the ridge height was gradually increased in the mode solver in 50 nm increments. It was found that the mode was well confined while remaining single-mode at a ridge height of 1.25 μm . Beyond this depth, the waveguide becomes multimode. However, the uncertainty in the refractive index of the superlattice introduces error in the relative amount of confinement for a given etch depth. Thus, an etch depth of 1.30 μm was chosen to ensure sufficient confinement, albeit at the cost of possibly being multimode in the fabricated waveguide samples. Figure 3.5 shows the mode profile for a 1.3 μm -deep ridge waveguide for a wavelength of 775 nm in the TE polarization. Here, the mode distribution is well confined with 95.5% of the power contained beneath the ridge.

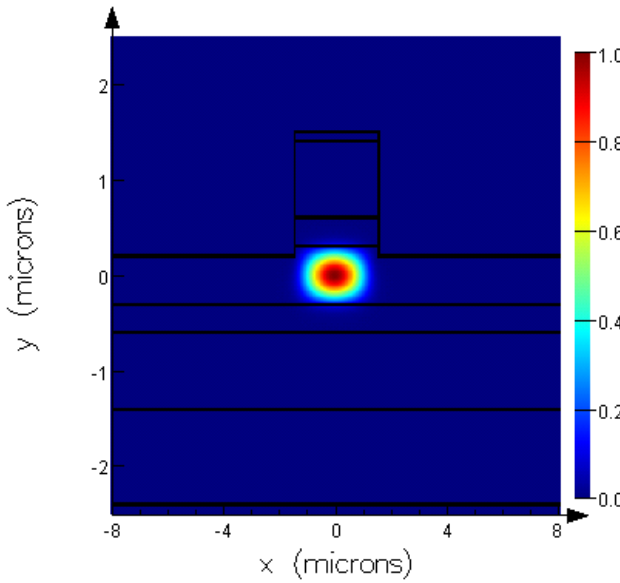


Figure 3.5: Mode profile of a 3.0 μm -wide, 1.3 μm -deep ridge waveguide for the TE polarization at 775 nm.

Likewise, the TM mode confinement is 92.9%. Thus, radiation losses are expected to be lower than in the 1.0 μm -deep waveguides. However, scattering losses are expected to be larger with the surface and sidewalls (and their ensuing roughness) being closer to the more intense portion of the mode distribution.

At 1550 nm, good confinement is obtained with either etch depth in both polarizations for as-grown and intermixed superlattice. The fractional index contrast between the core and buffer layers is only 0.0141 for as-grown superlattice in the TE mode. Thus, the mode extends vertically beyond the core layer and sufficiently into the ridge to be confined horizontally. However, etching deeper does improve confinement of the mode. For instance, the TE mode confinement increases from 49.4% in the 1.0 μm -deep waveguide to 61.4% in the 1.3 μm -deep waveguide, an improvement of nearly 25%. When considering the improved confinement at 775 nm, the overlap between the fundamental/signal wavelength mode and the second-harmonic/pump mode was expected to improve significantly. Thus, it was anticipated that the more deeply etched waveguides would have improved conversion efficiency.

3.3.3 Transmission and Linear Loss at Second-Harmonic/Pump Wavelengths

The transmission characteristics of physical waveguides were tested in order to confirm the conclusions made on the waveguide etch depth and the photoluminescence. Two samples of as-grown waveguides were fabricated: a) one with a 1.3 μm -deep waveguides, and b) one with 1.0 μm -deep waveguides. A Ti:sapphire laser was used as the source for wavelengths between 750-850 nm. Light was end-fire coupled to the waveguides using a $40\times$ objective lens. Output light was collected with a second objective lens and focused onto either a camera during waveguide alignment and coupling, or a silicon photodetector for measuring output power. Detected power values were scaled according to measured calibration ratios which accounted for path losses in the characterization setup, thus providing true measures of the transmission factor of the waveguide sample alone. In the tests carried out, it was assumed that the coupling and collection efficiencies were about the same at each wavelength, which is reasonable given that the mode distributions were found to not change significantly from one wavelength to another within a small range.

First, tests on coupling light into the 1.0 μm -deep waveguides were carried out. In the TM polarization case, confinement was seen on the camera as a distinguishable waveguide mode. However, a large amount of light was observed in the slab mode on either side of the waveguide mode indicating that the mode was close to cut-off. When switching to the TE polarization, no confinement was observed on the camera and any waveguide mode under a waveguide ridge was indiscernible from the band of light propagated in the slab mode. These results agreed with the simulated mode profiles in Section 3.3.2 for 1.0 μm -deep waveguides. Transmission measurements were not carried out for these waveguides as the slab mode light interfered with the results.

Experiments using the 1.3 μm were much more definitive. Guided waveguide modes were clearly observable on the camera in either the TE and TM polarization and were distinguishable from light in the slab mode on either side of the ridges. This agreed well with the mode solver results. Transmission measurements were made at several wavelengths to investigate the relative amount of loss in the superlattice due to absorption.

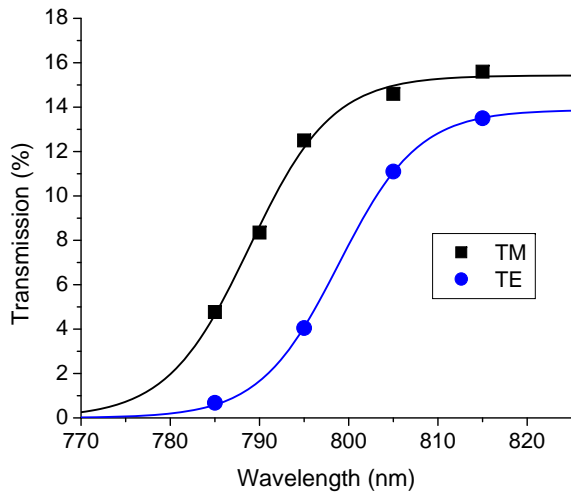


Figure 3.6: Transmission data with sigmoidal fits for 1.3 μm -deep waveguides at pump/second-harmonic wavelengths

Results are shown in Figure 3.6 for the TE and TM polarizations along with sigmoidal fits of the data. In both cases, the transmission increases as the wavelength increases further away from the band gap energy. Below 785 nm, the transmission was very low and effectively zero, as was expected since this was within the band tail observed in the room-temperature photoluminescence. Thus, it is expected that SHG and DFG conversion efficiencies will be significantly reduced below this point. At longer wavelengths, the transmission saturates as the wavelength moves beyond the band tail and into a regime where absorption is nil. Here, scattering losses dominate instead. Over the wavelength range studied, the TM mode had better transmission values than the TE mode. This agrees with the lifted degeneracy of the valance band, which would shift the absorption peak for TM polarized photons to higher energies.

The absorption loss coefficient can be determined from the transmission data. Assuming that the scattering loss coefficient, α_{sc} , coupling efficiency, C , and facet reflectivity are the same over the measured range of wavelengths, the baseline transmission at long wavelengths where the band edge absorption loss is zero is

$$T_0 = C(1 - R)^2 \exp(-\alpha_{sc}L) \quad (3.1)$$

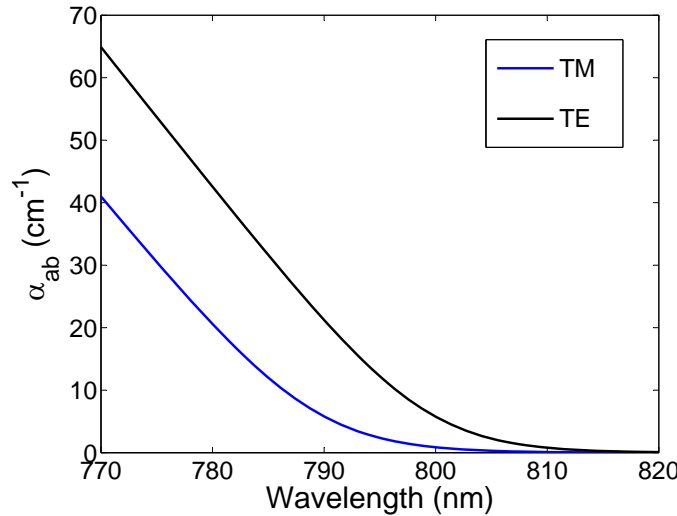


Figure 3.7: Absorption loss coefficient at pump/second-harmonic wavelengths.

where L is the waveguide length. At shorter wavelengths where the absorption loss is significant, the absorption coefficient can be calculated as

$$\alpha_{ab} = -\frac{1}{L} \ln\left(\frac{T}{T_0}\right). \quad (3.2)$$

Figure 3.7 shows the calculated absorption coefficient using the sigmoidal fit of the transmission data. As expected, the loss in the TE polarization is much larger than the TM polarization. Below 785 nm, the difference is more than 20 cm^{-1} . As a result of this, the TE polarization is expected to experience greater amounts of loss, which will reduce the efficiency of the Type-II phase matching process for SHG and DFG.

Scattering losses could not be measured directly at the wavelengths of interest due to lack of an appropriate tunable laser source. However, Fabry-Perot measurements were made using a 980 nm tunable laser. For as-grown waveguides, the loss in the TE and TM modes were 6.2 and 6.7 cm^{-1} , respectively. Intermixed waveguides showed far larger loss coefficients of 16 and 17.5 cm^{-1} , which was likely due to defects created during the implantation process that were not annealed out. By the Rayleigh scattering law, the loss coefficient at shorter wavelengths should be larger. However, simulations of the mode distribution at 980 nm show a 10% reduction in confinement compared to 800 nm. Thus, the exposure of the 980 nm mode to the surface and sidewall roughness would be larger

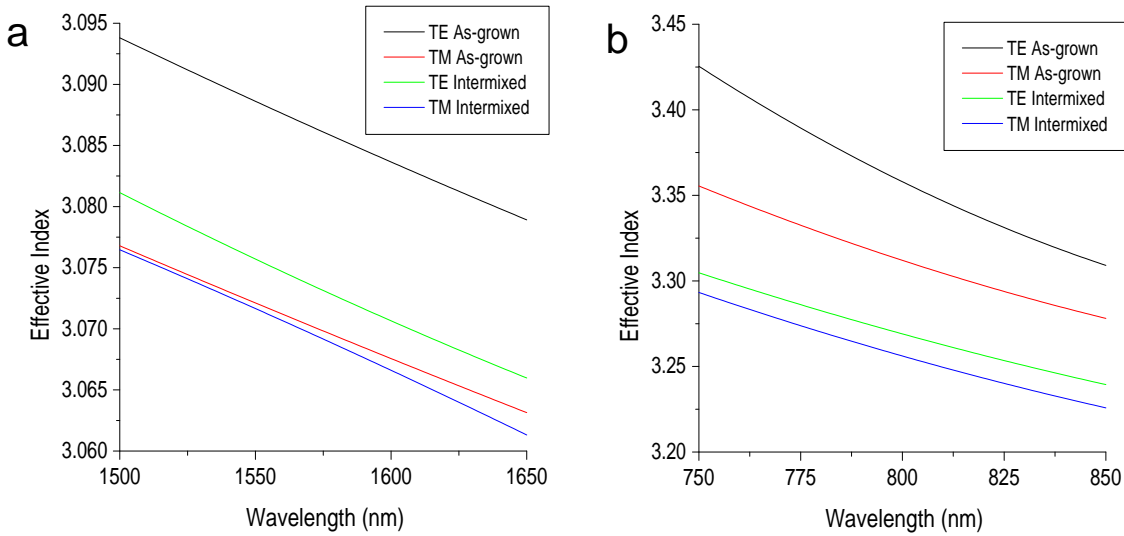


Figure 3.8: Calculated effective mode indexes for 3.0 μm -wide, 1.3 μm -deep superlattice waveguides for a) fundamental, and b) second-harmonic wavelengths.

than at 800 nm. Therefore, we can assume that the two effects balance each other out and that the scattering loss at the pump/second-harmonic wavelengths is similar to that at 980 nm.

3.3.4 Effective Index and Predicted QPM Periods

The effective index of the ridge waveguides at both etch depths for the second-harmonic and fundamental modes was obtained over a range of wavelengths at even increments using the mode solver. Data for the lowest order transverse mode was then fit to quadratic polynomials (see Appendix B). An example of the resulting curve fits is shown in Figure 3.8 for a 3.0 μm -wide, 1.3 μm -deep waveguide. For the as-grown case, the maximum error is taken to be the difference between the interpolated index values and those of the previous superlattice. For the intermixed case, maximum error is taken to be the difference between the effective index when using the previous superlattice index values and the interpolated as-grown effective index values. The uncertainty here stems from the fact that the superlattice is only partially intermixed as indicated by the sub-maximal photoluminescence shift.

QPM grating periods can be predicted using the effective index data. For optimal

conversion efficiency, the superlattice should be periodically intermixed such that the interacting waves propagate in the as-grown regions until they are exactly out of phase in order to maximize parametric generation and minimize back conversion in the intermixed regions. In general three-wave mixing, the waves will be out of phase upon reaching the coherence length, L_c , such that

$$(\beta_{0,3} - \beta_{0,1} - \beta_{0,2})L_c = \pi \quad (3.3)$$

For the case of Type-I phase matched SHG, the coherence length becomes

$$L_{c,I} = \frac{\lambda_\omega}{4(n_{2\omega}(TM) - n_\omega(TE))} \quad (3.4)$$

where $n_{2\omega}$ is the effective index of the second-harmonic and n_ω is the effective index of the fundamental. For the Type-II interaction, the TE and TM modes of the fundamental do not have the same propagation constant and the coherence length becomes

$$L_{c,II} = \frac{\lambda_\omega}{2(2n_{2\omega}(TE) - n_\omega(TE) - n_\omega(TM))} \quad (3.5)$$

The QPM period, Λ , is the sum of the coherence lengths in the as-grown and intermixed sections of the waveguide. Figure 3.9 shows the calculated periods for Type-I and Type-II second-harmonic generation in 1.0 μm - and 1.3 μm -deep ridges. The difference in the phase matching wavelengths is 49 nm between the predicted Type-I and Type-II phase matching wavelengths for the same QPM period for 1.0 μm -deep waveguides. For the 1.3 μm -deep waveguides, this difference is about 70 nm. The slopes of the curves are similar with the phase matching wavelength increasing at a rate of about 14 nm per 0.1 μm increase in the QPM grating period. Since the effective indexes in the as-grown and intermixed sections of the waveguide are different, the optimal duty cycle will not be 50:50 but instead will be generally defined as

$$\text{Duty Cycle} = \frac{L_{c,AG}}{\Lambda} \quad (3.6)$$

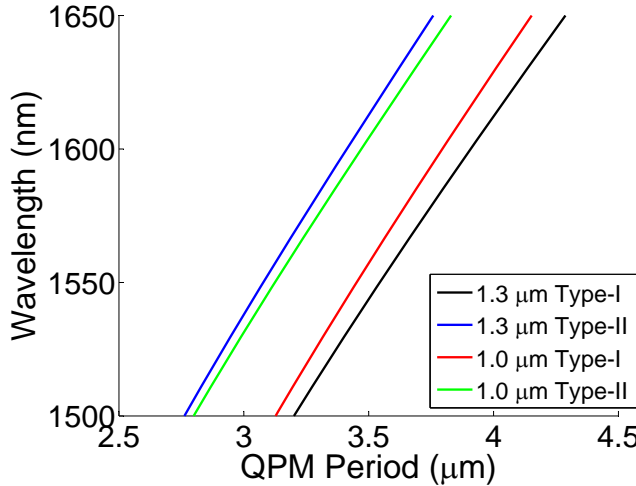


Figure 3.9: Predicted phase matching wavelength versus QPM period.

where $L_{c,AG}$ is the coherence length in the as-grown regions. Over the range investigated, the duty cycle averages around 0.45 for the Type-I interaction and 0.41 for the Type-II interaction when the 1.3 μm -deep waveguide is considered. For the 1.0 μm -deep waveguides, the ideal duty cycle averages around 0.46 for Type-I and 0.42 for Type-II.

3.4 High-Order Nonlinear Properties

Several high-order nonlinear processes must be considered when operating at large optical intensities. Those that are most significant include self-phase modulation, two-photon absorption, and three-photon absorption. SPM is a consequence of nonlinear refraction which emerges from the third-order nonlinear susceptibility. Since SPM is intensity-dependent, it is strongly affected by the TPA and 3PA processes. Thus, nonlinear absorption must be taken into account when determining the magnitude of the nonlinear refractive index. In this section, measurements of the nonlinear absorption coefficients and the nonlinear refractive index will be presented. The methods for determining these properties are based on those established previously for similar superlattice waveguides [81]. Since the design of the waveguides was changed in the present study to alleviate problems with parasitic TPA encountered in the previous study, it was necessary to evaluate these properties again for the current waveguide structure. Furthermore, the

QWI method was changed to IID from IFVD and thus the properties of the intermixed material changed significantly as well.

3.4.1 Experimental Setup

The nonlinear properties of the as-grown and intermixed waveguide samples were characterized using the setup shown in Figure 3.10. The laser source was a singly-resonant CTA-based OPO pumped by a mode-locked Ti:sapphire laser system. Output pulse lengths ranged from 1.3-2.0 ps and the pulse repetition rate was 75.6 MHz. The light was linearly polarized in either the TE polarization or the TM polarization relative to the waveguide using a half-waveplate and a polarizing beam cube (PBC). The polarized beam was then end-fire coupled to the waveguides using a $40\times$ objective lens anti-reflection coated for wavelengths around 1550 nm. Average powers at the waveguide facet were up to 250 mW. Output light from the waveguides was collected by a $40\times$ objective lens. A flip mirror was used to direct the output beam to either a camera for viewing the output waveguide mode, or to a Ge detector that was used to measure the output light and an optical spectrum analyzer (OSA) that was used to observe changes to the output pulse spectrum.

As-grown and intermixed waveguide samples were prepared for this experiment by colleagues in Glasgow. The intermixed waveguides were fabricated from the samples used in the photoluminescence experiments. Ridge waveguides 3.0 μm wide were patterned by electron beam lithography (EBL) and etched by RIE to a depth of 1.0 μm . Linear losses were measured by the Fabry-Perot method [87] with a narrow-linewidth tunable diode laser. The as-grown sample had loss coefficients averaging 0.48 cm^{-1} for the TE mode and 0.55 cm^{-1} for the TM mode for wavelengths between 1505 nm and 1625 nm, which are similar to previous superlattice waveguides [81]. For the intermixed sample with an ion dosage of $0.5 \times 10^{13} \text{ cm}^{-2}$, losses were 0.65 cm^{-1} for the TE mode and 1.38 cm^{-1} for the TM mode. Losses for the higher-dosage samples exceeded 2.5 cm^{-1} and generally increased with increasing dosage. The high losses of these samples limited the amount of observable high-order nonlinear effects, which precluded accurate determination of the nonlinear coefficients. Thus, when evaluating the effect of intermixing, the waveguide

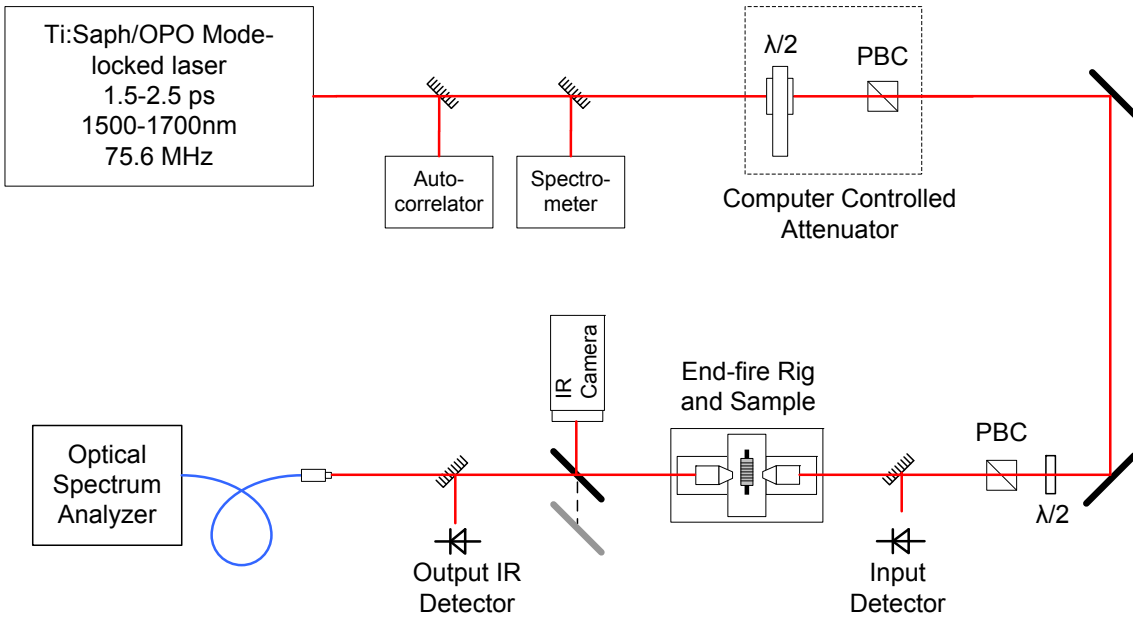


Figure 3.10: Experimental setup for measuring self-phase modulation and nonlinear absorption in superlattice waveguides.

sample with an intermixing dosage of $0.5 \times 10^{13} \text{ cm}^{-2}$ was used. As the low-dosage sample showed the lowest band gap energy shift, the magnitude of the nonlinear refraction, two-photon absorption, and three-photon coefficients should be larger than the samples with larger band gap shifts as is dictated by the band gap scaling laws [88]. Therefore, the coefficients found in this sample can be considered to be the worst case. However, the difference in the photoluminescence peaks for each dosage level is small compared to the overall shift in the band gap energy from the as-grown superlattice, and the dispersion of the nonlinear coefficients tends to flatten out at wavelengths sufficiently distant from the half-band gap resonance. Thus, the coefficients at higher dosages will be similar or at least within the error range of the values obtained for the low-dosage sample.

3.4.2 Two- and Three-Photon Absorption Coefficients

Nonlinear absorption is observed as changes in the transmission through the waveguide as the input power is increased. Using inverse transmission methods [89, 22] for the as-grown material, coefficients α_2 and α_3 can be determined. This was found to be appropriate for as-grown waveguides since only either TPA or 3PA was found to be dominate at

the wavelengths of interest. However, for the intermixed sample, both TPA and 3PA were found to operate at the same time with significant strength. In this case, inverse transmission methods could not accurately determine the coefficients. Instead, more rigorous calculations were required. From the propagation equations found in Appendix A, three-wave mixing, dispersion effects, and SPM can be neglected, giving

$$\frac{dP}{dz} = -\alpha_0 P(z) - \alpha_2 \frac{P^2(z)}{A_{\text{eff}}^{(3)}} - \alpha_3 \frac{P^3(z)}{(A_{\text{eff}}^{(5)})^2} \quad (3.7)$$

where P is the optical power, $A_{\text{eff}}^{(3)}$ is the third-order effective mode area, and $A_{\text{eff}}^{(5)}$ is the fifth-order effective mode area. Given known values of the linear loss coefficient α_0 and the effective areas, α_2 and α_3 for the waveguide structure were determined through numerical simulation and fitting of the measured transmission curves. Coefficient values for the cladding layers were determined using empirical data sourced from Ref. [22] and the band gap scaling laws [88]. Along with the computed overlap of the optical modes with the cladding layers, the coefficient values for the superlattice layer alone could be calculated using Equations A.54b and A.55.

Figure 3.11 shows the measured values of α_2 for the superlattice core for both as-grown and intermixed material. Error bars represent the uncertainty in the numerical fitting and the uncertainty in the value of $A_{\text{eff}}^{(3)}$. As-expected, the as-grown TE case had the largest coefficient value since the half-band energy occurs at approximately 1537 nm. As the wavelength was increased, the TPA decreased to nearly zero at which point the tail of the half band edge had been reached for the TE polarization. The TM case exhibited much lower α_2 values at least an order of magnitude below that of the TE polarization. In this respect, the values are nearly zero and are likely an artifact of the numerical fit resulting from variance in the measured data. The lower values for the TM polarization are consistent with values from previously measured GaAs-AlAs superlattice waveguides [81]. The polarization dependence is attributed to the larger half-band gap energy for the TM polarization than the TE polarization due to the lifted valence band degeneracy in the superlattice. According to the scaling laws, a larger band gap results in lower $\chi^{(3)}$ values [88]. In addition, the detuning of the wavelengths used from the TM half band gap

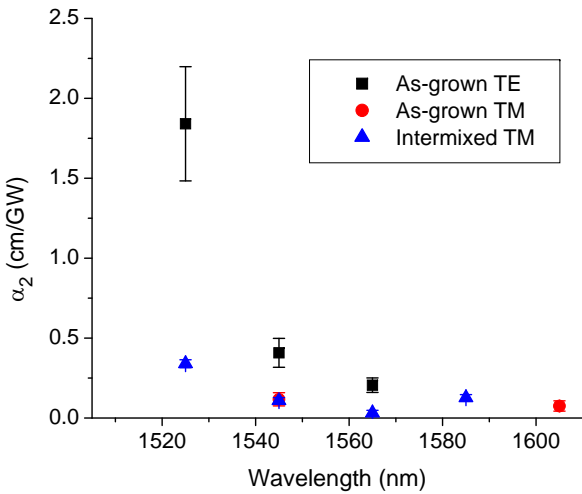


Figure 3.11: Measured values of the two-photon absorption coefficient for the superlattice core layer

leads to even lower α_2 values. Based on the red shift of the photoluminescence in the new superlattice relative to the previous superlattice, the half-band gap resonance is expected at a wavelength below 1500 nm. However, unlike those previous superlattice waveguides, the effect of the parasitic quantum wells have been eliminated as no secondary peaks in the α_2 values were observed at longer wavelengths.

Data from the intermixed waveguides was also analyzed for TPA. The TE polarization tended to exhibit an insignificant amount of TPA or no TPA at all, and thus no coefficients for α_2 are included in Figure 3.11. This is consistent with the half-band gap resonance being shifted to shorter wavelengths. However, significant TPA coefficients were produced from the numerical fits of the TM polarization transmission data. In this case, α_2 was more than 80% lower in the intermixed TM case compared to the as-grown TE case. The presence of any TPA in the intermixed waveguides may indicate that some of the superlattice remained intact after QWI. However, it was expected that the TE polarization would experience larger TPA than the TM polarization in a similar fashion to the as-grown material. In light of this, these non-zero α_2 are attributed instead to artifacts of the numerical fit. The inclusion of these coefficients in other calculations was only done to accurately model the transmission characteristics.

Coefficients for 3PA are shown in Figure 3.12 for both as-grown and intermixed wave-

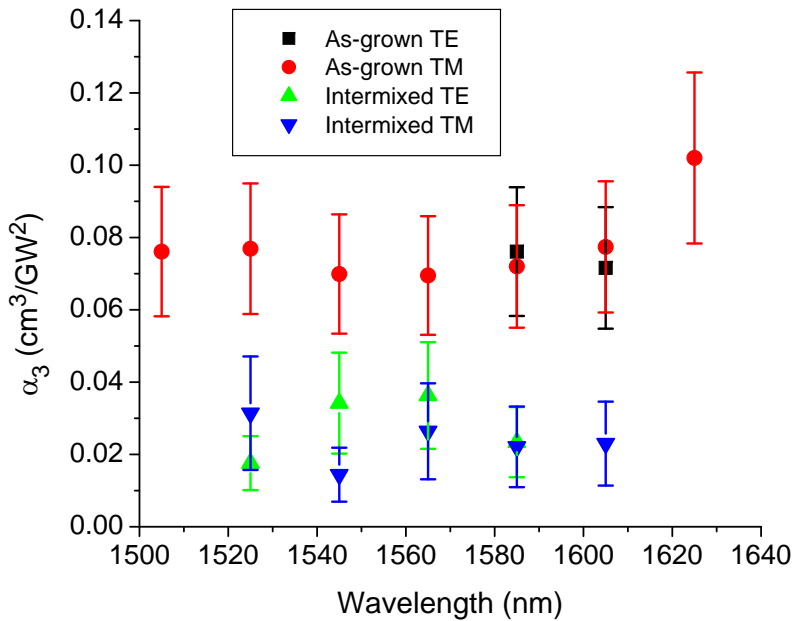


Figure 3.12: Measured values of the three-photon absorption coefficient for the superlattice core layer

uides. For the TE polarization in the as-grown waveguides, TPA was found to dominate over 3PA for wavelengths shorter than 1585 nm. Hence, the 3PA coefficients were taken to be zero. In the TM polarization, little or no TPA was observed and 3PA dominated. The dispersion of α_3 is relatively flat from 1505 nm to 1600 nm. At 1625 nm, α_3 appears to be increasing which would be consistent with the known increase of α_3 in semiconductors as the 1/3 band gap energy is approached [22].

For the intermixed waveguides, α_3 is consistently lower than the as-grown material in either polarization by between 77% and 50%. This reduction is likely the result of the lowered band gap energy in the intermixed superlattice. According to theory, $\alpha_3 \propto E_g^{-7}$. It appears that this factor outweighs the shift of the dispersion curve peak from the predicted 1/3 band edge of the as-grown superlattice at 2300 nm to 2000 nm in the intermixed superlattice.

The observed trends in TPA and 3PA have several consequences on the operating parameters for three-wave mixing processes. In order to obtain the maximum amount of power in the converted/generated waves, the amount of nonlinear absorption should

be limited. As such, TPA can be limited by operating at wavelengths beyond 1565 nm. 3PA will be present at all wavelengths within the telecommunications band, especially for Type-II phase matching which involves both TE and TM polarizations. It should be noted that the coefficients obtained signify that nonlinear absorption is only significant when ultra-short pulses with peak powers on the order of 10-1000 W are used. When continuous waves are used, TPA and 3PA will be insignificant and should not limit second-order nonlinear processes.

3.4.3 Nonlinear Refractive Index

A consequence of SPM with ultra-short pulses is that the nonlinear phase shift will change over the time-varying envelope of each pulse and lead to broadening of the pulse spectrum. The amount of broadening is directly related to the magnitude of n_2 . Thus, the value of n_2 can be determined by examining the evolution of the output pulse spectrum as the optical intensity is increased. An example of the output spectral broadening pattern is shown in Figure 3.13 measured for an as-grown waveguide at a center wavelength of 1545 nm in the TM mode. At a particular power level, the spectrum splits into two peaks with a maximum dip in the middle. This signifies the point at which the nonlinear phase shift is about 1.5π . Under simple models, the value of the nonlinear refractive index could be determined by using analytical equations and the input power level at this point. However, in AlGaAs-based waveguides, the effects of dispersion, linear loss, TPA, and 3PA are too large to be ignored. Instead, the analysis must resort to a more complete model and computer simulations.

The nonlinear Schrödinger equation (NLSE) describing a pulse propagating in a waveguide with the mentioned effects can be written as [81, 91]

$$\frac{\partial A}{\partial z} - j \frac{1}{2} \beta_2 \frac{\partial^2 A}{\partial t^2} + \frac{\alpha_0}{2} A - \left(j \frac{2\pi n_2}{\lambda} - \frac{\alpha_2}{2} \right) \frac{|A|^2}{A_{\text{eff}}^{(3)}} A + \frac{\alpha_3}{2} \frac{|A|^4}{A_{\text{eff}}^{(5)}} A = 0 \quad (3.8)$$

where β_2 is the group velocity dispersion (GVD) parameter and α_0 is the linear loss coefficient. The pulse envelope, A , represents the square root of the optical power and has units of \sqrt{W} . Pulses were modeled as a chirped super-Gaussian function, which is

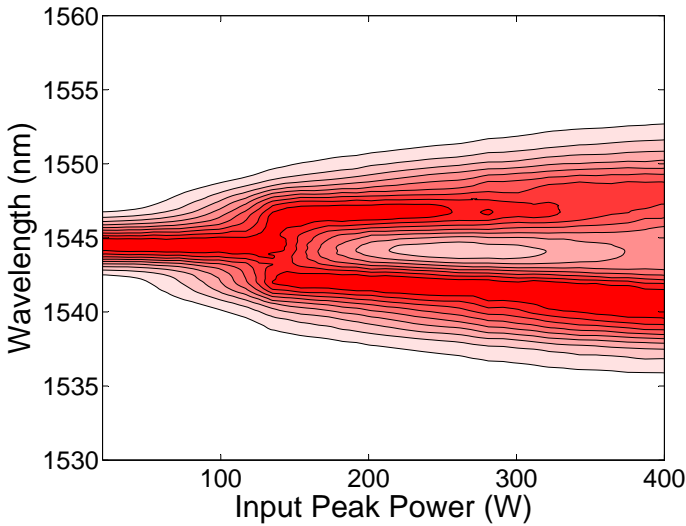


Figure 3.13: Measured output spectral broadening in as-grown waveguides at 1545 nm for the TM polarization. The horizontal axis represents the instantaneous power at the peak of the pulses. Reproduced from [90]. ©2009, IEEE.

defined as

$$A(0, t) = A_0 \exp \left[-\frac{1+jC}{2} \left(\frac{t}{T_0} \right)^{2m} \right] \quad (3.9)$$

where A_0 is the peak value of the pulse envelope, C is the chirp parameter, m is the super-Gaussian parameter, and T_0 is the $1/e$ -intensity point related to the full-width at half-maximum (FWHM) by $T_{\text{FWHM}} = 2\sqrt{\ln(2)}T_0$. The NLSE was solved numerically using the split-step Fourier method [92] and known coefficients for GVD, linear loss, and nonlinear loss. TPA and 3PA coefficients and nonlinear effective areas used were those of the effective waveguide structure as a whole. Nonlinear refractive index coefficients, n_2 , were determined by matching simulated spectral broadening patterns to measured data from the optical spectrum analyzer.

As with α_2 and α_3 , the fit values of n_2 were those of the waveguide structure as a whole. To obtain the n_2 of the superlattice layer alone, the overlap of the optical mode with the cladding layers must be accounted for. Values of n_2 for the bulk cladding layers were determined from measured data [22] and the scaling laws [93]. The Kerr coefficient values for the superlattice layer were then calculated using Equation A.54b. Figure 3.14 shows the values of n_2 for both as-grown and intermixed waveguides at several wavelengths. Error bars represent uncertainty in the linear loss values, nonlinear loss coefficients, and

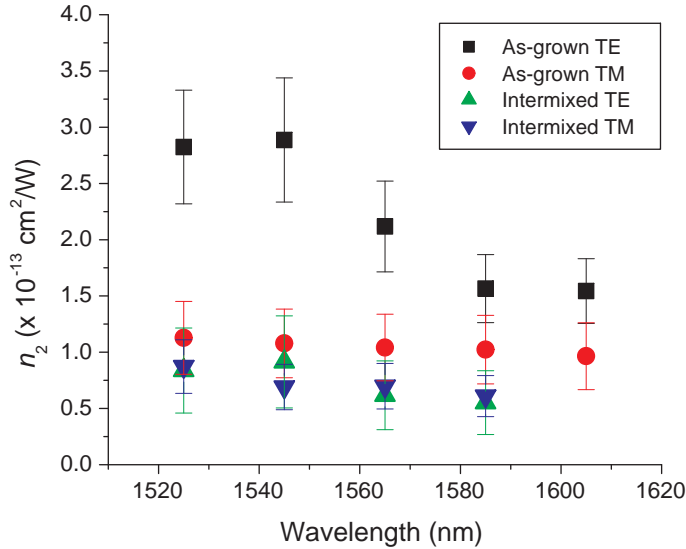


Figure 3.14: Measured values of the nonlinear refraction coefficient for the superlattice core layer. Reproduced from [90]. ©2009, IEEE.

the effective areas. The order of magnitude in the as-grown waveguides is similar to those for bulk AlGaAs waveguides and previous superlattice waveguides. As expected, a strong polarization dependence was observed, especially as the wavelength approached the half-band gap energy of 1537 nm. Around here, n_2 peaks for the TE polarization and has a value nearly three times larger than in the TM polarization. As with the polarization dependence in α_2 , this is attributed to the lifted light-/heavy-hole valence band degeneracy. Since this places the effective half-band gap resonance peak for the TM polarization at a shorter wavelengths, n_2 for the TM polarization remains flat for the wavelengths studied.

The intermixed waveguides showed significantly suppressed values of n_2 . In the TE polarization, n_2 is reduced by up to 71% at the original peak for the as-grown waveguides. The reduction in the TM polarization was somewhat lower (up to 33%) which is attributed to the flatness of the n_2 for as-grown waveguides in the TM mode. Polarization dependencies are reduced substantially in the intermixed waveguides. This indicates that the superlattice has reverted to a more bulk-like AlGaAs material with the valence band degeneracy restored. However, as seen in the as-grown material, the polarization dependence is most obvious near the half-band gap energy. As the wavelengths studied

were distant from the half-band gap energy of the intermixed material, restoration of the valence band degeneracy can not be assured.

As with nonlinear absorption, the measured nonlinear refraction in superlattice waveguides has several consequences for SHG and DFG. Equation 1.4 shows that the refractive index will change with intensity. This will disrupt the second-order nonlinear processes by changing the phase matching condition. Thus, SPM must be limited in order to ensure efficient frequency conversion. The measured data suggests that it is best to operate further away from the half-band gap energy where n_2 peaks. At 1585 nm, the nonlinear refraction coefficient curve for the TE mode flattens out and SPM will negligible for wavelengths beyond here. However, since $\chi^{(2)}$ also peaks at wavelengths near the half-band gap, operating at longer wavelengths will also reduce the conversion efficiency. Thus, the optimum operating wavelength involves a tradeoff between a low n_2 value and a high $\chi^{(2)}$ value. Again, the limitations imposed by nonlinear refraction will only be significant when using high peak powers with ultra-short pulses. It is anticipated that continuous wave conversion/generation at practical input powers will not be affected.

3.5 Conclusions

In this chapter, the design and properties of superlattice-core waveguides were discussed. The original GaAs/AlAs superlattice was altered to reduce oxidation and to remove parasitic quantum wells from the edges. However, these modifications resulted in a shift of the band gap to lower energy and a reduction in the maximum modulation depth by quantum well intermixing. Photoluminescence and waveguide transmission measurements also showed that the operating wavelengths should be such that the second-harmonic/pump is beyond the absorption tail which extends to 800 nm. Mode profile simulations of 1.0 μm -deep waveguides showed that the TE second-harmonic/pump mode is poorly confined and that 1.3 μm -deep waveguides should be investigated albeit at the cost of being multimode and having potentially greater scattering loss from the etched surface. Measurements of the nonlinear optical properties showed relatively large coefficients and the absence of parasitic effects observed in the previous superlattice.

The dispersion curves for nonlinear refraction and two-photon absorption coefficients revealed that the best operating range to avoid these effects is beyond 1600 nm for the fundamental/signal. However, three-photon absorption was found to dominate at these wavelengths and could potentially affect the performance of second-order nonlinear processes.

Chapter 4

Advanced Modeling of Quasi-Phase Matching Waveguides

4.1 Introduction

Wavelength conversion processes in domain-disordered quasi-phase matched superlattice waveguides have the potential to yield high efficiency parametric devices. However, there are several effects that work against the second-order nonlinear processes such that the overall conversion efficiency will be lower than the ideal. These effects include linear loss, dispersion, and high-order nonlinearities. Since the wavelength operating ranges for the superlattice waveguides developed here are near material resonances where these effects can be strong, the impact on conversion processes could be large. However, the simple models of TWM and SHG in Chapter 2 are not adequate enough to account for these effects. Instead, a new, more sophisticated model must be developed. Using this model, the impact of these phenomena in actual experiments with DD-QPM waveguides can be estimated.

In this chapter, an advanced model for three-wave mixing and second-harmonic generation in DD-QPM waveguides will be examined. First, comprehensive equations are presented which accurately model relevant phenomena in conjunction with SHG and TWM. These equations will be applied to both Type-I and Type-II phase matching. Using analytical equations and computer simulations, the effects of linear loss, $\chi^{(2)}$ mod-

ulation, high-order nonlinear effects, and group velocity mismatch and dispersion on SHG conversion efficiency and bandwidth are evaluated.

4.2 Nonlinear Propagation Equations

In order to accurately model the behaviour of three-wave mixing, equations describing the propagation of each wave must include all effects of interest. A complete derivation from the wave equation is detailed in Appendix A. In short, the equations are one dimensional in the propagation direction. The polarizations of the waves are assumed to be linear and set such as to invoke only certain susceptibility tensor elements. This also allows the equations to be scalarized. The resulting nonlinear propagation equations for general three-wave mixing are defined as,

$$\frac{\partial A_1}{\partial z} - \beta_{1,1} \frac{\partial A_1}{\partial t} + j \frac{1}{2} \beta_{2,1} \frac{\partial^2 A_1}{\partial t^2} + \frac{\alpha_{0,1}}{2} A_1 + j \frac{\kappa_1}{\lambda_1} A_2^* A_3 \exp[-j\Delta\beta z] + \zeta_1^{(3)} |A_1|^2 A_1 + \zeta_1^{(5)} |A_1|^4 A_1 = 0 \quad (4.1a)$$

$$\frac{\partial A_2}{\partial z} - \beta_{1,2} \frac{\partial A_2}{\partial t} + j \frac{1}{2} \beta_{2,2} \frac{\partial^2 A_2}{\partial t^2} + \frac{\alpha_{0,2}}{2} A_2 + j \frac{\kappa_2}{\lambda_2} A_1^* A_3 \exp[-j\Delta\beta z] + \zeta_2^{(3)} |A_2|^2 A_2 + \zeta_2^{(5)} |A_2|^4 A_2 = 0 \quad (4.1b)$$

$$\frac{\partial A_3}{\partial z} - \beta_{1,3} \frac{\partial A_3}{\partial t} + j \frac{1}{2} \beta_{2,3} \frac{\partial^2 A_3}{\partial t^2} + \frac{\alpha_{0,3}}{2} A_3 + j \frac{\kappa_3}{\lambda_3} A_1 A_2 \exp[j\Delta\beta z] + \zeta_3^{(3)} |A_3|^2 A_3 + \zeta_3^{(5)} |A_3|^4 A_3 = 0 \quad (4.1c)$$

where $\beta_{1,i}$ is the first-order dispersion coefficient which is related to group velocity, $\beta_{2,i}$ is the second-order dispersion coefficient which is related to GVD, and $\alpha_{0,i}$ is the linear loss coefficient. The second-order nonlinear coupling coefficient is defined as before in Equation 2.4. Under the assumption that the effective area is real valued, the κ coefficients

are all the same. The third-order nonlinear coefficients are defined as

$$\zeta_i^{(3)} = j \frac{2\pi n_{2,i}}{\lambda_i A_{\text{eff},i}^{(3)}} + \frac{\alpha_{2,i}}{2A_{\text{eff},i}^{(3)}} \quad (4.2)$$

where $n_{2,i}$ is the optical Kerr coefficient, $\alpha_{2,i}$ is the two-photon absorption coefficient, and $A_{\text{eff},i}^{(3)}$ is the third-order effective area. The fifth-order nonlinear coefficients are defined as

$$\zeta_i^{(5)} = \frac{\alpha_{3,i}}{2(A_{\text{eff},i}^{(5)})^2} \quad (4.3)$$

where $\alpha_{3,i}$ is the three-photon absorption coefficient, and $A_{\text{eff},i}^{(5)}$ is the fifth-order nonlinear effective area. These equations apply to all three-wave mixing interactions including SFG, DFG, and non-polarization-degenerate SHG. The later case applies to Type-II phase matching where the input fundamental is split between the TE and TM polarization modes. In the case of polarization-degenerate SHG, the Type-I interaction, there are only two waves involved and the nonlinear propagation equations become

$$\begin{aligned} \frac{\partial A_\omega}{\partial z} - \beta_{1,\omega} \frac{\partial A_\omega}{\partial t} + j \frac{1}{2} \beta_{2,\omega} \frac{\partial^2 A_\omega}{\partial t^2} + \frac{\alpha_{0,\omega}}{2} A_\omega \\ + j \frac{\kappa}{\lambda_\omega} A_\omega^* A_{2\omega} \exp[-j\Delta\beta z] + \zeta_\omega^{(3)} |A_\omega|^2 A_\omega + \zeta_\omega^{(5)} |A_\omega|^4 A_\omega = 0 \end{aligned} \quad (4.4a)$$

$$\begin{aligned} \frac{\partial A_{2\omega}}{\partial z} - \beta_{1,2\omega} \frac{\partial A_{2\omega}}{\partial t} + j \beta_{2,2\omega} \frac{\partial^2 A_{2\omega}}{\partial t^2} + \frac{\alpha_{0,2\omega}}{2} A_{2\omega} \\ + j \frac{\kappa}{\lambda_\omega} A_\omega A_{2\omega} \exp[j\Delta\beta z] + \zeta_{2\omega}^{(3)} |A_{2\omega}|^2 A_{2\omega} + \zeta_{2\omega}^{(5)} |A_{2\omega}|^4 A_{2\omega} = 0 \end{aligned} \quad (4.4b)$$

where A_ω is the envelope function for the TE polarized fundamental and $A_{2\omega}$ is the envelope function for the TM polarized second-harmonic. These same equations also apply to the reverse process of degenerate Type-I DFG.

Under the most general conditions, Equations 4.1 and 4.4 do not lend themselves well to analytical solutions. Instead, they are more easily solved using numerical methods. Since the equations involve both time dependent terms and nonlinear terms, they must be solved simultaneously in time and space. Finite difference methods can be used to solve

these equations [94], however they often require lengthy computing times. Instead, these equations can be solved using a pseudospectral techniques such as the split-step Fourier method [92]. In this method, the propagation equations are split into two components. The first component includes all of the dispersion terms and the linear loss term:

$$D_i = \beta_{1,i} \frac{\partial A_i}{\partial t} - j \frac{1}{2} \beta_{2,i} \frac{\partial^2 A_i}{\partial t^2} - \frac{\alpha_{0,i}}{2} A_i. \quad (4.5)$$

The second component contains the nonlinear terms:

$$N_i = -j \frac{\kappa}{\lambda_i} \Psi_i - \zeta_i^{(3)} |A_i|^2 A_i - \zeta_i^{(5)} |A_i|^4 A_i \quad (4.6)$$

where Ψ_i is the unique combination of the field amplitudes and the phase mismatch factor for each equation. While both dispersion, loss, and the nonlinearities act simultaneously, they are solved for separately over short intervals and then added together in each step. In a modified version of the split-step method used here, the dispersion component is solved in the Fourier domain using FFT algorithms, while the nonlinear component is solved using a fourth-order Runge-Kutta method [95]. This algorithm was implemented in MATLAB with underlying code originally from Dr. D. Modotto of the Università di Brescia, which was further developed by the author and Mr. A. Al-Muhairi at the University of Toronto.

Numerical computation of the solutions to Equations 4.1 and 4.4 are only necessary when the dispersion and high-order nonlinear effects are included. It is also helpful when simulating structures with changing material and structural parameters along the propagation direction. However, under simpler circumstances, several assumptions can be made in order to permit analytical solutions and simplify analysis. The first such assumption is that the dispersion and high-order nonlinear effects are nil, which is most appropriately the case when operating with continuous waves instead of pulses. Another common assumption is that the second-order nonlinear effect is weak and the power of the pumping wave is large enough that it does not experience appreciable depletion except by linear loss. These simplifications will be used in some of the following sections.

4.3 Effect of Linear Loss

The effect of linear loss on the conversion efficiency for SHG can be found under several simplifications of the nonlinear propagation equations. The derivation of analytical equations follows the methodology of Bortz [96]. Assuming the undepleted pump approximation, no dispersion effects, and no high-order nonlinear effects, and perfect phase matching such that $\Delta\beta = 0$, the propagation equations for Type-I SHG become

$$\frac{\partial A_\omega}{\partial z} = -\frac{\alpha_\omega}{2} \quad (4.7a)$$

$$\frac{\partial A_{2\omega}}{\partial z} = -j \frac{\kappa}{\lambda_\omega} A_\omega A_{2\omega} - \frac{\alpha_{2\omega}}{2}. \quad (4.7b)$$

Solving these equations by using the integrating factor method yields

$$A_{2\omega}(z) = -j \frac{\kappa}{\lambda_\omega} A_\omega^2(0) \frac{\exp[-\alpha_\omega z]}{(\alpha_{2\omega}/2 - \alpha_\omega)z} [1 - \exp[-(\alpha_{2\omega}/2 - \alpha_\omega)z]]. \quad (4.8)$$

Note that the conversion efficiency in the lossless case is $\eta_0 = (\kappa/\lambda_\omega)^2$. Rearranging Equation 4.8, the ratio of the normalized conversion efficiency η and η_0 for Type-I SHG as defined by Equation 2.20 in a sample of length L is [52]

$$\frac{\eta_I}{\eta_0} = \exp[-2\alpha_\omega L] \left[\frac{1 - \exp[-(\alpha_{2\omega}/2 - \alpha_\omega)L]}{(\alpha_{2\omega}/2 - \alpha_\omega)L} \right]^2. \quad (4.9)$$

This ratio is referred to here as the *conversion efficiency loss factor*. The conversion efficiency reduces with either increasing loss coefficients or increasing length. For Type-II SHG, a similar relationship can be found using the same assumptions:

$$\frac{\eta_{II}}{\eta_0} = \exp[-2\bar{\alpha}_\omega L] \left[\frac{1 - \exp[-(\alpha_{2\omega}/2 - \bar{\alpha}_\omega)L]}{(\alpha_{2\omega}/2 - \bar{\alpha}_\omega)L} \right]^2 \quad (4.10)$$

where $\bar{\alpha}_\omega = \frac{1}{2}(\alpha_{\omega,TE} + \alpha_{\omega,TM})$ is the average loss coefficient of the fundamental wavelength polarizations. Figure 4.1 is a contour plot of the loss factor value for different combinations of the second-harmonic and fundamental loss coefficients for a sample length of

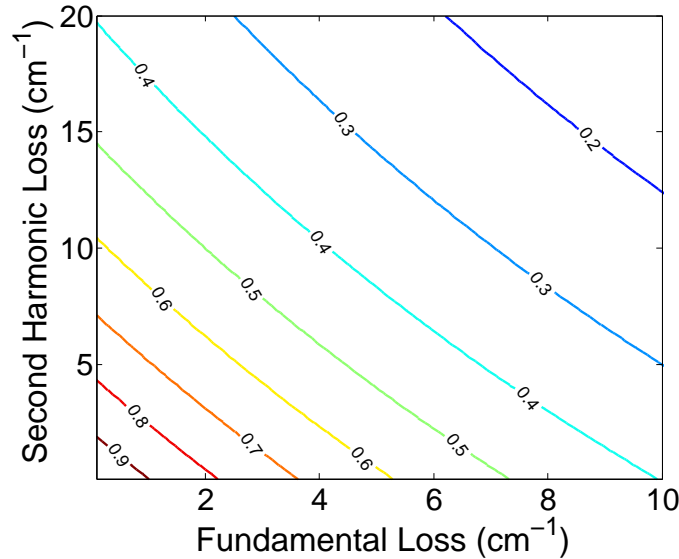


Figure 4.1: Contour plot of the conversion efficiency loss factor dependence on the second-harmonic and fundamental loss coefficients for a 1 mm-long waveguide.

1 mm. Note that the loss factor reduces more rapidly as the fundamental loss increases than as the second-harmonic loss increases. Thus, it is greatly important to keep the fundamental loss coefficient low.

The effect of linear loss on the overall conversion efficiency will also rise as the length of the QPM waveguide increases. Figure 4.2 shows the calculated loss factor over length for reasonable fundamental and second-harmonic loss coefficients of 1 cm^{-1} and 20 cm^{-1} , respectively. The efficiency falls quickly with increasing length, meaning that the second-harmonic power will be generated at a diminishing rate as the beams propagate. Overall, the length dependence of SHG under lossy conditions will not be quadratic as in the simple model of Equation 2.10. The efficiency drops by about 35% of the maximum within 1 mm, and down to 10% after only 2.4 mm. Beyond this point, there will be only a small increase in the generated second-harmonic power and there will be no advantage in increasing the length.

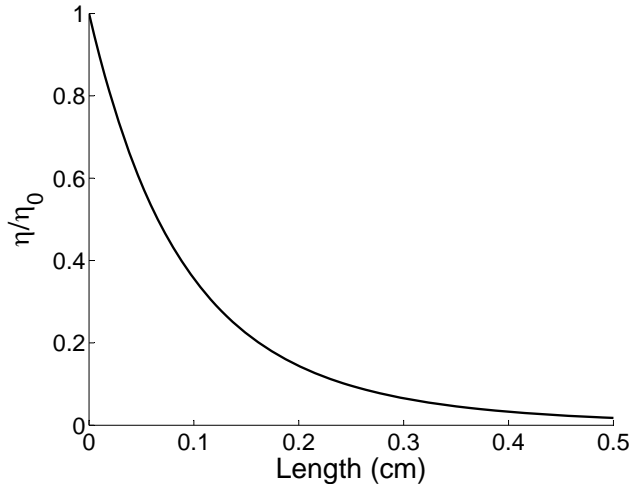


Figure 4.2: Conversion efficiency loss factor dependence on the waveguide length. Fundamental loss is set to 1 cm^{-1} and the second-harmonic loss is set to 20 cm^{-1} .

4.4 Conversion Bandwidth

Efficient SHG will occur in QPM waveguides only within a certain band of wavelengths around the point where the phase matching condition is satisfied. The width of this band depends on the material and structural dispersion of the waveguide, which affects the value of $\Delta\beta$ around the phase matching point. Figure 4.3 shows the tuning curve calculated by Equation 2.10 for Type-I SHG in a QPM waveguide with a $3.5 \mu\text{m}$ period, 50:50 duty cycle, and length of 0.5 mm. The full width at half maximum of the curve is 2.9 nm (364 GHz). Secondary lobes on either side of the phase matching peak are less than 5% of the maximum. For Type-II phase matching, the calculated bandwidth is 2.3 nm (287 GHz), which is slightly smaller than the Type-I bandwidth. This is due to larger dispersion in the TE polarized second-harmonic than in the TM polarization.

The width of the conversion band will also depend on the length of the QPM waveguide. Figure 4.4a shows how the tuning curve changes with the length of the QPM grating. The peak of the curve becomes narrower as the length is increased. This is the result of only those wavelengths closest to the phase matching point being able to maintain coherence over longer distances than those wavelength farther from the peak. From these curves, the FWHM for different lengths was found and is shown in Figure 4.4b. The bandwidth is expected to fall from 3.1 nm for a 0.5 mm long waveguide to 0.3 nm

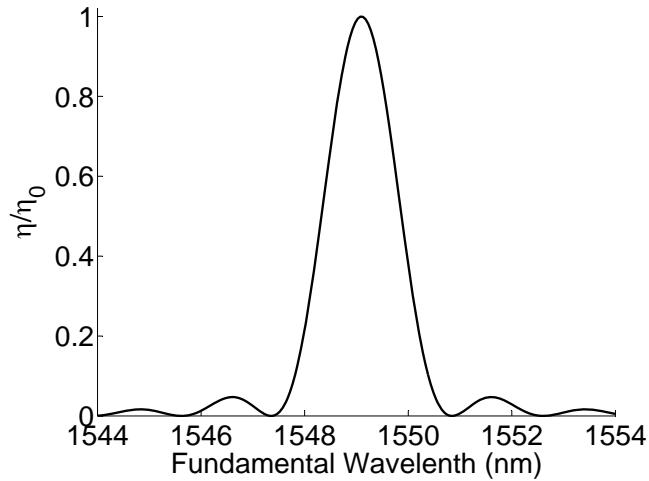


Figure 4.3: Computed tuning curve for Type-I SHG in a QPM waveguide with a $3.8 \mu\text{m}$ period, 50:50 duty cycle, and 1 mm length. The phase matching peak occurs at approximately 1549 nm.

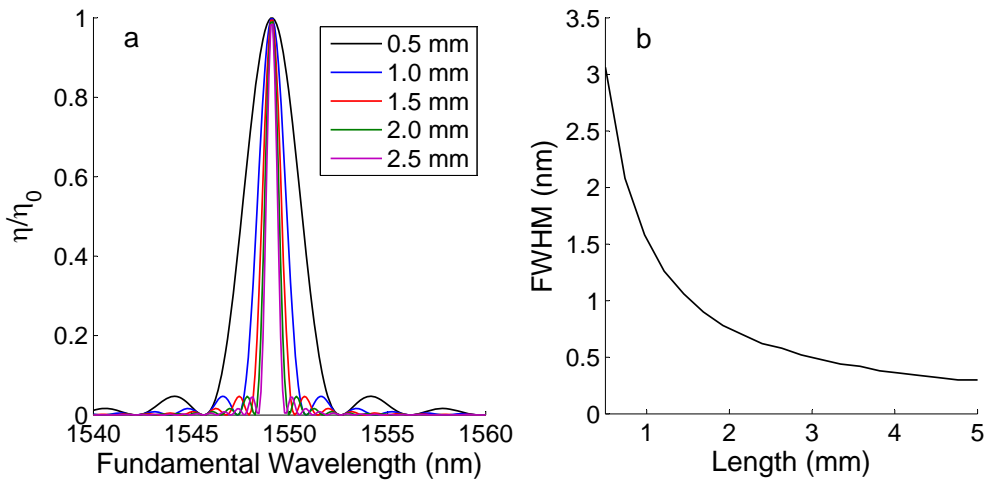


Figure 4.4: a) Computed tuning curves for Type-I SHG in a QPM waveguide with a $3.8 \mu\text{m}$ period and 50:50 duty cycle for different waveguide lengths. b) FWHM of phase matching peak versus length of the QPM waveguide.

for at 5.0 mm long waveguide.

The phase matching process will also be affected by linear losses of both the fundamental and second harmonic. In turn, this will affect the conversion bandwidth. For

Type-I conversion, the second-harmonic power becomes [96]

$$P_{2\omega} = \frac{|\kappa|^2}{\lambda_\omega^2} P_{\omega,0}^2 L^2 \exp[-(\alpha_\omega + \frac{1}{2}\alpha_{2\omega})L] \left[\frac{\sinh^2[\frac{1}{2}(\alpha_\omega - \frac{1}{2}\alpha_{2\omega})L] - \sin^2[\frac{1}{2}\Delta\beta L]}{[\frac{1}{2}\Delta\beta L]^2 + [\frac{1}{2}(\alpha_\omega - \frac{1}{2}\alpha_{2\omega})L]^2} \right]. \quad (4.11)$$

In the case of a short waveguide on the order of 0.5 mm, for reasonable loss values of 1.0 cm^{-1} for the fundamental and $10-40 \text{ cm}^{-1}$ for the second-harmonic, the increase in the bandwidth is less than 10%. However, for longer waveguides on the order of 5 mm, the bandwidth increases by a factor of nearly 3.6 for 40 cm^{-1} of second-harmonic loss. Thus, the effect of loss on the bandwidth becomes more significant as the waveguide becomes longer.

The bandwidth of the SHG conversion process will also depend on the spectral width of the source. In particular, short pulses of around 1–2 ps can have spectral widths from 2–3 nm. Even if the center wavelength of the pulses is detuned from the phase matching wavelength, some part of the pulse spectrum will still overlap with the conversion bandwidth and some phase-matched SHG will occur. Thus, the conversion bandwidth will appear wider than when using a narrow linewidth source such as a continuous wave laser diode. If the pulse envelope has a Gaussian shape such as that described by Equation 3.9, then the second-harmonic power spectral density will be such that

$$\hat{P}_{2\omega} \propto \exp[-(\omega - \omega_0)^2 T_0^2] \text{sinc}^2[\frac{1}{2}\Delta\beta(\omega)L] \quad (4.12)$$

where ω_0 is the center frequency of the input fundamental pulses. Figure 4.5 shows the original tuning curve for a $3.5 \mu\text{m}$ period, 0.5 mm long QPM waveguide as would be observed for a continuous wave source alongside the tuning curves that would be recorded when using short pulses. For pulses with a FWHM of 2.0 ps, the 3-dB conversion bandwidth increases by 14% over the continuous wave case. Note also that the wing lobes of the sinc^2 shape tend to flatten out, which signifies that the pulse spectrum overlap obscures the finer features of the tuning curve. Moving to 1.5 ps pulses further increases the bandwidth by 28%. Computations of the tuning curve using longer pulses on the order of 20 ps showed no significant increases in the conversion bandwidth. This happens

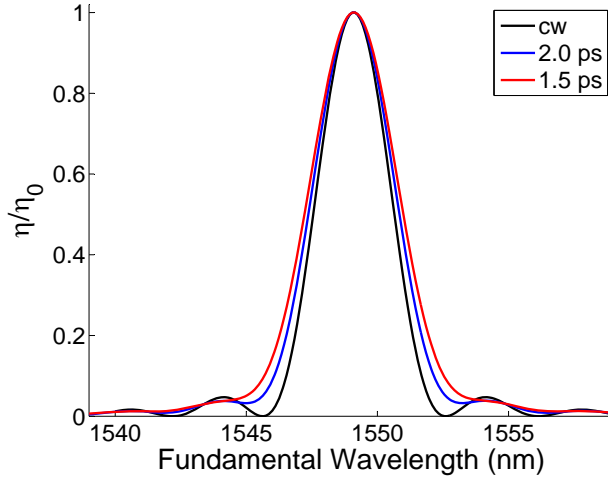


Figure 4.5: Comparison of tuning curves for Type-I SHG in a QPM waveguide with $3.8 \mu\text{m}$ period and 50:50 duty cycle when using a continuous wave source and short pulses.

because the spectral width of 20 ps pulses is an order of magnitude lower than 2 ps pulses. Thus, the spectrum of the 20 ps pulses overlaps with less of the underlying conversion bandwidth as the center wavelength is detuned from the phase matching peak.

4.5 Modulation Depth of $\chi^{(2)}$

The performance of the DD-QPM grating greatly depends on how much $\chi^{(2)}$ is suppressed by the intermixing process. This modulation of $\chi^{(2)}$ can be modeled as a Fourier series [33]

$$\chi^{(2)}(z) = \chi_0^{(2)} \sum_{m=-\infty}^{\infty} c_m \exp\left(im \frac{2\pi}{\Lambda} z\right). \quad (4.13)$$

where Λ is the modulation period and c_m are the Fourier expansion coefficients. Substituting this into the propagation equations without any dispersion, loss, or high-order nonlinearities, and integrating over all z gives the effective $\chi^{(2)}$ for a first-order, square-wave grating with a period that satisfies the phase matching condition [85]:

$$\chi_{\text{eff}}^{(2)} = \frac{\Delta\chi^{(2)}}{\pi} \sin(\varsigma\pi) \quad (4.14)$$

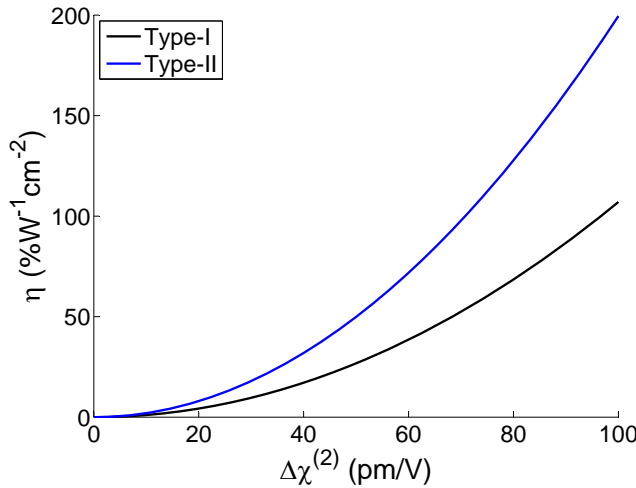


Figure 4.6: Effect of modulation in $\chi^{(2)}$ on SHG conversion efficiency

where $\Delta\chi^{(2)} = \chi_{ag}^{(2)} - \chi_{qwi}^{(2)}$ is the difference in $\chi^{(2)}$ between the as-grown and intermixed domains, and ς is the grating duty cycle defined as $L_{c,ag}/\Lambda$. Note that the effective $\chi^{(2)}$ and consequently the coupling coefficient depends only on the change in $\chi^{(2)}$ and not its absolute value in either domain. According to Equations 2.10 and 2.6, the second-harmonic power conversion efficiency increases with the square of $\chi^{(2)}$. Figure 4.6 shows the predicted nominal conversion efficiency for different values of $\Delta\chi^{(2)}$ for a superlattice waveguide with a 3.0 μm wide ridge and 1.0 μm etch depth. The difference between the Type-I and Type-II curves is due to the difference in refractive index value and effective areas in each configuration.

Estimates of the performance of a superlattice DD-QPM grating can be made given values of the $\chi^{(2)}$ tensor elements before and after QWI. Hutchings [35] predicted values of the $\chi^{(2)}$ tensor elements of as-grown and intermixed 14:14 monolayer GaAs/AlAs superlattices using $\mathbf{A} \cdot \mathbf{p}$ perturbation methods. Data from this publication can be found in Appendix B. For the Type-I interaction, $\Delta\chi^{(2)}$ was predicted to be about 50 pm/V near the half-band gap for complete intermixing of the superlattice in the suppressed domains (see Appendix B). In this case, the predicted $\chi_{\text{eff}}^{(2)}$ is 16 pm/V, which gives a predicted conversion efficiency of 27 %W⁻¹cm⁻². The Type-II interaction was predicted to have a $\Delta\chi^{(2)}$ of 100 pm/V, and thus the predicted $\chi_{\text{eff}}^{(2)}$ is 32 pm/V and the expected conversion efficiency is 200 %W⁻¹cm⁻², which is nearly eight times larger than the Type-I

case.

Achieving complete intermixing of the superlattice is challenging. Indeed, it was shown in Chapter 3 by photoluminescence measurements that the superlattice was not completely intermixed by the ion-implantation process. As a result, there will be less suppression of $\chi^{(2)}$ ultimately leading to lower conversion efficiencies. A reasonable prediction of the modulation in $\chi^{(2)}$ under partial intermixing can be made by assuming that the shift in the dispersion curve for $\chi^{(2)}$ is a simple linear translations dependent on the band gap shift. From the experimental PL data, the shift in the half band gap was about 0.085 eV. In this case, the modulation in the tensor element for Type-I phase matching, $\chi_{zxy}^{(2)}$, is expected to be about 40 pm/V, about an 11% drop from the ideal. Thus, the conversion efficiency reduces to about 17 %W⁻¹cm⁻². For Type-II phase matching, the modulation in $\chi_{xyz}^{(2)}$ is predicted fall to 50 pm/V, and the resulting conversion efficiency falls to 50 %W⁻¹cm⁻², one quarter of the ideal.

4.6 High-Order Nonlinear Effects

High-order nonlinear effects such as SPM, TPA, and 3PA will become significant when using high power, ultrafast pulses on the order of 2-ps. This was observed in Section 3.4 in which measurements of these effects in superlattice waveguides were discussed. In this section, the effect of high-order nonlinearities on the SHG process will be examined. Since few simplifications and approximations can be used under these conditions, the full nonlinear propagation equations must be solved numerically. However, in this analysis, dispersion effects will be ignored in order to isolate the effect of nonlinearities on their own.

Simulations were carried out using the parameters for a 3 μm -wide waveguide with a 1.3 μm -deep etch. The specific values used are summarized in Table 4.1 for a fundamental wavelength of 1550 nm. High order nonlinear effects for the second-harmonic were ignored since the amount of power generated was estimated to be too small to stimulate such effects. For the $A_{\text{eff}}^{(2)}$ values, the portion of the effective area pertaining only to the superlattice core layer was used since most of the overlap between the fundamental and

Table 4.1: Parameter values used in simulations of high-order nonlinear effects with DD-QPM waveguides for the Type-I SHG interaction. Effective area values are for 3.0 μm -wide waveguides with either the 1.0 or 1.3 μm etch depth. The parameters only apply to the 1550 nm wavelength.

Parameter	As-grown		Intermixed	
	1.3 μm	1.0 μm	1.3 μm	1.0 μm
$\chi^{(2)}$ (pm/V)		130		90
n_2 ($\times 10^{-13}$ cm 2 /W)		2.89		0.91
α_2 (cm/GW)		0.41		0.12
α_3 (cm 3 /GW 2)		0.07		0.03
$A_{\text{eff}}^{(2)}$ (μm^2)	5.55	8.88	8.98	11.3
$A_{\text{eff}}^{(3)}$ (μm^2)	4.59	6.37	6.71	8.42
$A_{\text{eff}}^{(5)}$ (μm^2)	3.22	4.41	4.33	5.43

second-harmonic occurs in this layer. The core layer values of $A_{\text{eff}}^{(3)}$ were also used under the assumption that the Kerr coefficient is nearly an order of magnitude smaller in the other layers and because of calculations that showed that the portion of $A_{\text{eff}}^{(3)}$ in these layers is an order of magnitude smaller than in the core layer. Consequently, this allows use of the material $\chi^{(2)}$ for the superlattice theoretically calculated by Hutchings [35], and the measured n_2 and α_2 values presented in Section 3.4.

The results of the simulations with 1.0 μm -deep waveguides are shown in Figure 4.7 when using 2 ps-long pulses and the Type-I interaction in a 1 mm long waveguide. All power levels are scaled to represent average powers in the case where the pulse repetition rate is 76 MHz, the same as the Ti:sapphire/OPO system used in experiments. In the hypothetical case where there are no high-order nonlinearities, the second-harmonic power increases quadratically with input power. When TPA was added, the trend in the second harmonic power deviates slightly from the quadratic behaviour. This was caused by the attenuation of the fundamental, which happens in larger proportions when the power is increased to high levels, thus leading to proportionally less second-harmonic generation. As a result, the second-harmonic power generated had a minor reduction by 5% compared to the case without nonlinear effects. If SPM is included without TPA, the second-harmonic power drastically deviated from the ideal quadratic behaviour, appearing to saturate at high power. This behaviour is a result of SPM disrupting the phase matching process, altering the refractive index for the fundamental such that

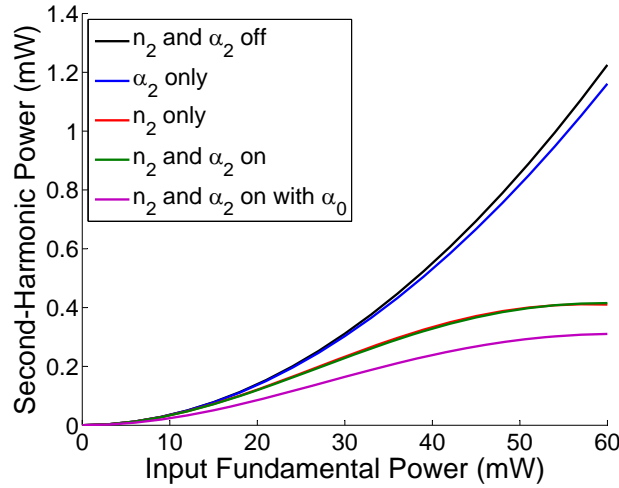


Figure 4.7: Simulated output second-harmonic power for Type-I phase matching in 1.0 μm -deep waveguides with SPM and TPA. Power levels are scaled to represent the average power for a pulse repetition rate of 76 MHz.

$\Delta\beta \neq 0$. The result is a 66% drop in the output second-harmonic power at the high power. When combined together, there was negligible difference with the n_2 only case. Adding 3PA to the simulations had a negligible effect on the SHG process as it was too weak to cause significant attenuation of the input fundamental wave. Overall, this shows that SPM is by far the dominant high-order nonlinear effect that disrupts the SHG process. When linear loss is added to the simulation, the output second-harmonic power is reduced further, falling a total of 75% from the lossless case without SPM and TPA.

Waveguides with the deeper 1.3 μm etch were shown to have better confinement of the second-harmonic mode. This led to better overlap of the second-harmonic and fundamental mode profiles as evidenced by the smaller $A_{\text{eff}}^{(2)}$, which should yield better conversion efficiency. However, as seen in Table 4.2, the consequence of higher confinement is reduction of the $A_{\text{eff}}^{(3)}$ and $A_{\text{eff}}^{(5)}$ as well. As a result, higher-order nonlinear effects will be stronger. Simulation results of the SHG process with increasing power for both etch depths are shown in Figure 4.8. It is assumed that the linear losses in both waveguides are the same. The more deeply etched waveguide achieves better performance. This shows that the improved confinement strengthens the SHG process more than the SPM and TPA processes. Also, saturation in the 1.0 μm -deep waveguides occurs at lower powers.

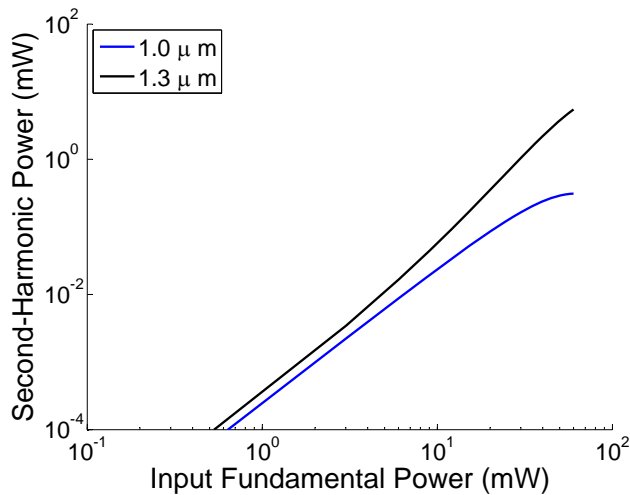


Figure 4.8: Simulated output second-harmonic power for Type-I phase matching in 1.0 and 1.3 μm -deep waveguides with SPM, TPA, and linear loss. Power levels are scaled to represent the average power for a pulse repetition rate of 76 MHz.

The effect of high-order nonlinearities will depend on whether Type-I and Type-II phase matching is used. This is due to the polarization dependence of the Kerr and TPA coefficients. In particular, the reduced strength of the third-order nonlinearity and increased mode size in the TM polarization should reduce the effect of SPM and TPA on the SHG process. Parameters used for simulation of Type-II phase matching in 1.0 μm -deep waveguides are listed in Table 4.2. Results from the simulation are shown in Figure 4.9 alongside results from Type-I phase matching. In both cases, linear losses are set to zero. The overall conversion efficiency is larger for Type-II phase matching due to the larger value of $\chi^{(2)}$ in the as-grown superlattice. Also, Type-II does not begin to saturate until higher powers than Type-I. This results from splitting the fundamental power between the TE and TM polarizations, which lowers the overall strength of SPM.

4.7 Group Velocity Mismatch and Dispersion

Dispersion in superlattice waveguides leads to two key effects that can limit wavelength conversion processes when using ultrafast pulses. Group velocity mismatch (GVM) causes the fundamental and second-harmonic pulses to walk-off from each other. As a result, there is a reduced interaction length. Group velocity dispersion causes spreading of

Table 4.2: Parameter values used in simulations of high-order nonlinear effects with DD-QPM waveguides for the Type-II SHG interaction. Effective area values are for 3.0 μm -wide waveguides with a 1.0 μm etch depth. The parameters only apply to the 1550 nm wavelength.

Parameter		As-grown	Intermixed
$\chi^{(2)}$ (pm/V)		190	90
$n_2 (\times 10^{-13} \text{ cm}^2/\text{W})$	TE	2.98	0.91
	TM	1.08	0.69
$A_{\text{eff}}^{(2)} (\mu\text{m}^2)$		5.16	6.79
$A_{\text{eff}}^{(3)} (\mu\text{m}^2)$	TE	6.37	8.42
	TM	8.34	9.23

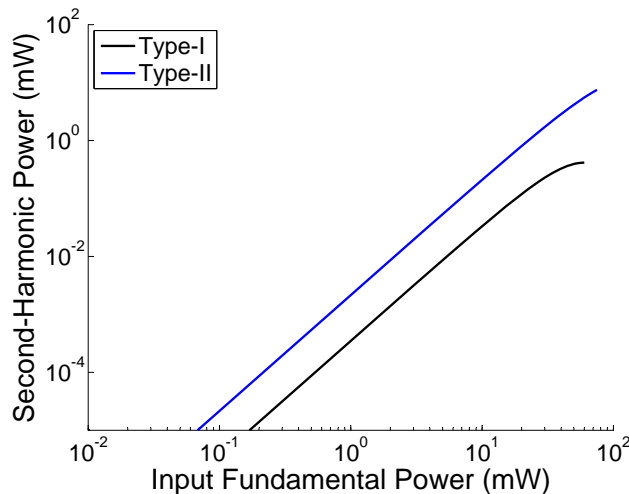


Figure 4.9: Simulated output second-harmonic power for Type-I and Type-II phase matching in 1.0 μm -deep waveguides. Power levels are scaled to represent the average power for a pulse repetition rate of 76 MHz.

the pulses in time which reduces the peak pulse power and disrupts the phase matching process. Overall, dispersion can cause a reduction in efficiency and it must be investigated in order to fully estimate the performance of quasi-phase matching waveguides.

Table 4.3 lists the dispersion parameters calculated from the waveguide effective index data for 1.0 μm -deep ridges. Simulation results with 2-ps pulses for several different cases are shown in Figure 4.10a. In all cases, the effect of GVD was found to be negligible. This is reasonable since the dispersion length [92], $L_D = T_0^2/|\beta_2|$, of 140 cm at 1550 nm is much larger than the 1 mm propagation length. GVM was found to have a relatively small impact on the output second-harmonic power generated, reducing the power by

Table 4.3: Parameter values used in simulations of dispersion effects with 1.0 μm -deep DD-QPM waveguides for SHG.

Parameter		As-grown		Intermixed	
		TE	TM	TE	TM
β_1 ($\times 10^{-8}\text{s/m}$)	1550 nm	1.08	1.07	1.08	1.08
	775 nm	1.48	1.34	1.28	1.28
β_2 ($\times 10^{-24}\text{s}^2/\text{m}$)	1550 nm	0.60	0.33	1.01	-0.59
	775 nm	6.10	3.15	2.00	2.01

a modest 6%. For Type-II phase matching, the reduction was slightly higher at about 8%, which is due to the larger GVM stemming from the higher dispersion of the TE polarized second-harmonic. Adding the loss coefficients did not change the differential reduction between the cases with and without GVM by a significant amount. The output second-harmonic pulses for Type-I shown in Figure 4.10b provide more insights. First, with GVM included in the simulation, the output pulse is observed to be delayed in time by about 0.5 ps relative to the case where there is no GVM. Thus, the second-harmonic pulse drifted away from the faster moving fundamental pulse. As a result, the peak of the second-harmonic pulse is lower by 12%. Second, the pulse length widens from the ideal 1.41 ps to 1.61 ps because of GVM. As the fundamental pulse moved ahead of the second-harmonic, SHG continued at the head of the pulse, thus lengthening the second-harmonic pulse in time. The amount of energy transferred to the second-harmonic continued to increase, but not at the peak point, hence why there was a smaller reduction in average power due to GVM. However, note that there is a small amount of distortion in the second-harmonic pulse shape with the trailing edge extending longer than the leading edge.

In the cases presented so far, the loss values were kept low in the simulations. If instead the losses are increased, some insightful trends become noticed as the interplay between GVM and linear loss becomes more obvious. To study this, the losses in the fundamental were set to 3.5 cm^{-1} and 7.5 cm^{-1} for the as-grown and intermixed regions, respectively. For the second-harmonic, loss coefficients were set to 35 cm^{-1} and 75 cm^{-1} . The results of the simulations are shown in Figure 4.11. The output data, shown as the faint background curves, has several small peaks along to the propagation direction

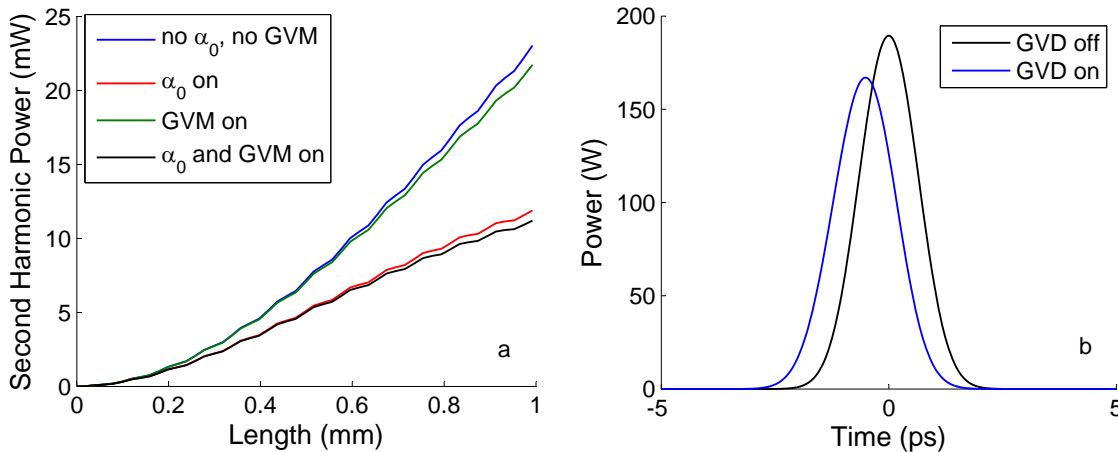


Figure 4.10: a) Effect of group velocity mismatch and linear loss on Type-I SHG over propagation distance. b) Output second-harmonic pulses with and without GVM.

show which is the result of the discretization process of the simulation. Fifth-order polynomial fits of the output data tended to reduce the “noise” and are shown as the smooth foreground curves. As expected, second-harmonic output power was reduced from the lower loss case. However, the high linear loss as also resulted in a peak point in the second-harmonic power at 0.67 mm after which the output power falls with longer propagation. This is the result of linear losses in the fundamental stalling the SHG process such that the second-harmonic generated before the peak point falls victim to high linear losses of its own. Adding GVM to the simulation produces similar behaviour, except that the peak location occurs 20 μm earlier and is 3% smaller. With further propagation to 1 mm, the reduction in power increases to 5.5% in the GVM case. Overall, this is not significant. However, the output power at 1 mm is 12% lower than the peak point. Thus, in an actual device, it is important to select the device length such that it corresponds to the peak length in the SHG process.

4.8 Conclusions

This chapter examined second-harmonic generation in DD-QPM waveguides using advanced models in an attempt to gain insights on the impact of several effects. The model developed was simplified where appropriate in order to obtain analytical solution forms,

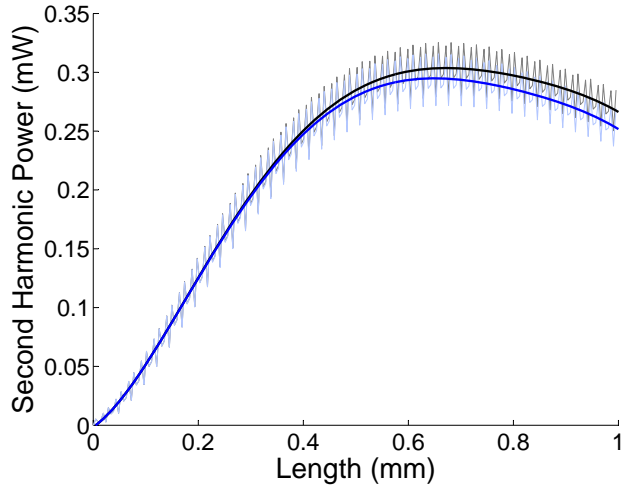


Figure 4.11: Effect of group velocity mismatch with large linear loss on Type-I SHG over propagation distance. The black curve is the case with no GVM, while the blue curve is the case with GVM. Dark solid lines are polynomial fits to the actual data shown as the light coloured curves in the background.

and was otherwise solved numerically using pseudo-spectral methods when necessary. Linear loss was found to have a large impact on the SHG conversion efficiency, reducing it by more than 50% given estimations and measurements of the loss coefficients. Fundamental losses were found to reduce the conversion efficiency by a factor of two larger than second-harmonic losses for the same coefficient value. It was also found that the conversion efficiency reduces significantly with increasing distance. Calculations of the SHG tuning curves showed that the conversion bandwidth was less than 3 nm for a 1 mm-long waveguide, and about 0.3 nm for a 5 mm-long waveguide. Adding linear losses to the model showed that the bandwidth increases significantly only if the loss and waveguide length are relatively large, on the order of a few millimeters. Using short pulses was also predicted to increase the apparent conversion bandwidth by up to 28%. The conversion efficiency was found to depend greatly on the suppression of $\chi^{(2)}$ in intermixed domains of the QPM grating. For the predicted $\chi^{(2)}$ values based on measured band gap shift, Type-II conversion efficiency was found to fall by a factor of four below the ideal theoretical value. High-order nonlinear effects were investigated thoroughly. While three-photon absorption was found to have an insignificant impact, two-photon absorption and especially self-phase modulation disrupted the SHG process significantly.

Second-harmonic power was found to drop by nearly 75% when both are present. SPM and TPA were found to have a less significant effect on Type-II phase matching than Type-I because of the reduced strength of these effects in the TM polarized fundamental. Group velocity dispersion did not significantly impact the SHG process for the waveguide lengths considered. Group velocity mismatch had a modest impact on conversion efficiency, which experienced a reduction of less than 10%. With the impact of these effects on SHG known, these phenomena can be identified and accounted for in experimental characterization of DD-QPM waveguides.

Chapter 5

Characterization of Second Harmonic Generation

5.1 Introduction

The most widely known second-order nonlinear optical process is second-harmonic generation. While SHG is in itself useful for a number of applications, it is not the process of interest for a wavelength conversion device such as that proposed here. Instead, the opposite processes, spontaneous parametric downconversion and difference frequency generation, are required. However, characterizing SHG in a QPM device is key to finding the operating parameters and determining the performance of DFG. The most important parameter to identify is the phase matching wavelength for different QPM grating periods. This will serve to determine the degeneracy pump wavelength for the DFG process at which the conversion bandwidth will be centered between and maximized for the desired signal and idler wavelengths. The SHG conversion efficiency elucidates the potential conversion efficiency of the DFG process around the degeneracy point. As seen in the previous chapter, several effects such as nonlinear absorption, self-phase modulation, linear loss, and group velocity mismatch will adversely affect the conversion efficiency. Thus, it is vitally important to measure the impact of these phenomena in order to design the device parameters and operating regimes for efficient DFG, which will be discussed in the subsequent chapter. Overall, this will determine the pump power required for

sufficient gain in either a parametric converter or oscillator.

In this chapter, several second-harmonic generation experiments performed with domain-disordered quasi-phase matching will be examined. First, the processes used to fabricate the DD-QPM waveguides are discussed, highlighting the improvements made over previous generations of samples. Then, measurements from three different SHG experiments each using different temporal regimes are presented. The first set utilized an ultrafast laser system emitting 2 ps-long pulses. The following section examines SHG with a tunable continuous wave laser system, which was achieved for the first time. Tests with a 20-ps pulse system are discussed and compared with results from the 2-ps pulse experiments. In all regimes, Type-II phase matching is demonstrated for the first time in a DD-QPM waveguide. The data from the SHG experiments is then analyzed to empirically determine several properties of the waveguides including the refractive index mismatch and effective second-order nonlinear susceptibility of the DD-QPM waveguides.

5.2 DD-QPM Waveguide Fabrication

All sample fabrication processes were developed and carried out by colleagues at the University of Glasgow. Several QPM waveguide samples were fabricated over the course of this study, each with varying degrees of success. In each subsequent generation, improvements were made to the fabrication process in order to reduce damage and surface/sidewall roughness. Here, only two of the sample generations will be discussed. The first, Sample A, is an early generation sample which was designed for 1.0 μm -deep waveguides. Despite this being one of the first set of samples, Sample A was produced with minimal problems and was used in several SHG experiments. The second, Sample B, was produced in a later generation of samples and was designed for 1.3 μm -deep waveguides. Several improvements in the fabrication process were incorporated into this sample, which are detailed in the following discussion.

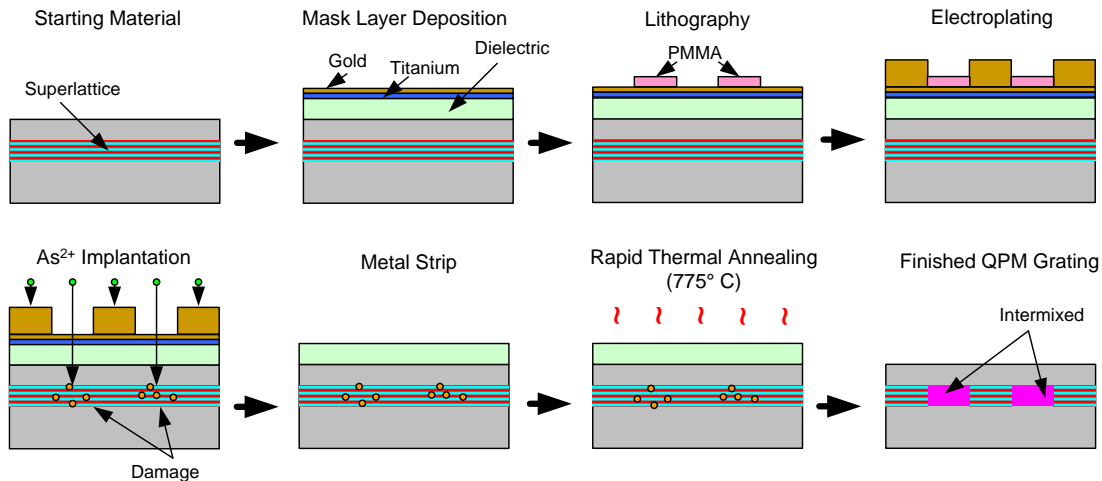


Figure 5.1: Fabrication process for forming QPM gratings in a superlattice via IID.

5.2.1 Grating Formation

The overall process of fabricating the QPM gratings in the superlattice is depicted in Figure 5.1. The fabrication process began with the creation of a patterned metal mask on the substrate for the selective ion implantation process. First, a dielectric layer was deposited onto the surface using PECVD. The purpose of this layer was to protect the substrate from damage due to metal etching processes at later stages in the fabrication [80]. For Sample A, 40 nm of SiN was used as the dielectric layer. However, SiN deposition was found to be nonuniform leading to yield problems in later samples. In subsequent generations, including Sample B, 200 nm of SiO₂ was used as the dielectric layer instead. On top of the dielectric layer, a thin layer (5-10 nm) of titanium was deposited by sputtering as an adhesion layer for the 40-60 nm conductive gold layer which was then sputtered on top. A double-layer of polymethyl methacrylate (PMMA) was spun onto the wafer as a resist for EBL. The QPM grating patterns were written into the PMMA via EBL with grating periods between 3.4-4.4 μm on Sample A and between 3.1-3.8 μm on Sample B. Each period had sets of gratings with as-grown:intermixed duty cycles drawn to 50:50, 40:60, and 60:40. Patterns written into the resist were developed in IPA:MIBK.

Patterning was followed by an electroplating process to grow a thick gold mask. One electrical lead was attached to the sample such that the thin gold layer was charged.

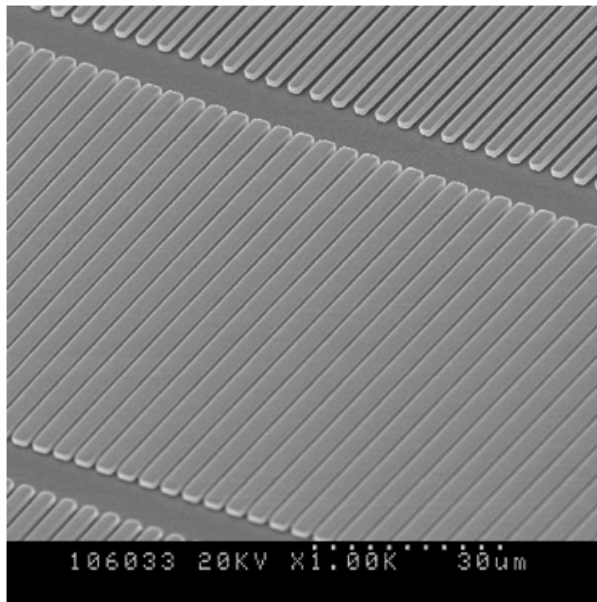


Figure 5.2: Scanning electron microscope image of the ion implantation mask for Sample A after electroplating (image courtesy of Dr. B. M. Holmes)

Gold growth proceeded in areas of the initial thin gold layer which were not covered by PMMA, thus forming the “closed” portions of the implantation mask. The total height of the electroplated gold was 2.0-2.3 μm , which was thick enough to deflect ions during the implantation process. The PMMA in the “open” areas of the mask was then stripped. The thin gold layer in these open areas was thin enough such that ion deflection would be minimal. A scanning electron micrograph of the gold implantation mask from Sample A is shown in Figure 5.2. Measurements of mask openings showed that the actual duty cycles were different from those patterned into the PMMA. Table 5.1 lists the drawn and actual duty cycles. In general, the openings were smaller than designed, which is the result of lateral growth of the gold islands during electroplating. While this was unintended, the smaller mask opening may actually have been of benefit. Simulations of the implantation process using the TRIM software package showed that the lateral ion straggle length is about 330 nm. Thus, the intermixed regions will be wider than the mask openings. Furthermore, lateral diffusion of the lattice constituents during annealing will spread the intermixed region even wider. Thus, despite the mask openings being off the designed ones, the lateral spread of intermixing serves to at least partially correct the error, bringing the actual QPM duty cycle in the superlattice closer to the ideal.

Table 5.1: Designed and actual duty cycles in the ion implantation mask. Duty cycle ratios are expressed as closed:open. (Measurements were carried out by Dr. B. M. Holmes)

Designed	Actual	
	Sample A	Sample B
40:60	53:47	57:43
60:40	89:11	81:19
50:50	72:28	68:32

After the mask was completed, ion implantation quantum well intermixing was carried out. The process began with implantation of As^{2+} ions accelerated to an energy of 4 MeV using the facilities at the University of Surrey. The dosage used was 2×10^{13} ions/cm², which was chosen for several reasons. First, based on earlier tests, this dosage provided an appropriate balance between linear loss at the fundamental wavelengths and band gap shift. Higher dosages provided a marginal amount of increase in the band gap shift, and thus it was assumed that the incremental modulation of $\chi^{(2)}$ would be insignificant. The dosage is five-times less than used in earlier attempts by [79] in which amorphism of the superlattice by the implantation was suspected as a large source of scattering loss. Second, the actual implanted dosage is thought to be less than would ordinarily be implanted due to proximity effects in the relatively small openings of the mask. Third, lateral diffusion of defects will tend to “blur” the interface between the as-grown and intermixed areas thus resulting in less average intermixing in the implanted areas.

Following implantation, the metal mask layers were etched off. However, removal of the titanium layer was problematic. Heat generated during the implantation process was thought to cause the formation of titanium oxide in samples with a SiO_2 dielectric layer, which was difficult to remove. While this did not affect Sample A, subsequent generations were affected. To remedy this problem, the SiO_2 layer was removed by wet etching in hydrofluoric acid. This process was applied to Sample B. Mask removal was followed by RTA. In Sample A, the SiN layer was left on as a cap layer to inhibit outdiffusion of gallium atoms from the wafer thus suppressing intermixing by the IFVD process. For Sample B, a fresh 200 nm layer of SiO_2 was deposited. Annealing proceeded at a temperature of 775°C for 60 s. Photoluminescence measurements at 77K of large open

areas of the Sample A chip, which were subjected to intermixing, showed a blue shift of 76 nm relative to the photoluminescence peak of the starting material. For Sample B, photoluminescence measurements at room temperature showed the large open areas had blue shifts of 70 nm. However, in the grating patterns, the peak shift was 10 nm less. This confirmed that the effective dosage was smaller due to the mask pattern and lateral defect diffusion. The photoluminescence peak of the as-grown superlattice in the grating patterns also appeared to shift by about 15 nm. This was likely due to lateral diffusion of defects from implanted regions, and vertical thermal diffusion of the superlattice constituents during RTA. Using data from Ref. [37], such a shift indicates a vertical diffusion length of about 2-3 monolayers. Thus, the net band gap difference between the as-grown and intermixed regions in Sample B was about 45 nm.

5.2.2 Waveguide Formation

The next step in the fabrication process was to form ridge waveguides. First, the dielectric cap layer from the annealing step was removed by wet etching in hydrofluoric acid followed by an oxygen ash. Hydrogen silsesquioxane (HSQ) was used as the electron beam resist and hard mask for etching. EBL was used to write the waveguide patterns into the HSQ. Waveguides ranged in width from 2-4 μm in 0.5 μm increments and were positioned to provide a range of waveguide sizes over a range of different QPM periods and duty cycles. The written patterns were developed using a solution of tetramethylammonium hydroxide (TMAH). This was followed by reactive ion etching of the AlGaAs in a SiCl_4 chemistry to form the ridge waveguides. Sample A, shown in Figure 5.3a was etched to a depth of 1.0 μm , while Sample B was etched to a depth of 1.3 μm as seen in Figure 5.3b. A difference is noticeable with Sample B showing much more surface and sidewall roughness than Sample A. This was traced to problems during the etching step of Sample B. However, Sample B was still usable and results on its performance are detailed in the following sections.

After fabrication was complete, the samples were cleaved into smaller pieces for testing. At least one sample was cut to 1 mm or less for testing with pulsed systems in which GVD and GVM would affect the performance of SHG. Longer samples were also cut

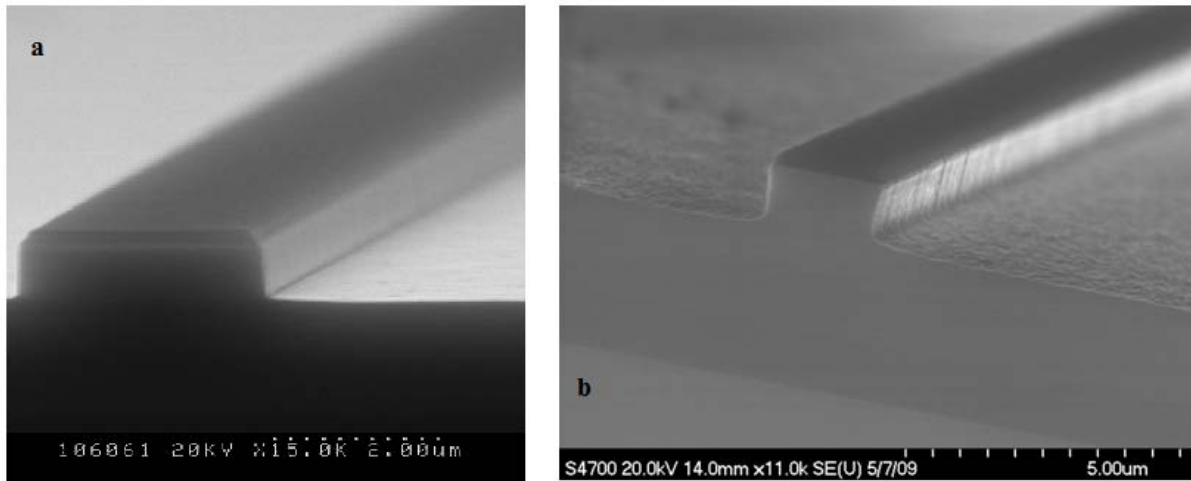


Figure 5.3: Scanning electron microscope image of QPM ridge waveguide samples with a) 1.0 μm etch depth, and b) 1.3 μm etch depth. (Images courtesy of Dr. B. M. Holmes)

for continuous wave measurements in which dispersion effects are negligible, and for loss measurements since accuracy of the Fabry-Perot method was found to be improved for longer cavity lengths. Visual inspection of the fabricated samples showed that the overall yield was improved over previous generations. However, many waveguides suffered damage at various stages during fabrication. As each waveguide was unique, some particular period/duty cycle/waveguide width combinations were not available for testing. Overall, Sample B had more working waveguides than Sample A, the result of improvements to the production procedures.

Linear loss measurements were carried out on Sample A and Sample B using the Fabry-Perot method at wavelengths around 1550 nm. Sample A had loss coefficients averaging 1.0 cm^{-1} in the TE mode and 1.6 cm^{-1} in the TM mode for QPM waveguides. This was a significant improvement over previous generations of DD-QPM waveguides in which losses were 6 cm^{-1} [80]. As expected from the deeper etch and the relatively poor surface and sidewall roughness, Sample B had losses averaging 2.1 cm^{-1} in the TE mode and 4.2 cm^{-1} in the TM mode for waveguides with QPM gratings.

5.3 2-ps Pulse Experiments

Initial experiments began with use of an ultrafast pulsed laser system emitting pulses of about 2-ps in duration. The advantage of using this system was that it provided high peak powers with small spectral bandwidth while limiting the average power to values below the damage threshold for the samples. Significant conversion efficiency improvements were observed previously when transitioning from 200-fs pulses to 2-ps pulses due to improved spectral overlap with the narrow SHG conversion bandwidth despite the tenfold reduction in peak power [80]. The 2-ps system used was also widely tunable, allowing several QPM periods to be tested, especially those waveguide with phase matching wavelengths beyond 1600 nm. However, the peak powers were high enough to induce high-order nonlinear effects. Also, group velocity mismatch was predicted to be significant at short pulse lengths. However, despite these shortcomings, conversion efficiencies and second-harmonic powers measured were the largest recorded over previous generations of DD-QPM waveguides.

5.3.1 Experimental Setup

The experimental setup used to test for SHG with ultrashort pulses was similar to that used to characterize the high-order nonlinear coefficients discussed in Section 3.4. As shown in the schematic of Figure 5.4, it consisted of the mode-locked Ti:sapphire/OPO laser system as the source of fundamental wavelengths in the 1550 nm spectral region. On the output side of the end-fire rig, a long-pass filter with a 1000 nm cutoff (at normal incidence) was added and angled such that the generated second-harmonic power in the output beam was reflected to a silicon photodetector. Some fundamental power was reflected to the silicon detector, however, this did not affect the measured second-harmonic power as the sensitivity of this detector is nil for the fundamental wavelengths used. The output fundamental was passed through the filter and directed to a germanium photodetector for measurements of waveguide transmission. The optical spectrum analyzer was used to measure the output second-harmonic spectrum to detect changes when on and off of the phase matching wavelengths. Two pieces of Sample A, one 0.7 mm long and

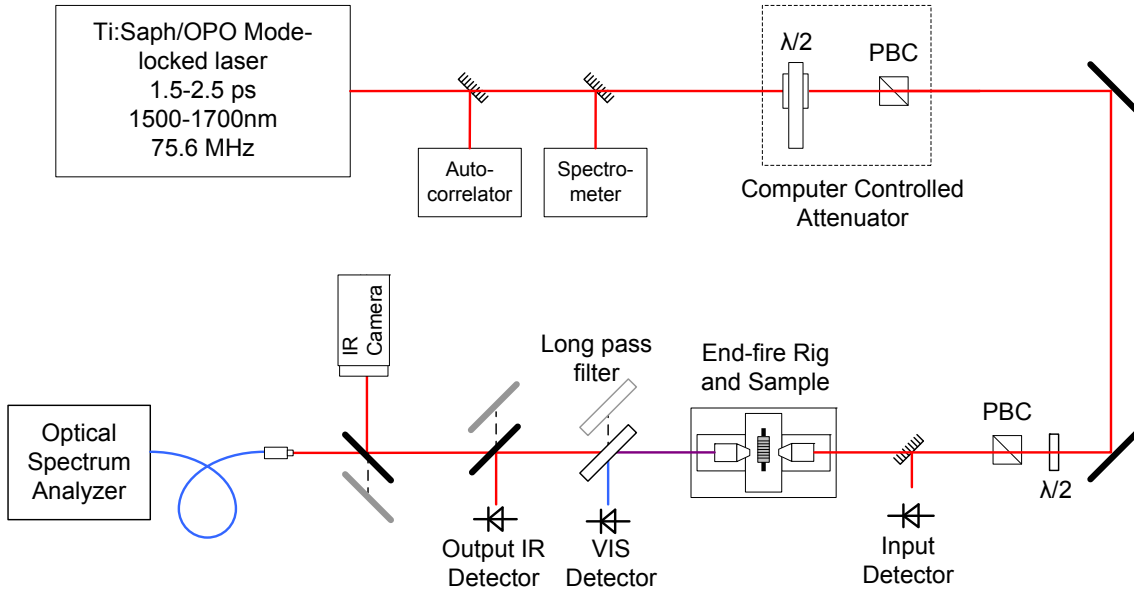


Figure 5.4: Schematic of the experimental setup for SHG experiments with a 2-ps pulsed source

the other 0.6 mm long were tested. Sample B was 1.0 mm in length.

For Type-I phase matching, the input polarization was set horizontal such that the TE mode of the waveguides would be excited. The output second-harmonic light collected was then confirmed to be TM polarized using a beam cube before the silicon detector. In experiments for the Type-II interaction, the input polarizing beam cube was set such that the fundamental beam was linearly polarized 45° relative to the plane of the waveguide layers. This launched both the TE and TM polarizations with equal power amounts into the waveguide to maximize the Type-II interaction. In this configuration, output second-harmonic power produced by the QPM waveguide was a combination of the TM polarized second-harmonic produced by the TE component of the fundamental via the Type-I interaction, and the TE polarized second-harmonic produced via Type-II interaction. Thus, a polarizing beam cube was placed between the long-pass filter and the silicon photodetector and set to pass the TE polarization to isolate the power produced from the Type-II process. Phase matching wavelengths for Type-I and Type-II phase matching were found for various QPM period and duty cycle combinations by tuning the wavelength of the Ti:saph/OPO system until the output second-harmonic power peaked on the silicon

photodetector.

5.3.2 Results

SHG Performance

A summary of the best performing waveguides from Sample A and Sample B is listed in Table 5.2. Initial experiments were carried out with Sample A in the Type-I configuration. In most waveguides, more than 1.5 μW of second-harmonic average power was produced at the respective phase matching wavelengths when using average fundamental powers over 130 mW. When off of the phase matching wavelengths, a pedestal of second-harmonic power was still detected, which was attributed to non-phase matched SHG. The ratio of phase-matched-to-non-phase-matched (QPM:NPM) second harmonic power varied from one waveguide to the next and averaged 4:1 in value. Also, the amount of TM polarized second harmonic power detected exceed the TE polarized power by a ratio of at least 30:1 when at the phase matching wavelength, confirming that the SHG process was dominated by the Type-I interaction.

The best Type-I result was found with a waveguide having a QPM period of 3.6 μm and drawn duty cycle of 60:40. Second-harmonic powers of 4.2 μW were detected with input fundamental average powers of 152 mW. The internal power generated can be calculated by accounting for the path losses from the waveguide facet to the detector. Facet reflectivity was estimated as 29%, collection efficiency of the objective lens was 77%, and reflectivity of the long-pass filter was 86%. This yields an internal second-harmonic power of 9.4 μW at the output facet. The internal input fundamental power can be calculated once the coupling efficiency into the waveguides is known. This can be calculated given the transmission ratio of the fundamental through the waveguide, facet reflectivity, and the linear loss coefficient. Transmission ratios were measured at low power to discount the effects of nonlinear absorption. Facet reflectivity was estimated as 36% from the effective index values. The coupling efficiency ranged between 35-50% for the various waveguides tested and, in particular, 40% for the waveguide currently under discussion. This yielded internal fundamental powers of 45 mW. The normalized internal

Table 5.2: Summary of SHG performance for Sample A and Sample B with 2 ps pulses. Best performing waveguides are listed. All waveguides had a draw duty cycle of 60:40.

	Period (μm)	λ _{pm} (nm)	Internal SH Power (μW)	η (%W ⁻¹ cm ⁻²)
Sample A				
Type-I	3.6	1559.6	9.4	130
Type-II	3.5	1577.4	3.0	32
Sample B				
Type-I	3.6	1558.8	6.8	44
Type-II	3.5	1596.5	2.3	8.8

conversion efficiency, calculated using Equation 2.20, was 130 %W⁻¹cm⁻², which was more than twice as large than in previous DD-QPM waveguides when using a 2-picosecond laser system [80]. In terms of the equivalent instantaneous efficiency of Equation 2.25, this particular waveguide had an efficiency of 0.037 %W⁻¹cm⁻². This is an improvement by two-orders of magnitude when compared to the initial demonstrations of SHG in DD-QPM waveguides [36]. The performance increase is attributed to the improved sample quality over previous generations. However, the conversion efficiency still falls two-orders of magnitude lower than BRW waveguides by either measure [53].

Type-II phase matching in the waveguides was characterized in subsequent experiments. As predicted, the Type-II interaction phase matches at a longer wavelength than the Type-I interaction due to strong birefringence in the superlattice. Second-harmonic powers detected were somewhat less than in the Type-I configuration, ranging between 0.85-1.3 μW for input fundamental average powers over 130 mW. QPM:NPM ratios were also lower, averaging only 2:1. As both TE and TM polarizations of the fundamental are launched, both Type-I and Type-II interactions were taking place. When non-phase-matched, the proportion of TE-polarized second-harmonic power to TM power was around 2.8:1, showing that there was a significant amount non-phase matched Type-I SHG. When at the phase matching wavelength, the proportion of TE:TM power at the phase matching wavelengths rose to above 4:1, signifying that phase matching was taking place only for the Type-II process. However, this ratio is still nearly eight-times lower than in Type-I phase matching, illustrating that the mixed polarization configuration of the fundamental is not as selective as in the purely Type-I configuration.

The best performance for Type-II phase matching was achieved with a waveguide having a period of 3.5 μm and drawn duty cycle of 60:40. With 51 mW of fundamental average power on the inside of the input facet, nearly 3 μW of second harmonic power was produced at the inside of the exit facet of the waveguide. This gave an internal normalized conversion efficiency of $32 \text{ \%W}^{-1}\text{cm}^{-2}$, which is more than four times less than the best result for Type-I phase matching. The initial prediction forecast that the Type-II process would yield greater conversion efficiency than Type-I because of the larger modulation depth achievable in the former. However, this was not the case. There are several possible reasons for this. First, the linear losses in the TE polarized second-harmonic were larger than in the TM polarization due to poor mode confinement and increased absorption loss in the band tail. Second, the loss of the TM polarized fundamental was generally higher than the TE polarized fundamental. Thus, the average loss coefficient for the fundamental was larger in the Type-II process than in the Type-I process, leading to lower conversion efficiency as shown in Equation 4.10. Lastly, the mismatch in group velocities is larger for Type-II due to the slower group velocity in the TE polarized second-harmonic and due to the mixed polarization of the fundamental. This would have led to a shorter walk-off length than in Type-I phase matching, which would have stalled the Type-II process earlier. As a result, the second-harmonic pulses generated would have had a longer lead out length in which they were susceptible to linear loss without gain.

Sample B also demonstrated significantly strong SHG in both Type-I and Type-II configurations. However, the absolute second-harmonic powers were at best about 28% less in Type-I and 16% less in Type-II. Since Sample B is longer than Sample A by over 50%, it was expected to produce more than twice as much power assuming that the normalized conversion efficiency remains the same. Furthermore, the conversion efficiency should have been larger due to the improved overlap of the transverse mode for the fundamental and second-harmonic wavelengths. However, the best Type-I conversion efficiency was $44 \text{ \%W}^{-1}\text{cm}^{-2}$, nearly three times less than obtained for Sample A. Type-II phase matching yielded conversion efficiencies of $8.8 \text{ \%W}^{-1}\text{cm}^{-2}$ at best, nearly four-times less than in Sample A. One reason for this drop in efficiency is the greater linear loss in

Sample B due to increased surface and sidewall roughness, and due to the deeper etch which exposes the guided mode to more of that surface/sidewall roughness. Another reason could be higher confinement of the optical modes to the core layer, which would tend to increase the effect of high-order nonlinearities such as SPM and TPA/3PA.

Tuning Curves and Pulse Spectrum

Figure 5.5 shows the tuning curves (second-harmonic power versus fundamental wavelength) for Type-I and Type-II phase matching in Sample A waveguides with a QPM period of 3.5 μm measured with average fundamental powers of about 130 mW. The FWHM of the conversion bandwidth was about 4.7 nm for the Type-I curve shown. This was larger than predicted in Section 4.4, which may be attributed to several reasons. First, large linear losses at the second harmonic can result in a broadening of the conversion bandwidth. As the loss was thought to be larger in the TE polarization, this may explain why the Type-II interaction had a larger bandwidth than the Type-I interaction. Second, SPM of the fundamental may have broadened the conversion bandwidth by affecting the phase matching condition. Lastly, the 2-3 nm spectral width of the fundamental pulses will overlap the conversion bandwidth even as the wavelength is tuned outside the peak. Thus, the bandwidth appeared larger than in the case where a narrow linewidth source is used. For the Type-II case shown in Figure 5.5b, the bandwidth was 7.0 nm, which is somewhat larger than the Type-I case. Overall, the Type-II bandwidth was larger than the Type-I bandwidth in all waveguides tested, which may in part be due to higher linear loss in the Type-II configuration. However, the bandwidth increase observed here is much larger than predicted for reasonable loss values, which indicates that the TE polarized second-harmonic losses may be much larger than originally estimated.

The spectrum of the output second harmonic pulses was measured using the OSA. Figure 5.6 shows the results for both Type-I and Type-II phase matching in a waveguides with 3.5 μm QPM periods. When distant from the phase matching wavelength, the output second harmonic pulses have a spectral width of about 1 nm, which is about one half the spectral width of the fundamental pulses. This is reasonable since the conversion efficiency is somewhat flat when away from the phase matching peak. When

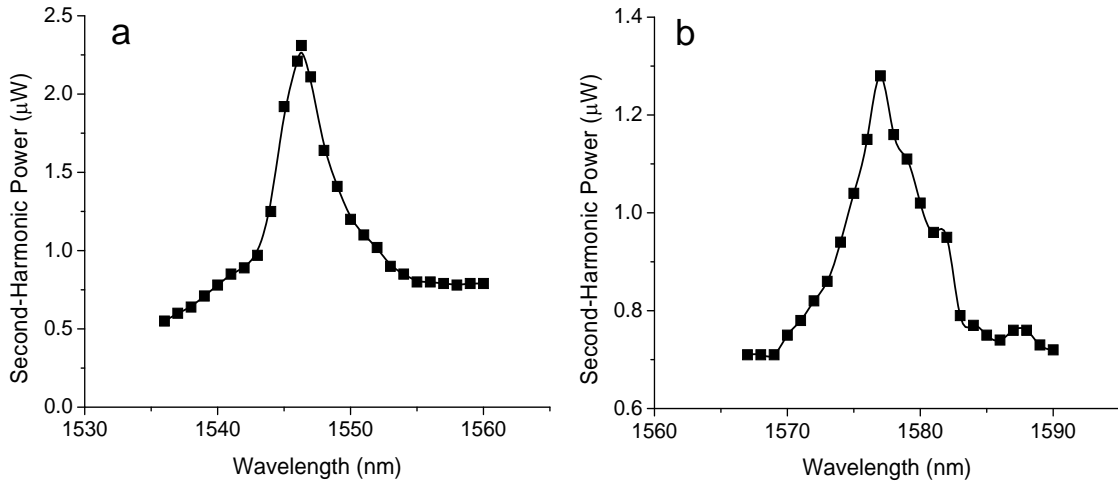


Figure 5.5: SHG tuning curves for Sample A waveguides with QPM periods of $3.5 \mu\text{m}$ in the a) Type-I, and b) Type-II interactions.

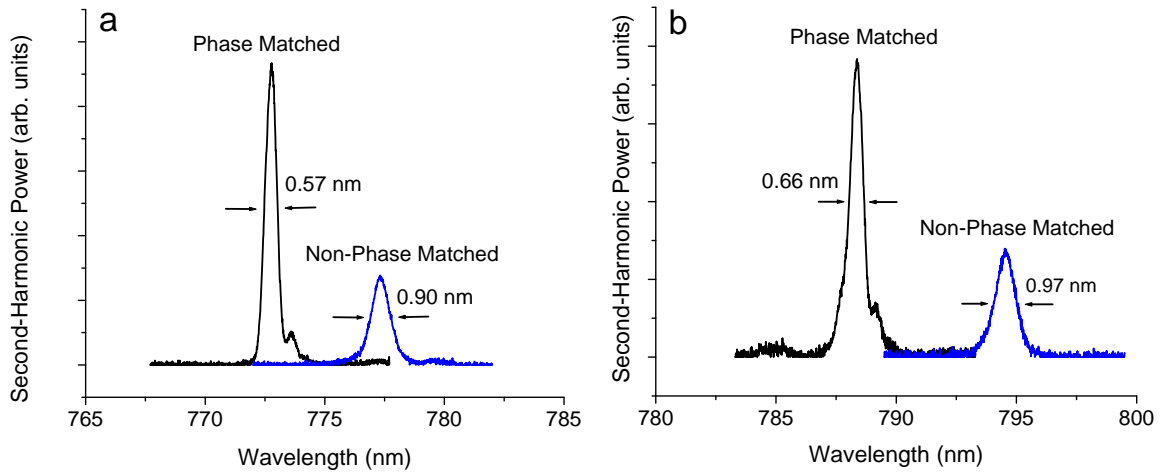


Figure 5.6: Spectrum of second harmonic pulses on and off phase match generated by a) Type-I, and b) Type-II interactions in Sample A QPM waveguides with $3.5 \mu\text{m}$ periods.

at the phase matching wavelength, the second-harmonic spectrum narrowed by over 30%. This is the result of the shape of the conversion bandwidth as shown in the tuning curves of Figure 5.5 which is narrow at the peak. Wavelengths on either side of the phase matching peak experience less conversion than those at the center, which acts to narrow the second harmonic spectrum produced. This characteristic narrowing was taken to be further indication of a phase matched process.

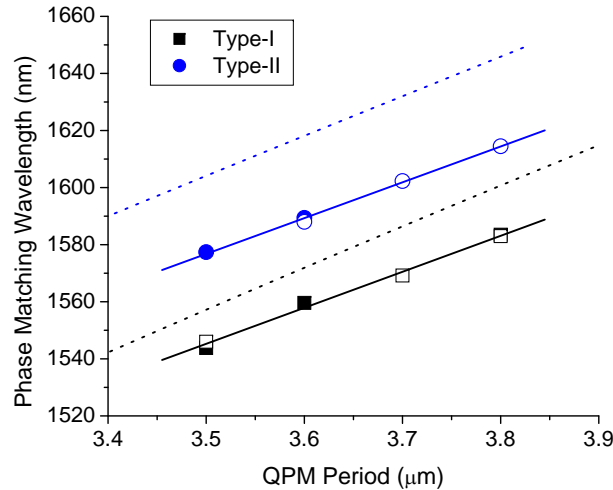


Figure 5.7: Phase matching wavelengths for Type-I and Type-II SHG in Sample A ($1.0 \mu\text{m}$ deep waveguides). Measured data is shown for 60:40 (solid symbols) and 50:50 (open symbols) duty cycles, along with fit trends (solid lines). Predicted phase matching wavelengths are shown as dotted lines.

Phase Matching Wavelengths

Figure 5.7 shows the measured phase matching wavelengths for Sample A alongside predicted curves. The tuning resolution of the laser introduced an estimated error of 1 nm in the phase matching wavelength. As predicted, phase matching wavelengths increase with the QPM period. A numerical fit of the data yielded an average increase in the phase matching wavelength of 12.6 nm per $0.1 \mu\text{m}$ increase in the QPM period for both Type-I and Type-II interactions. This is close to the predicted value of 14 nm per $0.1 \mu\text{m}$. However, there is a significant discrepancy between the absolute measured and predicted phase matching wavelengths. In the case of Type-I phase matching, the measured values are 13-18 nm lower, while Type-II phase matching wavelengths were 27.5-30.5 nm off the predicted values. This mismatch between the measured and predicted phase matching wavelengths was observed for the previous superlattice structure [97]. Furthermore, the difference between the Type-I and Type-II phase matching wavelength for the same QPM period averaged 31.5 nm, which is lower than the predicted value of 49 nm.

Phase matching wavelengths for Sample B are shown in Figure 5.8. Measured values for Type-I phase matching were similar to those for Sample A. However, the Type-II

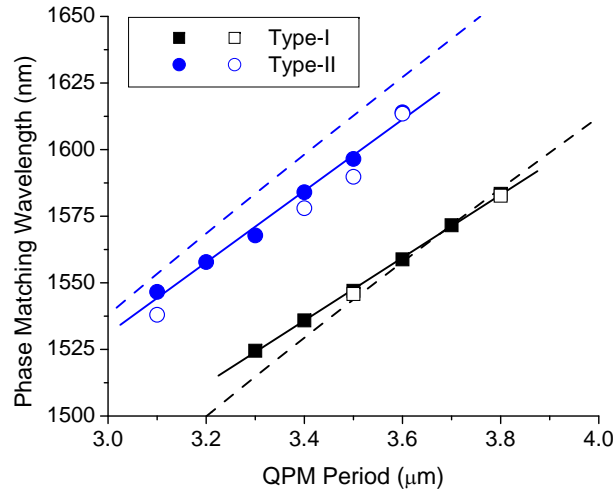


Figure 5.8: Phase matching wavelengths for Type-I and Type-II SHG in Sample B ($1.3 \mu\text{m}$ deep waveguides). Measured data is shown for 60:40 (solid symbols) and 50:50 (open symbols) duty cycles, along with fit trends (solid lines). Predicted phase matching wavelengths are shown as dotted lines.

values increased by over 20 nm in Sample A over Sample B for the same QPM period. This is consistent with the predictions made in Section 3.3.4. The discrepancy between the measured and predicted values is also much less than for Sample A, especially for Type-I. The slopes of the fit curves are 11.8 nm per $0.1 \mu\text{m}$ for Type-I, which is somewhat less than the predicted value. The Type-II curve fit had a slope of 13.4 nm per $0.1 \mu\text{m}$ for Type-II, which is much closer to the predicted slope. However, the absolute values for the phase matching wavelengths were off by between 12-16.5 nm the predicted values. The difference between the Type-I and Type-II phase matching wavelengths was between 43 and 56 nm, larger than observed in the Sample A data, which is in line with predictions.

There are several possible sources of the discrepancy in the absolute values of the phase matching wavelengths. First, the duty cycles in the QPM gratings do not exactly meet the ideal. As was shown in Table 5.1, the actual duty cycles in the fabricated implantation mask did not match those originally patterned in the lithography step. Also, ion straggle during implantation and defect diffusion during rapid thermal annealing would have also played a role in altering the duty cycles from the designed values. The

maximum shift can be found by assuming that the waveguides become intermixed in both domains (i.e. the duty cycle is 0:100). Calculations showed that the maximum shift in such a case is 38 nm from the predicted value for Type-I phase matching and 80 nm for Type-II phase matching. However, measurements of waveguides with the same QPM period but different designed duty cycle did not show differences in the phase matching wavelengths commensurate with the observed inconsistency with the predicted curves. Second, SPM may cause shifts in the phase matching wavelength at high power. As such, the phase matching wavelength should have shifted at lower powers. However, tests of this assertion failed to show shifts beyond the uncertainty range. Thus, SPM was not a significant factor in shifting the phase matching wavelength from the predicted values. Third, the predicted values may simply be incorrect due to uncertainty in the refractive index values used. There is a large amount of uncertainty in the values for predictions due to the alteration in the new GaAs/Al_{0.85}Ga_{0.15}As superlattice compared to the GaAs/AlAs superlattice of previous studies. Also, the index of the intermixed regions is uncertain since intermixing in the disordered regions was not complete as evidenced by photoluminescence measurements. Lastly, measurements of the original superlattice index may have been inaccurate. This is evidenced by the similar inconsistency between the predicted and measured phase matching wavelengths for that structure [97].

Power Dependence

The power dependence of the SHG in Sample A was studied in detail. Experiments with several different waveguides proceeded by setting the fundamental wavelength to the phase matching wavelength for the particular QPM period while operating the laser at high power (> 100 mW). The power was then attenuated downward at logarithmic intervals while the second-harmonic power produced by the QPM sample was recorded. Figure 5.9 shows the internal second-harmonic power produced for different internal fundamental input powers on logarithmic scales. At low power, the second-harmonic power increases steadily in exponential fashion, which is observed as a straight line on a log-log plot. The differences in the absolute power produced between the various QPM periods for the same input power signifies differences in the conversion efficiency. At

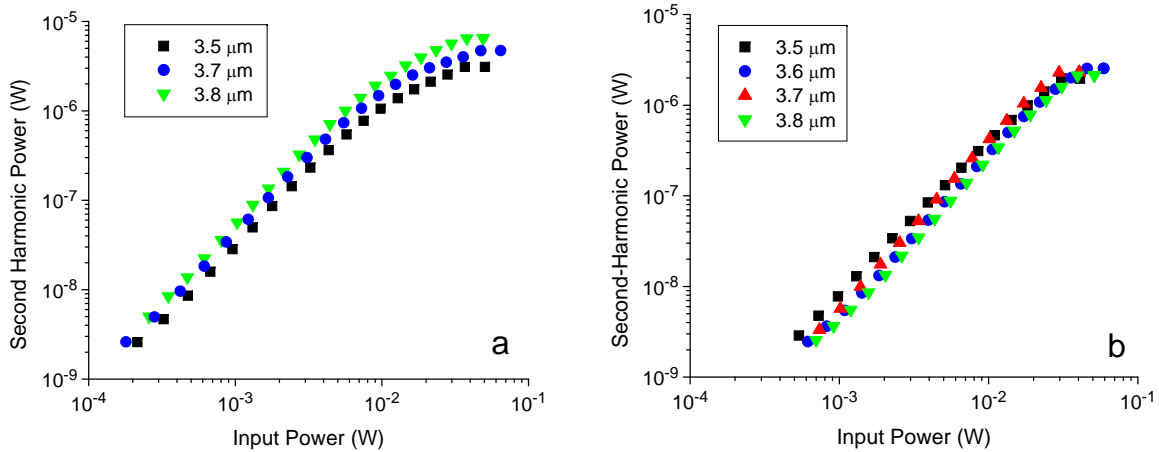


Figure 5.9: Power dependence of phase matched SHG for several QPM periods in Sample A for a) Type-I, and b) Type-II interactions. Part b) reproduced from [98]. ©2010, Optical Society of America.

high input powers, the curves deviate from this trend and the second-harmonic power eventually saturates with further increases in fundamental power. This saturation was most likely due to high-order nonlinear effects, as was predicted in Section 4.6. In at least one case for Type-II phase matching, the $3.5\text{ }\mu\text{m}$ QPM period outperforms the other waveguides at low power, then saturates and ends up producing less second-harmonic than the others at input powers above 20 mW. For the purposes of determining the slope of the log-log curves, the high power data points were ignored. At best, the slope was 1.85, which is nearly quadratic as is expected for the SHG process. However, other curves showed slopes down to 1.65, which is significantly off of the expected quadratic behaviour.

There are several notable differences in the power dependence between Type-I and Type-II phase matching. Figure 5.10 shows the log-log curves for a Sample A waveguide with a $3.5\text{ }\mu\text{m}$ QPM period. Curve fits shown represent the best least-square fit to the lower power data points where the dependence of the the second-harmonic power on the input power is nearly quadratic. Type-I phase matching outperforms Type-II phase matching at all lower power levels by at least 5 dB. However, the second-harmonic power from Type-I tends to begin saturating below 10 mW of average input power, lower than the Type-II case which saturates above 10 mW. This is likely due to the difference

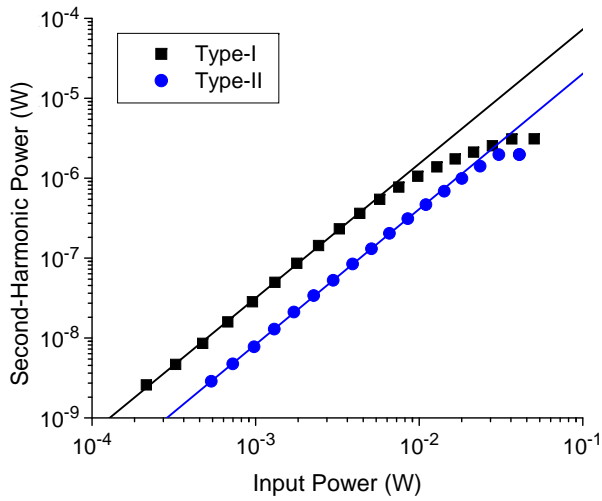


Figure 5.10: Power dependence SHG at the phase matching wavelengths for Type-I and Type-II interactions in Sample A for a QPM period of 3.5 μm . Solid lines show numerical fits of data points well below saturation.

in the strength of the high-order nonlinearities between the TE and TM fundamental modes. As described in Section 3.4, the TE polarization exhibits larger values for the nonlinear refraction and TPA coefficients than the TM polarization. As such, the hybrid polarization of the fundamental involved in Type-II phase matching would experience lower overall SPM and nonlinear absorption, leading to less saturation as predicted in Section 4.6. Note that the phase matching wavelength for Type-I was lower and thus closer to the half-band gap resonance. However, the difference in the saturation behaviour is consistent between all of the Type-I and Type-II log-log curves shown in Figure 5.9. The curve fits also show the extrapolated behaviour of the waveguides in the absence of any nonlinear effects. For instance, the Type-I interaction could have produced as much as 25 μW of second-harmonic power for 50 mW of fundamental power, nearly an order of magnitude more second-harmonic than obtained in the experiment. Type-II phase matching would have had a modest increase of 2.3-times more power for 41 mW of average fundamental power.

Power dependence experiments were also carried out with Sample B. Figure 5.11 shows the Type-I SHG log-log curves for waveguides from both Sample A and Sample B with QPM periods of 3.5 μm . At lower powers, Sample B outperforms Sample A, producing

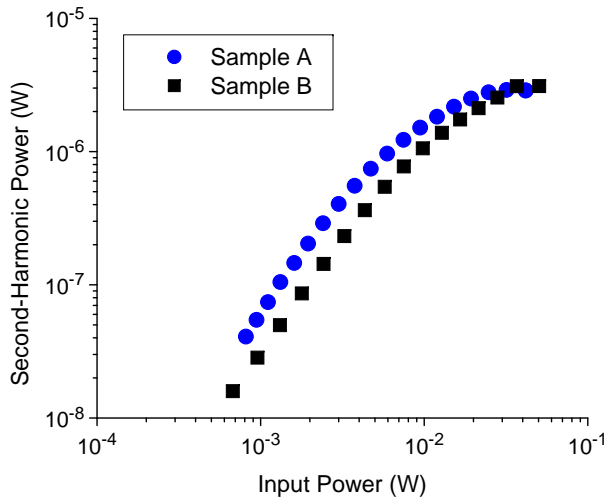


Figure 5.11: Power dependence of Type-I SHG at the phase matching wavelengths for Sample A and Sample B in waveguides with a QPM period of 3.5 μm .

nearly twice as much second-harmonic power. Note that this is not necessarily the case for all of the Sample B waveguides tested. This happens despite the larger linear losses for this waveguide. As the power is increased, Sample B begins to saturate at a lower power than Sample A, contrary to the predictions of Section 4.6. Eventually, the power produced by either sample nearly equalizes at input powers above 30 mW. Since the phase matching wavelength for Type-I phase matching is similar for both samples, the difference in behaviour cannot be explained as a differences in values the for the high-order nonlinear coefficients. Instead, this behaviour is consistent with the higher confinement of the fundamental wavelength mode in Sample B. This raises the effective intensity of the fundamental, which enhances third-order nonlinear effects. Thus, saturation in the second-harmonic power begins at lower input powers for Sample B than in Sample A. Thus, the tradeoff for achieving better confinement of the second-harmonic wavelength is saturation at lower power due to enhanced SPM and TPA.

Conversion Efficiency

The saturation effects observed in the power dependence of the second-harmonic power generated imply that the conversion efficiency must also be changing. Figure 5.12 shows the normalized average power internal conversion efficiency for Type-I and Type-II SHG

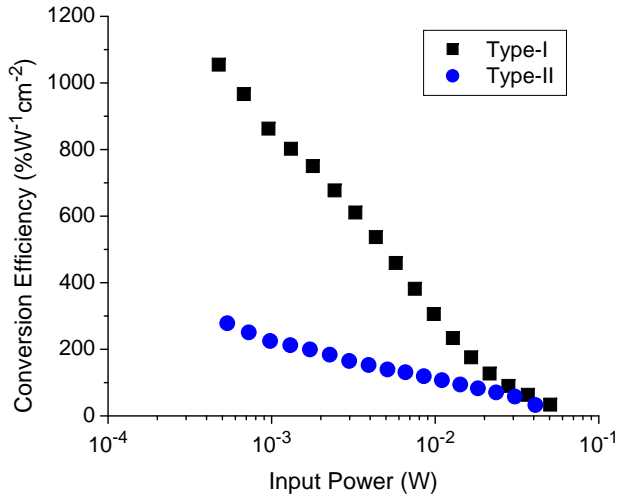


Figure 5.12: Average power conversion efficiency variation with power for a waveguide in Sample A with a QPM period of 3.5 μm

in a Sample A waveguide with a QPM period of 3.5 μm at different average internal input powers. Overall, Type-I phase matching outperforms Type-II phase matching as observed before. At low power, the conversion efficiency was as high as $1055 \text{ \%W}^{-1}\text{cm}^{-2}$ for Type-I and $278 \text{ \%W}^{-1}\text{cm}^{-2}$ for Type-II, nearly a fourfold difference. As expected, the conversion efficiency steadily fell as the input power was increased. The Type-I conversion efficiency fell more rapidly, eventually arriving at a value of $34 \text{ \%W}^{-1}\text{cm}^{-2}$, nearly the same as in the Type-II interaction. This clearly demonstrates how the Type-I interaction was affected more strongly by the large amount of SPM and TPA in the TE polarized fundamental.

Figure 5.13 shows the Type-I conversion efficiency as a function of input power for equivalent waveguides in Sample A and B. As expected, Sample B exhibited better conversion efficiency at low powers, as much as 50% higher than Sample A at equivalent input power. This was likely due to greater confinement and overlap of the fundamental and second-harmonic modes in Sample B. As the power is increased, Sample B's conversion efficiency fell more rapidly than Sample A, the result of the larger SPM and TPA due to enhanced confinement of the fundamental. Eventually, the efficiencies nearly equalize at powers above 10 mW. There are several notable differences in behaviour of the conversion efficiency curves of Sample A and Sample B. First, the slope in the curve changes more

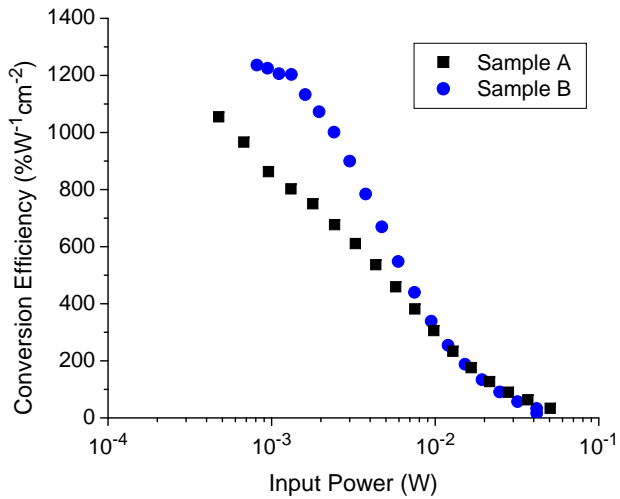


Figure 5.13: Power dependence of Type-I SHG normalized average power conversion efficiency for Sample A and Sample B in waveguides with a QPM period of 3.5 μm when using 2-ps pulses.

dramatically for Sample B at higher powers. As SPM is found to dominate over nonlinear absorption at moderate powers, this may be due to stalling of the SPM effect due to the increased nonlinear absorption at high power. Second, the conversion efficiency for Sample B also levels off at low power. This signifies that the power level was too small for SPM and TPA to affect the SHG process. Here, the conversion efficiency appears to have converged towards its unperturbed value. Contrary to this, Sample A's conversion efficiency continued to climb steadily as the power was decreased. This may have been due to an increased signal-to-noise ratio as the second-harmonic power detected fell to below 10 nW for internal input power less than 1 mW in Sample A. As such, it was difficult to pinpoint the value at which the conversion efficiency is no longer affected by high-order nonlinear effects.

The conversion efficiency was evaluated for several different waveguides with different QPM periods on both Sample A and Sample B. In the case of Sample B, the conversion efficiency value was selected as the peak in the region at low input power where the efficiency values level off. For Sample A, as the values did not level off, the point closest to where the detected output second harmonic power was greater than 10 nW was selected. Figure 5.14 shows the conversion efficiencies versus phase matching wavelength

for several different QPM periods in both samples for Type-I and Type-II interactions. Also shown are conversion efficiency values accounting for the linear losses in the fundamental as per Equations 4.9 and 4.10. Using these equations, values increased by up to 10% for Sample A, and by up to 20% in Sample B. Overall, the conversion efficiency of Type-I phase matching exceeds that of Type-II phase matching by a wide margin. The exception is the 3.6 μm QPM period in Sample A (phase matching wavelength near 1560 nm), which has a much lower Type-I conversion efficiency relative to all other QPM periods. It is believed that the waveguide was damaged either before or during the experiment. Otherwise, the other points appear to follow a trend with the conversion efficiency reducing with smaller phase matching wavelengths. It was expected that the conversion efficiency would increase with shorter phase matching wavelengths since the value of $\chi^{(2)}$ increases when approaching the half-band gap energy. However, the presence of the opposite trend suggests that the increased strength in $\chi^{(2)}$ was being overwhelmed by the increase in absorption loss as the second-harmonic wavelength generated moved into the absorption band tail of the as-grown superlattice. This is much more clearly observed in the Sample B data, where the conversion efficiency for the shortest QPM period (shortest phase matching wavelength) drops to less than 4% of the maximum recorded efficiency value measured for a longer QPM period. Another notable observation is that Sample A appears to have a larger conversion efficiency than Sample B at the longest phase matching wavelength shown for Type-I. This is contrary to the assertion that conversion efficiency would be higher in Sample B due to enhanced confinement of the second-harmonic. Both the quantifiable error in the value of the Sample A conversion efficiencies and measurement error in both samples may account for some of this discrepancy. Type-II phase matching also appears to be more efficient in Sample A, despite the improved confinement and anticipated reduction of second-harmonic radiation losses in Sample B. However, note that there is a lack of coinciding phase matching wavelengths, so this is not a definite conclusion.

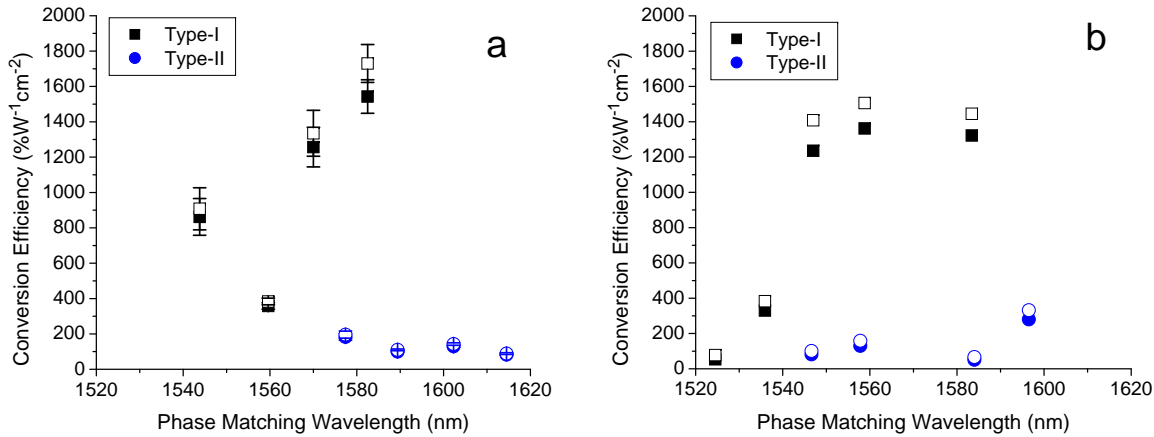


Figure 5.14: Low power Type-I SHG normalized conversion efficiency for a) Sample A and b) Sample B for several QPM periods (and their corresponding phase matching wavelengths) using 2-ps pulses. Open symbols show the efficiency values when linear losses in the fundamental are accounted for.

5.4 Continuous Wave Experiments

Several experiments with DD-QPM samples were carried out using a continuous wave laser system. The advantage of using continuous wave is that the peak power levels are not large enough to induce high-order nonlinear effects, which greatly affected the 2-ps pulse experiments. However, the overall second-harmonic power production is less for the same reason. Continuous wave experiments were not carried out in previous DD-QPM studies due to high linear losses that would have limited the amount of SHG below reliably detectable amounts. In the latest generation of DD-QPM samples, linear loss were deemed to be sufficiently low to permit ample continuous wave SHG. This section highlights the results of SHG experiments by a continuous wave laser, showing large second-harmonic powers generated and several phenomena encountered including bistability and thermal shifts of the phase matching wavelength.

5.4.1 Experimental Setup

The setup used for continuous wave SHG was similar to that of pulsed SHG. As shown in Figure 5.15, a tunable, external cavity laser diode was used as the fundamental source. This laser emitted wavelengths between 1500 nm and 1600 nm and had a narrow linewidth

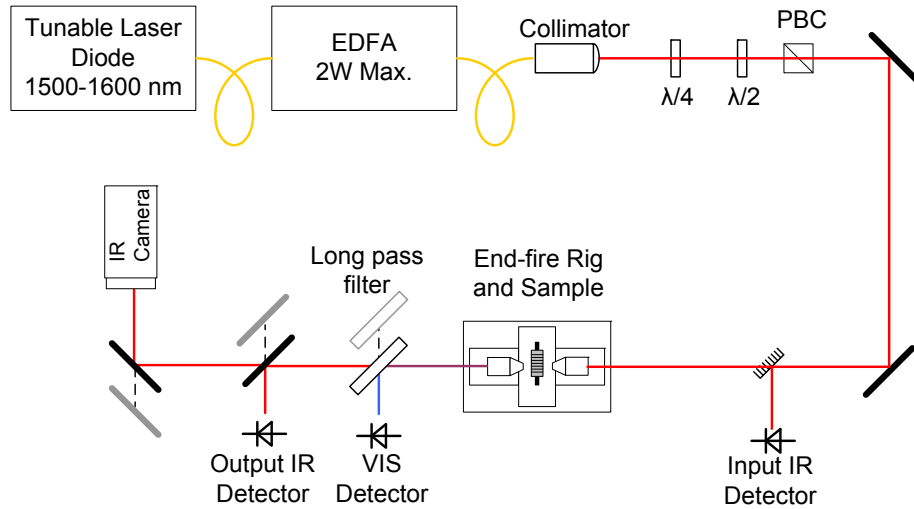


Figure 5.15: Schematic of the experimental setup for SHG experiments with a continuous wave source

of 100 kHz. The power of this laser was boosted by using an erbium-doped fiber amplifier (EDFA) capable of delivering powers of up to 2 W. However, no more than 350 mW at the waveguide sample facet was used. Any more power than this caused catastrophic damage to the input of the waveguide, likely due to large absorption of the fundamental via defects on the cleaved surface. A fixed collimator was used to launch the fundamental light from the output fiber of the EDFA into the free-space beam path. Quarter- and half-wave plates were used to set the elliptically polarized light from the fiber as close as possible to a linear polarization before being passed through a polarizing beam cube used to isolate the desired polarization. Light was end-fire coupled through a $40\times$ anti-reflection coated objective lens and output light was collected with a standard $40\times$ objective lens.

In experiments involving Sample A waveguides, a longer sample (3.5 mm) was used instead of the shorter one for several reasons. First, the longer sample had a smaller free-spectral range (FSR) of about 0.1 nm between Fabry-Perot resonances. This allowed the phase matching wavelengths to be pinpointed better during spectral sweeps. Second, the longer interaction length permitted the generation of larger amounts of second-harmonic power than would have been generated in the shorter sample. Only Type-I SHG was

observed in Sample A, and only for three different QPM periods (3.5, 3.6, and 3.7 μm) since only those waveguides had phase matching wavelengths within the EDFA gain bandwidth. QPM periods having Type-II phase matching wavelengths within the EDFA gain bandwidth were not available in Sample A. In experiments with Sample B, both long (4 mm) and short (1 mm) samples were used. Several shorter QPM periods included in this sample set allowed both Type-I and Type-II SHG within the EDFA bandwidth. However, only Type-I phase matching was observed in the long sample. Phase matching peaks for Type-II were not definitively observed. Instead, Type-II SHG was achieved more readily in the shorter samples than in the long sample, despite exhibiting the same issue with the large FSR in Type-I experiments in Sample A. This is due to having both the TE and TM polarizations of the fundamental resonating in the cavity at different wavelengths. Since the FSR was similar for both polarizations, the output spectral transmission behaviour was the composite of longitudinal modes of both polarizations, which effectively cut the FSR by half, allowing more accurate determination of the phase matching wavelengths.

5.4.2 Results

Performance

Several Sample A waveguides with different QPM periods and duty cycles were characterized for Type-I SHG. As opposed to other experiments with pulses, waveguides with a width of 3.5 μm were used due to damage to many of the 3.0 μm -wide waveguides. Thus, there were differences in the coupling efficiencies and in the optical intensity inside the waveguides. As such, SHG may or may not have been enhanced depending on the balance between these opposing factors. However, the overall performance should be similar to the narrower waveguides used in other experiments discussed previously.

The phase matching wavelengths were found by scanning the wavelength of the tunable laser with 250 mW of total power reaching the input facet. However, the output fundamental power level fluctuated over the course of the scan as the laser wavelength moved through several Fabry-Perot resonances. Figure 5.16 shows the transmission ratio

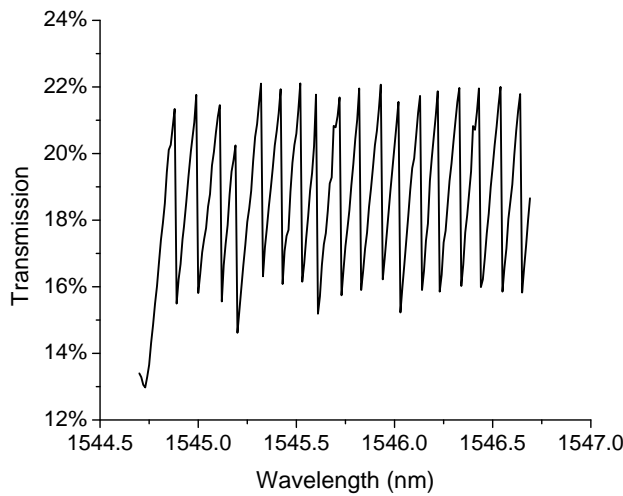


Figure 5.16: Transmission of fundamental through a QPM waveguide with a $3.5 \mu\text{m}$ period

of the fundamental of the waveguides. Immediately noticeable are the resonance peaks, which appear to abruptly drop on the long-wavelength side of the peak. Mechanical settling in the tunable laser laser was ruled out as the source of this behaviour since Fabry-Perot loss measurements at powers less than 5 mW with this same laser and experimental setup did not show similar asymmetric transmission peaks. Thus, it appeared that the cavity had a bistability, similar to that observed in silicon microring resonators [99]. Despite this behaviour, the phase matching wavelengths were found within 1 nm of the corresponding phase matching wavelengths found in the 2 ps pulse experiments shown in Figure 5.7.

At the phase matching wavelength, output second-harmonic powers detected were in the 100's of nanowatts for input powers in excess of 200 mW for several different QPM waveguides. In the best performing waveguide, which had a QPM period of $3.5 \mu\text{m}$ and duty cycle of 60:40, the detected second-harmonic power was as high as 594 nW for 310 mW of fundamental power at the external side of the input facet. Accounting for the path losses, which included the collection efficiency of the output objective lens and the filter reflectivity, the internal second-harmonic power in this instance was $1.67 \mu\text{W}$. As expected, this was significantly lower than the nearly $10 \mu\text{W}$ generated using 2-ps pulses and a lower average power at the facet of 150 mW. Thus, the overall conversion

efficiency was lower for the continuous wave case.

In order to calculate the internal conversion efficiency, the Fabry-Perot resonance behaviour of the waveguide must be accounted for when finding the internal fundamental input power. The output power through such a cavity on a resonance is

$$P_o = \frac{(1 - R)^2 \exp(-\alpha L)}{[1 - \exp(-\alpha L)R]^2} \eta_c P_i \quad (5.1)$$

where R is the facet reflectivity, α is the linear loss coefficient, L is the cavity length, η_c is the input coupling efficiency, and P_i is the external input power. Knowing the transmission value through the waveguide on such a resonance, the coupling efficiency can be deduced. If there were no resonance in the waveguide, the internal input power would ordinarily be calculated as $\eta_c(1 - R)P_i$. However, because of the cavity resonance, the input power level on the internal side of the input facet will be larger. Instead, assuming that nonlinear absorption is negligible, the internal input power can be calculated as

$$P_{i,int} = \frac{P_o}{(1 - R) \exp(-\alpha L)}. \quad (5.2)$$

Given a facet reflectivity of 26% and a loss coefficient of 0.8 cm^{-1} , the 68 mW measured for the output fundamental power yields an internal input power of 118 mW in the case of the best performing waveguide. If there were no resonance, the internal power would have been 79 mW at the input facet taking into account the calculated 34.4% coupling efficiency. Thus, the Fabry-Perot resonance enhances the internal fundamental power by over 49% in this case. Similar resonant enhancement values were found for other waveguides.

Table 5.3 lists the normalized conversion efficiencies for several Sample A waveguides. Compared to the 2-ps pulse experiments, the average value efficiency values are nearly four orders of magnitude smaller, which is the result of the reduced peak fundamental power. However, the conversion efficiency values were more consistent in the continuous wave experiments across different input power levels and did not show any significant decrease as the input power was increased. This indicated that the continuous wave SHG process was not afflicted by SPM or nonlinear absorption. The best overall per-

Table 5.3: Continuous wave SHG performance of Sample A QPM waveguides for Type-I phase matching. The right-most column shows the calculated efficiency with the fundamental wavelength (FH) loss accounted for according to Equation 4.9.

Period	FH Loss (cm ⁻¹)	η [%W ⁻¹ cm ⁻²]	η with Loss
60:40 Duty Cycle			
3.5	0.80	0.092	0.121
3.6	1.23	0.032	0.050
3.7	0.58	0.064	0.079
50:50 Duty Cycle			
3.5	1.32	0.042	0.066
3.6	1.88	0.028	0.053
3.7	0.97	0.052	0.073

formance was from a 60:40 3.5 μm period waveguide, in which the conversion efficiency was 0.092 %W⁻¹cm⁻². This is still well below continuous wave conversion efficiencies reported for other phase matching methods, by as much as two orders of magnitude. At first inspection, the 60:40 duty cycle waveguides appear to outperform the 50:50 duty cycle waveguides. However, the 50:50 waveguides also showed larger loss, most likely owing to the increased length of the intermixed domains. When the loss of the fundamental is factored in using Equation 4.9, the relative difference between the 60:40 and 50:50 duty cycle is reduced. No clear trend in the dependence of the efficiency on the QPM period was observed, and thus no conclusion can be made on the influence of the second harmonic loss or the spectral dependence of $\chi^{(2)}$.

Several waveguides from a 4 mm long piece of Sample B were tested for Type-I SHG. Overall, generated second-harmonic powers were much lower than in Sample A, no more than 360 nW internally. The best performance was measured for a QPM period of 3.5 μm and duty cycle of 60:40 (same as the best waveguide in Sample A). The normalized internal conversion efficiency was 0.029 %W⁻¹cm⁻², 3.2 times less than the best results for Sample A. This agrees with the results from experiments with 2-ps pulses. Again, this was unexpected since the larger confinement in the more deeply-etched waveguides of Sample B should have raised the internal optical intensity and modal overlap, and thus the conversion efficiency. One possible cause is the greater linear loss of Sample B. Recalculating the conversion efficiency to account for the loss coefficients of the fun-

damental and second-harmonic gives $1.98 \text{ \%W}^{-1}\text{cm}^{-2}$. However, without reliable loss data at the second-harmonic for Sample A, it is difficult to say whether or not this is an improvement.

Type-II SHG was obtained only in Sample B which had QPM periods short enough to place the phase matching wavelengths within the EDFA gain bandwidth. Also, a shorter piece (1 mm) was used as it yielded higher output second-harmonic powers. The best performance was from a waveguide with a $3.3 \mu\text{m}$ QPM period and 50:50 duty cycle, which produced an internal second-harmonic power of 117 nW for about 130 mW of internal fundamental power. This yielded a conversion efficiency of $0.067 \text{ \%W}^{-1}\text{cm}^{-2}$, more than twice that achieved for Type-I SHG in the longer Sample B piece. Accounting for the fundamental and second-harmonic loss placed the conversion efficiency at $0.482 \text{ \%W}^{-1}\text{cm}^{-2}$, nearly four times lower than Type-I conversion. Again, this does not agree with the prediction that Type-II should have been more efficient due to larger $\chi^{(2)}$ modulation.

Tuning Curves and Conversion Bandwidth

Scans of the input fundamental wavelength were performed around the phase-matching wavelength. The wavelength was initially set at the shorter wavelength of the scan region, then increased at intervals of 0.01 nm . A three second delay was added between scan points to allow the output powers to settle before measurements were taken. The resulting SHG tuning curve for a Sample A waveguide with a $3.5 \mu\text{m}$ QPM period is shown in Figure 5.17 for an external input power of 310 mW . Fabry-Perot resonance features matched those of the fundamental transmission curve of Figure 5.16. Also notable is the asymmetric shape of the resonance peaks, with the second-harmonic power abruptly dropping on the long wavelength side of the peak in a similar fashion to the transmission curve. This demonstrates that the SHG process followed the internal fundamental power of the cavity. The dotted red line show the tuning curve with the Fabry-Perot features removed by low-pass filtering of the data. It resembles a sinc^2 function, which is consistent with a phase-matched SHG process. However, some asymmetry is observable in this curve with the short-wavelength side of the curve not exhibiting side-lobes as the the long-

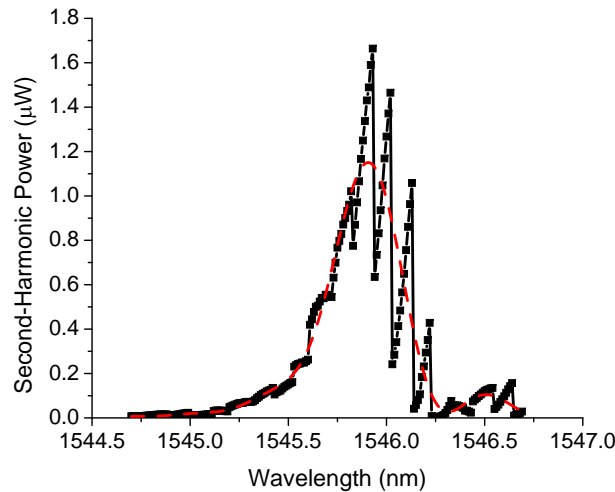


Figure 5.17: Tuning curve for continuous wave SHG in a 1.0 μm -deep, 3.5 μm wide, 3.5 mm-long waveguide with a 3.5 μm QPM period. Fabry-Perot peaks are due to cavity resonances in the waveguide. The dashed line shows the tuning curve with the Fabry-Perot peaks filtered out. Reprinted with permission from [100]. ©2009, American Institute of Physics.

wavelength side does. This may stem from the same phenomenon that causes the Fabry-Perot peaks to be asymmetric. The FWHM bandwidth of the filtered curve was 0.41 nm, which is an order of magnitude smaller than that measured for the shorter sample with 2-ps pulses. Part of this difference is due to the difference in grating length, which accounts for about a factor of three. The remaining portion of the bandwidth difference is the result of using a very narrowband source in the continuous wave experiments over the use of the relatively wide spectral width of the ultrafast source. The phase matching peak was taken to be the peak of the filtered curve and not of the raw data since the Fabry-Perot peaks may not have exactly aligned with the phase matching wavelength. However, the asymmetric shape of the peaks may have also obscured the fit. The error in the phase matching wavelength is, at most, the FSR. This represents an error of nearly one-quarter of the conversion bandwidth.

Wavelength scans were also conducted with different power levels. Tuning curves after filtering out the Fabry-Perot features are shown in Figure 5.18. The peak was found to shift to longer wavelengths as the power was increased. For a change in power from 250 mW to 310 mW, the phase matching wavelength shifted by 0.26 nm, which is

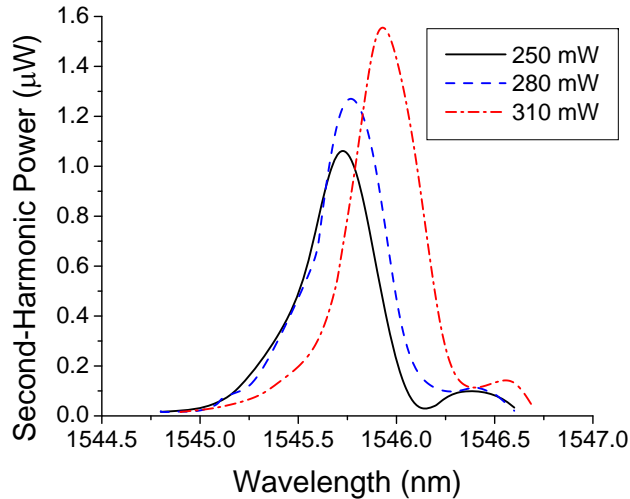


Figure 5.18: Filtered envelopes of tuning curves for continuous wave SHG in a 1.0 μm -deep, 3.5 μm wide, 3.5 mm-long waveguide with a 3.5 μm QPM period at different input powers. Reprinted with permission from [100]. ©2009, American Institute of Physics.

over half the conversion bandwidth. Such a shift is an indication of the phase matching condition changing. One possible cause would be nonlinear refraction, which was shown to cause disruption in the 2-ps pulse experiments. However, the peak optical intensities when using the continuous wave source are far too low to cause such a large change in the phase mismatch. Another possible cause is the thermo-optic effect, which would have altered the refractive index of the waveguide materials resulting in a shift of the phase matching wavelength. In this case, the change in the phase matching wavelength due to changes in the temperature T would be

$$\frac{d\lambda_{pm}}{dT} = 2\Lambda \frac{d\Delta n}{dT} \quad (5.3)$$

where $d\Delta n/dT = dn_{2\omega}/dT - dn_\omega/dT$. By the Gehrtsitz model [84], the thermo-optic coefficients for the equivalent bulk alloy of the superlattice, $\text{Al}_{0.425}\text{Ga}_{0.575}\text{As}$, are $2.37 \times 10^{-4}\text{K}^{-1}$ for the second-harmonic wavelengths and $1.75 \times 10^{-4}\text{K}^{-1}$ for the fundamental wavelengths. By this, the temperature increase to cause a 0.26 nm shift in the phase matching wavelength is 0.6 K. Such a temperature increase could have been caused by absorption of the fundamental through defects.

The observed thermal shifts in the phase matching wavelength has many consequences for an integrated wavelength conversion device. It could cause disruptions in the performance of such a device. As the temperature of the device is sure to change during normal operation, the phase matching wavelength and the conversion efficiency are likely to fluctuate. Furthermore, any variance in the temperature of an integrated device could destabilize the pump laser wavelength, which would further disrupt the conversion process [101]. Robust thermal management will have to be employed to stabilize the temperature of the device and maintain the phase matching wavelength at the designed point. However, being able to control the phase matching wavelength would also be an advantage as it would allow some flexibility. For instance, such control could be used to compensate for fabrication errors either in the QPM period or in the material composition during wafer growth.

Bistability

Several forms of bistable behaviour in the QPM waveguides were observed during the continuous wave experiments at constant input power. The first was found while tuning the fundamental wavelength either up or down. When tuning downward, the second-harmonic power produced was less than when tuning upward. Ordinarily, this should not have been the case. To investigate this phenomenon, a wavelength scan was performed around one of the Fabry-Perot peaks shown in Figure 5.17. The scan proceeded in the upward direction with a reduced step interval of 0.002 nm, then the scan direction was reversed. The resulting hysteresis loop is shown in Figure 5.19. Tuning in the upward direction produced a higher second-harmonic power peak, after which the power drops rapidly. In the reversed scan, the second-harmonic power decreases, but at a decreasing rate. At some point, the power suddenly increases and the tuning curve meets with the curve from when the wavelength was tuned upward. Such a hysteresis loop indicates that the Fabry-Perot modes of the waveguide cavity were being shifted by some dependence on the internal cavity power, which likely affected the effective index of the waveguide. In the case of the upward scan, the increasing internal cavity power may have moved the Fabry-Perot resonance out to longer wavelengths, thus the scan “chases” the resonance

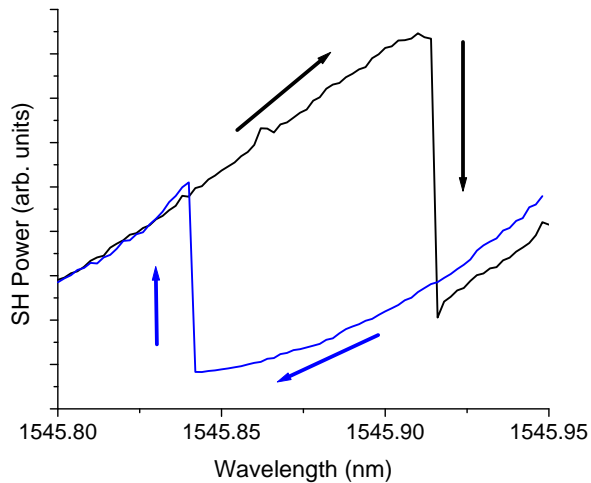


Figure 5.19: Hysteresis loop in second-harmonic power when tuning the wavelength in upward direction, followed by downward direction.

peak. After reaching the peak, moving the wavelength slightly beyond it causes the power to drop by a minute amount. This triggers a positive feedback effect that causes the cavity power to drop and the Fabry-Perot resonance peak to be restored to its original wavelength. In the reverse scan direction, the positive feedback mechanism causes the Fabry-Perot mode to be “dragged” upward in wavelength, which causes the sudden power increase observed. In both the case of the sudden power increase and abrupt power drop, the detected power was observed by eye to settle over a period of a few seconds. As with the shift in phase matching wavelength with input power discussed in the previous section, the thermo-optic effect was the most likely cause of this behaviour. An index increase of 2.2×10^{-4} is sufficient to shift the resonance peaks by one interval of the free-spectral range. Using the thermo-optic coefficient from before, a 1.3 K increase in temperature would have been sufficient to cause such a shift.

Bistable behaviour was also observed when changing the input power level. In one experiment, the wavelength was set to the phase-matching wavelength of the QPM waveguide under test. The input power was gradually increased at regular power intervals up to a power of 340 mW. Then the power scan was reversed. Figure 5.20 shows the recorded output powers of the fundamental and second-harmonic. At least three hysteresis loops and switching points were observed. Within each loop, the fundamental power mostly

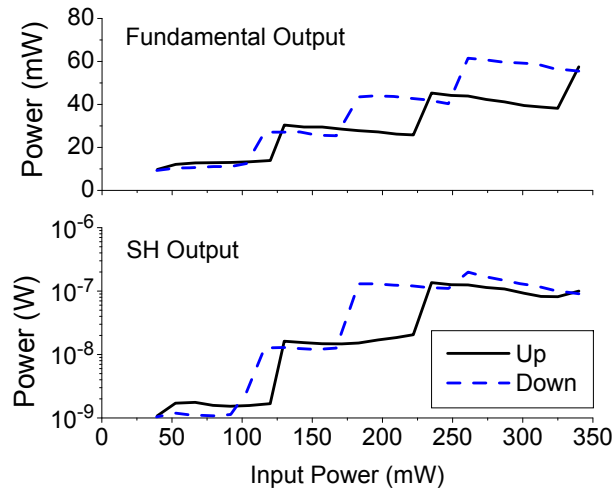


Figure 5.20: Dependence of output fundamental and second-harmonic power on input fundamental power in a $1.0 \mu\text{m}$ -deep, $3.5 \mu\text{m}$ wide, 3.5 mm -long waveguide with a $3.5 \mu\text{m}$ QPM period. Bistable behaviour is observed with the presence of rapid increases and hysteresis loops. Reprinted with permission from [100]. ©2009, American Institute of Physics.

decreases as the power is increased and increases when the power is decreased, except at the switching points where the behaviour is opposite. The generated second-harmonic power appears to track the behaviour of the fundamental. It increases at a nonlinear rate (note the logarithmic scale of the figure), which is consistent with the SHG process. Again, such sudden switches and hysteresis loops are consistent with thermo-optic shifting of the Fabry-Perot cavity modes.

In all the experiments on bistability, a noticeable temporal delay was observed near the switching points in the hysteresis loops. When blocking and unblocking the output beam from the sample, the detector measurements were relatively instantaneous, thus ruling out the detector response as the cause for this effect. However, doing the same to the input beam did produce a significant settling time on the output detectors. Essentially, blocking and unblocking the input beam causes an instantaneous input power ramp. This procedure was carried out for several input power levels, which were all above 250 mW where the third switching point was observed in Figure 5.20. The output fundamental and second-harmonic powers were recorded at a sampling rate of 10 Hz over a ten second period. Figure 5.21 shows the output second-harmonic power over that time period. The

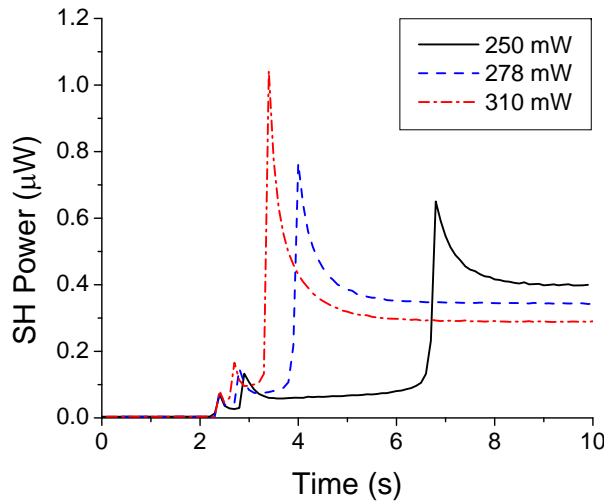


Figure 5.21: Second-harmonic power generated over time after applying an input step of three different fundamental powers. Rapid jumps in generated power followed by declines show the bistable behaviour of the waveguide. Reprinted with permission from [100]. ©2009, American Institute of Physics.

input beam was released at the 2 s point. Three peaks in the second-harmonic power occur over the time interval. This corresponds to the three switching points observed in Figure 5.20. The largest peak was found in the case where 310 mW of input power was used. However, the power dropped off and settled to a level below the curve for 250 mW, which also matches the behaviour in Figure 5.20. The time scales to reach these peaks indicates a slow thermal effect. Furthermore, it was found that the time to reach the largest peak was dependent on the input power level. For instance, at the 310 mW power level, the peak occurs after 1.4 s after the input power is applied, whereas it takes over 4 s for 250 mW. Such behaviour is indicative of a critical slowing down dynamic, which is a well known phenomena in optical bistability [102].

Overall, the bistable and temporal behaviour indicate the presence of a significant thermo-optic effect. In order to cause temperature increases, optical absorption and subsequent thermalization of excited carriers was likely the source. It is unlikely that absorption of the generated second-harmonic is the underlying source of power since the amount of second-harmonic produced is well below what would be required to cause the temperature increases required. Also, bistable behaviour was observed at wavelengths

outside the phase matching bandwidth for the SHG process, further indicating that second-harmonic absorption was not the ultimate cause. Instead, absorption of the fundamental is more likely to be the source of the bistable behaviour. Despite being well below the band gap energy, the fundamental wavelength can be absorbed by other mechanisms such as impurities, lattice and surface defects, and free-carrier absorption from the residual background doping. By this, several 10's of milliwatts of fundamental power could have been absorbed leading to thermo-optic effects.

Bistability could cause several problems in the operation of an integrated frequency conversion device. For instance, it could introduce distortions in the converted signals of an OPA. The relatively slow thermal buildup could also limit the bit rate. Unwanted bistability in the QPM waveguides could be resolved by eliminating the Fabry-Perot cavity formed by the end facets. This can be done by applying anti-reflection coatings to the facets or by patterning the waveguides at an angle to the cleave planes of the wafer to reduce the amount of internal reflection. While this may solve some of the problems for an OPA, an integrated OPO requires a cavity for the signal/idler wavelengths. Such thermal bistability could make the behaviour of the OPO unpredictable and unstable. Again, a good thermal management system must be implemented with either device to stabilize device operation.

5.5 20-ps Pulse Experiments

Experiments in the ultrafast pulse and continuous wave regimes were met with several complications that obscured clear measurements of the potential conversion efficiency of the QPM waveguides. Tests with 2-ps pulses resulted in large amounts of nonlinear absorption and SPM that led to saturation effects in the SHG process. Also, the spectral bandwidth of the pulses was on the order of the conversion bandwidth of the short QPM samples, thus leading to poor spectral overlap. Using continuous wave excitation resolved the problems related to high-order nonlinearities and spectral resolution. However, Fabry-Perot resonances and bistable behaviour made it difficult to verify the power dependency of the SHG process and to definitively calculate the conversion efficiency.

Hence, another excitation regime was necessary to provide more information about the conversion efficiency. Thus, 20-ps pulses were chosen for several reasons. The spectral width of 20-ps pulses is theoretically ten times less than 2-ps pulses assuming no significant chirp. Also, the pulse peak powers, despite being ten times smaller, would be high enough to induce significant amounts of SHG while limiting nonlinear absorption and SPM. Furthermore, with longer pulses, the effect of GVM would be reduced. As shall be seen in this section, the combined advantages of using 20-ps pulses showed improved trends in the conversion efficiency with minimal parasitic effects.

5.5.1 Experimental Setup

In experiments involving 20-ps pulses, the setup shown in Figure 5.22 was used. This system was developed by and housed at the Institut de Ciències Fotòniques, and the experiments detailed here were carried out in collaboration with Prof. M. Ebrahim-Zadeh's group at ICFO. The laser source consisted of a mode-locked ytterbium-doped fiber laser emitting at 1064 nm with pulse lengths of about 20 ps at a repetition rate of 81 MHz. This was used to synchronously pump a singly-resonant PPLN-based OPO that produced signal wavelengths between 1500 nm and 1700 nm. Maximum average power available from this system was 300 mW. The end-fire and launch setup was otherwise the same as that used in the 2-ps pulse experiments. Coupling efficiencies were similar to those measured in the 2-ps experiments.

For the experiments, focus was placed on the short piece of Sample B. The long Sample B sample was also tested successfully for a few waveguides, but several were damaged in previous experiments. The short Sample A piece appeared to demonstrate behaviour consistent with a Fabry-Perot cavity as in the continuous wave experiments. Thus, it was difficult to isolate the phase matching wavelength since the FSR of this sample was large. However, the longer Sample A piece did produce significant amounts of second-harmonic power when the phase matching wavelength was located.

It should be noted that the OPO was not entirely stable. The emitted center wavelength was observed to fluctuate rapidly over a range of up to 2 nm as observed on the spectrometer. At times, it was difficult to tune the laser to the exact phase matching

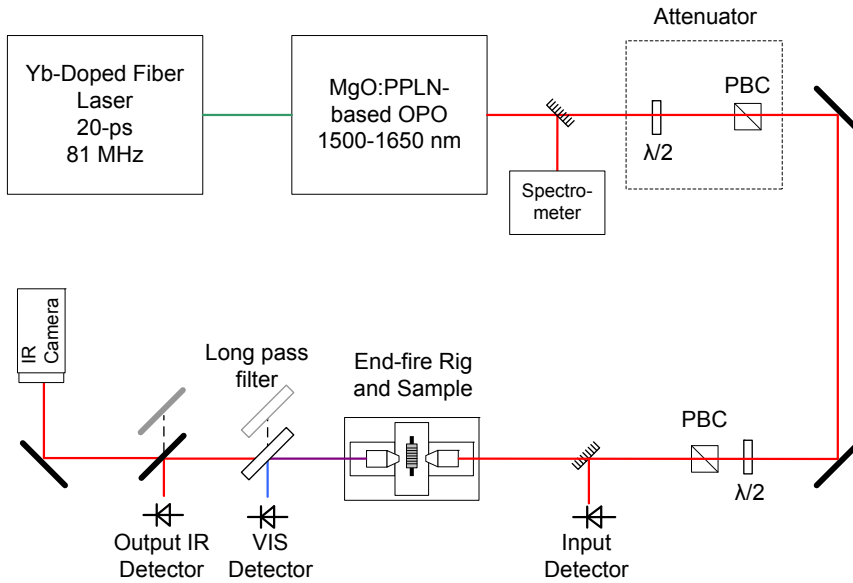


Figure 5.22: Schematic of the experimental setup for SHG experiments with a 20-ps pulsed source.

wavelengths. Thus, quoted second-harmonic powers were likely below the potential and conversion efficiencies were not as high as anticipated. Despite this, several insightful results were obtained on a number of samples and QPM waveguides.

5.5.2 Results

Performance

Several Sample B waveguides were tested for both Type-I and Type-II interactions. Phase matching wavelengths were found close to those found in 2-ps pulse and continuous wave experiments. For Type-I phase matching, internal second-harmonic powers of up to $9.3 \mu\text{W}$ were generated with an internal input fundamental power 55 mW using a waveguide with a $3.8 \mu\text{m}$ QPM period and 60:40 duty cycle. Thus, the maximum normalized conversion efficiency was $30 \% \text{W}^{-1}\text{cm}^{-2}$. Type-II phase matching produced much less power as in previous experiments. At best, $0.5 \mu\text{W}$ of second-harmonic power was generated in the TE polarization, also in a waveguide with a $3.8 \mu\text{m}$ period, but 50:50 duty cycle. The normalized conversion efficiency was $5.3 \% \text{W}^{-1}\text{cm}^{-2}$.

Second-harmonic generation was also achieved with the long Sample A piece. The

largest internal second-harmonic powers generated by a DD-QPM waveguide were achieved with this sample. Using a waveguide with a $3.6\text{ }\mu\text{m}$ QPM period and 60:40 duty cycle, the Type-I interaction produced nearly $16\text{ }\mu\text{W}$ of second-harmonic power at the exit facet for about 70 mW of internal fundamental power. However, the conversion efficiency was somewhat low, only $2.7\text{ \%W}^{-1}\text{cm}^{-2}$, which is lower than that achieved with the short Sample B. It is also over an order of magnitude smaller than that achieved with 2-ps pulses in the shorter Sample A piece. This demonstrates that the conversion efficiency did not scale with length and may indicate that the losses in the second-harmonic were high, thus depressing the normalized conversion efficiency.

Despite the slightly lower overall performance with 20-ps pulses, the normalized conversion efficiencies for Sample B were within the same order of magnitude as with the 2-ps experiments. This means that the quantum conversion efficiency with either pulse length is similar. Thus, there is an equivalency in performance. However, since the pulse peak power was about ten-times less for the 20-ps pulses, the instantaneous conversion efficiency was nearly one order of magnitude higher at large input powers. Thus, from this perspective, the SHG performance was better when using 20-ps pulses than 2-ps pulses. The average power conversion efficiencies are also at least two-orders of magnitude larger than those of the continuous wave experiments, meaning that far more second-harmonic photons were produced in the 20-ps case.

Power Dependence

The power dependence of the SHG process with 20-ps pulses was investigated. Figure 5.23 shows the output second-harmonic power in a Sample B waveguide with a $3.8\text{ }\mu\text{m}$ QPM period as the internal input power was increased. Also shown is data from the 2-ps pulse experiments with the same waveguide. At low powers, the 2-ps system produced output second harmonic powers nearly 13 times larger than in the 20 ps case. As the input power is increased, second-harmonic power steadily increased in the 20-ps system without saturation at high powers. The “kink” in the shown curve at 30 mW is attributed to measurement error, laser instability, and potentially thermal bistability similar to that observed in continuous wave measurements. No consistent trend related to this behaviour

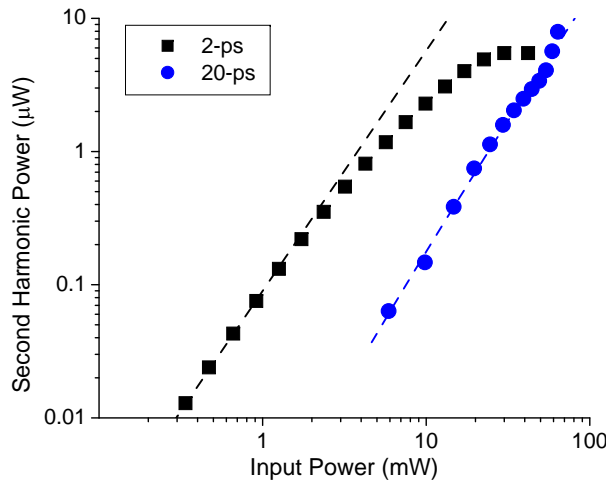


Figure 5.23: Power dependence of second-harmonic power for 20-ps pulses and 2-ps pulses in a 1.3 μm -deep waveguide with a 3.8 μm QPM grating period.

was found in other waveguides. Overall, no significant fluctuations or deviations from linear behaviour on the log-log plot were observed. However, for 2-ps system, the power does saturate and converges toward the same value as in the 20-ps system. The slope of the logarithmic curve from the best fit of the 20-ps data was 1.95, which is nearly quadratic and confirms the theoretical dependence of the SHG process on input power. This is an improvement over the 2-ps experiments where the slope was much less than quadratic. The power dependence demonstrates that the 20-ps is not afflicted by either SPM or nonlinear absorption to the same degree as the 2-ps system over the input power levels investigated. At input powers greater than used here, it is anticipated that the 20-ps pulses would outperform 2-ps pulses and produce more output second-harmonic power.

The behaviour of the normalized conversion efficiency was also different in each pulse length regime. Figure 5.24 shows how the conversion efficiency changes with input power. For the 20-ps case, the conversion remains steady around a mean value of $23 \text{ \%W}^{-1}\text{cm}^{-2}$ over the span of 50 mW of input power. This is over an order of magnitude lower than the 2-ps case at lowest input power shown where the conversion efficiency is nearly $365 \text{ \%W}^{-1}\text{cm}^{-2}$. As before, at even lower powers, the efficiency in the 2-ps case levels out and reaches a value of over $1300 \text{ \%W}^{-1}\text{cm}^{-2}$. As the power was increased for the 2-ps

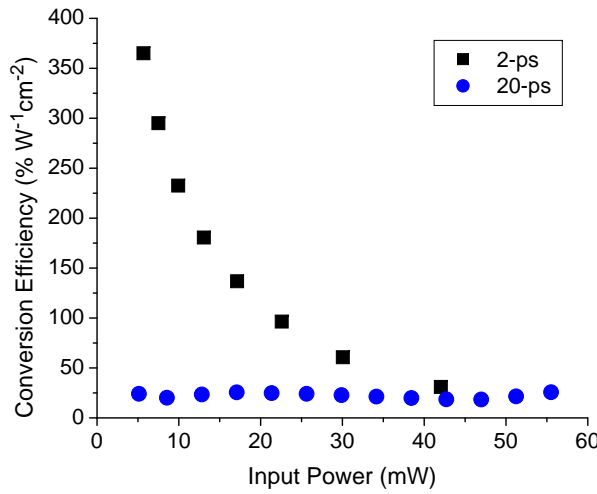


Figure 5.24: Power dependence of the SHG conversion efficiency for 20-ps pulses and 2-ps pulses in a $1.3 \mu\text{m}$ -deep waveguide with a $3.8 \mu\text{m}$ QPM grating period.

system, the conversion efficiency drops to $31 \text{ \%W}^{-1}\text{cm}^{-2}$, which is a similar value to the 20-ps system. This again shows that the 2-ps pulses are strongly affected by higher order nonlinear effects while the 20 ps pulses are relatively unaffected due to their reduced peak power.

Further insight can be gained by comparing the performance via the equivalent instantaneous efficiency as described by Equation 2.25. For instance, in a Sample B waveguide with a $3.8 \mu\text{m}$ QPM period, the Type-I instantaneous efficiency with loss accounted for was $0.32 \text{ \%W}^{-1}\text{cm}^{-2}$ when using 20-ps pulses. However, the 2-ps system yielded an efficiency of $1.18 \text{ \%W}^{-1}\text{cm}^{-2}$ at low power, which is nearly four times higher. The efficiency was expected to be nearly equal by this measure. A similar discrepancy was observed for Type-II phase matching. It is suspected that the laser instability in the 20-ps experiments was the cause of this discrepancy. Despite this, the 20-ps system had superior performance at high power. Here, the instantaneous conversion efficiency in the 2-ps case fell to $0.033 \text{ \%W}^{-1}\text{cm}^{-2}$, which is an order of magnitude lower than in the 20-ps case. Since more input power can be used in the 20-ps case without saturation effects, even more power can be generated. Thus, the 20-ps system is more appropriate when operating at high power, which will usually be the case in order to generate sufficiently high power for useful purposes.

5.6 Analysis

The measured data from the SHG experiments can be used to resolve the inconsistencies with predictions. In this section, two characteristics of the superlattice QPM waveguides are examined in more detail. In the first, the mismatch in the effective indexes of the fundamental and second-harmonic wavelengths is calculated from the measured trends in the phase matching wavelengths. This will elucidate the error in the predictions and provide a new model on which to base future predictions. The second characteristic of interest is the modulation in $\chi^{(2)}$ achieved by the intermixing process. This will provide an explanation of the lower than expected conversion efficiency.

5.6.1 Effective Index Mismatch

Measured values of the phase matching wavelengths did not correspond to the predicted values in Chapter 3. As discussed in Section 5.3.2, one possible reason for this was uncertainty in the refractive index data for the superlattice used to find the mode effective indexes at the fundamental and second-harmonic wavelengths. The source of this uncertainty in part may have been due to alterations made to the superlattice structure from the previous structure, partial intermixing in the disordered domains, thermal intermixing in the as-grown domains, and systemic problems in the measured refractive index data for the previous superlattice. Corrected data could be obtained by re-measuring the effective slab index of the new superlattice via the grating coupler technique [103]. This would give accurate data, but it is a time consuming process. Instead, information about the index mismatch between the second-harmonic and fundamental waves in the actual samples used for QPM can be extracted using the data obtained on the phase matching wavelengths. While such an analysis does not yield the actual effective refractive indexes, for the purposes of QPM, only the mismatch in the indexes is ultimately important for finding the phase matching wavelengths.

Recall that the QPM period given a particular phase matching wavelength is given by summing the coherence lengths of the as-grown and intermixed domains. Using Equa-

tions 3.4 and 3.5, the equation for the QPM period is

$$\Lambda = \frac{\lambda_\omega}{4} \left(\frac{1}{\Delta N_{\text{ag}}} + \frac{1}{\Delta N_{\text{qwi}}} \right) \quad (5.4)$$

where the index mismatch for Type-I and Type-II phase matching are defined as

$$\text{Type-I} : \Delta N = n_{2\omega}(TM) - n_\omega(TE) \quad (5.5a)$$

$$\text{Type-II} : \Delta N = n_{2\omega}(TE) - \frac{1}{2}[n_\omega(TE) + n_\omega(TM)]. \quad (5.5b)$$

In the case where $\Delta N_{\text{ag}} = \Delta N_{\text{qwi}}$, the duty cycle is 50:50. While this is not necessarily true in the case of the superlattice, an equivalent index mismatch assuming that the duty cycle is 50:50 can be defined as

$$\overline{\Delta N} = 2 \left(\frac{1}{\Delta N_{\text{ag}}} + \frac{1}{\Delta N_{\text{qwi}}} \right)^{-1} = \frac{\lambda_\omega}{2\Lambda}. \quad (5.6)$$

The equivalent mismatch of the above equation is a sort of “average” of the mismatch in each domain. Also, this equation shows that the mismatch can be determined for the 50:50 case knowing the nominal QPM period and the measured phase matching wavelength. Calculated mismatch values are shown in Figure 5.25 for both Sample A and Sample B using the linear fit of the phase matching wavelengths shown in Figures 5.7 and 5.8. It is assumed that the duty cycle in the actual waveguides is around 50:50, which is supported by the lack of a clear trend between the 60:40 and 50:50 drawn duty cycles in the actual samples. Predicted mismatch values are shown as dashed lines and represent the equivalent index mismatch calculated via Equation 5.6 and the effective refractive index data from Chapter 3. With the exception of the Sample B Type-I case where there is a crossover point, the measured index mismatch is consistently less than the predicted values. There are two possible causes for this: 1) the index values for the superlattice at the fundamental wavelengths could be larger than anticipated, 2) the index at the second-harmonic is smaller than anticipated, or 3) a combination of both. Another trend observed is that the gap between the measured and predicted curves reduces as

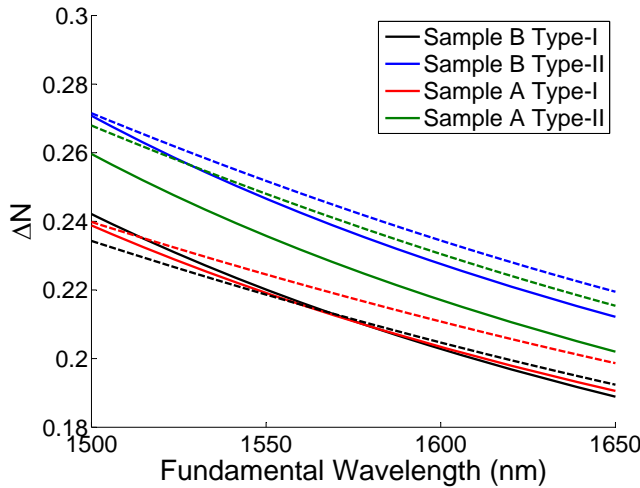


Figure 5.25: Effective refractive index mismatch values extracted from the measured phase matching wavelengths for Samples A and B. Dashed lines represent the predicted mismatch values averaged between the as-grown and intermixed refractive index data.

the measured curves bow upward with decreasing wavelength. One possible reason for this behaviour is the decrease in the band gap energy in the new superlattice structure. As the wavelength approaches the resonance energy of the superlattice, the index of refraction should increase rapidly. Since the predicted mismatch values were based on shifted dispersion curves of the refractive index of the original superlattice, the resonance effect may not be well accounted for and the model deviates from the actual. Thus, this points to an inaccuracy of the second-harmonic refractive index data as the chief cause of the disparity between the predicted and measured index mismatch.

5.6.2 Effective $\chi^{(2)}$

The value of the effective $\chi^{(2)}$ for the DD-QPM structure can be calculated from the conversion efficiency data of the SHG experiments. For this analysis, the data from the 2-ps pulse experiments with Sample B were used. This was done for several reasons. First, loss data at the second-harmonic wavelengths was more forthcoming for Sample B and it is necessary to account for the loss coefficient in order to extract the parametric gain factor from the normalized conversion efficiency. Second, more QPM periods and phase-matching wavelengths were covered in the 2-ps experiments than in the continuous wave

experiments, thus allowing a wider picture of the spectral variation. Lastly, data from the 2-ps experiments was more complete and consistent than in the 20-ps experiments and also showed better performance at low powers.

In order to calculate $\chi_{\text{eff}}^{(2)}$, the low-power conversion efficiencies of Figure 5.14 were first scaled by the loss coefficients of the fundamental and second-harmonic wavelengths according to Equations 4.9 and 4.10. Next, the effective instantaneous conversion efficiencies were calculated by Equation 2.25, thus yielding the parametric gain coefficient which is proportional to $|\kappa|^2$. Effective $\chi^{(2)}$ values were then calculated using Equation 2.9. Since $A_{\text{eff}}^{(2)}$ generally changes between the as-grown and intermixed sections of the QPM waveguides, the average is used. Thus, the error in the calculated $\chi_{\text{eff}}^{(2)}$ values is the difference between using the average effective area, and using the actual effective areas of either domain as though they were uniform. The results are shown in Figure 5.26 for both Type-I and Type-II phase matching. Immediately apparent is that the values are lower than predicted. At best, $\chi_{\text{eff}}^{(2)}$ is 8.2 pm/V in the Type-I interaction, which is about half of the value for a superlattice-based DD-QPM structure predicted in Section 4.5. Type-II values were 4.7 pm/V in the best performing waveguide, which is about one sixth of the predicted value. As with the conversion efficiency, the values for Type-II are consistently lower than Type-I, however the difference is only a factor of two in $\chi_{\text{eff}}^{(2)}$ rather than a factor of four as was the case for η . This is the result of taking into account the larger linear losses in Type-II configuration.

The effective $\chi^{(2)}$ for the Type-I interaction appears to gradually increase from low photon energies and reaches a peak just beyond 0.8 eV. This agrees with the prediction that $\chi^{(2)}$ should increase as the half-band gap is approached. Beyond the peak, the extracted $\chi_{\text{eff}}^{(2)}$ values plummet. There are several possible reasons for this apparent trend. In the first explanation, the loss data for second-harmonic wavelengths beyond the band gap energy discussed in Chapter 3 may be inaccurate. Transmission data was difficult to obtain above the band gap since little or no transmission was detectable in this range. Thus, the calculated loss factors may be inaccurate for photon energies beyond 0.8 eV, which affected the extracted $\chi_{\text{eff}}^{(2)}$ values. Another possible explanation is the potential duty cycle variation discussed in Section 5.6.1. As was discussed in Chapter 4, deviation

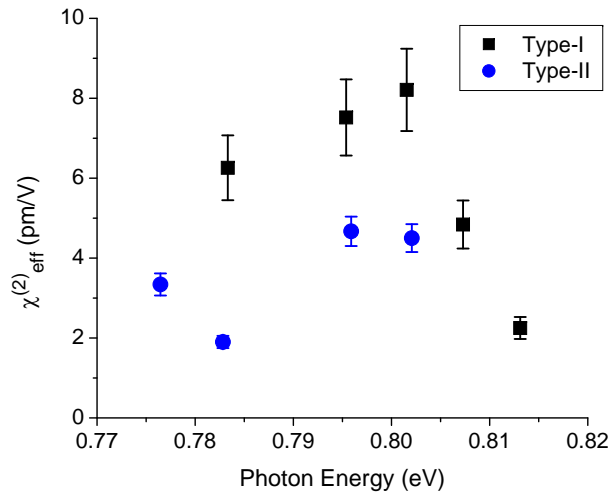


Figure 5.26: Effective $\chi^{(2)}$ values for Type-I and Type-II SHG in Sample B using data from 2-ps experiments

from the ideal 50:50 duty cycle in the actual QPM grating results in a reduction in conversion efficiency. Since the duty cycles of the shorter QPM periods are proportionally more susceptible to the lateral diffusion of the intermixed regions, those shorter periods will have lower conversion efficiencies. Lastly, in another explanation, such a drop in $\chi^{(2)}$ beyond the half-band gap may be a natural property of the superlattice. While no theoretical predictions were made for the superlattice at wavelengths beyond the half-band gap, this explanation is supported by theoretical studies on the dispersion of $\chi^{(2)}$ in GaAs and other semiconductors [104, 105, 106].

The modulation in $\chi^{(2)}$ can be calculated from the $\chi_{\text{eff}}^{(2)}$ values using Equation 4.14. Figure 5.27 shows the value of the change in $\chi^{(2)}$ for several photon energies. For the Type-I data, $\Delta\chi^{(2)}$ represents the change in the $\chi_{zxy}^{(2)}$ tensor element, while the Type-II data represents the change in the $\chi_{xyz}^{(2)}$ element. In the calculations, it was assumed that the duty cycle is 50:50. The error results from uncertainty in the effective area as before, and the additional uncertainty in the duty cycle of the QPM grating, which is taken to be up to 10%. The values are much lower than anticipated from theoretical calculations [35], and about four-times lower than what can be achieved in PPLN [107]. For the $\chi_{zxy}^{(2)}$ coefficient, the modulation depth is about half of what was predicted. This was partly the result of only partially intermixing the superlattice in the disordered

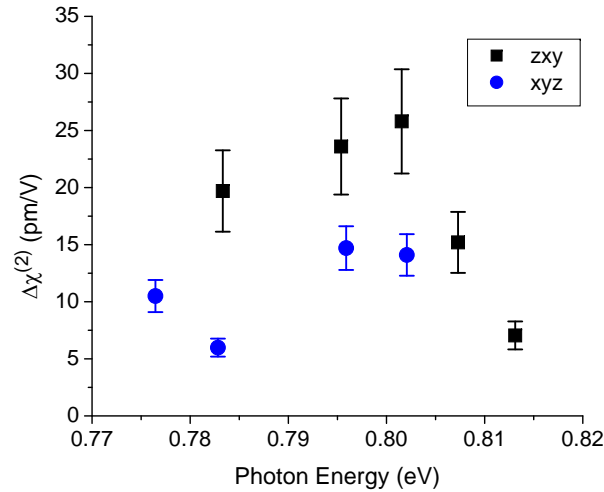


Figure 5.27: Modulation in $\chi_{xyz}^{(2)}$ and $\chi_{zxy}^{(2)}$ between as-grown and intermixed superlattice for SHG in Sample B using data from 2-ps experiments

domains, which reduced the amount of suppression in $\chi^{(2)}$. Also, the PL shift measured for as-grown superlattice in the QPM gratings indicated that the intact domains were actually partially intermixed as well by thermal diffusion. However, the suppression of $\chi^{(2)}$ for diffusion lengths of 2-3 monolayers was predicted to be insignificant relative to larger diffusion lengths that would occur in regions where intermixing is promoted by ion implantation [37]. In the case of the $\chi_{xyz}^{(2)}$ element, the modulation is less than 20% of the theoretical value. This lower relative modulation in the $\chi_{xyz}^{(2)}$ element compared to $\chi_{zxy}^{(2)}$ does not agree with predictions. One reasonable explanation for this are the inaccuracy of loss data at the second-harmonic wavelength, especially near the band edge. Another explanation is that there is a constant term error in the theoretically calculated $\chi^{(2)}$ values. Such an error can result from limitations in the band structure model used to calculate the electric susceptibilities from quantum mechanics [108].

5.7 Conclusions

In this chapter, the performance of superlattice DD-QPM waveguides when generating second-harmonic wavelengths was discussed. Table 5.4 summarizes the best measured equivalent instantaneous efficiencies when using 2 ps pulses, 20 ps pulses, and continuous

Table 5.4: Summary of the best second harmonic generation conversion efficiency results. All conversion efficiencies are normalized to represent the equivalent instantaneous efficiency. Losses are calculated out of the conversion efficiencies thus representing the actual overall efficiency of the waveguides. Note that the different sample lengths affect the conversion efficiency because of the loss.

	Length (mm)	Type-I			Type-II		
		Period (μm)	λ_{pm} (nm)	η (%W ⁻¹ cm ⁻²)	Period	λ_{pm}	η
Sample A							
2-ps	0.6	3.8	1582.5	0.700	3.5	1577.4	0.079
20-ps	3.5	3.6	1571.0	0.013	3.8	1613.5	0.003
cw	3.5	3.5	1546.1	0.092		N/A	
Sample B							
2-ps	1	3.6	1558.8	0.552	3.5	1596.5	0.113
20-ps	1	3.8	1583.5	0.146	3.8	1629.5	0.026
cw ^a	4	3.5	1545.8	0.029	3.3	1564.5	0.067

^a For Type-II, the shorter 1 mm sample was used, hence the larger Type-II efficiency.

wave. In all cases, instantaneous efficiencies were less than 1 %W⁻¹cm⁻² and were below that achievable using other phase matching methods. However, the SHG conversion efficiencies were improved over past generations of DD-QPM waveguides. This was due to improvements in the fabrication processes that reduced scattering losses and increased band gap modulation.

Experiments with 2-ps pulses showed reduced conversion efficiencies and power saturation at high input powers. It was determined that high order nonlinear effects such as nonlinear absorption and SPM were to blame. Linear losses were low enough that continuous-wave SHG was possible and decent conversion efficiencies were achieved. However, continuous-wave experiments were plagued by bistability phenomena, which was determined to be the result of thermo-optic effects. In contrast, experiments using 20-ps pulse were not affected to an observable degree by thermo-optic effects or high-order nonlinearities. Conversion efficiencies in this case remained consistent at various input power levels. Type-II phase matching was achieved, which is important for integrating QPM waveguide with a pump laser. Index mismatch values calculated from

the measured phase matching wavelengths were lower than predicted and suggest that the refractive index data for the second-harmonic wavelengths was inaccurate. Effective $\chi^{(2)}$ values calculated from the normalized conversion efficiencies were also lower than those predicted in Section 4.5, which is the result of a smaller change in $\chi^{(2)}$ due to partial intermixing instead of full intermixing of the superlattice in disordered domains. Overall, these experiments provide information necessary to perform difference frequency generation experiments and to determine the parameters for an integrated wavelength conversion device.

Chapter 6

Wavelength Conversion by Difference Frequency Generation

6.1 Introduction

The second-harmonic generation experiments discussed in the previous chapter provided much insight on the strength of the second-order nonlinearity in domain-disordered superlattice waveguides. Improvements made to the waveguide design and fabrication processes led to greater performance than previous generations of samples. These improvements were necessary in order to demonstrate difference frequency generation, the key second-order nonlinear process for wavelength conversion and amplification. However, observing DFG is generally more challenging to achieve than SHG. The highly dispersive material properties of AlGaAs and the requirement for coupling two input beams with disparate wavelengths into the waveguides with sufficient power levels complicates experimental verification. Hence, there have only been a handful reported demonstrations of DFG in AlGaAs waveguides in the literature [54, 43, 46, 57], and, with the exception of the first reference on BRWs, none of these reported waveguides are appropriate for monolithic integration with an onboard pump laser. As superlattice DD-QPM waveguides were designed specifically for the purpose of integration, they hold better potential for producing such a device.

In this chapter, difference frequency generation in domain-disordered quasi-phase

matching waveguides is examined. First, the DFG process is modeled with a theoretical approach that includes linear losses in the interacting waves. By using the model, predictions of the conversion bands and the conversion efficiency are made based on data collected from the SHG experiments of the previous chapter. This allows determination of the operating ranges for subsequent DFG experiments. Results from these experiments are discussed in detail, showing the first ever demonstration of DFG in DD-QPM superlattice waveguides. Both Type-I and Type-II interactions are observed and the performance of each is evaluated. Next, the application of DFG in DD-QPM waveguides for wavelength conversion devices monolithically integrated with an onboard pump laser is examined in detail. With data from the DFG and SHG experiments, predictions are made on the performance of a parametric converter and an optical parametric oscillator using simplified analytical models and numerical simulations of more complete models. Lastly, several improvements to the QPM waveguides and integrated device design are proposed that would allow better performance and more practical operating parameters.

6.2 Modeling

Before conducting DFG experiments, it is necessary to determine the approximate operating ranges. Data from the SHG experiments provides information about the efficiency of the processes and on the phase matching wavelengths. However, the other parameters specific to the DFG process must also be examined. In this section, two important aspects of DFG are discussed from a theoretical standpoint: the conversion efficiency and the conversion bandwidth. The model here uses analytical solutions to the coupled mode equations for three-wave mixing under several simplifying assumptions including no pump depletion and no parametric gain in the signal. High-order nonlinear and dispersion effects will not be considered as the experimental arrangements used did not utilize short pulses that would be required to cause such effects. Empirical data from the SHG experiments is used in the models along with effective index dispersion data from Chapter 3.

6.2.1 Conversion Bands

The performance of the DFG process will vary depending on the wavelength used. As with SHG, the conversion process will be most efficient when the wavelengths involved satisfy the phase matching condition. However, the situation becomes more complicated in DFG since three distinct and independent wavelengths are involved instead of just two. Ordinarily, the pump wavelength is fixed at a particular wavelength while the signal/idler pair vary. However, the range of signal wavelengths that will produce significant idler power is limited to the conversion band within which the phase matching condition is met. Thus, it is important to know the spectral characteristics of the conversion band and its width.

In the simple case of DFG under the assumptions of no pump depletion, insignificant parametric gain in the signal, and no linear loss, the generated idler power can be found using Equation 2.7. The bandwidth of the DFG process is solely due to the sinc^2 factor involving the phase mismatch $\Delta\beta$. Thus, the conversion band is determined by the dispersion of the effective index of the signal, idler, and pump. However, the dispersion in the spectral region of the signal and idler is relatively flat. Thus, for a fixed pump wavelength near the SHG phase matching wavelength, the 3 dB conversion bandwidth is expected to be large.

The spectral variation for a fixed pump wavelength near the degeneracy point was carried out to using effective refractive index data shown in Chapter 3. Initially, the conversion bandwidth would have been centered at the theoretical degeneracy wavelength. However, the actual degeneracy wavelengths were found at different wavelengths in SHG experiments as shown in Figure 5.8. Thus, a correction factor was added to $\Delta\beta$ such that

$$\Delta\beta = \beta_p - \beta_s - \beta_i - \frac{2\pi}{\Lambda} - \frac{2\pi}{\lambda_{pm}}\delta n \quad (6.1)$$

where λ_{pm} is the SHG phase matching wavelength and δn is the index difference correction factor calculated using the ΔN data of Figure 5.25. Figure 6.1 shows the Type-I DFG conversion efficiency η normalized to the maximum possible conversion efficiency for a Sample B QPM waveguide with a 3.8 μm period, 50:50 duty cycle, and 3.0 μm ridge width.

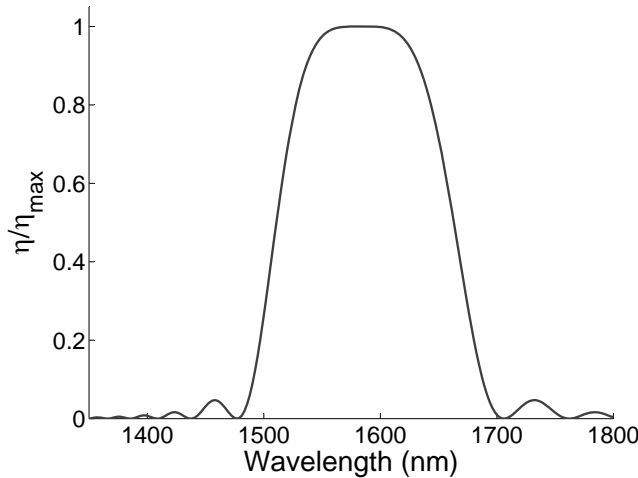


Figure 6.1: Simulated Type-I DFG conversion band for Sample B waveguide with $3.8 \mu\text{m}$ QPM period at the degeneracy pump wavelength. A correction was made to the pump refractive index such that the degeneracy wavelength coincided with the SHG phase matching wavelength.

The pump wavelength was set to the measured degeneracy wavelength of 791.7 nm. Near 1583 nm, which is the SHG fundamental phase matching wavelength, the conversion efficiency is relatively flat, varying by less than 10% over 90 nm of spectrum. The 3-dB bandwidth is over 150 nm (18 THz) wide centered around 1583 nm. This covers the C, L, and U telecommunications bands. Outside of the conversion band, the efficiency is reduced to less than 5% of the maximum. With a small detuning of 0.2 nm shorter from the degeneracy wavelength, the 3-dB bandwidth expands to nearly 185 nm (22 THz) with a non-flat peak in the conversion band. However, in this case, the conversion efficiency is still reasonably uniform with the dip in the center of the conversion band being less than 1 dB.

The shape of the conversion band changes with the pump wavelength. Figure 6.2 shows the normalized conversion efficiency for several different pump wavelengths near the degeneracy wavelength for $3.8 \mu\text{m}$ QPM period in the Type-I interaction. A small detuning of about 0.2 nm from the degeneracy wavelength of 791.7 nm drastically alters the conversion band. This is the result of the high dispersion in the refractive index of the pump wavelengths, which are located near the as-grown superlattice linear absorption peak. Moving to longer wavelengths reduces the maximum efficiency and narrows the gain

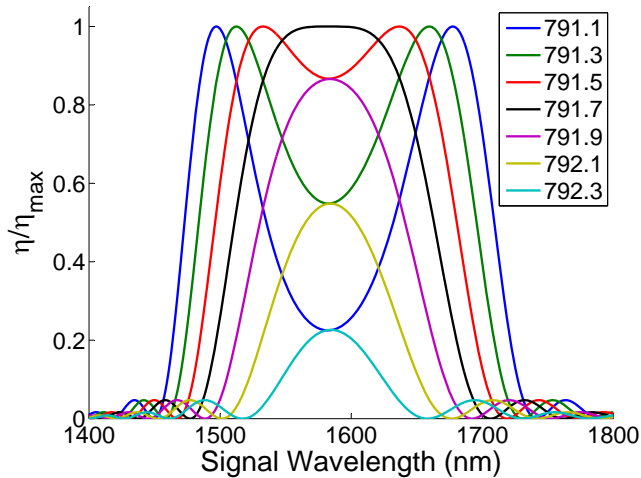


Figure 6.2: Simulated Type-I DFG conversion bands for Sample B waveguide with $3.8 \mu\text{m}$ QPM period at for several pump wavelengths. The degeneracy wavelength is 791.7 nm.

bandwidth. The top of the curve becomes less flat, thus affecting the gain uniformity over variation in the signal and idler wavelengths. Shifting the pump to shorter wavelengths causes the conversion band to expand, but at the expense of a dip in efficiency centered at the degeneracy wavelength. Two peaks in the conversion efficiency appear at symmetric points about the degeneracy wavelength. In this way, the peak conversion efficiency can be shifted to different signal/idler spectral regions by a relatively small detuning of the pump wavelength. However, the high sensitivity of the conversion efficiency at any one signal/idler wavelength pair requires careful tuning of the pump wavelength to obtain maximum conversion efficiency.

The behaviour of Type-II DFG is somewhat different from that of Type-I. Since the Type-II interaction requires that the input signal and generated idler are in different polarizations, the large birefringence of the superlattice will strongly affect the phase matching condition. In particular, the phase mismatch will be different depending on whether the signal is in the TE polarization or in the TM polarization. Figure 6.3 shows the simulated conversion bands for Type-II DFG for a Sample B waveguide with a $3.4 \mu\text{m}$ QPM period with a pump wavelength of 793 nm. There are two separate conversion bands, one for each polarization arrangement: TE-signal/TM-idler, and TM-signal/TE-idler. In each case, the symmetry point in the curves differs with the TE-signal/TM-

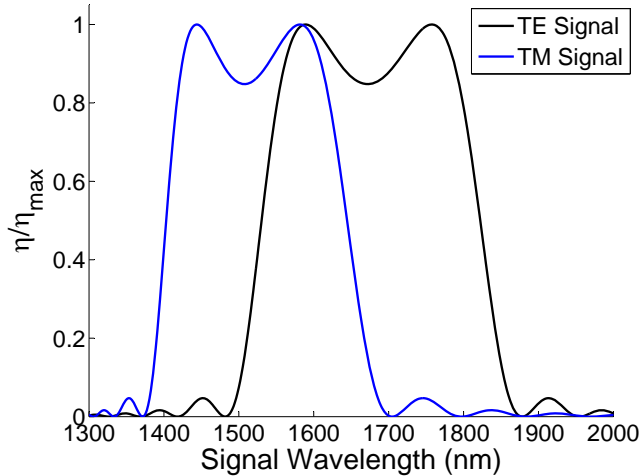


Figure 6.3: Simulated Type-II DFG conversion bands for a Sample B waveguide with $3.4 \mu\text{m}$ QPM period at the degeneracy pump wavelength for a TE and TM polarized signal.

idler curve being centered around 1672 nm, and the TM-signal/TE-idler curve being centered around 1507 nm. The curves intersect at twice the pump wavelength, which is 1586 nm. Since this is the degeneracy wavelength, the conversion efficiency also peaks at this point. At points around this peak in either curve, the conversion efficiency is not symmetric about the degeneracy wavelength. Furthermore, it is not flat around the peak, dropping 10% within 14 nm on the outer edge of each conversion band. However, the 3-dB conversion bandwidth in each polarization case spans over 31 THz, which is nearly 50% larger than the Type-I bandwidth at a pump detuning of 0.2 nm from degeneracy.

Linear loss affects the DFG conversion bandwidth in a similar manner to SHG. In the absence of dispersion effects and high order nonlinear effects, the coupled mode equations become

$$\frac{\partial A_s}{\partial z} = -j \frac{\kappa}{\lambda_s} A_i^* A_p \exp[-j\Delta\beta z] - \frac{1}{2} \alpha_s A_s \quad (6.2a)$$

$$\frac{\partial A_i^*}{\partial z} = j \frac{\kappa}{\lambda_i} A_s A_p^* \exp[j\Delta\beta z] - \frac{1}{2} \alpha_i A_i^* \quad (6.2b)$$

$$\frac{\partial A_p}{\partial z} = -j \frac{\kappa}{\lambda_p} A_s A_i \exp[j\Delta\beta z] - \frac{1}{2} \alpha_p A_p \quad (6.2c)$$

where A_s , A_i , and A_p represent the field of the signal, idler, and pump waves. Assuming no pump depletion and insignificant parametric gain for the signal, an analytical

expression for the generated idler power is found as

$$P_i = \frac{|\kappa|^2}{\lambda_i^2} P_{s,0} P_{p,0} L^2 \exp[-\frac{1}{2}(\alpha_s + \alpha_i + \alpha_p)L] \frac{\sinh^2(\frac{1}{2}\Delta\alpha L) + \sin^2(\frac{1}{2}\Delta\beta L)}{(\frac{1}{2}\Delta\alpha L)^2 + (\frac{1}{2}\Delta\beta L)^2} \quad (6.3)$$

where P_i , P_s , and P_p are the idler, signal, and pump powers respectively, λ_i is the idler wavelength, and $\Delta\alpha = \frac{1}{2}(\alpha_s + \alpha_p - \alpha_i)$. However, as shown by Bortz et al. [96], linear losses only affect the conversion bandwidth significantly when the $\Delta\alpha L > 1$. Since the length of the sample considered here is 1 mm long, the conversion bandwidth is expected to increase by less than 1% given the measured loss coefficients for Sample B.

6.2.2 Conversion Efficiency and Coupling Coefficient

In order to predict the conversion efficiency and the generated idler power for DFG, several assumptions must be made. First, it is assumed that $\chi^{(2)}$ exhibits overall permutation symmetry as defined in [17]. In this case, $\chi^{(2)}$ for DFG is the same as $\chi^{(2)}$ for SHG, and thus the conversion efficiency for DFG can be calculated from the measured data for SHG. However, this assumption is made with caution since the pump wavelengths lie near material resonances. Second, the variance of $\chi^{(2)}$ is assumed to be small as the signal and idler wavelengths are tuned away from the degeneracy point, but only within a small range. As such, the conversion efficiency should change very little within the vicinity of the SHG phase matching wavelength.

The maximum conversion efficiency achievable occurs when the signal and idler wavelengths are within the peak(s) of the conversion band where $\Delta\beta \approx 0$. Using the data on the SHG conversion efficiency, the absolute efficiency and generated idler power by DFG in the same waveguides can be predicted around the degeneracy wavelengths. The conversion efficiency for the DFG process under the non-depletion/non-gain approximation is defined as shown in Equation 2.22 such that

$$\eta_{\text{DFG}} = \frac{|\kappa|^2}{\lambda_i^2} = \frac{2\pi^2(\chi_{\text{eff}}^{(2)})^2}{c\epsilon_0 n_p n_s n_i A_{\text{eff}}^{(2)} \lambda_i^2} \quad (6.4)$$

where n_p , n_s , and n_i are the pump, signal, and idler refractive indexes, and λ_i is the idler

wavelength. One notable issue with this definition of the DFG conversion efficiency is that it is defined using the target wavelength, λ_i . Since DFG operates over a broad range of wavelengths, the value of η_{DFG} will vary depending on the specific wavelengths involved in the process. Instead, the coupling coefficient κ becomes the preferred metric since it remains relatively uniform within a given range of wavelengths. However, some variation will occur due to dispersion of various properties of the structure. The overlap area $A_{\text{eff}}^{(2)}$ will vary depending on the signal/idler pair, but the variation is small when operating at wavelengths near the SHG phase matching wavelength. The value of $\chi^{(2)}$ also depends on the set of wavelengths involved, thus $\chi^{(2)}$ will vary with different signal/idler pairs. However, near the SHG phase matching wavelength, the variation in $\chi^{(2)}$ is assumed to be small and thus it can be considered constant and the same as that measured in the SHG experiments. The conversion efficiency and coupling coefficient of DFG can be calculated using the $\chi_{\text{eff}}^{(2)}$ of Figure 5.26 from SHG experiments with Sample B waveguides. For Type-I phase matching, the value of $\chi_{\text{eff}}^{(2)}$ was 8.2 pm/V at best for the 3.5 μm QPM period waveguide at a phase matching wavelength of 1547 nm. Using the computed overlap area for SHG, the predicted coupling coefficient is $4.6 \times 10^{-5}\text{W}^{-1/2}$ and the conversion efficiency for DFG at the degeneracy point is 9.0 % $\text{W}^{-1}\text{cm}^{-2}$. For Type-II phase matching, $\chi_{\text{eff}}^{(2)}$ was 4.7 pm/V at best in a waveguide with a 1558 nm phase matching wavelength (QPM period of 3.2 μm). In this case, the coupling coefficient is predicted to be $2.6 \times 10^{-5}\text{W}^{-1/2}$ and the DFG conversion efficiency at degeneracy is 2.7 % $\text{W}^{-1}\text{cm}^{-2}$.

Linear loss has a similar effect on the DFG conversion efficiency as in SHG. Using Equation 6.3 in the case where the phase matching condition is met ($\Delta\beta = 0$), the DFG conversion efficiency loss factor is

$$\frac{\eta}{\eta_0} = \exp[-\frac{1}{2}(\alpha_s + \alpha_i + \alpha_p)L] \frac{\sinh^2(\frac{1}{2}\Delta\alpha L)}{(\frac{1}{2}\Delta\alpha L)^2}. \quad (6.5)$$

For the waveguides with the best $\chi_{\text{eff}}^{(2)}$, the efficiency is reduced by 78% in the Type-I case and by 92% in the Type-II case because of the proximity of the degeneracy pump wavelength to the linear absorption peak. Better performance can be gained by using QPM

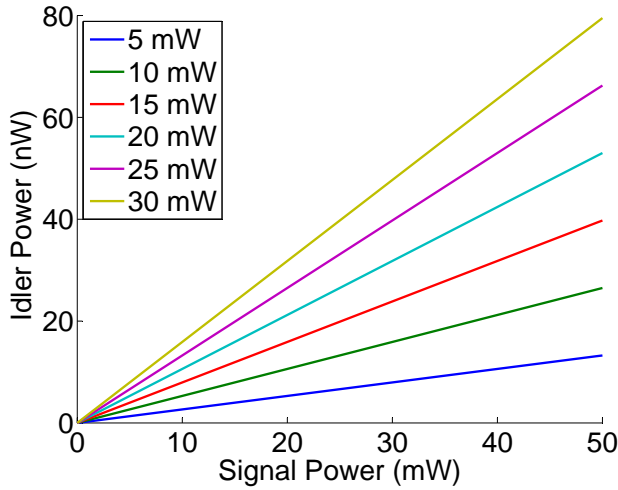


Figure 6.4: Predicted power levels for generated idler in Sample B waveguide with a $3.8 \mu\text{m}$ QPM period when phase matched at several input pump powers.

waveguides with longer phase matching wavelengths in order to move the degeneracy pump wavelength to the edge of the band tail. However, moving farther away from the band edge also reduces $\chi_{\text{eff}}^{(2)}$. For Type-I phase matching, QPM waveguide with a period of $3.8 \mu\text{m}$ and a degeneracy pump wavelength of 791.7 nm is expected to yield the best balance between a large $\chi_{\text{eff}}^{(2)}$ and a low pump absorption loss. When accounting for losses by Equation 6.5, the conversion efficiency is expected to be about $0.53 \text{ \%W}^{-1}\text{cm}^{-2}$.

From the conversion efficiency, the approximate idler power levels can be predicted. Figure 6.4 shows the expected idler powers generated in a $3.8 \mu\text{m}$ period Sample B waveguide at several continuous wave input pump powers by Type-I phase matching. For signal and pump powers of a few 10's of milliwatts, the generated idler power is expected to be on the order of a 10's of nanowatts. This represents a signal-to-idler conversion ratio of between -66 to -58 dB depending on the pump power.

6.3 Conversion Experiments

6.3.1 Experimental Setup

The experimental setup for the DFG experiments is shown in the schematic of Figure 6.5. A Ti:sapphire laser was used as the pump wavelength source operated in either continuous

wave mode or 2-ps pulsed mode. While the maximum power for this laser was in excess of 1 W, the power was attenuated by path losses and filters to less than 70 mW at the sample facet. Larger powers caused catastrophic damage to the DD-QPM samples. The signal wavelength source was a C-band tunable diode laser followed by an EDFA with an amplification bandwidth between 1535 and 1565 nm. Total signal power available at the facet of the waveguide sample was limited to 250 mW. The pump and signal beams were combined by using a 50:50 beam splitting cube. The input objective lens was problematic since the focal lengths for the signal and pump wavelengths were different. Thus, coupling efficiencies using an objective lens alone was low. In order to rectify this, a spherical lens with a 300 mm focal length was inserted into the pump beam path. Along with using a 10 \times anti-reflection coated objective lens with a working distance of 6 mm, the focal distance of the pump wavelength was corrected to equalize with the signal wavelength. Output light from the waveguides was collected by a standard 40 \times objective lens. The output pump wavelength was directed to a silicon photodetector by using a long-pass filter. Output signal and the generated idler wavelengths passed through the filter and were directed to a germanium photodetector. Both the filter and the mirror directing the beam to the germanium detector were on flip mounts, which allowed the beam to pass directly to an optical spectrum analyzer.

For Type-I phase matching, the pump polarization was set to vertical to launch into the TM mode of the waveguides, and the signal polarization was set to horizontal to launch into the TE mode. In experiments on Type-II phase matching, the pump polarization was set to TE while the signal polarization was set to either TE or TM. The polarization of the output idler wavelength was isolated by inserting a polarizing beam cube into the output beam path and setting its orientation to pass the polarization orthogonal to the signal polarization. Generation of the output idler wavelength was confirmed by measuring the output spectrum using the OSA.

Suitable waveguides and operating wavelengths for Type-I and Type-II were chosen for DFG by considering several criteria. First, the degeneracy pump wavelength was chosen to lie above the high absorption range of the as-grown superlattice. In this way, the effect of pump loss could be minimized. This necessitated using waveguides in which

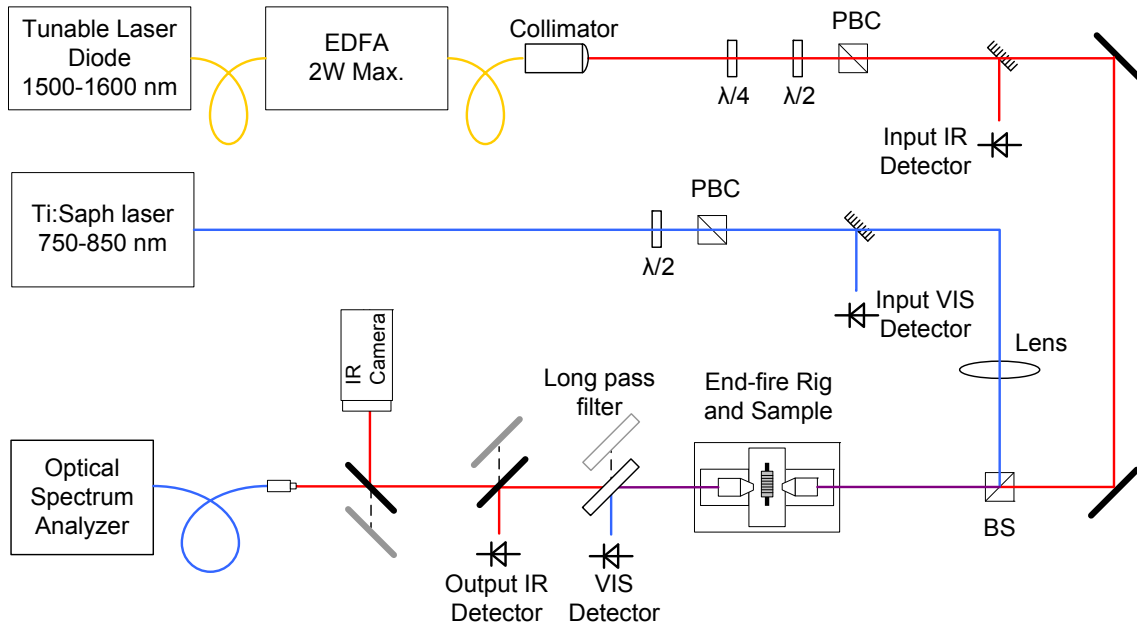


Figure 6.5: Schematic of the experimental setup for DFG experiments

the SHG phase matching second-harmonic wavelength was greater than 785 nm. For Sample B, experiments were thus limited to QPM periods of 3.7 μm and up for Type-I phase matching, and 3.4 μm and up for Type-II phase matching. Second, the detectable range for the idler wavelengths was limited to 1650 nm because of reduced sensitivity of the OSA beyond this wavelength. As the generated idlers were expected to be weak, it was important to generate the idlers at wavelengths that would not be obscured by detector noise. Since the signal wavelengths were limited to 1565 nm by the EDFA gain bandwidth, this limited the pump wavelength to 803 nm according to the frequency matching condition. Thus, the QPM period was limited to 3.5 μm for Type-II phase matching. Type-I was only limited by the longest QPM period available on Sample B, which was 3.8 μm . Lastly, detectable idler wavelengths were limited by the ASE noise of the EDFA. Since the idler powers were anticipated to be weak, the best spectral range in which to generate the idler wavelengths was above 1600 nm where the ASE noise rolls off. This limited the signal wavelength to below 1560 nm.

6.3.2 Results

In initial DFG tests, QPM waveguides on Sample A were used. However, no DFG was observed. It is believed that the poor confinement of the pump wavelength, which was discussed in Section 3.3.3, prohibited sufficient DFG to be observable. Confinement of the pump was improved in Sample B as observed on the camera at the waveguide output. DFG was observable with Sample B despite the larger linear losses. Thus, the remaining discussion in this section is limited to a Sample B piece which was 1 mm long.

Both the signal and the pump beams were operated in continuous wave. Operating the pump beam in mode-locked mode with 2-ps pulses did not improve performance of the DFG process. One possible reason for this was the spectral overlap of the pump pulse spectrum with the conversion bandwidth. As shown in the previous section, the DFG conversion band changes drastically with small shifts from the degeneracy pump wavelength. Thus, operating in pulsed mode spreads the energy of the pump over a larger spectrum, which increases the bandwidth at the expense of parametric gain. As a result, conversion efficiency in the C/L/U bands drops despite the increase in pump peak power.

Type-I DFG

The best DFG performance for Type-I phase matching was achieved in a waveguide with a 3.8 μm QPM period, 60:40 drawn duty cycle, and 3.0 μm waveguide width. Initially, the pump wavelength was set to the degeneracy wavelength of 791.7 nm. The input signal power at the waveguide facet was 252 mW and input pump power was 45 mW. Transmission through the waveguide was 12.3% for the signal and 10% for the pump. The signal wavelength was adjusted over a few 10's of picometers to coincide with a Fabry-Perot resonance of the waveguide such that transmission and internal signal power were maximized. The pump wavelength was slowly adjusted to the point where the observed idler power peaked on the OSA. This power dependency on the the pump wavelength confirmed that the process was phase matched. The output idler wavelength was found to be TE polarized, which is consistent with the Type-I phase matching configuration.

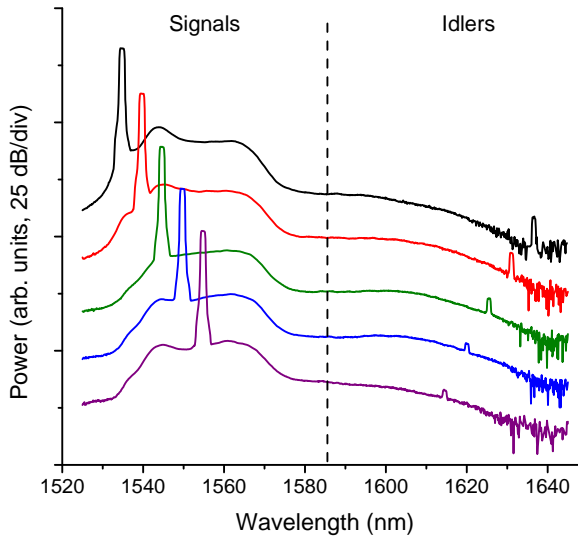


Figure 6.6: Output spectrum from a Sample B waveguide with QPM period of $3.8 \mu\text{m}$ for several signal wavelengths. The pump wavelength was set to 791.7 nm. Signal wavelengths are shown on the left and the generated idler wavelengths are shown on the right for Type-I DFG.

Figure 6.6 shows the recorded output spectra from the QPM waveguide for several input signal wavelengths. The generated idler wavelengths are found in the L- and U-bands, just beyond the rolloff of the ASE from the EDFA. The idler peaks rose at least 5 dB above the background ASE, and were thus clearly distinguishable from the noise. In all cases, the idler wavelength was found to obey the frequency matching condition. For instance, an idler wavelength at 1620.7 nm was produced for a signal wavelength of 1550.1 nm.

To obtain the output idler power value, it was necessary account for the coupling ratio into the OSA. This was done by comparing the signal wavelength peak power on the OSA with the power measured on the photodetector to derive a scaling factor. The idler power could then be determined by multiplying the idler peak in the output spectrum measured by the OSA by this factor. Subtracting the ASE power and accounting for the output facet reflectivity yielded an internal output idler power of 8.6 nW for an idler wavelength of 1620.7 nm. This is nearly an order of magnitude lower than predicted. The internal input signal power and pump power were calculated as 48.7 mW and 24.4 mW respectively after accounting for the facet reflectivity and linear losses. Thus, the signal/idler

conversion efficiency was -67.5 dB. This is considerably less than the efficiency achieved in domain-reversed AlGaAs structures [57]. Using Equation 2.22, the DFG normalized conversion efficiency was calculated as $0.072 \text{ \%W}^{-1}\text{cm}^{-2}$. Accounting for the losses in the waveguides by Equation 6.5, the conversion efficiency was $0.19 \text{ \%W}^{-1}\text{cm}^{-2}$. In both cases, the efficiency is significantly below what was predicted. The experimentally determined coupling coefficient κ can be calculated using

$$\kappa = \lambda_i \sqrt{\eta}. \quad (6.6)$$

By this, the coupling coefficient of DFG in this waveguide was $7.0 \times 10^{-6}\text{W}^{-1/2}$, which is six times lower than predicted in Section 6.2.2.

The signal wavelength was scanned from 1535 to 1555 nm to test tuning of the idler and to demonstrate the conversion bandwidth. Figure 6.6 shows the recorded output spectra from the QPM waveguide for several signal wavelengths. Peak idler powers were within 5 dB, which was mostly due to input signal power variations, indicating relatively uniform conversion efficiency across at least 20 nm of spectrum. Considering that the gain is expected to be relatively flat over this region, the conversion band likely extends from at least 1535 to 1637 nm. This represents a conversion bandwidth of over 100 nm, which spans the C, L, and U communications bands. The bandwidth may extend farther, however, limitations on the source wavelengths available and the detection ranges precluded complete testing of this hypothesis.

Wavelength conversion by Type-I DFG was also observed in a waveguide with a QPM period of 3.7 μm and 3.5 μm ridge width. The pump wavelength was set to 786 nm. Figure 6.7 shows the output spectrum for several input signal wavelengths. As before, the generated idler wavelengths appear on the right side of the plot just beyond the ASE rolloff. While the idler peaks are clearly visible, the contrast with the ASE noise was less than 2 dB. Thus, it was difficult to properly distinguish the power of the idler alone. This may have been at least partially due to reduced conversion efficiency as a result of lowering the pump wavelength deeper into the absorption regime for the superlattice. Despite this, results from this waveguide still show that the DFG process worked in other

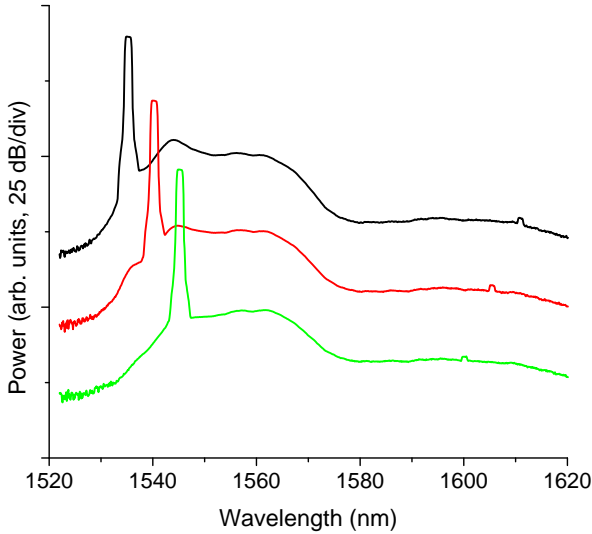


Figure 6.7: Output spectrum from a Sample B waveguide with QPM period of $3.7 \mu\text{m}$ for several signal wavelengths. The pump wavelength was set to 786 nm. Signal wavelengths are shown on the left and the generated idler wavelengths are shown on the right for Type-I DFG.

QPM periods.

Type-II DFG

Type-II DFG was observed in a waveguide with a $3.4 \mu\text{m}$ QPM period. The pump was set to the Type-II degeneracy wavelength for this waveguide, which was near 792.9 nm. Figure 6.8 shows the recorded output spectrum for two different polarization setups: a) TE signal, TM idler, and b) TM signal, TE idler. In both cases, the polarization of the idler was confirmed by inserting a polarizer just before coupling into the fiber attached to the OSA input. The signal wavelength still shows up in the spectral plots since the polarizer only rejects about 20 dB of the orthogonal polarization. The polarizer also had the effect of reducing the noise in the spectral measurements by rejecting the orthogonally polarized ASE noise present in the input beam. This made the idler peak more distinguishable. The measured data from the OSA also shows the high-order diffraction from the pump wavelength, which is aliased to 1586 nm. However, the presence of the pump in the spectrum did not affect the measurement.

Using the scaling factor method as outlined previously, the output idler power was

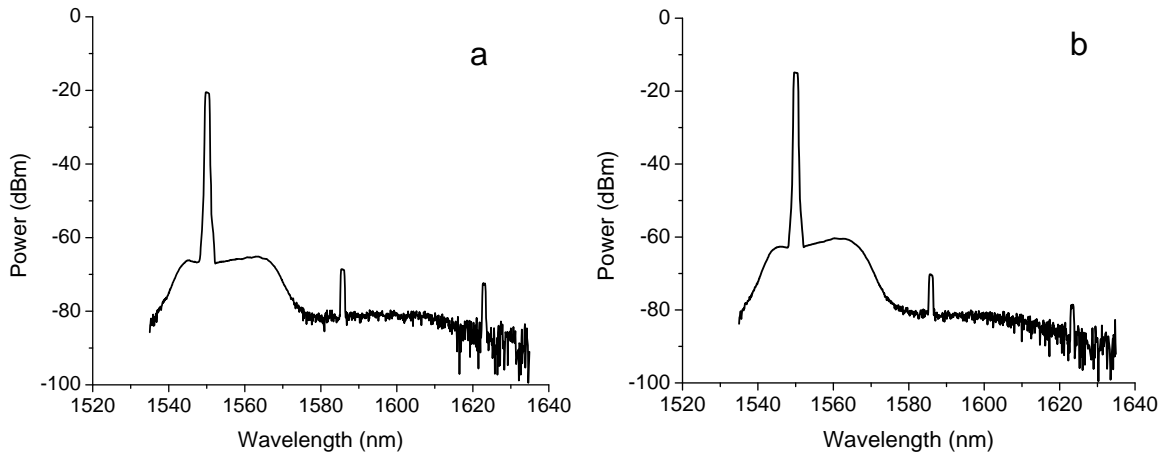


Figure 6.8: Output spectrum from a Sample B waveguide with QPM period of $3.4 \mu\text{m}$ for Type-II DFG. The pump wavelength was set to 792.9 nm. The signal polarization was set to a) TE and b) TM, while the polarization into the OSA was isolated to the orthogonal polarization using a polarizer.

calculated to be 1.9 nW at the exit facet of the waveguide for the TE signal, TM idler case. This is four times lower than in the Type-I measurements, which agrees with similar trends observed in SHG experiments. The internal input pump power was 31.3 mW, and the internal input signal power was 51.7 mW. The signal-to-idler conversion efficiency is -74.3 dB . From this, the conversion efficiency was calculated as $0.012 \text{ \%W}^{-1}\text{cm}^{-2}$, which is six times lower than in the Type-I case. Larger pump loss in the TE polarization used for Type-II phase matching is partially to blame. When accounting for the linear losses, the conversion efficiency becomes $0.044 \text{ \%W}^{-1}\text{cm}^{-2}$. This is still over four times lower than the Type-I interaction. The coupling coefficient for the process was calculated as $3.4 \times 10^{-6} \text{ W}^{-1/2}$, which is nearly an order of magnitude lower than expected.

6.4 Application to Integrated Wavelength Conversion Devices

Experimental demonstrations of DFG in the previous section show the potential for using DD-QPM waveguide technology for creating all-optical wavelength converters. The compatibility of this technique with onboard pump lasers make this method highly at-

tractive. Additionally, integrating a pump source could potentially raise the potential output power in the converted wavelength to practical levels. In this section, two different potential frequency conversion devices based on DD-QPM waveguides are investigated: a parametric converter and a parametric oscillator.

6.4.1 Parametric Converter

Integration of an onboard pump laser has several advantages in addition to reducing the device footprint and improving robustness of a parametric converter. One of the limitations imposed on the DFG experiments with discrete DD-QPM waveguides by coupling the pump from an external source was that the pump power could not be raised to high levels without catastrophic damage to the sample facet. With an integrated pump laser onboard, that limitation is relaxed since the internal waveguide powers can be much greater without risking damage. Furthermore, internal circulating power of the laser is much larger than the typical external output power of the laser. Thus, by placing the conversion element inside the laser cavity, the DFG process can be boosted and the output idler power can be raised to more usable levels.

An optimal device must balance several parameters. One of those parameters is the length of the QPM device. For a compact device, the QPM waveguide should be as short as possible while providing sufficient conversion to the idler. Also, since the QPM waveguide is within the laser cavity, the length will affect stability and longitudinal mode spacing. The output idler power generated can be calculated as

$$P_i = \eta_0 P_{s,0} P_{p,0} L^2 \exp[-\frac{1}{2}(\alpha_s + \alpha_i + \alpha_p)L] \frac{\sinh^2(\frac{1}{2}\Delta\alpha L)}{(\frac{1}{2}\Delta\alpha L)^2} \quad (6.7)$$

where η_0 is the conversion efficiency without loss. In this case, η_0 can be taken to be the an experimentally determined value. Figure 6.9 shows the calculated output idler power generated over the length to Type-I and Type-II interactions in the best performing Sample B waveguide. In both cases, the internal circulating power of the laser was assumed to be 300 mW and the signal power was set to 50 mW. The loss coefficients used for the pump are 31 cm^{-1} and 44 cm^{-1} , which are the projected losses at the pump laser

wavelength of 770 nm in the QPM waveguide for the Type-I and Type-II interactions, respectively. The idler power initially increases over length, but at a deceasing rate. A peak is reached, after which the power decreases due to linear attenuation of the pump and signal which stalls the conversion process. For Type-II, this point occurs at a length of only 1.1 mm, which is about half of that in Type-I. This is due to the lower loss in the Type-I interaction for similar wavelengths. Furthermore, the Type-I interaction outperforms the Type-II interaction by over an order of magnitude, which is also due to the greater parametric conversion efficiency coefficient. The Type-II interaction only produces 15 nW of idler power, which is nearly 13 dB less than the peak in the Type-I interaction. Output idler power reaches nearly 90 nW in the Type-I interaction after 2 mm. While this is larger than observed in experiments, it is still not large enough for practical use, particularly for telecommunications systems in which optical powers range from a few 100's of microwatts up to a few milliwatts. If instead it is assumed that the coupling coefficient is the same as that measured from the SHG experiments, the conversion efficiency increases by a factor of 43 for Type-I phase matching and the maximum generated idler power is calculated as 3.9 μ W. For Type-II phase matching under the same assumption, the maximum output power would be 0.88 μ W. Again, even these are too low for effective use in a typical communications system.

In order to reach input and output power levels for practical operation, external amplification can be added. Figure 6.10 shows the semiconductor parametric converter with EDFA's. A booster amplifier at the input raises the signal wavelength power to over 100 mW in order to stimulate sufficient idler generation. The preamplifier at the output amplifies the weak idler generated by the converter. Commercially available preamplifiers can boost power levels as low as -40 dBm (100 nW) by over 30 dB. Tunable filters can be added to isolate the signal and idler wavelengths after their respective amplifiers. While this solution does not represent a fully monolithic device, it does have a speed advantage over OEO conversion systems since all conversion and amplification is done all-optically. Thus, in this case, the purpose of the creating an integrated parametric device is to take advantage of the high internal circulation power of the onboard pump laser to boost the DFG process.

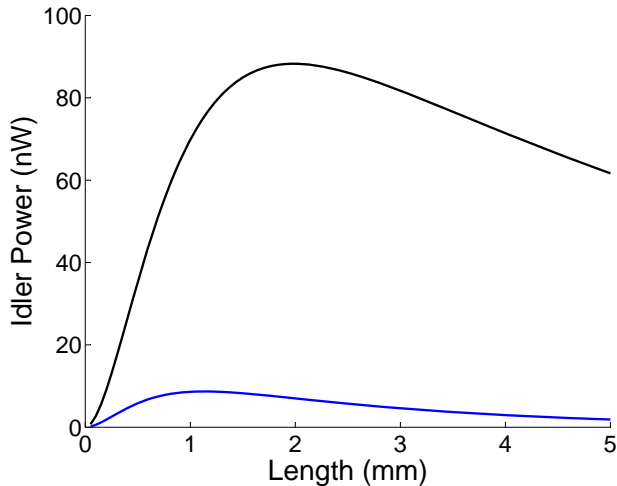


Figure 6.9: Simulated idler power generated in integrated parametric devices with different QPM waveguide lengths. Measured conversion efficiencies and linear loss values for Sample B were used in the calculation. Internal pump and signal powers were 300 mW and 50 mW respectively.

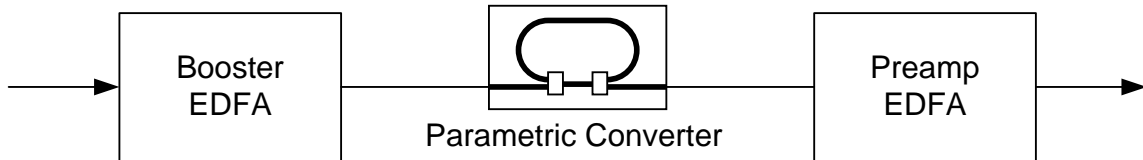


Figure 6.10: Schematic of all-optical wavelength converter based on an integrated parametric conversion device with a DD-QPM waveguide

Using Type-II phase matching requires additional considerations. For instance, the polarization states of the signal and idler will greatly affect the operation of the device. As seen in Figure 6.3, the center of the conversion band depends on the polarization of the input signal. Thus, the Type-II process is not polarization independent and the input signal can not be polarized arbitrary. Instead, the polarization that the signal should be set to depends on its wavelength. If the wavelength is longer than the phase matching peak, then the signal should be polarized TE, and vice versa.

The Type-II interaction has an advantage over Type-I that it is more naturally compatible with integration of an onboard pump since the laser will emit in the TE polarization. However, since Type-II phase matching does not have a polarization diversity advantage over Type-I phase matching for DFG, it becomes less attractive because of

its lower conversion efficiency. In this case, Type-I is the preferred configuration. To enable using Type-I with an onboard pump source, it would be necessary to convert the emitted TE mode of the laser to the TM mode before the QPM waveguide section of the cavity. Several compact waveguide-based polarization rotators have been developed [109, 110, 111] which could be used to rotate the pump wave into the TM polarization for the Type-I interaction in the DFG waveguide, and then back to the TE polarization when fed back into the gain section of the laser. Such devices have been demonstrated to have low losses of around 1-2 dB, which would not greatly impact the performance of the laser. In this manner, the high parametric conversion efficiency of the Type-I interaction can be taken advantage of in the integrated device.

6.4.2 Optical Parametric Oscillator

The parametric oscillator is an extension of the integrated parametric converter. As such, the device will benefit from the high circulating pump power in the integrated laser ring cavity. However, in order to achieve oscillation in the OPO ring, the QPM waveguide must not simply just act as a wavelength converter but must act as a parametric amplifier as well. The net parametric gain of the QPM waveguide must compensate for the linear losses of the cavity. In the integrated OPO design of Figure 1.2, the losses come from three primary sources: 1) the dichroic couplers, 2) the power tap on the outer side of the ring, and 3) propagation losses in the ring waveguide. The net power gain of the QPM waveguide will be generally less than unity for low pump power due to linear loss in the QPM waveguide itself. In a similar manner with laser systems, the net gain will increase with increasing pump power to the transparency point and then beyond. Oscillation occurs at some threshold pump power where the gain balances the loss. Thus, it is vitally important to estimate how much power is needed in order to reach this threshold.

In order to find the net gain of the QPM waveguide, several of the assumptions used in the model of the previous section cannot be used. In particular, amplification of the signal wave must be considered. Under the assumption that the pump loss by either depletion or linear loss is small, the signal and idler fields under phase matched conditions

are solved from Equation 6.2 as

$$A_s = \exp\left[\frac{1}{4}(\alpha_s + \alpha_i)L\right] \left[A_{s,0} \cosh[sL] + \frac{1}{s} \left[\frac{1}{2}g_s A_{i,0}^* + \frac{1}{4}(\alpha_i - \alpha_s) A_{s,0} \right] \sinh[sL] \right] \quad (6.8a)$$

$$A_i^* = \exp\left[\frac{1}{4}(\alpha_s + \alpha_i)L\right] \left[A_{i,0}^* \cosh[sL] + \frac{1}{s} \left[\frac{1}{2}g_i A_{s,0} + \frac{1}{4}(\alpha_s - \alpha_i) A_{i,0}^* \right] \sinh[sL] \right] \quad (6.8b)$$

where $A_{s,0}$ and $A_{i,0}$ are the initial signal and idler fields, $g_s = -j2\frac{\kappa}{\lambda_s}A_{3,0}$, $g_i = j2\frac{\kappa^*}{\lambda_i}A_{3,0}^*$, and $s = \frac{1}{4}\sqrt{(\alpha_s - \alpha_i)^2 + 4g_i g_s}$. In general, the single-pass gain in the signal wavelength depends on the initial value of the idler and vice-versa. However, depending on the configuration of the OPO, some simplifications can be made.

For an intracavity-pumped OPO, two configurations for the signal and idler waves exist: a singly-resonant oscillator (SRO), and a doubly-resonant oscillator (DRO). For the SRO, only the signal or idler wavelength is resonant in the cavity, but not both. In this case, the circulating signal power can be regarded as being much larger than the circulating power such that $A_{i,0} \approx 0$. Equation 6.8a can then be rearranged such that the parametric gain in the signal

$$G = \frac{|A_s|^2}{|A_{s,0}|^2} = \exp\left[\frac{1}{2}(\alpha_s + \alpha_i)L\right] \left[\cosh[sL] + \frac{1}{4s}(\alpha_i - \alpha_s) \sinh[sL] \right]^2. \quad (6.9)$$

If the losses in the signal and idler are the same, Equation 6.9 becomes [112],

$$G = \exp(-\alpha L) \cosh(\frac{1}{2}\sqrt{g_i g_s}L) \quad (6.10)$$

This is such the case for Type-I phase matching at the degeneracy wavelength. Using the experimentally determined value of κ for the 3.8 μm period QPM waveguide, the net gain of the signal over various pump powers can be predicted and is shown in Figure 6.11 for a 1 mm long waveguide. Here, the loss is given the experimental value of 1.5 cm^{-1} and the degeneracy (signal/idler) wavelength is 1581.7 nm. The black line represents the gain calculated using the κ value determined in DFG experiments. In this case, the gain does not even reach unity. The blue line represents the gain using the predicted κ value from

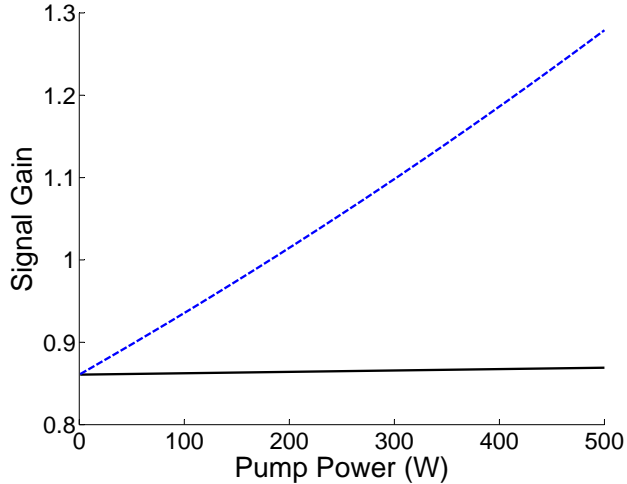


Figure 6.11: Predicted signal gain versus input pump power for Type-I phase matching in Sample B under the undepleted pump approximation. The black (solid) line represents the gain calculated using the κ value determined in DFG experiments. The blue (dashed) line represents the gain using the predicted κ value from SHG measurements.

SHG measurements. Assuming that this is the correct value for κ , the transparency level is reached at about 180 W and net positive gain is achieved for pump powers beyond.

The gain of the QPM waveguide can be improved by making it longer. To investigate this, it is assumed that the coupling coefficient from the SHG experiments is achievable for DFG, and that the pump depletion/loss is insignificant for lengths up to 5 mm. Figure 6.12 shows gain curves for several QPM waveguide lengths. Doubling the length of the waveguide from 1 mm approximately halves the transparency level. Moving to a 5 mm waveguide further reduces the transparency pump power to about than 40 W. However, increasing the QPM waveguide length will also increase length of the passive section of the ring cavity, and thus the total cavity loss. This will affect the threshold pump power for oscillation. By adding up the round-trip loss in the ring, the oscillation condition becomes

$$T_{\text{coupler}}^2 \times \exp[-\alpha_{\text{bend}} L_{\text{bend}}] \times \exp[-\alpha_{\text{straight}}(L_{\text{QPM}} + 2L_{\text{coupler}})] \times G = 1 \quad (6.11)$$

where T_{coupler} is the transmission through the dichroic couplers, α_{bend} and α_{straight} are the loss coefficients for the bent and straight sections of the ring, and L_{bend} , L_{QPM} ,

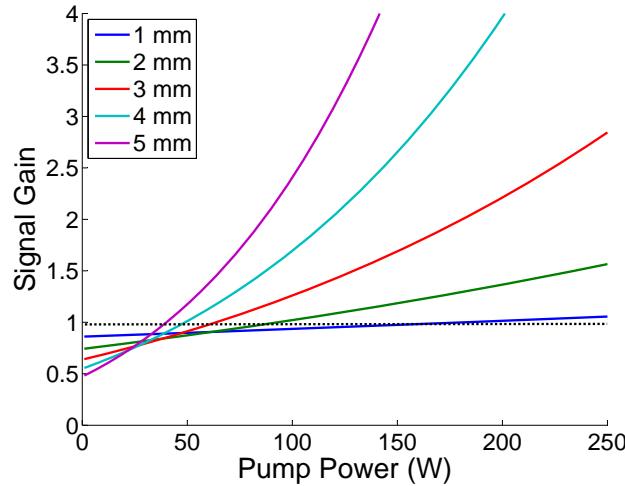


Figure 6.12: Predicted signal gain versus input pump power for Type-I phase matching in Sample B under the undepleted pump approximation for several different QPM waveguide lengths. The dashed line marks the transparency gain level.

and L_{coupler} are the lengths of the bends, QPM waveguide, and couplers, respectively. Figure 6.13 shows the threshold pump power required to meet this criteria for different QPM waveguide lengths. Here, α_{bend} was taken to be the same value as the loss coefficient in the QPM waveguide (1.5 cm^{-1}), while α_{straight} was given a value of 0.7 cm^{-1} which was measured from the fully as-grown test waveguides of Sample B. The length of the couplers was taken to be $220 \mu\text{m}$ as per the design by Younis [113]. The threshold power appears to be well over 1000 W for the shortest QPM waveguide length, but falls rapidly as the length is increased. At 5 mm , the threshold becomes a more reasonable 141 W . At longer lengths, the threshold power was observed to asymptotically approach a value of about 20 W , but only for lengths ten times longer than considered here. Such a long device is deemed impractical. For Type-II phase matching, under measured loss conditions for this case, the calculated threshold powers were up to an order of magnitude larger for similar QPM waveguide lengths. This is mostly attributed to the lower κ value for this interaction.

Lower pump power thresholds for the OPO can be achieved by moving to a DRO [9]. To gain insight on the possible performance improvement, the model of Equations 6.8 can be simplified under several assumptions. First, the OPO is assumed to operate near the degeneracy point such that $\lambda_s \approx \lambda_i$. Second, the loss coefficients for the signal and idler

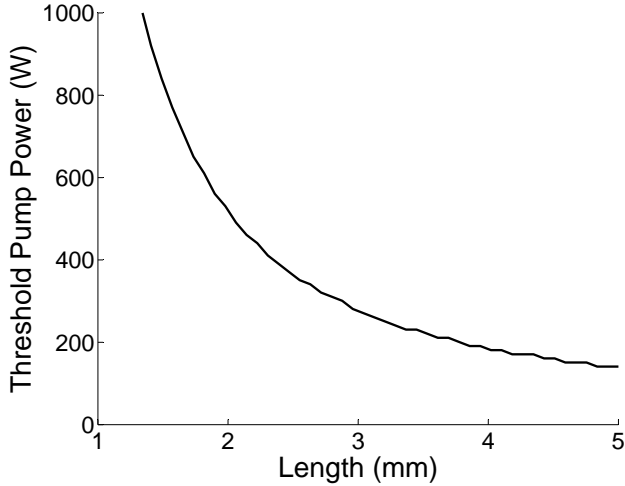


Figure 6.13: Predicted SRO OPO threshold pump powers for different QPM waveguide lengths

can be considered to be the same, which is reasonable for the Type-I interaction near degeneracy. Third, since the losses in the signal and idler are the same, then the initial amplitudes are such that $A_{s,0} = A_{i,0}$. Lastly, the pump, signal, and idler are assumed to have zero phase at the beginning of the QPM waveguide such that the initial value of the envelope functions $A_{x,0}$ are equal to their own complex conjugate. Under these assumptions and simplifications, the gain function for the signal becomes

$$G = \exp(-\alpha L) \cosh(\sqrt{g_i g_s} L). \quad (6.12)$$

The only difference between the DRO and SRO gain is that the argument to the cosh function is twice as large compared to the SRO case. Thus, the transparency pump power should be reduced by a factor of $\sqrt{2}$, and the threshold power for an OPO should drop similarly. For the 5 mm long QPM waveguide, the threshold power drops to about 100 W. While this is an improvement over the SRO threshold, DROs are inherently more difficult to operate due to instability and unpredictable tuning behaviour [114]. Thus, remaining discussions will focus on the SRO configuration.

The scenarios discussed so far have ignored pump loss for simplicity. However, unlike other material systems used for OPOs, pump losses were somewhat large for GaAs/AlGaAs superlattice waveguides. It is even more significant in the proposed inte-

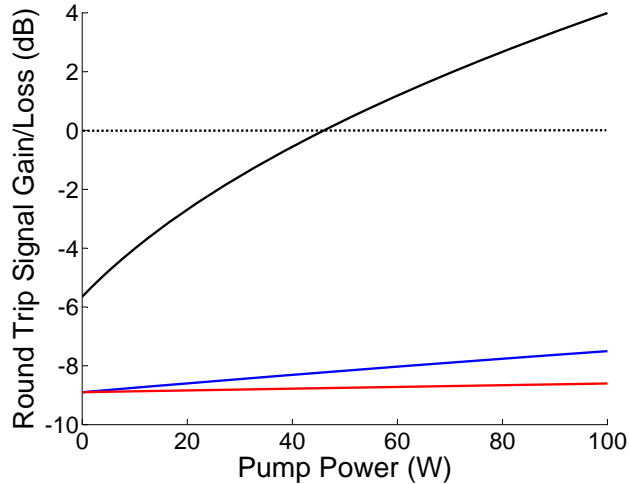


Figure 6.14: Predicted SRO OPO round trip signal gain with pump loss included for a QPM waveguide length of 5 mm in the Type-I DFG configuration. The measured pump loss was 13.25 cm^{-1} . The projected loss for the pump generated by an integrated laser source is 31 cm^{-1} .

grated design in which the pump wavelength will be close to the band gap energy of the as-grown superlattice. Unlike the DFG experiments discussed in this chapter, the pump wavelength will be shorter and experience larger absorption loss in the QPM waveguide. In order to estimate the impact of the pump loss, it was necessary to numerically solve Equation 6.2 as no simple analytical solution is forthcoming. The results of calculations for the round trip signal gain through the OPO ring are shown in Figure 6.14 for the Type-I case. The parameters used were the same as those for the $3.8 \mu\text{m}$ period Sample B waveguide. Coupling coefficients used were those measured from SHG experiments and the QPM waveguide length was set to 5 mm. The measured loss case shown uses the loss coefficient measured for the actual waveguide used in DFG and SHG experiments at a pump wavelength of 791.7 nm. Here, the pump power required for threshold is around 900 W, which is over ten times greater than in the lossless case. However, since 791.7 nm is below the band gap of the as-grown superlattice, the loss in this situation is an underestimate of the actual loss in the integrated device. The actual pump wavelength will be around 770 nm and the loss at this wavelength is estimated to be around 31 cm^{-1} according to Figure 3.7. For losses this high, threshold is not reached for pump powers below 1000 W. As this is the most realistic case, a workable device is unlikely.

In all cases for the OPO configuration, the threshold powers were on the order of 10's to 100's of Watts in simplistic cases, and over 1000 W for the most realistic case. Such power levels would not be feasible for an integrated continuous wave laser. However, even if it were possible to reach the lower threshold powers required for a 5 mm long waveguide, the pump laser current threshold would be very high due to the long length of the laser ring cavity, leading to increased power consumption. One possible means by which to achieve such high peak powers would be to mode-lock the onboard pump laser to produce pulses on the order of a few picoseconds. Such lasers have been demonstrated previously in semiconductors and are compatible with monolithic integration via quantum well intermixing [115, 116]. With a relatively low repetition rate of around 1 GHz, it would be possible to reach peak powers on the order of what is required to achieve parametric oscillation. However, several deleterious effects seen earlier when using short pulses would occur such as to stymie the performance of the parametric conversion process, perhaps precluding the ability to reach the OPO threshold. These include high-order nonlinear effects and group velocity mismatch, all of which played a role in reducing the efficiency of the SHG process. Also, the large linewidth of picosecond pump pulses may be too large, which would effectively cancel out some if not most of the efficiency increase, as was observed in DFG experiments where the pump was pulsed. Overall, achieving parametric oscillation using DD-QPM waveguides similar to those examined here would be very challenging, or perhaps not feasible with the current state of the technology. In order to obtain a working monolithic OPO device with practical power levels, several improvements must be made to the technology.

6.5 Design Improvements

Discussions of the potential device applications for DD-QPM waveguides showed that the current conversion efficiencies are too low for a practical device. This was especially the case for the integrated OPO, which was deemed to have threshold powers too high to even obtain a working device. However, several improvements could potentially raise the performance of superlattice DD-QPM waveguides such that practical devices can

be achieved. Optimization of the microfabrication processes could potentially reduce the scattering losses and increase modulation in $\chi^{(2)}$. Moving to high confinement waveguides could raise the optical intensity and the overlap area between the interacting waves of the DFG process. Lastly, employing vertical integration techniques could potentially improve performance of the integrated device and allow greater flexibility in setting the operating parameters for better efficiency. In this section, each of these paths to improvement are explored and the potential performance of an integrated device employing these methods will be evaluated.

6.5.1 Fabrication Optimization

In the course of creating the waveguide devices studied in this thesis, much work was done to improve the processes used to fabricate the QPM waveguides. However, while this resulted in samples that performed better than earlier generations, the samples were still suboptimal. This is evidenced in Figure 5.3b of Sample B, which shows significant sidewall and surface roughness. By comparison, Sample A had much less roughness and lower average linear loss coefficients. Furthermore, similar superlattice waveguide from a previous study had measured loss coefficients as low as 0.25 cm^{-1} for as-grown waveguides [81], three times less than those measured in Sample B. Other studies of GaAs/AlGaAs waveguides show that it is possible to bring the losses down even further [87, 117]. Thus, there is ample room for potential improvements in scattering loss. Such low loss could be achieved by improving the processes related to waveguide etching. This may include optimization of the lithographic patterning process and of the dry etching process.

Another major source of loss is the intermixing process. Loss coefficients in fully intermixed waveguides were at least two times larger than as-grown waveguide in Sample B. The source of this increased loss is the damage caused by the ion implantation process. While the rapid thermal annealing step is supposed to cause the crystal lattice to repair itself, many defects may still remain. It is thought that the annealing process is unable to properly get rid of aggregations of defects, which coalesce into larger defects leading to increased optical scattering. In DD-QPM waveguides, the larger loss of the intermixed regions raises the loss of the waveguide as a whole. Improvements to the intermixing

process may help to reduce the damage in the final waveguides. This will require further optimization and exploration of the parameter space for all of the steps involved in creating the QPM gratings, which includes the mask patterning, ion implantation, and annealing steps. It may also be necessary to modify the waveguide design to better accommodate the QWI process. For instance, the upper cladding layer could be modified so that it can be thinner such that lower implantation energies and ion doses can be used. Also, a thinner superlattice core could be used as it would require less ion dosage in order to achieve similar band gap energy shifts. However, a thinner core layer would trade off overlap of the optical modes with the superlattice layer, which would reduce the nonlinear coupling coefficient.

The QWI process also produces less band gap energy shift than anticipated. While it was larger than attempts in previous generations [79], the amount of shift in Samples A and B were still much lower than what has been achieved in similar GaAs/AlGaAs superlattice structures using IFVD [81]. As a result of the lower band gap shift, the suppression of $\chi^{(2)}$ was lower than expected as evidenced by the SHG experiments. This led to lower conversion efficiency and the high predicated OPO thresholds. Increasing the suppression of $\chi^{(2)}$ will require further optimization of the QWI process.

6.5.2 High Confinement Waveguides

One of the deficiencies of the QPM waveguides studied was that the coupling coefficient κ was low. This was due in part to the low effective $\chi^{(2)}$ value for the grating. While improving this requires process optimization, it can be compensated by changing the waveguide structure. One such change would be to move to a high confinement structure in which the modal area is reduced. As a result, the intensity of the propagating fields are increased for the same power levels. Since nonlinear interactions such as three-wave mixing are intensity dependent, the efficiency of the conversion process should increase. This concept has been applied to other nonlinear optical devices in different material systems in order to reduce the operating powers required to more practical levels [118, 119, 120].

A simple high confinement waveguide design is used here to demonstrate the potential

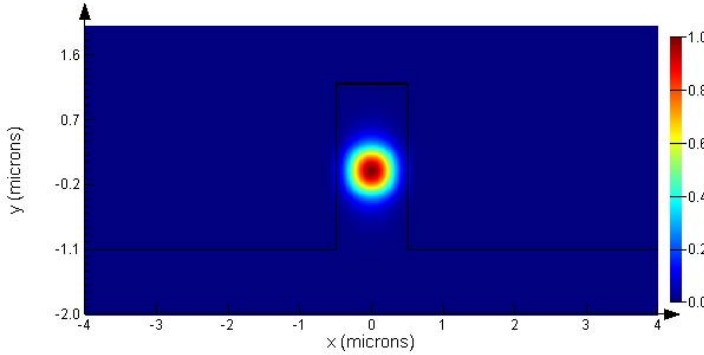


Figure 6.15: Optical mode profile of high confinement waveguide at 1550 nm in the TE polarization

improvement gained over the low confinement waveguides used in this study. The layer structure of Figure 3.1 is modified to contain the optical mode at 1550 nm almost entirely within the superlattice core. This can be done by removing the buffer layers and changing the cladding layers to $\text{Al}_{0.85}\text{Ga}_{0.15}\text{As}$ to provide a larger vertical index contrast. As these layers were originally designed for improving external end-fire coupling efficiency, they are not necessary in a fully integrated OPO device anyway. Furthermore, waveguide nanotapers [121] can be used to facilitate efficient end-fire coupling into high-confinement waveguides instead without compromising waveguide design. The waveguide can also be etched deeper such that there is air on either side of the waveguide to provide a larger index contrast in the horizontal direction. Lastly, the waveguide ridge can be narrowed to 1 μm such as to squeeze the optical mode into a smaller area. This also reduces the number of transverse modes such that the waveguide is nearly single-mode. Figure 6.15 shows the resulting TE polarized mode profile at 1550 nm for such a waveguide. Here, 77% of the optical power is confined to the superlattice layer compared to 62% in the shallow etched waveguides discussed in Chapter 3. The effective overlap area with the 775 nm fundamental mode reduces to $0.68 \mu\text{m}^2$, which is an 88% reduction. As a result, κ increases by a factor of 2.9 and the normalized conversion efficiency rises by nearly an order of magnitude. Further enhancement could be achieved with more rigorous design of the waveguide structure, however, the simple design presented here at least demonstrates the potential of such waveguides.

Moving to a high confinement structure has its merits, but there are several tradeoffs

that must be considered. First, the described structure is multimode at 775 nm and is thus likely to have higher losses, especially around waveguide bends. However, note that it is only necessary to use a high confinement waveguide in the QPM waveguide section of the integrated device. Other sections of the pump laser cavity where high confinement is not necessary could be designed with shallow etches. Second, etching into the core layer will expose more of the guided optical mode to sidewall roughness and thus increase scattering losses. However, low loss coefficients of less than 0.2 cm^{-1} has been demonstrated in high confinement SOI waveguides using oxidation techniques [122]. Similar techniques for reducing sidewall roughness have been explored for AlGaAs ridge structures [123]. Third, the effective index of the high confinement waveguides can become very sensitive to variations in the waveguide width. As a result, the phase matching wavelengths will be strongly affected by the waveguide width. This phenomenon has been demonstrated in high confinement form-birefringent AlGaAs waveguides with phase matching wavelength shifts of up to 100 nm for width variations of 100 nm [45]. Thus, fabrication procedures must be tightened to reduce deviations from the intended dimensions from one sample to the next. Lastly, while the large optical intensities in a high confinement structure would enhance the second-order nonlinear interaction, it would also strengthen higher-order nonlinear effects. Thus, SPM, TPA, and 3PA would become significant at lower power levels and interfere with the DFG process.

6.5.3 Vertical Integration

The waveguide structure developed and studied here was a compromise to facilitate integration of the pump laser and QPM waveguide. However, these compromises led to two problems that are unlikely to be overcome in the current wafer design. First, the absorption losses at the pump wavelength proved to be too high in order to allow efficient operation of the QPM waveguide as an amplifier. Indeed, DFG experiments had to be conducted with waveguides in which the degeneracy pump wavelength used was below the band gap energy where absorption losses are low. However, the pump wavelength will be near or at the band gap energy of the as-grown superlattice and absorption in the QPM waveguide will be high. As a result, OPO thresholds are predicted

to be too high for practical operation. One solution would be to partially intermix the as-grown regions of the QPM grating, but this would tradeoff modulation in $\chi^{(2)}$. Second, fabrication of a working diode laser by colleagues using the same wafer structure proved futile as even simple broad-area and ridge lasers failed to reach threshold. The problem was thought to be thickness of the superlattice layer, which is relatively large compared to conventional bulk-layer laser diode structures in which the active layer thickness is generally less than 100 nm thick. The solution to this problem was to reduce the superlattice thickness, and indeed, working ridge waveguide Fabry-Perot lasers were demonstrated [113]. However, thinning the core layer trades off confinement and overlap between the interacting waves of the parametric conversion process. Another solution must be sought in order to alleviate these difficulties.

One possible solution to the integration problem is to use vertical integration [124]. In this technique, the active and passive sections of the integrated device are separated into different waveguiding layers. Light is coupled between the active and the passive layers using taper structures. Figure 6.16 depicts a simplified structure for integrating a DD-QPM waveguide with a pump laser using vertical integration. The active region of the pump laser is located in the upper layer, while the QPM waveguide is located in the lower layer. Each layer is optimized for the particular devices to be contained within it. For instance, the active layer can be designed as a double quantum well structure with a thin core optimized to reduce the threshold current for lasing. The passive layer can be designed such that the core layer is thick to provide high overlap between the pump, signal, and idler waves of the parametric conversion process. Furthermore, the passive superlattice in this layer would be designed to have a band gap energy larger than the active layer such that absorption of the pump light is minimized. Lastly, only the active layer need be doped while the passive layer can be left undoped, which would avoid free-carrier absorption losses in the QPM waveguide. This relative independence in designing each layer adds much flexibility and potentially better performance from the system as a whole.

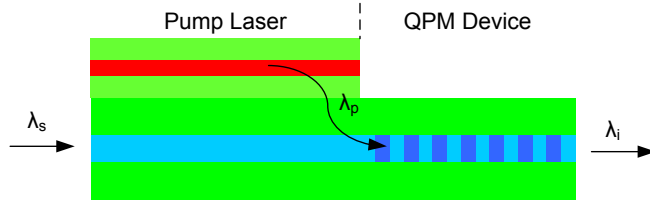


Figure 6.16: Simplified schematic of a vertical integration structure. The pump laser active sections would be located in the upper layer while the QPM device and passive sections would be located in the lower layer.

6.5.4 Potential Device Performance

The proposed design improvements in the previous sections open the possibility of better performance of an integrated conversion device. For each of the proposed changes, approximations of the QPM waveguide characteristics can be made. Optimization of the fabrication procedures could reduce the loss coefficients to the same level as those observed in silicon nanowaveguides. In this case, the loss at wavelengths around 1550 nm will be assumed to be 0.2 cm^{-1} for as-grown superlattice. Intermixed waveguides showed loss coefficients about twice as high as in as-grown waveguides, thus the loss for intermixed sections are assumed to be 0.4 cm^{-1} . Thus, the average loss coefficient for a 50:50 duty cycle QPM grating is 0.3 cm^{-1} . Scattering losses near the pump wavelength were originally measured to be four times larger than at pump wavelengths near 775 nm, thus giving losses of 1.2 cm^{-1} . Absorption losses for the pump are assumed to be negligible for a vertically integrated structure in which the superlattice band gap is larger than the photon energies emitted by the pump laser in the active layer. Improvements in the intermixing process are assumed to lead to an increase in $\chi_{\text{eff}}^{(2)}$ by a factor of two. From these approximations, the potential performance of an optimized integrated device can be calculated.

The optical parametric converter is examined first. As in Section 6.4.1, it is assumed that the pump is undepleted by the parametric process and that the signal is not amplified such that Equation 6.7 applies. Four different cases are considered:

1. Original measured values of signal/idler loss, projected pump loss at 770 nm, and

- originally measured $\chi_{\text{eff}}^{(2)}$
2. Reduced losses in signal/idler wavelengths only
 3. Vertically integrated structure with reduced losses in signal/idler wavelengths and no pump absorption loss
 4. Vertically integrated structure with reduced losses in signal/idler wavelengths, no pump absorption loss, and doubled $\chi_{\text{eff}}^{(2)}$

The predicted idler powers are shown in Figure 6.17 for Type-I phase matching with a signal power of 50 mW and a pump power of 300 mW. In all cases, the nominal κ is set to the measured value determined from SHG experiments. Reducing the losses in the signal and idler improve the output idler power marginally, as can be seen in the difference between Case 1 and Case 2. A much more significant improvement is observed in Case 3 where the pump loss has been improved as well. Here, the idler power is over an order of magnitude better than in Case 2 at just below 3 mm where Case 2 peaks. Also, no peak is found for Case 3 with the 5 mm QPM waveguide length considered. At 5 mm, the output power is -6.9 dBm (0.20 mW), which is well within the practical range for telecommunications systems. The improvement in $\chi^{(2)}$ of Case 4 raises the output power by an additional 6 dB. Reducing the signal power to 5 mW would only reduce the idler power down to -10.9 dBm for Case 4, which is still well within detectable ranges for telecommunications-grade optical receivers. In this case, high power EDFA's would not be required in certain system configurations and the parametric converter could operate on its own.

An OPO would also realize similar performance improvements. For the analysis, the full model including pump losses and signal amplification is used as per Equation 6.2. Figure 6.18 shows the round trip signal gain/loss for an SRO under the same improvement cases as examined for the the parametric converter. Simply reducing the losses in the signal and idlers as per Case 2 does not improve the OPO performance such that the threshold pump power is below 100 W. Instead, it is necessary to implement the vertically integrated structure as in Case 3 in order to reduce the pump loss. In this case, the threshold power is found at around 33 W. If the modulation in $\chi^{(2)}$ is doubled via QWI improvements in Case 4, a threshold power of around 8 W is possible. Even with such

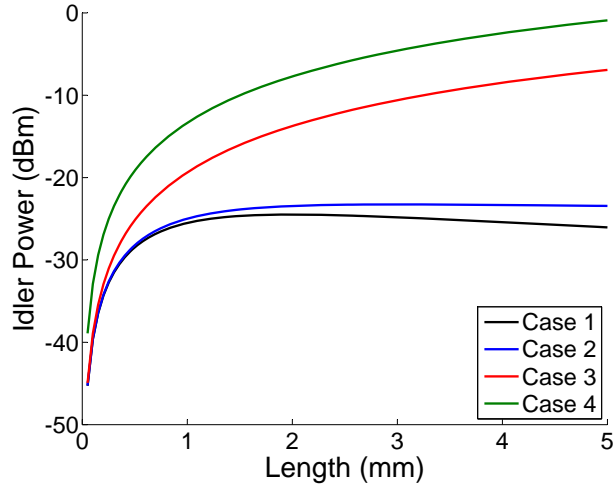


Figure 6.17: Output power from a potential integrated parametric converter with improvements under different cases

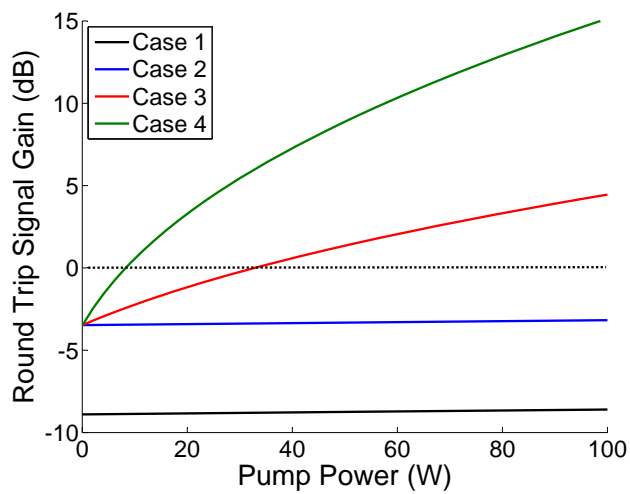


Figure 6.18: Round trip signal gain in a potential integrated singly-resonant OPO with improvements under different cases

improvements, the threshold power levels are still above 1 W, which would necessitate implementation of a mode-locked pump laser instead of a simple continuous wave laser. However, the reduction in peak power required would allow the use of longer pulses with narrower spectral widths.

6.6 Conclusions

This chapter examined difference frequency generation in DD-QPM waveguides and their application to integrated wavelength conversion devices. By using data from the second-harmonic generation experiments of the Chapter 5, the DFG conversion bands and conversion efficiency were calculated using simplified models. When the pump wavelength was placed at the degeneracy point, the conversion band for Type-I was found to be relatively flat and had a bandwidth over 150 nm covering the C-, L-, and U-bands. Deviations larger than 0.2 nm caused significant changes to the conversion band shape and shifted the peak conversion points. The conversion bands for Type-II were polarization dependent and not flat. Experiments with Sample B waveguides demonstrated phase matched DFG for both Type-I and Type-II interactions by using continuous wave beams for both the signal and pump. By using C-band wavelengths for the input signal, idler wavelength were observed in the L- and U-bands. Nearly 9 nW of idler power was produced for Type-I phase matching, which was below the predicted value of over 50 nW given the input powers used. The Type-II configuration produced lower powers as expected, but also fell short of predictions. As a result, the conversion efficiencies and coupling coefficients were lower than originally calculated using SHG data. Using the results from both DFG and SHG experiments, monolithically integrated wavelength conversion devices using DD-QPM waveguides were modeled in order to gain insights on their potential performance. For a parametric converter, integrating a pump laser on board the chip and exploiting the intracavity circulating power would lead to greater amounts of idler power being generated. However, high linear losses in signal, idler, and especially the pump were found to significantly limit the performance of this device. Thus, external amplification of the signal and idler would be required in order reach the required power levels in a typical telecommunications system. Analysis of a monolithically integrated optical parametric oscillator concluded that reaching the threshold for oscillation would require unreasonably high pump powers. Thus, in the current state of the DD-QPM technology, practical integrated wavelength conversion devices were deemed unfeasible. Several improvements to the design and fabrication of an integrated device were pro-

posed. Scattering losses could be reduced with improvements to the microfabrication processes and $\chi^{(2)}$ modulation could be increased via further optimization of the QWI procedure. Transitioning to high confinement waveguides could improve modal overlap and raise the optical intensity in order to boost the nonlinear interaction. Lastly, vertical integration could allow greater flexibility by allowing both the pump laser and the QPM waveguide design to be optimized separately, and reduce pump losses in the QPM waveguide. With these improvements, both the parametric converter and the OPO were predicted to allow more practical power levels. Thus, there is still good potential for using DD-QPM superlattice waveguides for integrated wavelength conversion devices.

Chapter 7

Conclusions

7.1 Summary of Results

This thesis examined second-order nonlinear wavelength conversion processes using domain-disordered quasi-phase matched GaAs/AlGaAs superlattices-core waveguides. The purpose of this study was to evaluate the potential for creating compact all-optical wavelength conversion devices in a monolithically integrated form. Such a device would have wide ranging applications in a number of fields, and provided a low cost and robust alternative to current wavelength conversion technologies.

Several phase matching techniques applied to compound semiconductors, including DD-QPM, were compared and discussed. These included artificial form birefringence, modal phase matching, exact phase matching using Bragg reflection waveguides, domain-reversal quasi-phase matching, and domain-suppression quasi-phase matching. By using equations for the normalized conversion efficiency and the effective instantaneous conversion efficiency, it was found that most of these methods outperform previous generations of DD-QPM waveguides. However, most of these other methods had high inherent linear losses and were built on platforms that were poor candidates for monolithic integration of a pump laser diode, which is one of the key purposes of AlGaAs as the base material. In contrast, DD-QPM is more amenable to integration and has shown significant improvement in conversion efficiency over the last few years due to advancements in wafer design and fabrication processes.

A new superlattice wafer structure was designed to alleviate problems encountered with previous designs, but at the expense of less potential modulation in the band gap energy. Photoluminescence measurements showed that the shift in band gap energy using the ion-implantation quantum well intermixing was about 38% less than the theoretical maximum and thus the superlattice was not completely intermixed. Computation of the optical mode profiles for ridge waveguides revealed poor confinement of wavelengths around 775 nm when using shallow etches, which motivated study of using more deeply-etch waveguides to achieve better confinement. Loss measurements around 775 nm showed that the absorption loss coefficients were large below 800 nm and that the preferred operating range the second-harmonic/pump wavelength in experiments is above 800 nm. Kerr, two-photon absorption, and three-photon absorption coefficients of the superlattice measured and calculated by previously established methods were found to be highly polarization dependent and were suppressed by up to 71% after intermixing. Depending on the operating wavelength, these high-order nonlinear effects were found to be strong enough that they could affect the second-order nonlinear processes.

Advanced models and computer simulations were used to predict the performance of second-harmonic generation in DD-QPM waveguides with several parasitic effects present. Linear losses were found to reduce the conversion efficiency by a significant amount, with the fundamental wavelength losses causing twice as much reduction as the second-harmonic losses. The SHG conversion bandwidth was calculated to be less than 3 nm for 1 mm-long waveguides, and was affected by the total length of the waveguide, linear losses, and the duration of ultrafast pulses. Suboptimal suppression of $\chi^{(2)}$ in disordered domains was found to significantly reduce the conversion efficiency below the maximum theoretical value. Of the high-order nonlinear effects, self-phase modulation was the dominate effect on second-harmonic power at high power reducing efficiency by up to 66%, while two-photon absorption contributed a much smaller reduction and three-photon absorption had no significant impact. Group velocity mismatch had a modest impact of up to 6% on the output second-harmonic power, and was slightly larger in the Type-II configuration.

Improved processes for fabricating DD-QPM waveguides were developed by colleagues

at the University of Glasgow. This lead to waveguides with lower linear loss coefficients of around 1.5 cm^{-1} at 1550 nm and larger band gap energy shifts in intermixed domains. As a result, SHG performance was improved over past generations of superlattice DD-QPM waveguides by over a factor of 2 when using 2 ps pulses. Type-II phase matched SHG was demonstrated for the first time in DD-QPM waveguides, but had an efficiency that was four times less than Type-I. High-order nonlinear effects caused saturation of the generated second-harmonic power, and resulted in significant reductions of the conversion efficiency at high input power. Continuous wave SHG was also achieved for the first time in DD-QPM structures, but the conversion efficiencies were not as high as in the 2 ps pulsed experiments. Several bistability effects were observed with temporal response times on the order of a few seconds, which was attributed to absorption and the thermo-optic effect. Experiments with 20 ps pulses gave results in which the conversion efficiency was more consistent over a wide range of power levels and did not show saturation in the generated second-harmonic power. Using such longer pulses may allow greater powers to be generated than with shorter pulses.

Difference frequency generation in DD-QPM waveguides was examined next. Using the data from SHG experiments and simplified modes of three-wave mixing, predictions were made on the conversion bandwidth and efficiency of the DFG process. It was found that the conversion band changed drastically with small detunings of the pump wavelength, and that the Type-II conversion bands were also polarization dependent. In DFG experiments using continuous wave beams, both Type-I and Type-II phase matching was observed with conversion ratios of up to -67.5 dB and output idler powers of nearly 9 nW. When the experimental data was applied to models of a parametric conversion device integrated with an onboard pump source, it was found that the output idler power would be on the order of hundreds of microwatts and thus external amplification would be necessary. An optical parametric oscillator based on the present device performance would require large pump powers on the order of hundreds of Watts that would unlikely be achievable with an onboard source. In order to improve performance, several improvements to the QPM waveguide were proposed including improving fabrication processes, utilizing high confinement waveguides, and implementing vertical integration. With these

improvements, the parametric converter could potentially produce usable power levels and the OPO could have lower threshold powers that are achievable by using an onboard mode-locked pump laser. Thus, GaAs/AlGaAs superlattice-based DD-QPM waveguides still hold potential for allowing practical monolithically integrated wavelength conversion devices based on second-order nonlinear optical effects.

7.2 Future Work

The work presented in this thesis showed the largest SHG conversion efficiencies of all previous work on DD-QPM waveguides, and demonstrated Type-II phase matching, continuous-wave SHG, and DFG for the first time in this technology. However, as plainly stated in the summary of the results, wavelength conversion devices based on this technology in its present form are not practical. In order to make such devices viable, much work must be done to improve performance and demonstrate new operating regimes not covered in this thesis.

Despite the lower than expected performance observed with the QPM samples reported here, development on fabrication has been ongoing by colleagues in Glasgow. Working lasers have been demonstrated using a modified wafer design, which permitted practical threshold currents. Integrated converter and OPO devices with onboard pump laser rings have been fabricated. Several experiments will be required once these devices are ready for testing. One such experiment would be to determine the phase matching wavelengths of different QPM periods for the modified wafer design. The methods, data and analysis from this thesis will provide direction for this effort.

Continuous-wave experiments were conducted with samples that demonstrated bistability due to the thermo-optic effect and the Fabry-Perot cavity created by the reflective end-facets. As a result, it was difficult to obtain reliable data on the conversion efficiency under continuous-wave operation. One possible solution is to suppress the Fabry-Perot effect, which can be done by applying antireflection coatings to the facets or by patterning the waveguides at a small angle relative to the facet. New continuous-wave experiments can then be performed, and perhaps provide better data from which to evaluate the

second-order nonlinear coefficients of the superlattice.

Experiments with the 20 ps pulse source were fraught with problems related to the stability of the wavelength produced by the OPO. While mitigation of high-order nonlinear effects was observed, the effective instantaneous conversion efficiencies were still lower than in the 2 ps pulse experiments. These experiments should be repeated with newly available all-fiber-based pulsed sources that have superior wavelength stability.

Evaluation of the device performance required knowledge of the losses at the second-harmonic/pump wavelengths. Data on this was obtained using a combination of transmission measurements with the Ti:sapphire laser and a tunable source at 980 nm, but the accuracy of this method is not as good as using an all-Fabry-Perot method. It would be beneficial to obtain an appropriate narrow linewidth tunable source around 775 nm in order to perform Fabry-Perot measurements.

One of the target applications of superlattice DD-QPM technology was to generate mid-infrared wavelengths. Experiments should be carried out to demonstrate this using DFG with external pumping. This will require modeling of the behaviour of the waveguides at long wavelengths. However, the refractive index models used for the superlattice were based on measurements for wavelength only up to 1600 nm and their validity at longer wavelengths is uncertain. Thus, new measurements of the refractive index of the superlattice at longer wavelength may be required. In order to demonstrate mid-infrared generation, new equipment will be necessary including a shorter wavelength signal laser with sufficient power to drive DFG, and appropriate optics and detectors to observe wavelengths beyond 2.0 μm . If mid-infrared generation is achieved, experiments demonstrating gas detection should be performed to show the potential of this technology.

In Section 6.5, several improvements to the DD-QPM platform were discussed. These included improving fabrication processes for lower loss, obtaining a large differential band gap energy shift via improved QWI processes, moving to high-confinement waveguides to raise internal intensities, and moving to vertically integrated structures to reduce pump loss and increase design flexibility. To realize the full potential of an integrated device, all of these improvements should be pursued. All of this will require considerable effort,

especially in developing the required microfabrication processes. However, such efforts are warranted as superlattice DD-QPM is still predicted by the conclusions of this thesis to be a viable technology for compact nonlinear wavelength conversion devices.

Appendix A

Nonlinear Propagation Equations

The following derivation is based on works by Zheng [125], Kurz [126], and Agrawal [92]. For generality, nonlinear susceptibilities are initially taken to be functions of the transverse directions x and y as would be the case in a multilayered waveguiding structure. Otherwise, the waveguide structure will be viewed as an “effective medium” with all other material parameters being uniform in the transverse directions.

A.1 Three-Wave Mixing

Starting with the wave equation for a sourceless, non-magnetic, and lossy medium:

$$\nabla^2 \vec{E} - \mu_0 \epsilon \frac{\partial^2 \vec{E}}{\partial t^2} - \mu_0 \sigma \frac{\partial \vec{E}}{\partial t} - \mu_0 \frac{\partial^2 \vec{P}_{NL}}{\partial t^2} = 0 \quad (\text{A.1})$$

The nonlinear polarization is

$$\vec{P}_{NL} = \epsilon_0 [\overleftrightarrow{\chi}^{(2)} : \vec{E} \vec{E} + \overleftrightarrow{\chi}^{(3)} : \vec{E} \vec{E} \vec{E} + \overleftrightarrow{\chi}^{(4)} : \vec{E} \vec{E} \vec{E} \vec{E} + \overleftrightarrow{\chi}^{(5)} : \vec{E} \vec{E} \vec{E} \vec{E} \vec{E} ...]. \quad (\text{A.2})$$

Assuming that the participating waves are linearly polarized, propagating in the z-direction, and that the medium is linearly isotropic, the wave equation can be scalarized. Furthermore, if the polarization directions of the participating waves are set to give a valid interaction, the nonlinear susceptibility tensors of Eqn. A.1 can be reduced to scalar

values $\chi^{(2)}$ and $\chi^{(3)}$.

For generalized three-wave mixing, the total electric field is

$$E = E_1 + E_2 + E_3 \quad (\text{A.3})$$

where

$$E_i = \frac{1}{2} \left[\tilde{E}_i(x, y, z, t) \exp[j(\omega_i t - \beta_{0,i} z)] + c.c. \right] \quad (\text{A.4})$$

Substituting Eqn. A.3 into the scalarized Eqn. A.1, accounting for permutation symmetry in $\chi_{ijk}^{(2)}$, and forcing the frequency matching condition $\omega_3 = \omega_1 + \omega_2$, the second-order nonlinear polarization, $P_{NL}^{(2)} = \epsilon_0 \chi^{(2)} E E$, becomes

$$P_{NL,1}^{(2)} = \epsilon_0 \chi^{(2)} \tilde{E}_2^* \tilde{E}_3 \quad (\text{A.5a})$$

$$P_{NL,2}^{(2)} = \epsilon_0 \chi^{(2)} \tilde{E}_1^* \tilde{E}_3 \quad (\text{A.5b})$$

$$P_{NL,3}^{(2)} = \epsilon_0 \chi^{(2)} \tilde{E}_1 \tilde{E}_2. \quad (\text{A.5c})$$

For the third-order nonlinear polarization, if only self-phase modulation and two-photon absorption are considered, for each wave,

$$P_{NL,i}^{(3)} = \frac{3}{4} \epsilon_0 [\chi_i'^{(3)} + j \chi_i''^{(3)}] |\tilde{E}_i|^2 \tilde{E}_i. \quad (\text{A.6})$$

The real component of $\chi_i^{(3)}$ is related to SPM and the imaginary component is related to TPA. The fourth-order nonlinear polarization is assumed to be weak relative to the second-order nonlinear polarization and is thus neglected. For the fifth-order nonlinear polarization, the real part of the susceptibility is assumed to be weak relative to the third-order nonlinearity. However, the imaginary part of the susceptibility is considered significant as it is related to three-photon absorption which dominates over two-photon absorption at photon energies below the half band gap energy. Thus, the fifth-order nonlinear polarization is

$$P_{NL,i}^{(5)} = \frac{5}{8} \epsilon_0 [j \chi_i''^{(5)}] |\tilde{E}_i|^4 \tilde{E}_i. \quad (\text{A.7})$$

The wave equations for propagation along the z-direction become

$$\frac{\partial^2}{\partial z^2} \tilde{E}_i - \mu_0 \epsilon \frac{\partial^2}{\partial t^2} \tilde{E}_i - \mu_0 \sigma \frac{\partial \tilde{E}}{\partial t} - \mu_0 \frac{\partial^2}{\partial t^2} (P_{NL,i}^{(2)} + P_{NL,i}^{(3)} + P_{NL,i}^{(5)}) = 0. \quad (\text{A.8})$$

Taking the Fourier transform of Eqn. A.8 gives,

$$\frac{\partial^2 \hat{E}_i}{\partial z^2} + \mu_0 \epsilon(\omega) \omega^2 \hat{E}_i + \mu_0 \sigma \omega \hat{E}_i + \mu_0 \omega^2 (\hat{P}_{NL,i}^{(2)} + \hat{P}_{NL,i}^{(3)} + \hat{P}_{NL,i}^{(5)}) = 0. \quad (\text{A.9})$$

Assuming that the nonlinear effects are weak enough such that the transverse mode distribution does not change over the propagation through the waveguide, the electric fields, \hat{E}_i , can be decomposed into the mode distribution, $F_i(x, y)$, and the spectral envelope, $\hat{A}_i(z, \omega - \omega_i)$, such that

$$\hat{E}_i(x, y, z, \omega - \omega_i) = \gamma_i F_i(x, y) \hat{A}_i(z, \omega - \omega_i) \exp[-j\beta_{0,i}z] \quad (\text{A.10})$$

where

$$\gamma_i = \left[\frac{2}{c \epsilon_0 n_i} \right]^{\frac{1}{2}} \quad (\text{A.11})$$

and F is complex in general and is normalized such that

$$\int_{-\infty}^{\infty} \int_{-\infty}^{\infty} |F_i(x, y)|^2 dx dy = 1. \quad (\text{A.12})$$

By using this definition, $A(z, \omega - \omega_i)$ has units of $\text{W}^{\frac{1}{2}}$ and thus represents the power of the envelope. We can substitute Eqn. A.10 into Eqn. A.9. Starting with the z-derivative term

$$\frac{\partial^2 \hat{E}_i}{\partial z^2} = \gamma_i F_i(x, y) \left[\frac{\partial^2 \hat{A}_i}{\partial z^2} \exp[-j\beta_{0,i}z] - j2\beta_0 \frac{\partial \hat{A}_i}{\partial z} \exp[-j\beta_{0,i}z] - \beta_{0,i}^2 \hat{A}_i \exp[-j\beta_{0,i}z] \right]. \quad (\text{A.13})$$

By the slowly varying envelope approximation,

$$\frac{\partial^2 \hat{A}_i}{\partial z^2} \ll \frac{\partial \hat{A}_i}{\partial z}, \frac{\partial^2 \hat{A}_i}{\partial z^2} \ll \hat{A}_i \quad (\text{A.14})$$

and thus,

$$\frac{\partial^2 \hat{E}_i}{\partial z^2} = \gamma_i F_i(x, y) \left[-j2\beta_0 \frac{\partial \hat{A}_i}{\partial z} \exp[-j\beta_{0,i}z] - \beta_{0,i}^2 \hat{A}_i \exp[-j\beta_{0,i}z] \right] \quad (\text{A.15})$$

The linear term of Eqn. A.9 becomes

$$\mu_0 \epsilon(\omega) \omega^2 \hat{E}_i = \frac{\omega^2 n_i^2(\omega)}{c^2} \hat{E}_i \quad (\text{A.16})$$

$$= \beta_i^2(\omega) \gamma_i F_i \hat{A}_i \exp[-j\beta_{0,i}z]. \quad (\text{A.17})$$

Combining the terms together gives

$$\begin{aligned} \gamma_i F_i \exp[-j\beta_{0,i}z] & \left[-j2\beta_{0,i} \frac{\partial \hat{A}_i}{\partial z} - \left(\beta_{0,i}^2 - \beta_i^2(\omega) \right) \hat{A}_i - j\mu_0 \sigma \omega \hat{A}_i \right] + \\ & \mu_0 \omega^2 (\hat{P}_{NL,i}^{(2)} + \hat{P}_{NL,i}^{(3)} + \hat{P}_{NL,i}^{(5)}) = 0 \quad (\text{A.18}) \end{aligned}$$

Expanding $\beta_i(\omega)$ into a Taylor series up to second order gives

$$\beta_i(\omega) = \beta_{0,i} + \beta_{1,i}(\omega - \omega_i) + \frac{1}{2} \beta_{2,i}(\omega - \omega_i)^2 \quad (\text{A.19})$$

where

$$\beta_{0,i} = \beta(\omega) \Big|_{\omega_i}, \beta_{1,i} = \frac{\partial \beta_i(\omega)}{\partial \omega} \Big|_{\omega_i}, \beta_{2,i} = \frac{\partial^2 \beta_i(\omega)}{\partial \omega^2} \Big|_{\omega_i}. \quad (\text{A.20})$$

Using the approximation $a^2 - a_0^2 \approx 2a_0(a - a_0)$ and Eqn. A.20, the dispersive term of Eqn. A.18 becomes

$$\begin{aligned} 2\gamma_i \beta_{0,i} F_i \exp[-j\beta_{0,i}z] & \left[-j \frac{\partial \hat{A}_i}{\partial z} + \beta_{1,i}(\omega - \omega_i) \hat{A}_i + \frac{1}{2} \beta_{2,i}(\omega - \omega_i)^2 \hat{A}_i - j \frac{\mu_0 \sigma \omega}{2\beta_{0,i}} \hat{A}_i \right] + \\ & \mu_0 \omega^2 (\hat{P}_{NL,i}^{(2)} + \hat{P}_{NL,i}^{(3)}) = 0. \quad (\text{A.21}) \end{aligned}$$

Converting back to the time domain and rearranging gives,

$$F_i \left[\frac{\partial A_i}{\partial z} + \beta_{1,i} \frac{\partial A_i}{\partial t} - j \frac{1}{2} \beta_{2,i} \frac{\partial^2 A_i}{\partial t^2} + \frac{\alpha_{0,i}}{2} A_i \right] + j \frac{\mu_0 \omega_i^2}{2 \gamma_i \beta_{0,i}} (P_{NL,i}^{(2)} + P_{NL,i}^{(3)} + P_{NL,i}^{(5)}) \exp[j\beta_{0,i}z] = 0 \quad (\text{A.22})$$

where $\alpha_{0,i}$ is the linear loss coefficient defined as

$$\alpha_{0,i} = \frac{\mu_0 \sigma c}{n_{0,i}}. \quad (\text{A.23})$$

The second-order nonlinear terms can now be expanded out while using the inverse Fourier transform of Eqn. A.10

$$P_{NL,1}^{(2)} = \epsilon_0 \chi^{(2)} \gamma_2 \gamma_3 F_2^* F_3 A_2^* A_3 \exp[-j(\beta_{0,3} - \beta_{0,2})z] \quad (\text{A.24a})$$

$$P_{NL,2}^{(2)} = \epsilon_0 \chi^{(2)} \gamma_1 \gamma_3 F_1^* F_3 A_1^* A_3 \exp[-j(\beta_{0,3} - \beta_{0,1})z] \quad (\text{A.24b})$$

$$P_{NL,3}^{(2)} = \epsilon_0 \chi^{(2)} \gamma_1 \gamma_2 F_1 F_2 A_1 A_2 \exp[-j(\beta_{0,1} + \beta_{0,2})z]. \quad (\text{A.24c})$$

Using the definitions

$$\chi_i'^{(3)} = \frac{4}{3} n_{0,i}^2 c \epsilon_0 n_{2,i} \quad (\text{A.25})$$

$$\chi_i''^{(3)} = -\frac{4}{3} \frac{c \epsilon_0 n_i^2 \lambda}{\pi} \alpha_{2,i} \quad (\text{A.26})$$

where n_2 is the optical Kerr coefficient and α_2 is the two-photon absorption coefficient, the third-order nonlinear terms become

$$P_{NL,i}^{(3)} = \left[n_{0,i}^2 c \epsilon_0^2 n_{2,i} - j \frac{c \epsilon_0^2 n_{0,i}^2 \lambda_i}{\pi} \alpha_{2,i} \right] \gamma_i^3 |F_i|^2 |A_i|^2 A_i \exp[-j\beta_{0,i}z]. \quad (\text{A.27})$$

Also, using

$$\chi_i''^{(5)} = -\frac{16}{5} \frac{c^2 \epsilon_0^2 n_i^3 \lambda}{\pi} \alpha_{3,i} \quad (\text{A.28})$$

which leads to the fifth-order nonlinear term

$$P_{NL,i}^{(5)} = j \frac{2c^2 \epsilon_0^3 n_{0,i}^3}{\pi} \alpha_{3,i} \gamma_i^5 |F_i|^4 F_i |A_i|^4 A_i \exp[-j\beta_{0,i} z]. \quad (\text{A.29})$$

Substituting the nonlinear terms into Eqn. A.22 gives the coupled mode equations

$$\begin{aligned} F_1 & \left[\frac{\partial A_1}{\partial z} - \beta_{1,1} \frac{\partial A_1}{\partial t} + j \frac{1}{2} \beta_{2,1} \frac{\partial^2 A_1}{\partial t^2} + \frac{\alpha_{0,1}}{2} A_1 \right] \\ & + j \frac{2\pi\chi^{(2)}}{\lambda_1 \sqrt{2c\epsilon_0 n_{0,1} n_{0,2} n_{0,3}}} F_2^* F_3 A_2^* A_3 \exp[-j\Delta\beta z] \\ & + \left[j \frac{2\pi n_{2,1}}{\lambda_1} + \frac{1}{2} \alpha_{2,1} \right] |F_1|^2 F_1 |A_1|^2 A_1 + \frac{1}{2} \alpha_{3,1} |F_1|^4 F_1 |A_1|^4 A_1 = 0 \quad (\text{A.30a}) \end{aligned}$$

$$\begin{aligned} F_2 & \left[\frac{\partial A_2}{\partial z} - \beta_{1,2} \frac{\partial A_2}{\partial t} + j \frac{1}{2} \beta_{2,2} \frac{\partial^2 A_2}{\partial t^2} + \frac{\alpha_{0,2}}{2} A_2 \right] \\ & + j \frac{2\pi\chi^{(2)}}{\lambda_2 \sqrt{2c\epsilon_0 n_{0,1} n_{0,2} n_{0,3}}} F_1^* F_3 A_1^* A_3 \exp[-j\Delta\beta z] \\ & + \left[j \frac{2\pi n_{2,2}}{\lambda_2} + \frac{1}{2} \alpha_{2,2} \right] |F_2|^2 F_2 |A_2|^2 A_2 + \frac{1}{2} \alpha_{3,2} |F_2|^4 F_2 |A_2|^4 A_2 = 0 \quad (\text{A.30b}) \end{aligned}$$

$$\begin{aligned} F_3 & \left[\frac{\partial A_3}{\partial z} - \beta_{1,3} \frac{\partial A_3}{\partial t} + j \frac{1}{2} \beta_{2,3} \frac{\partial^2 A_3}{\partial t^2} + \frac{\alpha_{0,3}}{2} A_3 \right] \\ & + j \frac{2\pi\chi^{(2)}}{\lambda_3 \sqrt{2c\epsilon_0 n_{0,1} n_{0,2} n_{0,3}}} F_1 F_2 A_1 A_2 \exp[j\Delta\beta z] \\ & + \left[j \frac{2\pi n_{2,3}}{\lambda_3} + \frac{1}{2} \alpha_{2,3} \right] |F_3|^2 F_3 |A_3|^2 A_3 + \frac{1}{2} \alpha_{3,3} |F_3|^4 F_3 |A_3|^4 A_3 = 0 \quad (\text{A.30c}) \end{aligned}$$

where $\Delta\beta = \beta_{0,3} - \beta_{0,2} - \beta_{0,1}$ is the phase mismatch. Multiplying each equation by F_i^* ,

integrating over x and y , and using Eqn. A.12 yields

$$\begin{aligned} \frac{\partial A_1}{\partial z} - \beta_{1,1} \frac{\partial A_1}{\partial t} + j \frac{1}{2} \beta_{2,1} \frac{\partial^2 A_1}{\partial t^2} + \frac{\alpha_{0,1}}{2} A_1 + \\ j \frac{\kappa_1}{\lambda_1} A_2^* A_3 \exp[-j\Delta\beta z] + \zeta_1^{(3)} |A_1|^2 A_1 + \zeta_1^{(5)} |A_1|^4 A_1 = 0 \quad (\text{A.31a}) \end{aligned}$$

$$\begin{aligned} \frac{\partial A_2}{\partial z} - \beta_{1,2} \frac{\partial A_2}{\partial t} + j \frac{1}{2} \beta_{2,2} \frac{\partial^2 A_2}{\partial t^2} + \frac{\alpha_{0,2}}{2} A_2 + \\ j \frac{\kappa_2}{\lambda_2} A_1^* A_3 \exp[-j\Delta\beta z] + \zeta_2^{(3)} |A_2|^2 A_2 + \zeta_2^{(5)} |A_2|^4 A_2 = 0 \quad (\text{A.31b}) \end{aligned}$$

$$\begin{aligned} \frac{\partial A_3}{\partial z} - \beta_{1,3} \frac{\partial A_3}{\partial t} + j \frac{1}{2} \beta_{2,3} \frac{\partial^2 A_3}{\partial t^2} + \frac{\alpha_{0,3}}{2} A_3 + \\ j \frac{\kappa_3}{\lambda_3} A_1 A_2 \exp[j\Delta\beta z] + \zeta_3^{(3)} |A_3|^2 A_3 + \zeta_3^{(5)} |A_3|^4 A_3 = 0 \quad (\text{A.31c}) \end{aligned}$$

where the second-order nonlinear coupling coefficients are

$$\kappa_i = \frac{2\pi}{\sqrt{2c\epsilon_0 n_{0,1} n_{0,2} n_{0,3}}} f_i^{(2)} \quad (\text{A.32})$$

and the complex second-order overlap integral is

$$f_{1,2}^{(2)} = \iint_{-\infty}^{\infty} \chi^{(2)}(x, y) F_1^* F_2^* F_3 dx dy \quad (\text{A.33})$$

for waves 1 and 2, and

$$f_3^{(2)} = \iint_{-\infty}^{\infty} \chi^{(2)}(x, y) F_1 F_2 F_3^* dx dy \quad (\text{A.34})$$

for wave 3. The third-order nonlinear coefficients are

$$\zeta_i^{(3)} = j \frac{2\pi}{\lambda_i} f_i^{(3)'} + \frac{1}{2} f_i^{(3)''} \quad (\text{A.35})$$

where the overlap integrals are

$$f_i^{(3)'} = \iint_{-\infty}^{\infty} n_{2,i}(x, y) |F_i|^4 dx dy \quad (\text{A.36a})$$

$$f_i^{(3)''} = \iint_{-\infty}^{\infty} \alpha_{2,i}(x, y) |F_i|^4 dx dy. \quad (\text{A.36b})$$

The fifth-order nonlinear coefficients are

$$\zeta_i^{(5)} = \frac{1}{2} f_i^{(5)''} \quad (\text{A.37})$$

where the overlap integrals are

$$f_i^{(5)''} = \iint_{-\infty}^{\infty} \alpha_{3,i}(x, y) |F_i|^6 dx dy. \quad (\text{A.38})$$

In the absence of dispersion (as is the case when in continuous wave), linear loss, and high-order nonlinear effects, the propagation equations simplify to

$$\frac{\partial A_1}{\partial z} = -j \frac{\kappa_1}{\lambda_1} A_2^* A_3 \exp[-j\Delta\beta z] \quad (\text{A.39a})$$

$$\frac{\partial A_2}{\partial z} = -j \frac{\kappa_2}{\lambda_2} A_1^* A_3 \exp[-j\Delta\beta z] \quad (\text{A.39b})$$

$$\frac{\partial A_3}{\partial z} = -j \frac{\kappa_3}{\lambda_3} A_1 A_2 \exp[j\Delta\beta z] \quad (\text{A.39c})$$

which satisfy the Manley-Rowe relation

$$\frac{\partial}{\partial z} |A_1|^2 + \frac{\partial}{\partial z} |A_2|^2 + \frac{\partial}{\partial z} |A_3|^2 = 0. \quad (\text{A.40})$$

A.2 Effective Areas and Nonlinear Coefficients

In a waveguide, the nonlinear coefficients must in general be calculated as in the above equations. Assuming that $\chi^{(2)}$ is uniform within each material layer of the waveguide,

the second-order overlap integral for wave 1 can be expanded such that

$$f_1^{(2)} = \chi_1^{(2)} \iint_1 F_1^* F_2^* F_3 dx dy + \chi_2^{(2)} \iint_2 F_1^* F_2^* F_3 dx dy + \chi_3^{(2)} \iint_3 F_1^* F_2^* F_3 dx dy + \dots \quad (\text{A.41})$$

where $\chi_m^{(2)}$ is the second-order susceptibility for the material in layer m and each integration is taken over the x and y span of each layer. Expansions of the overlap integrals for the other two waves have similar forms. The third-order overlap integrals can be expanded such that

$$f_i^{(3)'} = n_{2,i,1} \iint_1 |F_i|^4 dx dy + n_{2,i,2} \iint_2 |F_i|^4 dx dy + n_{2,i,3} \iint_3 |F_i|^4 dx dy + \dots \quad (\text{A.42a})$$

$$f_i^{(3)''} = \alpha_{2,i,1} \iint_1 |F_i|^4 dx dy + \alpha_{2,i,2} \iint_2 |F_i|^4 dx dy + \alpha_{2,i,3} \iint_3 |F_i|^4 dx dy + \dots \quad (\text{A.42b})$$

The same can be done with the fifth-order overlap integrals:

$$f_i^{(5)''} = \alpha_{3,i,1} \iint_1 |F_i|^6 dx dy + \alpha_{3,i,2} \iint_2 |F_i|^6 dx dy + \alpha_{3,i,3} \iint_3 |F_i|^6 dx dy + \dots \quad (\text{A.43})$$

For further simplicity, the waveguide can be considered to have an effective nonlinear coefficient for the structure as a whole. Thus, to simplify the equations, it can be assumed that the material is uniform in x and y . The equations become

$$f_1^{(2)} = \bar{\chi}^{(2)} \iint_{-\infty}^{\infty} F_1^* F_2^* F_3 dx dy \quad (\text{A.44a})$$

$$f_i^{(3)'} = \bar{n}_{2,i} \iint_{-\infty}^{\infty} |F_i|^4 dx dy \quad (\text{A.44b})$$

$$f_i^{(3)''} = \bar{\alpha}_{2,i} \iint_{-\infty}^{\infty} |F_i|^4 dx dy \quad (\text{A.44c})$$

$$f_i^{(5)''} = \bar{\alpha}_{3,i} \iint_{-\infty}^{\infty} |F_i|^6 dx dy. \quad (\text{A.44d})$$

The integrals over the normalized field distributions can be rewritten in terms of the

non-normalized distributions \tilde{F}_i to give the second-order effective area

$$A_{\text{eff},1}^{(2)} = \frac{\left[\iint_{-\infty}^{\infty} |\tilde{F}_1|^2 dx dy \right] \left[\iint_{-\infty}^{\infty} |\tilde{F}_2|^2 dx dy \right] \left[\iint_{-\infty}^{\infty} |\tilde{F}_3|^2 dx dy \right]}{\left[\iint_{-\infty}^{\infty} \tilde{F}_1^* \tilde{F}_2^* \tilde{F}_3 dx dy \right]^2}. \quad (\text{A.45})$$

For waves 1 and 2, $A_{\text{eff},1}^{(2)} = A_{\text{eff},2}^{(2)}$. For wave 3, $A_{\text{eff},3}^{(2)} = A_{\text{eff},1}^{(2)*}$ since the denominator is the complex conjugate of that shown above. The third-order effective areas are

$$A_{\text{eff},i}^{(3)} = \frac{\left[\iint_{-\infty}^{\infty} |\tilde{F}_i|^2 dx dy \right]^2}{\iint_{-\infty}^{\infty} |\tilde{F}_i|^4 dx dy}, \quad (\text{A.46})$$

and the fifth-order areas are

$$A_{\text{eff},i}^{(5)} = \left[\frac{\left[\iint_{-\infty}^{\infty} |\tilde{F}_i|^2 dx dy \right]^3}{\iint_{-\infty}^{\infty} |\tilde{F}_i|^6 dx dy} \right]^{1/2}. \quad (\text{A.47})$$

Thus, the second-order coupling coefficient becomes

$$\kappa_i = \frac{2\pi}{\sqrt{2c\epsilon_0 n_{0,1} n_{0,2} n_{0,3} A_{\text{eff},i}^{(2)}}} \bar{\chi}^{(2)}, \quad (\text{A.48})$$

the third-order coefficients are

$$\zeta_i^{(3)} = j \frac{2\pi}{\lambda_i} \frac{\bar{n}_{2,i}}{A_{\text{eff}}^{(3)}} + \frac{1}{2} \frac{\bar{\alpha}_{2,i}}{A_{\text{eff}}^{(3)}} \quad (\text{A.49})$$

and the fifth-order nonlinear coefficients are

$$\zeta_i^{(5)} = \frac{1}{2} \frac{\bar{\alpha}_{3,i}}{(A_{\text{eff}}^{(5)})^2}. \quad (\text{A.50})$$

Furthermore, if each integral in Eqn. A.41 is expanded in the same way such that

$$A_{\text{eff},m}^{(2)} = \frac{\left[\iint_{-\infty}^{\infty} |\tilde{F}_1|^2 dx dy \right] \left[\iint_{-\infty}^{\infty} |\tilde{F}_2|^2 dx dy \right] \left[\iint_{-\infty}^{\infty} |\tilde{F}_3|^2 dx dy \right]}{\left[\iint_m \tilde{F}_1^* \tilde{F}_2^* \tilde{F}_3 dx dy \right]^2} \quad (\text{A.51})$$

is the effective mode overlap area for material layer m , the ratio of the effective susceptibility and overlap of the waveguide can be written as the sum of the individual susceptibility/area ratios of each layer:

$$\frac{\bar{\chi}^{(2)}}{\sqrt{A_{\text{eff}}^{(2)}}} = \frac{\chi_1^{(2)}}{\sqrt{A_{\text{eff},1}^{(2)}}} + \frac{\chi_2^{(2)}}{\sqrt{A_{\text{eff},2}^{(2)}}} + \frac{\chi_3^{(2)}}{\sqrt{A_{\text{eff},3}^{(2)}}} + \dots \quad (\text{A.52})$$

Also, the third-order effective areas for each layer can be written as

$$A_{\text{eff},i,m}^{(3)} = \frac{\left[\iint_{-\infty}^{\infty} |\tilde{F}_i|^2 dx dy \right]^2}{\iint_m |\tilde{F}_i|^4 dx dy}, \quad (\text{A.53})$$

the third-order effective waveguide coefficients are such that

$$\frac{\bar{n}_{2,i}}{A_{\text{eff},i}^{(3)}} = \frac{n_{2,1,i}}{A_{\text{eff},1,i}^{(3)}} + \frac{n_{2,1,i}}{A_{\text{eff},2,i}^{(3)}} + \frac{n_{2,3,i}}{A_{\text{eff},3,i}^{(3)}} + \dots \quad (\text{A.54a})$$

$$\frac{\bar{\alpha}_{2,i}}{A_{\text{eff},i}^{(3)}} = \frac{\alpha_{2,1,i}}{A_{\text{eff},1,i}^{(3)}} + \frac{\alpha_{2,1,i}}{A_{\text{eff},2,i}^{(3)}} + \frac{\alpha_{2,3,i}}{A_{\text{eff},3,i}^{(3)}} + \dots \quad (\text{A.54b})$$

and the fifth-order effective waveguide coefficients are such that

$$\frac{\bar{\alpha}_{3,i}}{(A_{\text{eff},i}^{(3)})^2} = \frac{\alpha_{3,1,i}}{(A_{\text{eff},1,i}^{(3)})^2} + \frac{\alpha_{3,1,i}}{(A_{\text{eff},2,i}^{(3)})^2} + \frac{\alpha_{3,3,i}}{(A_{\text{eff},3,i}^{(3)})^2} + \dots \quad (\text{A.55})$$

A.3 Second-Harmonic Generation

In the case of Type-I second-harmonic generation, there are only two waves in the interaction: the fundamental at frequency ω and the second-harmonic at frequency 2ω . The

second-order nonlinear polarizations are

$$P_{NL,\omega}^{(2)} = \epsilon_0 \chi^{(2)} \tilde{E}_\omega^* \tilde{E}_{2\omega} \quad (\text{A.56a})$$

$$P_{NL,2\omega}^{(2)} = \frac{1}{2} \epsilon_0 \chi^{(2)} \tilde{E}_\omega \tilde{E}_\omega. \quad (\text{A.56b})$$

The propagation equations become

$$\begin{aligned} \frac{\partial A_\omega}{\partial z} - \beta_{1,\omega} \frac{\partial A_\omega}{\partial t} + j \frac{1}{2} \beta_{2,\omega} \frac{\partial^2 A_\omega}{\partial t^2} + \frac{\alpha_{0,\omega}}{2} A_\omega \\ + j \frac{\kappa_\omega}{\lambda_\omega} A_\omega^* A_{2\omega} \exp[-j\Delta\beta z] + \zeta_\omega^{(3)} |A_\omega|^2 A_\omega + \zeta_\omega^{(5)} |A_\omega|^4 A_\omega = 0 \end{aligned} \quad (\text{A.57a})$$

$$\begin{aligned} \frac{\partial A_{2\omega}}{\partial z} - \beta_{1,2\omega} \frac{\partial A_{2\omega}}{\partial t} + j \beta_{2,2\omega} \frac{\partial^2 A_{2\omega}}{\partial t^2} + \frac{\alpha_{0,2\omega}}{2} A_{2\omega} \\ + j \frac{\kappa_{2\omega}}{\lambda_\omega} A_\omega A_{2\omega} \exp[j\Delta\beta z] + \zeta_{2\omega}^{(3)} |A_{2\omega}|^2 A_{2\omega} + \zeta_{2\omega}^{(5)} |A_{2\omega}|^4 A_{2\omega} = 0 \end{aligned} \quad (\text{A.57b})$$

where $\Delta\beta = \beta_{2\omega} - 2\beta_\omega$ and

$$\kappa_\omega = \pi \chi^{(2)} \sqrt{\frac{2}{c \epsilon_0 n_\omega^2 n_{2\omega} A_{\text{eff}}^{(2)}}} \quad (\text{A.58})$$

and

$$\kappa_{2\omega} = \pi \chi^{(2)} \sqrt{\frac{2}{c \epsilon_0 n_\omega^2 n_{2\omega} A_{\text{eff}}^{(2)*}}} \quad (\text{A.59})$$

The second-order effective area for the waveguide is defined as

$$A_{\text{eff}}^{(2)} = \frac{\left[\iint_{-\infty}^{\infty} |\tilde{F}_\omega|^2 dx dy \right]^2 \left[\iint_{-\infty}^{\infty} |\tilde{F}_{2\omega}|^2 dx dy \right]}{\left[\iint_{-\infty}^{\infty} \tilde{F}_\omega^* \tilde{F}_\omega^* \tilde{F}_{2\omega} \tilde{F}_{2\omega} dx dy \right]^2}. \quad (\text{A.60})$$

In the simple case with no dispersion, loss, or high-order nonlinear effects, the equations become

$$\frac{\partial A_\omega}{\partial z} = -j \frac{\kappa_\omega}{\lambda_\omega} A_\omega^* A_{2\omega} \exp[-j\Delta\beta z] \quad (\text{A.61a})$$

$$\frac{\partial A_{2\omega}}{\partial z} = -j \frac{\kappa_{2\omega}}{\lambda_\omega} A_\omega A_\omega \exp[j\Delta\beta z] \quad (\text{A.61b})$$

which are found to satisfy the Manley-Rowe relation

$$\frac{\partial |A_\omega|^2}{\partial z} = -\frac{\partial |A_{2\omega}|^2}{\partial z}. \quad (\text{A.62})$$

Appendix B

Detailed Waveguide Properties

B.1 Effective Mode Index

Refractive indexes for the superlattice layer were calculated using polynomial fits of the original 14:14 GaAs/AlAs superlattice found in Ref. [81]. Since the superlattice used in the devices of this thesis used an altered composition of GaAs/Al_{0.85}Ga_{0.15}As, the index vs. wavelength curves of the as-grown material were shifted in a linear fashion by an amount equivalent to the difference in the photoluminescence peak wavelength. For the intermixed superlattice, the original GaAs/AlAs superlattice values were used. Index values for all other layers of bulk AlGaAs were calculated using the semi-empirical model of Gehrsitz [84].

The effective mode indexes of the ridge waveguides were calculated for several wavelength points around 775 nm and around 1550 nm using the Lumerical MODE Solutions software. These points were then fit to quadratic polynomials such that

$$n_{\text{eff}} = A\lambda^2 + B\lambda + C \quad (\text{B.1})$$

where A, B, and C are coefficients of the fit, and λ is the wavelength in units of meters. These coefficients are listed in Table B.1 for 1.0 μm and 1.3 μm deep waveguides, respectively.

Table B.1: Coefficients for the quadratic regression of the waveguide mode effective index for 1.0 and 1.3 μm deep ridges.

λ Range	Material Type	Polarization	A	B	C
1.0 μm deep waveguides					
1550	as-grown	TE	4.579×10^{10}	-2.413×10^5	3.355
		TM	2.529×10^{10}	-1.691×10^5	3.275
	intermixed	TE	7.651×10^{10}	-3.403×10^5	3.421
		TM	-4.995×10^{10}	5.781×10^4	3.104
775	as-grown	TE	3.701×10^{12}	-7.083×10^6	6.647
		TM	1.911×10^{12}	-3.831×10^6	5.155
	intermixed	TE	1.213×10^{12}	-2.592×10^6	4.568
		TM	1.217×10^{12}	-2.601×10^6	4.571
1.3 μm deep waveguides					
1550	as-grown	TE	4.616×10^{10}	-2.447×10^5	3.357
		TM	2.533×10^{10}	-1.708×10^5	3.276
	intermixed	TE	7.524×10^{10}	-3.381×10^5	3.419
		TM	-4.806×10^{10}	5.040×10^4	3.109
775	as-grown	TE	3.719×10^{12}	-7.114×10^6	6.669
		TM	1.920×10^{12}	-3.846×10^6	5.160
	intermixed	TE	1.216×10^{12}	-2.599×10^6	4.570
		TM	1.368×10^{12}	-2.863×10^6	4.671

B.2 Group Velocity and Dispersion

The group velocity is defined as

$$\nu_g = \frac{1}{\beta_1} = \left(\frac{d\beta}{d\omega} \right)^{-1} \quad (\text{B.2})$$

where β_1 is the group velocity parameter. From the polynomial fits of the effective mode index, β_1 can be calculated as

$$\beta_1 = \frac{C - A\lambda^2}{c} [\text{s/m}] \quad (\text{B.3})$$

where c is the speed of light in a vacuum.

The group velocity dispersion parameter is defined as

$$\beta_2 = \frac{d^2\beta}{d\omega^2}. \quad (\text{B.4})$$

From the polynomial fits of the effective mode index, β_2 can be calculated as

$$\beta_2 = A \frac{\lambda^3}{\pi c^2} [\text{s}^2/\text{m}]. \quad (\text{B.5})$$

B.3 Second-Order Nonlinear Coefficients

Values for the second-order nonlinear susceptibilities of the superlattice were sourced from Ref. [35]. In this work, Hutchings calculated the $\chi^{(2)}$ tensor elements using the $\mathbf{A} \cdot \mathbf{p}$ perturbation method. A spatial Fourier technique was used to account for changes induced by the diffusion of lattice constituents during intermixing. The figures from that reference are replicated in Figure B.1. It was assumed that there is little difference in the $\chi^{(2)}$ values between the GaAs/AlAs superlattice of the reference, and the GaAs/Al_{0.85}Ga_{0.15}As superlattice studied in this thesis near their respective half band gap energies.

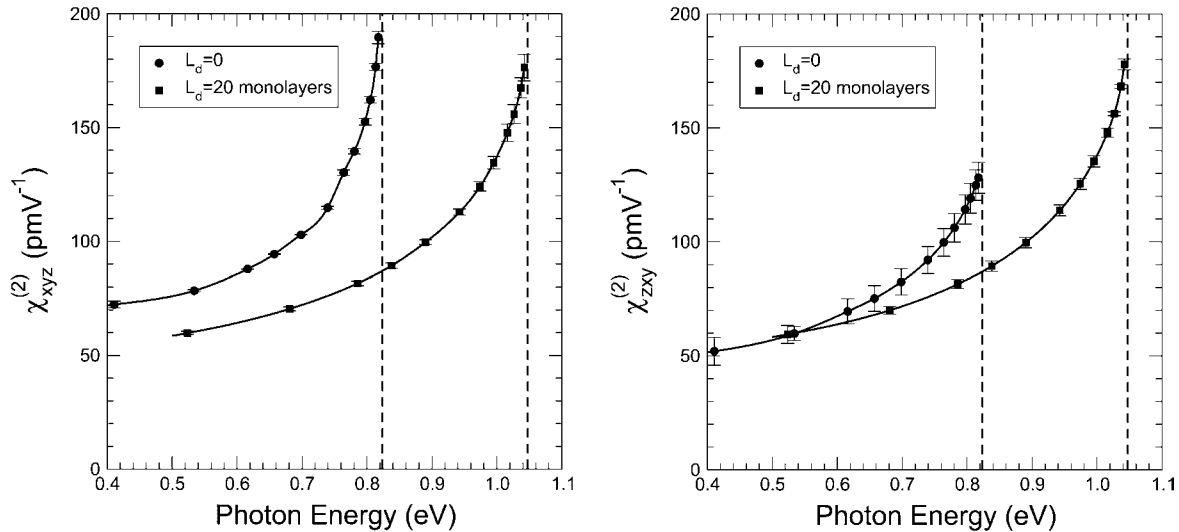


Figure B.1: Theoretical values for $\chi_{xyz}^{(2)}$ and $\chi_{zxy}^{(2)}$ in a 14:14 monolayer GaAs/AlAs superlattice without intermixing ($L_d = 0$), and with intermixing at a diffusion length of 20 monolayers ($L_d = 20$). The dashed lines mark the half band gap energy for both cases. Reproduced with permission from [35]. ©2004, IEEE.

Bibliography

- [1] H.-S. Kim, J.-H. Kim, E. D. Sim, Y. S. Baek, K. H. Kim, O. K. Kwon, and K.-R. Oh, “All-optical wavelength conversion in SOA-based Mach-Zehnder interferometer with monolithically integrated loss-coupled DFB laser diode,” *Semicon. Sci. Tech.*, vol. 19, no. 5, p. 574, 2004.
- [2] J. Leuthold, L. Moller, J. Jaques, S. Cabot, L. Zhang, P. Bernasconi, M. Cappuzzo, L. Gomez, E. Laskowski, E. Chen, A. Wong-Foy, and A. Griffin, “160 Gbit/s SOA all-optical wavelength converter and assessment of its regenerative properties,” *Electron. Lett.*, vol. 40, no. 9, pp. 554–555, 2004.
- [3] Y. Liu, E. Tangdiongga, Z. Li, H. de Waardt, A. Koonen, G. Khoe, X. Shu, I. Bennington, and H. Dorren, “Error-free 320-Gb/s all-optical wavelength conversion using a single semiconductor optical amplifier,” *J. Lightwave Tech.*, vol. 25, no. 1, pp. 103–108, 2007.
- [4] A. C. Turner-Foster, M. A. Foster, R. Salem, A. L. Gaeta, and M. Lipson, “Frequency conversion over two-thirds of an octave in silicon nanowaveguides,” *Opt. Express*, vol. 18, no. 3, pp. 1904–1908, 2010.
- [5] M. Pelusi, F. Luan, S. Madden, D.-Y. Choi, D. Bulla, B. Luther-Davies, and B. Eggleton, “Wavelength conversion of high-speed phase and intensity modulated signals using a highly nonlinear chalcogenide glass chip,” *IEEE Photonics Tech. Lett.*, vol. 22, no. 1, pp. 3–5, 2010.
- [6] P. Martelli, P. Boffi, M. Ferrario, L. Marazzi, P. Parolari, R. Siano, V. Pusino, P. Minzioni, I. Cristiani, C. Langrock, M. M. Fejer, M. Martinelli, and V. Degiorgio,

- “All-optical wavelength conversion of a 100-Gb/s polarization-multiplexed signal,” *Opt. Express*, vol. 17, no. 20, pp. 17 758–17 763, 2009.
- [7] A. J. Zilkie, “High-speed properties of 1.55- μm -wavelength quantum dot semiconductor amplifiers and comparison with higher-dimensional structures,” Ph.D. dissertation, University of Toronto, 2008.
- [8] A. Hugi, R. Maulini, and J. Faist, “External cavity quantum cascade laser,” *Semicon. Sci. Tech.*, vol. 25, no. 8, p. 083001, 2010.
- [9] C. L. Tang and L. K. Cheng, *Fundamentals of Optical Parameteric Processes and Oscillators*, ser. Laser Science and Technology: An International Handbook. Amsterdam: Harwood Academic Publishers GmbH, 1995, vol. 20.
- [10] K. C. Burr, C. L. Tang, M. A. Arbore, and M. M. Fejer, “Broadly tunable mid-infrared femtosecond optical parametric oscillator using all-solid-state-pumped periodically poled lithium niobate,” *Opt. Lett.*, vol. 22, no. 19, pp. 1458–1460, 1997.
- [11] R. Das, S. C. Kumar, G. K. Samanta, and M. Ebrahim-Zadeh, “Broadband, high-power, continuous-wave, mid-infrared source using extended phase-matching bandwidth in MgO:PPLN,” *Opt. Lett.*, vol. 34, no. 24, pp. 3836–3838, 2009.
- [12] Y. Silberberg and P. Smith, “All-optical guided-wave devices for switching and routing,” in *Nonlinear Photonics*, ser. Springer Series in Electronics and Photonics, H. M. Gibbs, G. Khitrova, and N. Peyghambarian, Eds. Berlin: Springer-Verlag, 1990, pp. 185–204.
- [13] V. R. Almeida, C. A. Barrios, R. R. Panepucci, and M. Lipson, “All-optical control of light on a silicon chip,” *Nature*, vol. 431, pp. 1081–1084, 2004.
- [14] B. Analui, D. Guckenberger, D. Kucharski, and A. Narasimha, “A fully integrated 20-Gb/s optoelectronic transceiver implemented in a standard 0.13- μm CMOS SOI technology,” *IEEE J. Solid-St. Circ.*, vol. 41, no. 12, pp. 2945–2955, 2006.

- [15] L. Chen, K. Preston, S. Manipatruni, and M. Lipson, "Integrated GHz silicon photonic interconnect with micrometer-scale modulators and detectors," *Opt. Express*, vol. 17, no. 17, pp. 15 248–15 256, 2009.
- [16] G. Roelkens, L. Liu, D. Liang, R. Jones, A. Fang, B. Koch, and J. Bowers, "III-V/silicon photonics for on-chip and intra-chip optical interconnects," *Laser & Photonics Rev.*, vol. 4, no. 6, 2010.
- [17] P. N. Butcher and D. Cotter, *The Elements of Nonlinear Optics*, ser. Cambridge Studies in Modern Optics. Cambridge, UK: Cambridge University Press, 1990, vol. 9.
- [18] R. Nagarajan, C. Joyner, J. Schneider, R.P., J. Bostak, T. Butrie, A. Dentai, V. Dominic, P. Evans, M. Kato, M. Kauffman, D. Lambert, S. Mathis, A. Mathur, R. Miles, M. Mitchell, M. Missey, S. Murthy, A. Nilsson, F. Peters, S. Pennypacker, J. Pleumeekers, R. Salvatore, R. Schlenker, R. Taylor, H.-S. Tsai, M. Van Leeuwen, J. Webjorn, M. Ziari, D. Perkins, J. Singh, S. Grubb, M. Reffle, D. Mehuyts, F. Kish, and D. Welch, "Large-scale photonic integrated circuits," *IEEE J. Sel. Top. Quantum Electron.*, vol. 11, no. 1, pp. 50–65, 2005.
- [19] R. Nagarajan, M. Kato, J. Pleumeekers, P. Evans, D. Lambert, A. Chen, V. Dominic, A. Mathur, P. Chavarkar, M. Missey, A. Dentai, S. Hurt, J. Back, R. Muthiah, S. Murthy, R. Salvatore, S. Grubb, C. Joyner, J. Rossi, R. Schneider, M. Ziari, F. Kish, and D. Welch, "Single-chip 40 channel InP transmitter photonic integrated circuit capable of aggregate date rate of 1.6Tbit/s," *Elect. Lett.*, vol. 42, no. 13, pp. 771–772, 2006.
- [20] T. Koch and U. Koren, "Semiconductor photonic integrated circuits," *IEEE J. Quantum Electron.*, vol. 27, no. 3, pp. 641–653, 1991.
- [21] V. Tolstikhin, A. Densmore, K. Pimenov, Y. Logvin, F. Wu, S. Lafraimboise, and S. Grabtchak, "Monolithically integrated optical channel monitor for DWDM transmission systems," *J. Lightwave Tech.*, vol. 22, no. 1, pp. 146–153, 2004.

- [22] J. Aitchison, D. Hutchings, J. Kang, G. Stegeman, and A. Villeneuve, "The nonlinear optical properties of AlGaAs at the half band gap," *IEEE J. Quantum Electron.*, vol. 33, no. 3, pp. 341–348, 1997.
- [23] M. M. Choy and R. L. Byer, "Accurate second-order susceptibility measurements of visible and infrared nonlinear crystals," *Phys. Rev. B.*, vol. 14, no. 4, pp. 1693–1706, 1976.
- [24] D. C. Hutchings, "Integrated self-pumped optical frequency conversion and generation in semiconductor waveguides," University of Glasgow, research proposal, March 9, 2006 2006.
- [25] M. Sorel, P. J. R. Laybourn, G. Giuliani, and S. Donati, "Unidirectional bistability in semiconductor waveguide ring lasers," *Appl. Phys. Lett.*, vol. 80, no. 17, pp. 3051–3053, 2002.
- [26] J. H. Marsh, "Quantum well intermixing," *Semicond. Sci. Tech.*, vol. 6, pp. 1136–1155, 1993.
- [27] B. Tell, J. Shah, P. M. Thomas, K. F. Brown-Goebeler, A. DiGiovanni, B. I. Miller, and U. Koren, "Phosphorus ion implantation induced intermixing of InGaAs-InP quantum well structures," *Appl. Phys. Lett.*, vol. 54, no. 16, pp. 1570–1572, 1989.
- [28] A. McKee, C. McLean, G. Lullo, A. Bryce, R. De La Rue, J. Marsh, and C. Button, "Monolithic integration in InGaAs-InGaAsP multiple-quantum-well structures using laser intermixing," *IEEE J. Quantum Electron.*, vol. 33, no. 1, pp. 45–55, 1997.
- [29] B. S. Ooi, K. McIlvaney, M. Street, A. Helmy, S. Ayling, A. Bryce, J. Marsh, and J. Roberts, "Selective quantum-well intermixing in GaAs-AlGaAs structures using impurity-free vacancy diffusion," *IEEE J. Quantum Electron.*, vol. 33, no. 10, pp. 1784–1793, 1997.
- [30] J. S. Aitchison, C. J. Hamilton, M. W. Street, N. D. Whitbread, D. C. Hutchings, J. H. Marsh, G. T. Kennedy, and W. Sibbett, "Control of the second- and third-

- order nonlinearities in GaAs-AlGaAs multiple quantum wells,” *Pure Appl. Opt.*, vol. 7, no. 2, pp. 327–333, 1998.
- [31] A. M. Kan’an, P. LiKamWa, Mitra-Dutta, and J. Pamulapati, “Area-selective disordering of multiple quantum well structures and its applications to all-optical devices,” *J. Appl. Phys.*, vol. 80, no. 6, pp. 3179–3183, 1996.
- [32] C. Kim, D. May-Arrioja, P. LiKamWa, P. Newman, and J. Pamulapati, “Ultrafast all-optical multiple quantum well integrated optic switch,” *Electron. Lett.*, vol. 36, no. 23, pp. 1929–1930, 2000.
- [33] A. Yariv and P. Yeh, *Photonics: optical electronics in modern communications*, 6th ed. Oxford, UK: Oxford University Press, 2007.
- [34] P. Scrutton, M. Sorel, D. C. Hutchings, J. S. Aitchison, and A. S. Helmy, “Characterizing bandgap gratings in GaAs:AlAs superlattice structures using interface phonons,” *IEEE Photon. Tech. Lett.*, vol. 19, no. 9, pp. 677–679, 2007.
- [35] D. Hutchings, “Theory of ultrafast nonlinear refraction in semiconductor superlattices,” *IEEE J. Sel. Top. Quantum Electron.*, vol. 10, no. 5, pp. 1124–1132, 2004.
- [36] A. S. Helmy, D. C. Hutchings, T. C. Kleckner, J. H. Marsh, A. C. Bryce, J. M. Arnold, C. R. Stanley, J. S. Aitchison, C. T. A. Brown, K. Moutzouris, and M. Ebrahimzadeh, “Quasi phase matching in GaAs-AlAs superlattice waveguides through bandgap tuning by use of quantum-well intermixing,” *Opt. Lett.*, vol. 25, no. 18, pp. 1370–1372, 2000.
- [37] D. C. Hutchings, “Modulation of the second-order susceptibility in GaAs/AlAs superlattices,” *Appl. Phys. Lett.*, vol. 76, no. 11, pp. 1362–1364, 2000.
- [38] A. Chowdhury and L. McCaughan, “Continuously phase-matched M-waveguides for second-order nonlinear upconversion,” *IEEE Photonics Technol. Lett.*, vol. 12, no. 5, pp. 486–488, 2000.

- [39] S. V. Rao, K. Moutzouris, and M. Ebrahmizadeh, "Nonlinear frequency conversion in semiconductor optical waveguides using birefringent, modal and quasi-phase-matching techniques," *J. Opt. A: Pure Appl. Opt.*, vol. 6, pp. 569–584, 2004.
- [40] A. S. Helmy, P. Abolghasem, J. S. Aitchison, B. J. Bijlani, J. Han, B. M. Holmes, D. Hutchings, U. Younis, and S. J. Wagner, "Recent advances in phase matching of second-order nonlinearities in monolithic semiconductor waveguides," *Laser Photonics Reviews*, 2010.
- [41] K. Moutzouris, S. V. Rao, M. Ebrahimzadeh, A. D. Rossi, V. Berger, M. Calligaro, and V. Ortiz, "Efficient second-harmonic generation in birefringently phase-matched GaAs/Al₂O₃ waveguides," *Opt. Lett.*, vol. 26, no. 22, pp. 1785–1787, 2001.
- [42] M. Ravaro, M. L. Du, J.-P. Likforman, S. Ducci, V. Berger, G. Leo, and X. Marcadet, "Estimation of parametric gain in GaAs/AlO_x waveguides by fluorescence and second harmonic generation measurements," *Appl. Phys. Lett.*, vol. 91, no. 19, pp. 191110–3, 2007.
- [43] A. Fiore, V. Berger, E. Rosencher, P. Bravetti, and J. Nagle, "Phase matching using an isotropic nonlinear optical material," *Nature*, vol. 391, pp. 463–466, 1998.
- [44] A. De Rossi, V. Berger, M. Calligaro, G. Leo, V. Ortiz, and X. Marcadet, "Parametric fluorescence in oxidized aluminum gallium arsenide waveguides," *Appl. Phys. Lett.*, vol. 79, no. 23, pp. 3758–3760, 2001.
- [45] L. Scaccabarozzi, M. M. Fejer, Y. Huo, S. Fan, X. Yu, and J. S. Harris, "Enhanced second-harmonic generation in AlGaAs/Al_xO_y tightly confining waveguides and resonant cavities," *Opt. Lett.*, vol. 31, no. 24, pp. 3626–3628, 2006.
- [46] E. Guillotel, M. Ravaro, F. Ghiglieno, C. Langlois, C. Ricolleau, S. Ducci, I. Favero, and G. Leo, "Parametric amplification in GaAs/AlO_x waveguide," *Appl. Phys. Lett.*, vol. 94, no. 17, pp. 171110–3, 2009.
- [47] K. Moutzouris, S. V. Rao, M. Ebrahimzadeh, A. De Rossi, M. Calligaro, V. Ortiz, and V. Berger, "Second-harmonic generation through optimized modal phase

- matching in semiconductor waveguides,” *Appl. Phys. Lett.*, vol. 83, no. 4, pp. 620–622, 2003.
- [48] S. Ducci, L. Lanco, V. Berger, A. De Rossi, V. Ortiz, and M. Calligaro, “Continuous-wave second-harmonic generation in modal phase matched semiconductor waveguides,” *Appl. Phys. Lett.*, vol. 84, no. 16, pp. 2974–2976, 2004.
- [49] A. S. Helmy, “Phase matching using Bragg reflection waveguides for monolithic nonlinear optics applications,” *Opt. Express*, vol. 14, no. 3, pp. 1243–1252, 2006.
- [50] B. R. West and A. S. Helmy, “Dispersion tailoring of the quarter-wave bragg reflection waveguide,” *Opt. Express*, vol. 14, no. 9, pp. 4073–4086, 2006.
- [51] A. S. Helmy, B. Bijlani, and P. Abolghasem, “Phase matching in monolithic Bragg reflection waveguides,” *Opt. Lett.*, vol. 32, no. 16, pp. 2399–2401, 2007.
- [52] B. Bijlani, P. Abolghasem, and A. S. Helmy, “Second harmonic generation in ridge Bragg reflection waveguides,” *Appl. Phys. Lett.*, vol. 92, no. 10, pp. 101124–3, 2008.
- [53] P. Abolghasem, J. Han, B. Bijlani, A. Arjmand, and A. Helmy, “Highly efficient second-harmonic generation in monolithic matching layer enhanced $\text{Al}_{1-x}\text{Ga}_x\text{As}$ Bragg reflection waveguides,” *IEEE Photon. Technol. Lett.*, vol. 21, no. 19, pp. 1462–1464, 2009.
- [54] J.-B. Han, P. Abolghasem, D. Kang, B. J. Bijlani, and A. S. Helmy, “Difference-frequency generation in AlGaAs bragg reflection waveguides,” *Opt. Lett.*, vol. 35, no. 14, pp. 2334–2336, 2010.
- [55] J. A. Armstrong, N. Bloembergen, J. Ducuing, and P. S. Pershan, “Interactions between light waves in a nonlinear dielectric,” *Phys. Rev.*, vol. 127, no. 6, pp. 1918–1939, 1962.
- [56] S. J. B. Yoo, R. Bhat, C. Caneau, and M. A. Koza, “Quasi-phase-matched second-harmonic generation in AlGaAs waveguides with periodic domain inversion achieved by wafer-bonding,” *Appl. Phys. Lett.*, vol. 66, pp. 3610–3412, 1995.

- [57] S. J. B. Yoo, C. Caneau, R. Bhat, M. A. Koza, A. Rajhel, and N. Antoniades, "Wavelength conversion by difference frequency generation in AlGaAs waveguides with periodic domain inversion achieved by wafer bonding," *Appl. Phys. Lett.*, vol. 68, no. 19, pp. 2609–2611, 1996.
- [58] C. B. Ebert, L. A. Eyres, M. M. Fejer, and J. S. Harris, "MBE growth of antiphase GaAs films using GaAs/Ge/GaAs heteroepitaxy," *J. Cryst. Growth*, vol. 201-202, pp. 187–193, 1999.
- [59] X. Yu, L. Scaccabarozzi, A. C. Lin, M. M. Fejer, and J. S. Harris, "Growth of GaAs with orientation-patterned structures for nonlinear optics," *J. Cryst. Growth*, vol. 301-302, pp. 163–167, 2007.
- [60] T. Kondo and I. Shoji, "Study on wavelength conversion by compound-semiconductor-base quasi phase-matching devices," in *Photonics Based on Wavelength Integration and Manipulation*, K. Tada, T. Suhara, K. Kikuchi, Y. Kokubun, K. Utaka, M. Asada, F. Koyama, and T. Arakawa, Eds. Tokyo: Institute of Pure and Applied Physics, 2005, pp. 151–160.
- [61] T. Skauli, K. L. Vodopyanov, T. J. Pinguet, A. Schober, O. Levi, L. A. Eyres, M. M. Fejer, J. S. Harris, B. Gerard, L. Becouarn, E. Lallier, and G. Arisholm, "Measurement of the nonlinear coefficient of orientation-patterned GaAs and demonstration of highly efficient second-harmonic generation," *Opt. Lett.*, vol. 27, no. 8, pp. 628–630, 2002.
- [62] X. Yu, L. Scaccabarozzi, O. Levi, T. J. Pinguet, M. M. Fejer, and J. S. Harris, Jr., "Template design and fabrication for low-loss orientation-patterned nonlinear AlGaAs waveguides pumped at 1.55 μm ," *J. Cryst. Growth*, vol. 251, no. 1-4, pp. 794–799, 2003.
- [63] X. Yu, L. Scaccabarozzi, J. J. S. Harris, P. S. Kuo, and M. M. Fejer, "Efficient continuous wave second harmonic generation pumped at 1.55 μm in quasi-phase-matched AlGaAs waveguides," *Opt. Express*, vol. 13, no. 26, pp. 10 742–10 748, 2005.

- [64] P. S. Kuo, K. L. Vodopyanov, M. M. Fejer, D. M. Simanovskii, X. Yu, J. S. Harris, D. Bliss, and D. Weyburne, “Optical parametric generation of a mid-infrared continuum in orientation-patterned GaAs,” *Opt. Lett.*, vol. 31, no. 1, pp. 71–73, 2006.
- [65] J. Schaar, K. Vodopyanov, P. Kuo, M. Fejer, X. Yu, A. Lin, J. Harris, D. Bliss, C. Lynch, V. Kozlov, and W. Hurlbut, “Terahertz sources based on intracavity parametric down-conversion in quasi-phase-matched gallium arsenide,” *IEEE J. Sel. Topics Quantum Electron.*, vol. 14, no. 2, pp. 354–362, 2008.
- [66] G. Bloom, A. Grisard, E. Lallier, C. Larat, M. Carras, and X. Marcadet, “Optical parametric amplification of a distributed-feedback quantum-cascade laser in orientation-patterned GaAs,” *Opt. Lett.*, vol. 35, no. 4, pp. 505–507, 2010.
- [67] J. Ota, W. Narita, I. Ohta, T. Matsushita, and T. Kondo, “Fabrication of periodically-inverted AlGaAs waveguides for quasi-phase-matched wavelength conversion at 1.55 μm,” *Jpn. J. Appl. Phys.*, vol. 48, no. 4, p. 04C110, 2009.
- [68] J. Khurgin, “Large-scale quantum well domain structures,” *J. Appl. Phys.*, vol. 64, no. 10, pp. 5026–5029, 1988.
- [69] A. Fiore, Y. Beaulieu, S. Janz, J. P. McCaffrey, Z. R. Wasilewski, and D. X. Xu, “Quasiphase matched surface emitting second harmonic generation in periodically reversed asymmetric GaAs/AlGaAs quantum well waveguide,” *Appl. Phys. Lett.*, vol. 70, no. 20, pp. 2655–2657, 1997.
- [70] S. Janz, M. Buchanan, P. van der Meer, Z. R. Wasilewski, D.-X. Xu, P. Piva, I. V. Mitchell, U. G. Akano, and A. Fiore, “Patterning the second-order optical nonlinearity of asymmetric quantum wells by ion implantation enhanced intermixing,” *Appl. Phys. Lett.*, vol. 72, no. 24, pp. 3097–3099, 1998.
- [71] D. Artigas, E. Rafailov, P. Loza-Alvarez, and W. Sibbett, “Periodically switched nonlinear structures for frequency conversion: theory and experimental demonstration,” *IEEE J. Quantum Electron.*, vol. 40, no. 8, pp. 1122–1130, 2004.

- [72] E. U. Rafailov, P. Loza-Alvarez, C. T. A. Brown, W. Sibbett, R. M. De La Rue, P. Millar, D. A. Yanson, J. S. Roberts, and P. A. Houston, “Second-harmonic generation from a first-order quasi-phase-matched GaAs/AlGaAs waveguide crystal,” *Opt. Lett.*, vol. 26, no. 24, pp. 1984–1986, 2001.
- [73] S. Janz, M. Buchanan, F. Chatenoud, J. P. McCaffrey, R. Normandin, U. G. Akano, and I. V. Mitchell, “Modification of the second-order optical susceptibility in $\text{Al}_x\text{Ga}_{1-x}\text{As}$ by ion-beam induced amorphization,” *Appl. Phys. Lett.*, vol. 65, no. 2, pp. 216–218, 1994.
- [74] J. Aitchison, M. Street, N. Whitbread, D. Hutchings, J. Marsh, G. Kennedy, and W. Sibbett, “Modulation of the second-order nonlinear tensor components in multiple-quantum-well structures,” *IEEE J. Sel. Topics in Quantum Electron.*, vol. 4, no. 4, pp. 695–700, 1998.
- [75] J.-P. Bouchard, M. Tetu, S. Janz, D.-X. Xu, Z. R. Wasilewski, P. Piva, U. G. Akano, and I. V. Mitchell, “Quasi-phase matched second-harmonic generation in an $\text{Al}_x\text{Ga}_{1-x}\text{As}$ asymmetric quantum-well waveguide using ion-implantation-enhanced intermixing,” *Appl. Phys. Lett.*, vol. 77, no. 26, pp. 4247–4249, 2000.
- [76] D. C. Hutchings and T. C. Kleckner, “Quasi phase matching in semiconductor waveguides by intermixing: optimization considerations,” *J. Opt. Soc. Am. B*, vol. 19, no. 4, pp. 890–894, 2002.
- [77] A. Helmy, N. Johnson, M. Ke, A. Bryce, J. Aitchison, J. Marsh, I. Gontijo, G. Buller, J. Davidson, and P. Dawson, “A study of impurity-free vacancy disordering in GaAs-AlGaAs for improved modeling,” *IEEE J. Sel. Topics in Quantum Electron.*, vol. 4, no. 4, pp. 661–668, 1998.
- [78] A. S. Helmy, A. C. Bryce, D. C. Hutchings, J. S. Aitchison, and J. H. Marsh, “Band gap gratings using quantum well intermixing for quasi-phase-matching,” *J. Appl. Phys.*, vol. 100, no. 12, pp. 123 107–8, 2006.

- [79] K. Zeaiter, D. C. Hutchings, R. M. Gwilliam, K. Moutzouris, S. V. Rao, and M. Ebrahimzadeh, “Quasi-phase-matched second-harmonic generation in a GaAs/AlAs superlattice waveguide by ion-implantation-induced intermixing,” *Opt. Lett.*, vol. 28, no. 11, pp. 911–913, 2003.
- [80] D. C. Hutchings, M. Sorel, K. Zeaiter, A. J. Zilkie, B. Leesti, A. S. Helmy, P. W. E. Smith, and J. S. Aitchison, “Quasi-phase-matched second harmonic generation with picosecond pulses in GaAs/AlAs superlattice waveguides,” in *Proceedings Nonlinear Guided Waves*. Toronto, Canada: OSA, 2004.
- [81] S. J. Wagner, “The nonlinear optical properties of GaAs/AlAs superlattice-core waveguides at telecommunications wavelengths,” M.A.Sc. thesis, University of Toronto, 2006.
- [82] P.-C. Ku and C. Chang-Hasnain, “Thermal oxidation of AlGaAs: modeling and process control,” *IEEE J. Quantum Electron.*, vol. 39, no. 4, pp. 577–585, 2003.
- [83] S. Adachi, “GaAs, AlAs, and $\text{Al}_x\text{Ga}_{1-x}\text{As}$: Material parameters for use in research and device applications,” *J. Appl. Phys.*, vol. 58, no. 3, pp. R1–R29, 1985.
- [84] S. Gehrsitz, F. K. Reinhart, C. Gourgon, N. Herres, A. Vonlanthen, and H. Sigg, “The refractive index of $\text{Al}_x\text{Ga}_{1-x}\text{As}$ below the band gap: Accurate determination and empirical modeling,” *J. Appl. Phys.*, vol. 87, no. 11, pp. 7825–7837, 2000.
- [85] T. C. Kleckner, “Quasi-phase-matched nonlinear frequency conversion in periodically disordered GaAs/AlAs superlattice-core waveguides,” Ph.D. dissertation, University of Glasgow, 2002.
- [86] V. Ramaswamy, “Strip-loaded film waveguides,” *Bell Sys. Tech. J.*, vol. 53, no. 4, pp. 697–704, 1974.
- [87] E. Kapon and R. Bhat, “Low-loss single-mode GaAs/AlGaAs optical waveguides grown by organometallic vapor phase epitaxy,” *Appl. Phys. Lett.*, vol. 50, no. 23, pp. 1628–1630, 1987.

- [88] B. S. Wherrett, "Scaling rules for multiphoton interband absorption in semiconductors," *J. Opt. Soc. Am. B*, vol. 1, no. 1, pp. 67–72, 1984.
- [89] J. U. Kang, "Spatial solitons in AlGaAs waveguides," Ph.D. dissertation, University of Central Florida, 1996.
- [90] S. J. Wagner, B. M. Holmes, U. Younis, A. S. Helmy, D. C. Hutchings, and J. S. Aitchison, "Controlling third-order nonlinearities by ion-implantation quantum-well intermixing," *IEEE Photon. Tech. Lett.*, vol. 21, no. 2, pp. 85–87, 2009.
- [91] D. Modotto, J. P. Mondia, S. Linden, H. W. Tan, R. Morandotti, T. C. Kleckner, A. Locatelli, C. D. Angelis, H. M. v. Driel, C. R. Stanley, and J. S. Aitchison, "Asymmetric spectrum evolution of high power short pulses in AlGaAs," *Opt. Communications*, vol. 249, pp. 201–208, 2005.
- [92] G. P. Agrawal, *Nonlinear Fiber Optics*, 4th ed. San Diego: Academic Press, 2007.
- [93] M. Sheik-Bahae, D. Hutchings, D. Hagan, and E. Van Stryland, "Dispersion of bound electron nonlinear refraction in solids," *IEEE J. Quantum Electron.*, vol. 27, no. 6, pp. 1296–1309, 1991.
- [94] M. Alsunaidi, H. Masoudi, and J. Arnold, "A time-domain algorithm for the analysis of second-harmonic generation in nonlinear optical structures," *IEEE Photonics Tech. Lett.*, vol. 12, no. 4, pp. 395–397, 2000.
- [95] N. C. Kothari and X. Carlotti, "Transient second-harmonic generation: influence of effective group-velocity dispersion," *J. Opt. Soc. Am. B*, vol. 5, no. 4, pp. 756–764, 1988.
- [96] M. Bortz, S. Field, M. Fejer, D. Nam, R. Waarts, and D. Welch, "Noncritical quasi-phase-matched second harmonic generation in an annealed proton-exchanged LiNbO₃ waveguide," *IEEE J. Quantum Electron.*, vol. 30, no. 12, pp. 2953–2960, 1994.

- [97] T. Kleckner, A. Helmy, K. Zeaiter, D. Hutchings, and J. Aitchison, “Dispersion and modulation of the linear optical properties of GaAs-AlAs superlattice waveguides using quantum-well intermixing,” *IEEE J. Quantum Electron.*, vol. 42, no. 3, pp. 280–286, 2006.
- [98] D. Hutchings, S. Wagner, B. Holmes, U. Younis, A. Helmy, and J. Aitchison, “Type-II quasi phase matching in periodically intermixed semiconductor superlattice waveguides,” *Opt. Lett.*, vol. 35, no. 8, pp. 1299–1301, 2010.
- [99] G. Priem, P. Dumon, W. Bogaerts, D. Van Thourhout, G. Morthier, and R. Baets, “Optical bistability and pulsating behaviour in silicon-on-insulator ring resonator structures,” *Opt. Express*, vol. 13, no. 23, pp. 9623–9628, 2005.
- [100] S. J. Wagner, B. M. Holmes, U. Younis, A. S. Helmy, J. S. Aitchison, and D. C. Hutchings, “Continuous wave second-harmonic generation using domain-disordered quasi-phase matching waveguides,” *Appl. Phys. Lett.*, vol. 94, no. 15, pp. 151107–3, 2009.
- [101] M. H. Chou, I. Brener, K. R. Parameswaran, and M. M. Fejer, “Stability and bandwidth enhancement of difference frequency generation (DFG)-based wavelength conversion by pump detuning,” *Electron. Lett.*, vol. 35, no. 12, pp. 978–980, 1999.
- [102] B. S. Wherrett and D. C. Hutchings, “Optical bistability,” in *Nonlinear Optics in Signal Processing*, R. W. Eason and A. Miller, Eds. London, UK: Chapman Hall, 1993, pp. 145–189.
- [103] G. Sonek, J. Ballantyne, Y. Chen, G. Carter, S. Brown, E. Koteles, and J. Salerno, “Dielectric properties of GaAs/AlGaAs multiple quantum well waveguides,” *IEEE J. Quantum Electron.*, vol. 22, no. 7, pp. 1015–1018, 1986.
- [104] H. P. Wagner, M. Khnelt, W. Langbein, and J. M. Hvam, “Dispersion of the second-order nonlinear susceptibility in ZnTe, ZnSe, and ZnS,” *Phys. Rev. B*, vol. 58, no. 16, pp. 10 494–10 501, 1998.

- [105] S. N. Rashkeev, W. R. L. Lambrecht, and B. Segall, "Efficient ab initio method for the calculation of frequency-dependent second-order optical response in semiconductors," *Phys. Rev. B*, vol. 57, no. 7, pp. 3905–3919, 1998.
- [106] J. L. P. Hughes and J. E. Sipe, "Calculation of second-order optical response in semiconductors," *Phys. Rev. B*, vol. 53, no. 16, pp. 10751–10763, 1996.
- [107] L. E. Myers, R. C. Eckardt, M. M. Fejer, R. L. Byer, W. R. Bosenberg, and J. W. Pierce, "Quasi-phase-matched optical parametric oscillators in bulk periodically poled LiNbO₃," *J. Opt. Soc. Am. B*, vol. 12, no. 11, pp. 2102–2116, 1995.
- [108] D. C. Hutchings and J. M. Arnold, "Determination of second-order nonlinear coefficients in semiconductors using pseudospin equations for three-level systems," *Phys. Rev. B*, vol. 56, no. 7, pp. 4056–4067, 1997.
- [109] B. Holmes and D. Hutchings, "Realization of novel low-loss monolithically integrated passive waveguide mode converters," *IEEE Photonics Tech. Lett.*, vol. 18, no. 1, pp. 43–45, 2006.
- [110] D. M. Beggs, M. Midrio, and T. F. Krauss, "Compact polarization rotators for integrated polarization diversity in InP-based waveguides," *Opt. Lett.*, vol. 32, no. 15, pp. 2176–2178, 2007.
- [111] J. Bregenzer, S. McMaster, M. Sorel, B. Holmes, and D. Hutchings, "Compact polarization mode converter monolithically integrated within a semiconductor laser," *J. Lightwave Tech.*, vol. 27, no. 14, pp. 2732–2736, 2009.
- [112] S. Brosnan and R. Byer, "Optical parametric oscillator threshold and linewidth studies," *IEEE J. Quantum Electron.*, vol. 15, no. 6, pp. 415–431, 1979.
- [113] U. Younis, "Monolithic integration for nonlinear optical frequency conversion in semiconductor waveguides," Ph.D. dissertation, University of Glasgow, 2010.
- [114] R. W. Boyd, *Nonlinear Optics*, 3rd ed. Burlington, MA: Academic Press, 2008.

- [115] A. Bryce, F. Camacho, P. Cusumano, and J. Marsh, "CW and mode-locked integrated extended cavity lasers fabricated using impurity free vacancy disordering," *IEEE Sel. Top. Quantum Electron.*, vol. 3, no. 3, pp. 885–892, 1997.
- [116] E. Avrutin, J. Marsh, and E. Portnoi, "Monolithic and multi-gigahertz mode-locked semiconductor lasers: constructions, experiments, models and applications," *IEE Proc. - Optoelectronics*, vol. 147, no. 4, pp. 251–278, 2000.
- [117] M. Menard and A. G. Kirk, "Integrated Fabry-Perot comb filters for optical space switching," *J. Lightwave Tech.*, vol. 28, no. 5, pp. 768–775, 2010.
- [118] H. Rong, R. Jones, A. Liu, O. Cohen, D. Hak, A. Fang, and M. Paniccia, "A continuous-wave Raman silicon laser," *Nature*, vol. 433, pp. 725–728, 2005.
- [119] H. Fukuda, K. Yamada, T. Shoji, M. Takahashi, T. Tsuchizawa, T. Watanabe, J.-i. Takahashi, and S.-i. Itabashi, "Four-wave mixing in silicon wire waveguides," *Opt. Express*, vol. 13, no. 12, pp. 4629–4637, 2005.
- [120] M. R. Lamont, B. Luther-Davies, D.-Y. Choi, S. Madden, and B. J. Eggleton, "Supercontinuum generation in dispersion engineered highly nonlinear ($\gamma = 10$ /w/m) As₂S₃ chalcogenide planar waveguide," *Opt. Express*, vol. 16, no. 19, pp. 14 938–14 944, 2008.
- [121] V. R. Almeida, R. R. Panepucci, and M. Lipson, "Nanotaper for compact mode conversion," *Opt. Lett.*, vol. 28, no. 15, pp. 1302–1304, 2003.
- [122] K. K. Lee, D. R. Lim, L. C. Kimerling, J. Shin, and F. Cerrina, "Fabrication of ultralow-loss Si/SiO₂ waveguides by roughness reduction," *Opt. Lett.*, vol. 26, no. 23, pp. 1888–1890, 2001.
- [123] C. Seibert, D. Hall, D. Liang, and Z. Shellenbarger, "Reduction of AlGaAs heterostructure high-index-contrast ridge waveguide scattering loss by sidewall smoothing through oxygen-enhanced wet thermal oxidation," *IEEE Photonics Tech. Lett.*, vol. 22, no. 1, pp. 18–20, 2010.

- [124] V. Tolstikhin, Y. Logvin, and K. Pimenov, "Integrated optics arrangement for wavelength (de)multiplexing in a multi-grade vertical stack," US Patent 7 444 055 B2, October 28, 2008.
- [125] Z. Zheng, "All-optical waveform recognition and its applications in ultrashort pulses optical CDMA systems," Ph.D. dissertation, Purdue University, 2000.
- [126] J. R. Kurz, "Integrated optical-frequency mixers," Ph.D. dissertation, Stanford University, 2003.